Plasmonic Superstructures via Self-Assembly of Colloidal Building Blocks

DISSERTATION

zur Erlangung des akademischen Grades eines
Doktors der Naturwissenschaften
(Dr. rer. nat.)
an der Universität Bayreuth,
Fakultät für Biologie, Chemie und Geowissenschaften

vorgelegt von

Tobias Honold

geboren in Günzburg

Bayreuth, Juli 2017

Die vorliegende Arbeit wurde in der Zeit von Juli 2013 bis Juli 2017 in Bayreuth am Lehrstuhl Physikalische Chemie I unter der Betreuung von Herrn Professor Dr. Matthias Karg angefertigt.

Vollständiger Abdruck der von der Fakultät für Biologie, Chemie und Geowissenschaften der Universität Bayreuth genehmigten Dissertation zur Erlangung des akademischen Grades eines Doktors der Naturwissenschaften (Dr. rer. nat).

Dissertation eingereicht am: 1.08.2017

Zulassung durch die Prüfungskommission: 10.08.2017

Wissenschaftliches Kolloquium: 7.12.2017

Amtierender Dekan: Prof. Dr. Stefan Pfeiffer

Prüfungsausschuss:

Prof. Dr. Matthias Karg (Erstgutachter)
Prof. Dr. Mukundan Thelakkat (Zweitgutachter)
Prof. Dr. Josef Breu (Vorsitz)
Jun.-Prof. Dr. Anna Schenk

Contents

List of Publications

Parts of this work are based on results published in the following peer-reviewed journals:

1. **Honold, T.**; Volk, K.; Rauh, A.; Fitzgerald, J. P. S.; Karg, M. Tunable Plasmonic Surfaces via Colloid Assembly. *J. Mater. Chem. C* **2015**, *3*, 11449–11457.

2. Singh, C. R.; **Honold, T.**; Gujar, T. P.; Retsch, M.; Fery, A.; Karg, M.; Thelakkat, M. The Role of Colloidal Plasmonic Nanostructures in Organic Solar Cells. *Phys. Chem. Chem. Phys.* **2016**, *18*, 23155–23163.

3. **Honold, T.**; Volk, K.; Retsch, M.; Karg, M. Binary Plasmonic Honeycomb Structures: High-Resolution EDX Mapping and Optical Properties. *Colloids Surf., A* **2016**, *510*, 198–204.

4. **Honold, T.**; Skrybeck, D.; Wagner, K. G.; Karg, M. Fully Reversible Quantitative Phase Transfer of Gold Nanoparticles Using Bifunctional PNIPAM Ligands. *Langmuir* **2017**, *33*, 253–261.

Further publications not mentioned in this work:

1. Dubbert, J.; **Honold, T.**; Pedersen, J. S.; Radulescu, A.; Drechsler, M.; Karg, M.; Richtering, W. How Hollow Are Thermoresponsive Hollow Nanogels? *Macromolecules* **2014**, *47*, 8700–8708.

2. Karg, M.; König, T. A. F.; Retsch, M.; Stelling, C.; Reichstein, P. M.; **Honold, T.**; Thelakkat, M.; Fery, A. Colloidal Self-Assembly Concepts for Light Management in Photovoltaics. *Mater. Today* **2015**, *18*, 185–205.

3. Zyuzin, M. V.; **Honold, T.**; Carregal-Romero, S.; Kantner, K.; Karg, M.; Parak, W. J. Influence of Temperature on the Colloidal Stability of Polymer-Coated Gold Nanoparticles in Cell Culture Media. *Small* **2016**, *12*, 1723–1731.

4. Ruckdeschel, P.; Dulle, M.; **Honold, T.**; Förster, S.; Karg, M.; Retsch, M. Monodisperse Hollow Silica Spheres: An In-Depth Scattering Analysis. *Nano Res.* **2016**, *9*, 1366–1376.

5. Rauh, A.; **Honold, T.**; Karg, M. Seeded Precipitation Polymerization for the Synthesis of Gold-Hydrogel Core-Shell Particles: The Role of Surface Functionalization and Seed Concentration. *Colloid. Polym. Sci.* **2016**, *294*, 37–47.

6. **Honold, T.**; Carl, N.; Karg, M. Hydrogel Shell Expansion in Core-Shell Microgels Upon Core Growth. *in preparation.*

List of Abbreviations and Symbols

A	Intercept
$Abs.$	Absorbance
AFM	Atomic force microscopy
α	Rotation angle
α_p	Polarizability
AM	Air mass
B	Baseline
BIS	*N,N'*-methylenebisacrylamide
$\bar{\Gamma}$	Average decay rate
γ	Electron damping
C_{abs}	Absorption cross section
c_i	Concentration of a constituent i in a mixture.
C_{ext}	Extinction cross section
C_{sca}	Scattering cross section
d_{cs}	Overall diameter of a core-shell particle
d_c	Core diameter of a core-shell particle
$d_{cuv.}$	Path length of a UV-Vis cuvette
d_l	Lattice constant
D_P	Periodicity of Moiré patterns
d_s	Shell thickness
D_t	Translational diffusion coefficient
$D_{t,app}$	Apparent diffusion coefficient
d_{c-c}	Interparticle center-to-center distance
d_h	Hydrodynamic diameter
DLS	Dynamic light scattering
E_f	Fermi level
EDX	Energy-dispersive X-ray spectroscopy
ϵ_E	Extinction coefficient
ϵ_i	Dielectric function of component i
ϵ_1	Real part of the dielectric function
ϵ_2	Imaginary part of the dielectric function
ϵ_H	Repulsive strength of the Hertzian interaction potential
EQE	External quantum efficiency
η	Dynamic viscosity

η_j	Photocurrent efficiency
η_{OPV}	Power conversion efficiency
η_{SLS}	Difference of scattering length density
η_{trans}	Efficiency of phase transfer experiments
FF	Fill factor
FFT	Fast fourier transformation
$FWHM$	Full width at half maximum
G	Autocorrelation function
$G(\Gamma)$	Distribution of decay rates
$g(r)$	Radial distribution function
$g^{(1)}(\tau)$	Field-time correlation function
$g^{(2)}(\tau)$	Intensity-time autocorrelation function
h	Hour
$HOMO$	Highest occupied molecular orbital
I	Intensity of scattered light
ITO	Indium tin oxide
IV-curve	Current-voltage curve
J	Current density
k	wave vector
k_B	Boltzmann constant
λ_b	Shell-to-core ratio
λ	Wavelength
L-B trough	Langmuir Blodgett trough
$LCST$	Lower critical solution temperature
LSPR	Localized surface plasmon resonance
$LUMO$	Lowest unoccupied molecular orbital
μ_2	Decay rate distribution
μ_E	Electrophoretic mobility
M_n	Number average molecular weight
M_w	Weight average molecular weight
min	Minute
MIM	Metal-insulator-metal
mol eq.	Molar equivalent
n	Refractive index
PNIPAM	Poly(N-isopropylacrylamide)
NMR	Nuclear magnetic resonance spectroscopy
ω	Angular frequency
ω_p	Plasma frequency
ω_{res}	Resonance frequency
$P(q)$	Form factor
$P_{E,max}$	Maximum generated electric power
P_I	Incident light power

P3HT	Poly-3-hexylthiophene
PCBM	Phenyl-C_{61}-butyric acid methyl ester PCBM
PDI	Polydispersity index
ϕ	Volume fraction
ϕ_w	Work function
PMMA	Poly(methyl methacrylate)
PNIPAM-*co*-AAc	Poly(*N*-isopropylacrylamide-*co*-acrylic acid)
PS	Polystyrene
q	Scattering vector
r	Radius
R_β	Rotation matrix
r_h	Hydrodynamic radius
r_s	Sphere radius
R_S	Series resistance
R_{SH}	Shunt resistance
RAFT	Reversible addition fragmentation chain transfer polymerization
rcf	Relative centrifugal force
r_g	Radius of gyration
ρ_s	Surface density of particles
$\vec{s}$	Stretching vector
S	Stretching factor
SCL-devices	Space charge limited solar cell devices
SEM	Scanning electron microscopy
SEC	Size exclusion chromatography
σ	Sphere diameter
σ_S	Standard deviation
SLS	Static light scattering
T	Temperature
t	Time
τ	Delay time
t_p	Polymerization time
T_s	Transformation matrix
TEM	Transmission electron microscopy
θ	Angle
θ_c	Contact angle
U_{Her}	Hertzian interaction potential
U_{HS}	Interaction potential
UV-Vis	Ultraviolet-visible spectroscopy
V	Volume
VPTT	Volume phase transition temperature
V_{bi}	Build-in potential
V_{OC}	Open-circuit voltage

W	Watt
X	Monomer conversion

Acknowledgements

First and foremost I want to thank my supervisor Prof. Matthias Karg, who cordially invited me to work in his group. Thank you for all the grateful support during my time as a PhD student which helped me to develop myself and grow.

I would also like to thank my colleagues Astrid, Kristina, Kirsten, Julian, and Arne for the good and productive time we had. Further, I would like to express my thanks to Nico, Anne, and Dominik.

Special thanks to Joe, Christoph, and my fellow group members for meticulously proof reading the manuscript.

I kindly acknowledge Prof. Paul Mulvaney from the University of Melbourne for inviting me as a visiting researcher in this group.

I would also like to thank Prof. Mukundan Thelakkat (MC I, University of Bayreuth) for fruitful collaborations. Support from Chetan and Anna is kindly acknolwedged for helping me with the fabrication of organic thin film solar cells. Further, I would like to thank Paul Reichstein for support with the SEC measurements.

Additionally, I would like to say a cordial thank you to all my colleagues of the PC I department. Prof. Markus Retsch is kindly acknowledged for assistance with interface-mediated self-assembly. I would also like to thank Dr. Martin Dulle for fruitful discussions on quasicrystalline structures of soft particles. Thank you Miriam and Christian for helpful support on square lattices.

Markus Drechsler, Martina Heider, and Dr. Beate Förster (BIMF, University of Bayreuth) are gratefully acknowledged for helpful discussions and assistance on TEM, SEM, and EDX measurements.

Finally, I kindly acknowledge financial support from the Deutsche Forschungsgemeinschaft via the SFB 840.

Abstract

The cost-efficient fabrication of plasmonic superstructures is a key challenge for the development of optoelectronic devices. This thesis is focused on the preparation of such superstructures via self-assembly of colloidal building blocks. In order to integrate plasmonic superstructures into optoelectronic devices, organic thin film solar cells are selected as a model system. Additionally, a brief theoretical background on the localized surface plasmon resonance, self-assembly of soft particles, image analysis, and thin film solar cells is provided.

Polymer-encapsulated gold nanoparticles are used as colloidal building blocks for plasmonic superstructures. The nanoparticles are encapsulated by non-cross-linked or cross-linked poly(*N*-isopropylacrylamide) shells. The shell thickness of the polymer-encapsulated gold nanoparticles is tunable from a few tens up to several hundreds of nanometers. Further modification of the gold nanoparticles is carried out by seed-mediated core overgrowth. The particles are overgrown with spherical gold or silver shells leading to superior optical properties. The synthetic protocol allows for size-controlled overgrowth of the particles up to a final particle diameter of 100 nm and produces neither secondary nucleation nor strongly anisotropic particle shapes. Thus, four key parameters are available for the design of colloidal core-shell building blocks for plasmonic superstructures: size and composition of the plasmonic core as well as thickness and architecture of the polymer shell. Using these parameters, a library of polymer-encapsulated gold nanoparticles is produced for self-assembly.

Focusing on interface-mediated self-assembly, plasmonic superstructures of polymer-encapsulated gold nanoparticles are prepared and collected on solid, cm^2-scale supports. By this process, hexagonally ordered plasmonic monolayers with exceptional long-range order are obtained. Atomic force microscopy measurements at multiple positions of the substrate reveal almost identical interparticle distances and particle densities, independent of size or composition of the plasmonic core. UV-Vis spectroscopy, also performed at multiple locations, highlights the optical homogeneity of the plasmonic monolayers making them perfectly suitable for organic thin film solar cell devices.

Plasmonic monolayers are systematically deposited at different interfaces of solar cell devices. Current-voltage measurements demonstrate that all plasmonic devices are fully operational. If the monolayer is located at any location underneath the active layer of the device, parasitic light absorption limits the efficiency of the device. This effect is most pronounced for monolayers with large gold nanoparticles. However, plasmonic monolayers improve the efficiency of space-charge limited solar cell devices considerably. Once the monolayer is located above the photoactive layer

of a solar cell, near the metal electrode, it acts as a light redistributing element. Thus, photogenerated charge carriers near the metal electrode increase the photocurrent of the device.

Further research investigates plasmonic superstructures beyond hexagonally ordered monolayers. Binary honeycomb structures are fabricated by the sequential double self-assembly of two hexagonally ordered monolayers on the same solid substrate. Each monolayer was prepared by interface-mediated self-assembly of polymer-encapsulated nanoparticles with either gold or silver cores. Elemental mapping unravels the exact location of each core in the honeycomb structure with submicron resolution.

The outcomes of this work are relevant for future applications such as sensors, nanolasers, and solar cells that rely on cost-efficient, optically homogeneous plasmonic superstructures.

Zusammenfassung

Die kostengünstige Herstellung von plasmonischen Überstrukturen ist essentiell für die Entwicklung von optoelektronischen Bauteilen. Ziel dieser Arbeit ist es, solche Überstrukturen durch kolloidale Selbstassemblierung zu erzeugen. Anschließend werden die Überstrukturen in organische Dünnschichtsolarzellen integriert, welche als Modellsystem für optoelektronische Bauteile dienen. Weiterhin werden kurz die Grundlagen der Partikelplasmonresonanz, Selbstanordnung von weichen Partikeln, Bildanalyse und Dünnschichtsolarzellen erläutert.

Für die Herstellung von plasmonischen Überstrukturen werden Goldnanopartikel als kolloidale Bausteine verwendet. Die Nanopartikel werden mit einer Polymerschale aus quervernetztem oder nicht-quervernetztem Poly(*N*-isopropylacrylamid) umhüllt. Dabei kann die Schalendicke von einigen zehn bis mehren hundert Nanometern variiert werden. Des Weiteren werden die Goldnanopartikel mit sphärischen Gold- oder Silberschalen überwachsen, wodurch sich die optischen Eigenschaften der Partikel außerordentlich verbessern. Das größenkontrollierte Überwachsen ermöglicht Kerngrößen von bis zu 100 nm, wobei weder Sekundärnukleation noch stark anisotrope Partikelformen entstehen. Daraus ergeben sich vier essentielle Parameter für das Design von kolloidalen Kern-Schale Bausteinen für plasmonische Überstrukturen: Größe und Zusammensetzung des plasmonischen Kerns, sowie Schalenarchitektur und Schalendicke der Polymerschale.

Plasmonische Überstrukturen werden durch Selbstanordnung der kolloidalen Bausteine an der Wasser/Luft Grenzfläche erzeugt und auf feste cm^2-große Substrate übertragen. Untersuchungen mittels Rasterkraftmikroskopie zeigen hexagonal geordnete Monolagen mit außergewöhnlicher Fernordnung. Aus Messungen an verschiedenen Positionen des Substrates wird deutlich, dass der Abstand zwischen den einzelnen Kolloiden der Monolage, sowie die Partikeldichte nahezu identisch sind – unabhängig von Größe und Zusammensetzung des plasmonischen Kerns. Folglich verfügen die Monolagen über eine exzellente optische Homogenität, was durch UV-Vis Spektroskopie, ebenfalls gemessen an verschiedenen Positionen, gezeigt werden kann. Somit sind die plasmonischen Monolagen bestens geeignet für organische Dünnschichtsolarzellen.

Plasmonische Monolagen werden systematisch an verschiedene Grenzflächen einer Solarzelle integriert. Strom-Spannungs-Kennlinien zeigen, dass alle plasmonischen Solarzellen vollständig funktionsfähig sind. Allerdings wird der Wirkungsgrad der Solarzellen durch parasitäre Lichtabsorption der Monolage verringert. Dieser Effekt ist am stärksten ausgeprägt für Monolagen, welche sich an beliebigen Grenzflächen unterhalb der aktiven Schicht der Solarzelle befinden. Jedoch führen plasmonische Monolagen zu einer erheblichen Leistungssteigerung in raumladungslimitierten

Solarzellen. Befindet sich eine plasmonische Monolage oberhalb der aktiven Schicht, nahe der Metallelektrode, so wirkt die Monolage wie ein Licht umverteilendes Element. Dadurch entstehen photogenerierte Ladungsträger nahe der Metallelektrode, welche den Photostrom der Solarzelle erhöhen.

Weiterhin werden in dieser Arbeit plasmonische Überstrukturen jenseits von hexagonalen Monolagen untersucht. Die sequentielle Selbstassemblierung von zwei hexagonalen Monolagen auf das Gleiche Substrat erzeugt binäre Bienenwabenstrukturen. Die einzelnen Monologen der Bienenwabenstruktur wurden zuvor durch Selbstassemblierung an der Wasser/Luft Grenzfläche erzeugt. Dafür wurden kolloidale Bausteine verwendet, die entweder einen Gold- oder Silberkern besaßen. Anschließend kann durch Element-Mapping die exakte Position der Kerne in der Bienenwabenstruktur mit submikrometergenauer Auflösung bestimmt werden.

Die Ergebnisse dieser Arbeit sind relevant für zukünftige Anwendungen im Bereich der Sensorik, Nanolaser oder Solarzellen, welche auf kostengünstige, optisch homogene plasmonische Oberflächen angewiesen sind.

Chapter 1

Introduction

Surface functionalization of gold nanoparticles. Colloidal nanoparticles are metastable and aggregate easily. One striking example is the destabilization of a colloidal suspension of citrate-stabilized gold nanoparticles by the addition of salt. Initially, the suspension is ruby red but changes quickly to black as the particles aggregate because of attractive van der Waals forces and the high Hamaker constant of gold in water.[1,2] Surface functionalization with surface ligands or optical dielectric shells is one clever strategy to enhance the colloidal stability of the particles. Common examples for the stabilization of gold nanoparticles are: Small molecules (citrate, alkyl ammonium chains, thiols),[3–7] silica,[8–10] DNA,[11–15] and polymers.[16–19] Thus, additional electrostatic repulsion and/or steric stabilization of the colloids is provided.

The particle functionalization can be conveniently followed by UV-Vis spectroscopy due to the strong interaction of gold nanoparticles with light. This stems from their ability to support a localized surface plasmon resonance (LSPR) – collective oscillations of the conducting electrons stimulated by the electric field component of incident light. The LSPR is sensitive to the refractive index close to the surface of the nanoparticles. Functionalization of gold nanoparticles with dielectric shells increases the refractive index close to the nanoparticle surface, and consequently, a small red shift of the LSPR is observed.[20–22] Polymers are particularly interesting shelling materials because the thickness of the shell can be easily controlled by the polymer molecular weight. For instance, Ebeling and Vana demonstrated that the interparticle distance between poly(*N*-isopropylacrylamide) (PNIPAM) stabilized gold nanoparticles increases from 11.6 nm to 40.9 nm with increasing molecular weight of the polymer shell.[23]

In principle, even larger polymer shells are possible by further increasing the molecular weight of the polymer. However, obtaining large polymer shells in the order of hundreds of nanometers is increasingly challenging because it is not trivial to synthesize monodisperse, high molecular weight polymer chains.[24] Another approach to large polymer shells are hydrogel shells – cross-linked polymer networks. Especially PNIPAM hydrogel shells are a common shelling material for gold nanoparticles. These core-shell particles are prepared by free radical precipitation polymerization of *N*-isopropylacrylamide and the cross-linker *N,N'*-methylenebisacrylamide in the presence of surface-functionalized gold nanoparticles. The nanoparticles act as seeds during the precipitation polymerization, and after the reaction, each gold nanoparticle is encapsulated by a cross-linked PNIPAM hydrogel. Functionalizing the nanoparticles with thin layers of silica,[25]

polystyrene,[26,27] or butenyl amine[28] ensures a stable and homogeneous encapsulation of the gold nanoparticles. Rauh et al. demonstrated that the hydrophobicity of the gold nanoparticles is essential for the hydrogel encapsulation reaction.[29] The yield of hydrogel-encapsulated gold nanoparticles was close to 100 % for nanoparticles stabilized by butenylamine. In contrast, only a fraction of hydrophilic gold nanoparticles – stabilized by citrate or mercaptoundecanoic acid – was encapsulated.

As the above examples illustrate, PNIPAM is a highly versatile polymer for the fabrication of core-shell metal-polymer nanoparticles with a wide range of shell thicknesses using either non-cross-linked or cross-linked architectures. In addition, PNIPAM is a stimuli responsive material, i.e., in water the shell thickness of PNIPAM-encapsulated particles experiences a temperature-induced volume phase transition. Subtle changes of the PNIPAM solvency in water with temperature drive this transformation. At room temperature, water is a good solvent for PNIPAM and the polymer shell is highly swollen because of hydrogen bonds between water and the amide groups of PNIPAM. Once the temperature is raised polymer-polymer hydrogen bonding (via the amide groups) and polymer-polymer hydrophobic interactions become increasingly favoured. The polymer shell collapses and water is expelled – the particle shrinks. As a result, PNIPAM hydrogel-encapsulated gold nanoparticles experience a drastic change in volume once the temperature is increased above a certain point – similar to pure colloidal PNIPAM hydrogels. Karg et al. determined volume phase transition temperatures (VPTT) of 34°C – 37°C of PNIPAM-encapsulated gold nanoparticles, slightly higher than the transition temperatures of pure colloidal PNIPAM hydrogels (32°C – 33°C).[28]

In addition to shell thickness control and thermal responsivity, the hydrogel shell offers another advantage. The porous nature of the shell enables further post-modification of PNIPAM-encapsulated gold nanoparticles once the hydrogel shell is highly swollen in water below its VPTT. Hence, small molecules can diffuse in and out of the PNIPAM network and reach the nanoparticle at the center. For instance, the gold core can be overgrown with other noble metals such as gold, silver, or platinum, respectively.[26,27,30,31] Overgrowth with gold was presented by Contreras-Cáceres et al.[26,27] They adapted a seed-mediated overgrowth protocol originally designed for the overgrowth of citrate-stabilized gold nanoparticles. The synthesis was carried out in water and required a gold salt precursor (tetrachloroauric acid, $HAuCl_4$), a reducing agent (ascorbic acid), and the cationic surfactant hexadecyltrimethylammonium bromide (CTAB).[32]

Briefly, the complexation of $HAuCl_4$ by CTAB changes the redox potential of Au^{III} so that a final reduction to Au^0 is only possible at the surface of gold nanoparticles acting as catalytic centers. Overgrowing gold nanoparticles changes the optical properties of the particles significantly. For example, spherical gold nanoparticles of 15 nm in diameter have a pronounced absorbance peak at 524 nm. The absorbance stems from the dipolar mode of the LSPR of the nanoparticles. The LSPR experiences a pronounced red shift as the particles get larger and an additional quadrupolar mode develops, once the particle size exceeds 100 nm.[32] The spherical core overgrowth works excellent for citrate-stabilized gold nanoparticles. However, overgrowth of PNIPAM hydrogel-encapsulated gold nanoparticles is more difficult as anisotropic particle shapes are observed

frequently.[26,27,30]

Application of plasmonic nanoparticles. Overgrowing PNIPAM-encapsulated gold nanoparticles highlights just one of the ways that the easy access to plasmonic particles of defined size and composition sparked a strong interest amongst the scientific community over the last decade. Plasmonic particles have a broad range of applications including sensing,[33–39] nanolasers,[40] and solar cells.[41–46] Particularly organic thin film solar cells can serve as an instructive example for the application of plasmonic particles. Briefly, such a device uses an organic semiconductor as photoactive material. The semiconductor is sandwiched between two electrodes – one of them is transparent.[47]

Currently, the benchmark for organic solar cells uses a blend of poly(3-hexylthiophene-2,5-diyl) and the fullerene derivative phenyl-C_{61}-butyric acid methyl ester as photoactive material (P3HT:PCBM).[48–52] However, such devices suffer from limited light absorbance because the thickness of the P3HT:PCBM layer is restricted to values below 200 nm due to low charge carrier mobility, short exciton diffusion lengths, and charge recombination in organic semiconductors.[53–56] Here, plasmonic particles are promising as light managing elements. They can improve the photocurrent of thin film solar cells by increasing the optical path length of light via scattering or by acting as light concentration centers via near-field enhancement.[45,57] The application of plasmonic particles in solar cell devices leads to a new class of solar cells termed "plasmonic solar cells".[57–59]

Most commonly, plasmonic particles are deposited on certain layers of the device by spin-coating or dip-coating from a particle solution. Alternatively, the particles are synthesized directly on the device by vapour-phase deposition as demonstrated by Morfa et al.[44] They produced silver nanoparticles on the transparent indium tin oxide (ITO) electrode of P3HT:PCBM solar cells. Evaluation of the solar cell performance revealed a strong increase of the solar cell efficiency by a factor of 1.7. Baek et al. systematically investigated size and concentration of plasmonic particles in organic thin film solar cells.[60] They incorporated silver nanoparticles of 10 nm – 100 nm in diameter in the anodic buffer layer of solar cell devices and determined their power conversion efficiencies (η_{OPV}). A clear enhancement of 7.6 % was found for silver nanoparticles of 67 nm in diameter and an optimized particle concentration of 4.5×10^9 particles/cm^2. Investigation of the solar cell performance revealed that the enhancement mainly stemmed from an increase of the photocurrent due to additional light absorption by the silver particles. Interestingly, η_{OPV} decreased for higher particle concentrations due to agglomeration of the nanoparticles. It follows that not only the particle size is important but also the particle separation and concentration are crucial parameters for the design of plasmonic solar cells.

Even though these parameters are essential, they are less frequently studied in many publications. Systematic investigations of particle concentration effects are scarce[60,61] and a thorough characterization of the particle distribution (structure, surface density, and interparticle distance) is neglected frequently.[44,62–72] Ultimately, this can lead to contradictory results as there is a

trade-off between enhancing effects such as scattering and near-field enhancement and weakening effects such as leakage currents, parasitic absorption, and quenching of excitons by plasmonic particles. It follows that there is a need for well-defined particle arrays with controllable interparticle spacing and a high degree of optical homogeneity – on the local *and* macroscopic scale.

Plasmonic superstructures. Currently, well-defined arrays of plasmonic particles are prepared easily by top-down lithographic methods such as photolithography,[73] electron beam lithography,[74] and focused ion beam milling.[75] These methods allow for the fabrication of two dimensional plasmonic superstructures with a precise control of structural parameters such as geometry, spacing, shape, and material. Although virtually any plasmonic superstructures can be prepared by lithographic techniques, they require expensive equipment and are often time-consuming processes.[76] This leaves top-down lithographic methods incommensurable with thin film organic solar cells that target markets for disposable, low-cost, or flexible solar cell applications.

Another approach to plasmonic superstructures are colloidal self-assembly methods. They can produce particle arrays with exceptional control of interparticle spacing, geometry, and long-range order on macroscopic domains. PNIPAM-encapsulated gold nanoparticles are ideal building blocks for such plasmonic superstructures because thickness of the polymer shell and size of the gold nanoparticle are tunable by simple synthetic protocols. Convenient methods for the self-assembly of PNIPAM-encapsulated gold nanoparticles are drop-casting, spin-coating, convective assembly, or interface-mediated self-assembly.

Using drop-casting, Clara-Rahola et al. prepared hexagonally ordered monolayers of PNIPAM-encapsulated gold nanoparticles.[77] The polymer shell acted as an inherent sterical spacer controlling the interparticle distance during the self-assembly process. Alternative fabrication methods for plasmonic superstructures were investigated by Jaber et al.[78] They prepared colloidal monolayers either by spin-coating or convective assembly of PNIPAM-encapsulated gold nanoparticles. They found that prefunctionalization of the substrates with polyelectrolytes improved the order of the monolayers due to enhanced particle-substrate interactions. Moreover, the surface density of plasmonic particles was tunable by encapsulating gold nanoparticles with PNIPAM shells of different thicknesses. Interface-mediated self-assembly is another powerful method for the self-assembly of PNIPAM-encapsulated gold nanoparticles. Using a Langmuir-Blodgett trough (L-B trough), Vogel et al. prepared colloidal monolayers at the air/water interface.[79] The monolayers had a hexagonal symmetry which was preserved after transfer onto solid substrates. Moreover, compression of the monolayers at the air/water interface allowed to tune the interparticle distance between 650 nm and 300 nm.

Even though these colloidal self-assembly methods provide access to well-defined monolayers of PNIPAM-encapsulated gold nanoparticles, they face certain limitations. For instance, all of the ordered monolayers had a hexagonal symmetry because the hexagonal lattice is the favoured minimum free energy position of these particles.[79] In order to realise other particle arrangements, templated particle assembly is a promising approach. This method uses a topographically or chemically structured surface in order to force specific arrangements of colloidal particles.[80]

Müller et al. used wrinkle-substrates as templates in order to organize PNIPAM-encapsulated silver or gold nanoparticles into linear particle assemblies.[38,81] However, the main drawback of templated particle assembly is the template itself, which must be specifically designed for the desired nanostructure. If the template can only be designed by photolithography, template fabrication can become expensive and complex and thus a bottle-neck for applications such as plasmonic solar cells.[80,82]

Templated particle assembly concludes state-of-the-art self-assembly methods for the fabrication of two-dimensional plasmonic superstructures of PNIPAM-encapsulated gold nanoparticles. Yet, it is still difficult to incorporate plasmonic superstructures in optoelectronic devices without relying on lithographic methods. Commonly, a standard solar cell test substrate has a surface area in the order of 1.2 cm x 1.2 cm – 2.25 cm x 2.25 cm.[47] It follows that structural parameters such as interparticle spacing, geometry, and long-range order of plasmonic superstructures must be controllable on the same scale. Consequently, the cost-efficient fabrication of homogeneous plasmonic superstructures on the macroscopic scale is a key challenge for the development of optoelectronic devices.

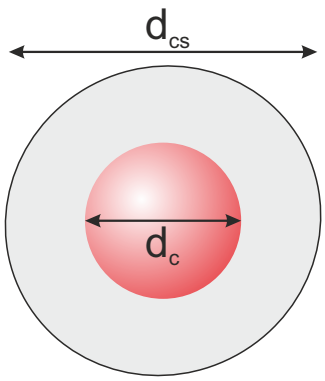

Figure 1.1. Illustration of a PNIPAM-encapsulated gold nanoparticle. The core-shell particle is defined by the core diameter d_c and the overall diameter d_{cs}.

Colloidal building blocks for plasmonic superstructures. This thesis is focused on the preparation of plasmonic superstructures using non-cross-linked and cross-linked PNIPAM-encapsulated gold nanoparticles as building blocks. Figure 1.1 shows a schematic illustration of a PNIPAM-encapsulated gold nanoparticle. The particle is defined by two important lengthscales: one due to the size of the polymer shell (d_{cs}) and one due to the size of the gold nanoparticle core (d_c).

Both lengthscales are found in self-assembled monolayers of PNIPAM-encapsulated gold nanoparticles as demonstrated in Figure 1.2. Transmission electron microscopy (TEM) images reveal a non-close packed monolayer in Figure 1.2 A. The particle arrangement of the monolayer is referred to as shell-to-shell arrangement because the particles do not interpenetrate. The interparticle center-to-center distance (d_{c-c}) is close to the hydrodynamic diameter of the particles in solution, even though the particles are clearly separated on the TEM grid. This apparent discrepancy can be explained considering the preparation conditions of the TEM measurements. A monolayer of

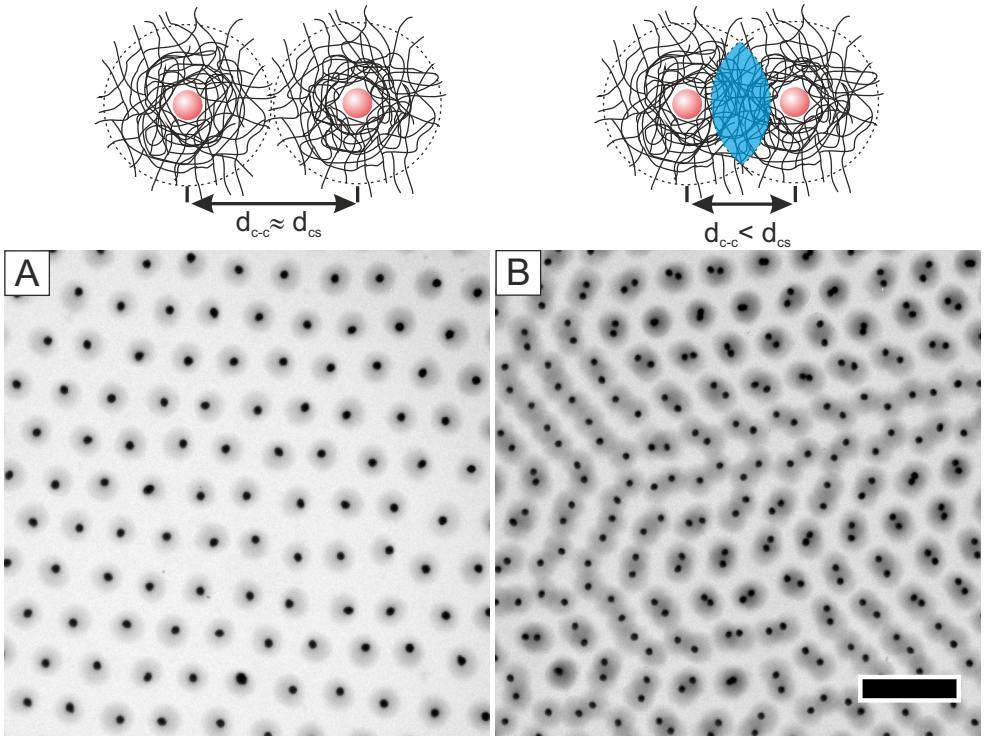

Figure 1.2. Different arrangements of PNIPAM-encapsulated gold nanoparticles. A, B, TEM images of the particles in shell-to-shell (A) or core-to-core arrangement (B). The scale bar is 1 μm. Sketches illustrate the two different scenarios. The overlapping region of the core-to-core arrangement is indicated in blue.

core-shell particles is transferred onto a TEM grid, dried, and subjected to a very high vaccuum during the TEM investigation. Hence, the PNIPAM shell of the core-shell particles is strongly collapsed which explains the large gaps between the particles in Figure 1.2 A. Initially, the particle monolayer was prepared by interface-mediated self-assembly at the water surface. Hence, the PNIPAM shell is strongly swollen by water (below the VPTT of the core-shell particles), and the core-shell particles are in a direct shell-to-shell contact on the water surface. The particle arrangement of the monolayer in Figure 1.2 B is referred to as core-to-core arrangement, because the particles interpenetrate each other. Consequently the interparticle distance is considerably smaller as compared to the particle diameter. Moreover, the density of core-shell particles is also significantly higher as compared to Figure 1.2 A. Importantly, such a scenario is impossible for hard sphere colloids such as polystyrene (PS) or poly(methyl methacrylate) (PMMA), for example.

Organization of the thesis. The thesis is organized in four major parts.

The first part of the thesis deals with the synthesis of gold-PNIPAM core-shell particles as colloidal building blocks for plasmonic superstructures. Shell size, shell architecture, and size of the plasmonic core are investigated as design parameters for the colloidal building blocks. Further diversity of the core-shell particles is achieved by post-modification. Therefore, the plasmonic core of the core-shell particles is overgrown with silver or gold. These design parameters are systematically changed in order to produce a diverse library of plasmonic building blocks. Char-

acterization of the building blocks is carried out using dynamic light scattering (DLS), TEM, and UV-Vis spectroscopy. Next, plasmonic superstructures are fabricated in **the second part of the thesis**. The impact of two different self-assembly methods – spin-coating and interface-mediated self-assembly – upon the order of the superstructures is investigated. The structures are probed by atomic force microscopy (AFM), and the optical properties are evaluated by UV-Vis spectroscopy. **In the third part of the thesis**, the role of plasmonic superstructures is investigated in organic thin film solar cells. Therefore, plasmonic superstructures are systematically integrated at different interfaces in the layer stack of organic solar cells. The performance of the devices is evaluated using current-voltage, external quantum efficiency, and reflectance measurements. The **last part of the thesis** investigates fabrication methods for plasmonic superstructures beyond hexagonal monolayers. The superstructures are fabricated using two distinctive methods: double deposition of two monolayers on top of each other and anisotropic stretching of a single monolayer. The superstructures are investigated using AFM and TEM. All in all, this work provides bottom-up self-assembly strategies for the fabrication of optically homogeneous plasmonic superstructures using simple self-assembly methods and well-defined colloidal building blocks.

Chapter 2

Theoretical Part

2.1 Plasmon Resonance of Noble Metal Nanoparticles

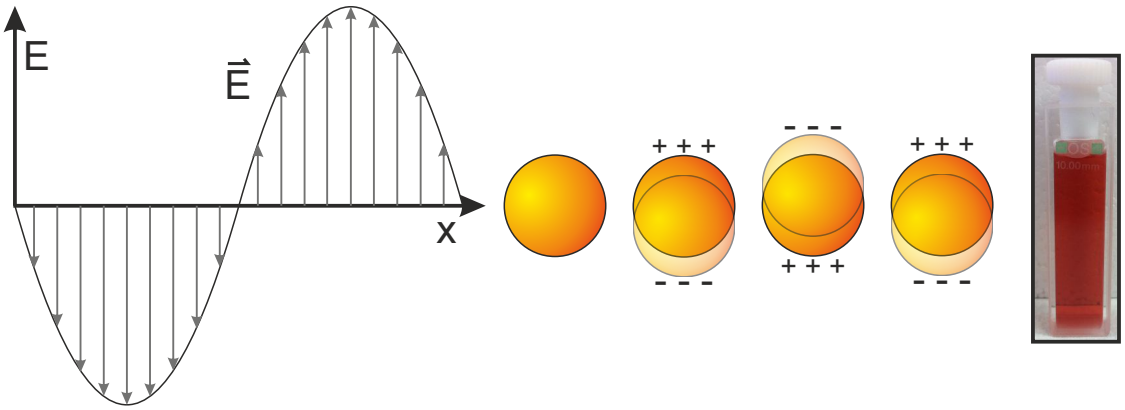

Figure 2.1. Schematic illustration of the interaction between the electric field component of incident light and a spherical metal nanoparticle. The electric field causes a collective oscillation of the electron gas of the nanoparticle. The photograph shows a typical gold nanoparticle dispersion. The particle diameter is 15 ± 2 nm.

Noble metal nanoparticles such as gold and silver have a pronounced absorbance in the visible range. Figure 2.1 shows a digital photograph of a gold nanoparticle dispersion. The nanoparticles have a size of 15 ± 2 nm in diameter. The dispersion appears ruby red because green light, with a wavelength of approx 520 nm, is strongly absorbed by the particles, while red light, with a wavelength of approx. 700 nm, is reflected. The electric field component of incident light causes a coherent oscillation of the conducting electrons relative to the immobile positive nuclei of the metal nanoparticle (cf. Figure 2.1). This phenomenon is known as localized surface plasmon resonance of metal nanoparticles.[83–85]

It is instructive to compare the LSPR with a mechanical oscillator. When the oscillator is displaced from its equilibrium state, a restoring force towards the equilibrium position is exerted and the system starts oscillating. The motion is described by a continuous sinusoidal wave until losses, caused by damping, bring the system to rest. However, the application of an oscillating external driving force can overcome this damping. For a particular driving force at least one frequency is found at which the oscillator will have a maximum amplitude, which is known as

the resonant frequency of the system. This occurs when the driving force is in phase with the natural frequency of the oscillator. In this case, a small periodic driving force will cause very large amplitude oscillations of the system because of an effective energy transfer between the external force and the harmonic oscillator.

The same concept can be applied to the plasmon oscillation of a metal nanoparticle stimulated by incident light. The electric field component of light corresponds to the external sinusoidal driving force causing an oscillation of the conduction electrons of the metal nanoparticle. The restoring force is the Coulomb attraction between the positive nuclei and the electron gas. Although all free electrons of the metal nanoparticle are oscillating, the main cause for the restoring force is the surface polarization of the particle.[83] Resonant conditions are found once the light is in phase with the plasmon oscillation of the particle. At this point, the maximum amount of incident electromagnetic radiation is absorbed by the particle resulting in the strongest charge displacement.[85] This process only works for metal nanoparticles, which are considerably smaller as compared to the wavelength of the incident light. Then, the surface plasmon is confined to a very small volume and an intense, oscillating electric field develops close to the nanoparticle surface. The electric field extends from a few nanometers up to a few tens of nanometers into the dielectric environment of the nanoparticle.[35,85,86]

Silver or gold metal nanoparticles are the most popular examples of plasmonic particles because of their high environmental stability and their accessibility by well-established synthetic protocols.[87–92] The LSPR of these nanoparticles is affected by many different factors such as the dielectric environment, size, shape, and material of the particle.[84,85,93–98] For instance, the gold nanoparticles of Figure 2.1 have a single, dipolar plasmonic mode. The entire electron gas of the particles oscillates under resonant conditions. In contrast, larger particles show a broadening of the LSPR and have additional absorption bands due to the excitation of higher order plasmon modes. Here, parts of the electron gas move parallel/anti parallel to the incident electric field.[85] Shape anisotropy also affects the LSPR, causing additional plasmon modes. This phenomenon is commonly observed for gold nanorods, where the dipole LSPR splits in a transverse and a longitudinal mode.[99–101] Moreover, coupling of the LSPR occurs if two independent nanoparticles approach each other below a certain distance, usually in the range of a few nanometers.[102,103] LSPR coupling is also observed when particle-particle aggregation takes place, for instance by destabilization of a colloidal gold nanoparticle dispersion. Then, a pronounced change of color is visible due to a significant shift and broadening of the LSPR.[15]

The LSPR of noble metal nanoparticles causes the particles to strongly absorb and scatter incident light. The absorption and scattering cross sections are considerably higher as compared to non-plasmonic particles of the same size and shape. The absorption and scattering cross sections are given by Equation 2.1 and 2.2 for nanoparticles that are considerably smaller than the wavelength of light[86,104,105]

$$C_{abs} = 4\pi k r^3 \,\mathrm{Im}\left\{\frac{\epsilon_s - \epsilon_m}{\epsilon_s + 2\epsilon_m}\right\} = k\,\mathrm{Im}\{\alpha_p\} \tag{2.1}$$

$$C_{sca} = \frac{8\pi}{3} k^4 r^6 \left| \frac{\epsilon_s - \epsilon_m}{\epsilon_s + 2\epsilon_m} \right|^2 = \frac{k^4}{6\pi} |\alpha_p|^2 \tag{2.2}$$

where k is the wavevector, ϵ_s and ϵ_m are the dielectric functions of the metal and the surrounding medium, r is the particle radius, and α_p is the dipolar polarizability of the spheres.[105] The extinction cross section $C_{ext} = C_{abs} + C_{sca}$ is given by Equation 2.3

$$C_{ext} = 9\frac{\omega}{c} \epsilon_m^{3/2} V \frac{\epsilon_2}{[\epsilon_1 + 2\epsilon_m]^2 + \epsilon_2^2} \tag{2.3}$$

where V is the volume of the spherical nanoparticle, and ϵ_1, ϵ_2 are the real and imaginary parts of the complex dielectric function $\epsilon_s(\omega) = \epsilon_1(\omega) + i\epsilon_2(\omega)$ of the metal. The calculations are valid for an isolated, spherical nanoparticle located in a nonabsorbing medium, and the nanoparticle is treated as an electric dipole. The polarization α_p of the nanoparticle is given by Equation 2.4[83,86,104,105]

$$\alpha_p = 4\pi r^3 \frac{\epsilon_s - \epsilon_m}{\epsilon_s + 2\epsilon_m} \tag{2.4}$$

For metal nanoparticles, ϵ_s is obtained by the Drude model according to Equation 2.5[83,104,105]

$$\epsilon_s(\omega) = \epsilon_1(\omega) + i\epsilon_2(\omega) = 1 - \frac{\omega_p^2}{\omega^2 + i\gamma\omega} \tag{2.5}$$

where ω_p is the plasma frequency of the free electron gas, ω is the angular frequency of light, and γ describes the electron damping in order to account for electron/phonon scattering in the metal.[104,105]

In Equation 2.4 the term $\frac{\epsilon_s - \epsilon_m}{\epsilon + 2\epsilon_m}$ describes the optical properties of the nanosphere.[105] α_p becomes very large if $|\epsilon_s + 2\epsilon_m|$ approaches a minimum. This criterion is fulfilled at the LSPR of the nanosphere. A UV-Vis spectrum shows the LSPR of gold nanoparticles at the resonance frequency (ω_{res}). $\omega_{res} = \frac{\omega_p}{\sqrt{3}}$ if the surrounding medium is vaccuum ($\epsilon_m = 1$). This frequency is called the dipolar surface plasmon resonance of a spherical metal nanoparticle.[104,105]

If the particle size exceeds a certain size then a strict dipolar approximation is no longer valid as additional multipolar modes are excited. Consequently, the electric field, induced by the incident light, is no longer constant as assumed before and retardation effects must be considered. Retardation is caused by the phase difference of electrodynamic fields propagating from different regions of the nanoparticle.[83,104,106] The optical properties of such particles are modelled using Mie theory.[86,104,107] According to Mie theory, the polarizability of a metal sphere is given by Equation 2.6[104,108,109]

$$\alpha_{p,mie} = \frac{1 - \frac{1}{10}(\epsilon_s + \epsilon_m)x^2 + O(x^4)}{(\frac{1}{3} + \frac{\epsilon_m}{\epsilon_s - \epsilon_m}) - \frac{1}{30}(\epsilon_s + 10\epsilon_m)x^2 - i\frac{4\pi^2\epsilon_m^{3/2}}{3}\frac{V}{\lambda_0^3} + O(x^4)} V \tag{2.6}$$

where $x = \pi r/\lambda_0$ is the size parameter of the metal sphere, and λ_0 is the wavelength in vacuum. As compared to α_p of smaller particles (Equation 2.4), additional terms are included in the numerator and denominator of $\alpha_{p,mie}$ in order to account for retardation and damping effects. The second terms in the numerator and denominator consider retardation effects.[104,109] Both terms are responsible for an energy shift of the LSPR towards lower energies (higher wavelengths). This can be understood by the increasing distance between charges at opposite interfaces for larger particles. Consequently, the restoring force is weaker and lowers the resonance frequency of larger particles.[21,32,93,110] The imaginary term in the denominator accounts for radiation damping of the LSPR. The damping is the result of radiative losses weakening the strength of the LSPR. This effect is more pronounced for larger particle volumes and causes a significant broadening of the LSPR.[108] The higher order terms O in the numerator and denominator of Equation 2.6 account for higher order plasmon resonances.[104,108,109] Accordingly, Mie theory provides a rigorous solution for the optical extinction of spherical plasmonic particles of arbitrary size.

In this work spherical gold nanoparticles of different sizes and with different surface modifications are encountered frequently. Both modifications affect the LSPR and can be modelled thoroughly using Mie theory. Figure 2.2 shows theoretical extinction spectra of spherical gold nanoparticles that were calculated using an adaptation of the multilayer recursive method by Moroz.[111] The refractive index of gold was selected from Johnson and Christy[112] and modified to account for electron surface scattering at small dimensions.[86]

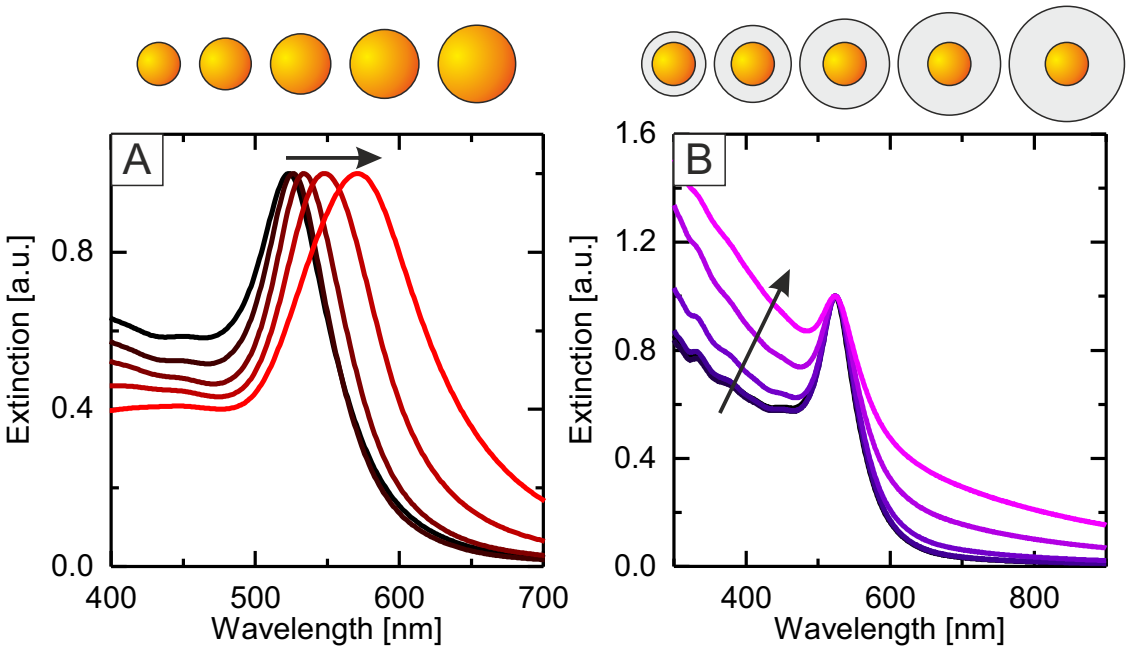

Figure 2.2. Simulated extinction spectra of gold nanoparticles in water. A, Influence of the particle size. The particle diameter increases from 15 nm (black) to 100 nm (red). B, Influence of a dielectric shell. The shell diameter increases from 0 nm (black) to 300 nm (pink) for gold nanoparticles of 15 nm in diameter. Simulations were carried out using refractive indices of 1.355 for the shell and 1.332 for water. The illustrations visualize the increase of particle diameter and shell thickness, respectively. All spectra are normalized to the peak maximum of the LSPR.

Figure 2.2 A demonstrates the size-dependence of the LSPR of spherical gold nanoparticles. Increasing their size from 15 nm to 100 nm results in a pronounced red-shift and a significant broadening of the LSPR due to retardation effects and damping. Figure 2.2 B shows the impact of a dielectric polymer shell upon the LSPR of gold nanoparticles of 15 nm in diameter. The extinction spectra is a combination of the LSPR of the nanoparticles and a superimposed Rayleigh-Debye-Gans scattering contribution of the dielectric shells.[28,113] It is assumed that the particles are isolated, and that the dielectric shell has a constant refractive index (n) of 1.355, close to water (n=1.332). The shell thickness is varied from 0 nm (no shell) to 143 nm. A thin shell with a thickness of 5 nm hardly affects the plasmon resonance. In contrast, the extinction increases at lower wavelengths once the shell size reaches 40 nm. This effect gets more and more pronounced for thicker shells. Finally, the scattering effect extends over the whole spectrum for very thick dielectric shells. Additionally, the dielectric shell increases the refractive index close to the nanoparticle surface and causes a small shift of the LSPR in the order of 1 nm –2 nm, which is invisible in the representation.

In conclusion, plasmonic nanoparticles strongly interact with light. The optical properties of plasmonic nanoparticles such as absorption and scattering cross sections depend on their size, shape, and surface modification. Additionally, if more than one particle is considered, the interparticle spacing also affects the LSPR. This strong interaction with incident lights makes plasmonic nanoparticles suitable for the fabrication of optoelectronic devices such as organic thin film solar cells.

2.2 Organic Thin Film Solar Cells

Organic thin film solar cells use organic semiconductors as photoactive materials in order to convert incident light into electricity by the photovoltaic effect. One advantage of organic semiconductors is that they combine the electronic properties of semiconducting materials with an organic structure that is easy to modify by chemical synthesis. Furthermore, organic semiconductors are solution processable, and thus inexpensive, flexible, and lightweight devices can be fabricated. P3HT is the current benchmark for organic semiconductors in organic thin film solar cells.[50–52] The semiconducting polymer has a band gap of 1.9 eV – 2.0 eV, which means that light with a wavelengths up to 650 nm is absorbed by P3HT. Great effort was put into synthetic strategies in order to increase light absorption by the semiconducting polymer. For instance, the bandgap of P3HT was lowered by introducing electron-donating or electron-withdrawing groups to the polymer backbone, or by increasing the quinoidal character of the macromolecule.[114,115]

However, an inherent problem of P3HT, and all organic semiconductors, is their low electrical conductivity because their dielectric constants are low ($\epsilon \approx 3.5$). Consequently, photogenerated electron-hole pairs (excitons) are subjected to strong coulomb interactions and charge separation becomes a critical issue. Moreover, excitons generated in organic semiconductors have a very low diffusion length (around 10 nm) before they recombine.[116] Both processes limit the maximum thickness of organic solar cells to 200 nm, and thus, light absorption becomes a challenging factor.[41,54,117,118] The design of low bandgap donor-acceptor copolymers such as PTB7, with a bandgap of 1.68 eV, is one way to enhance the light absorption of organic semiconductors. PTB7 absorbs incident light from the UV up to the NIR region.[115,119–121]

An alternative approach towards enhanced light absorption is modifying the solar cell device itself. For inorganic silicon-based solar cells it is common practice to use surface structures such as pyramidal textures as additional light scattering elements. Surface structuring increases the path length of light in the solar cell. However, the same approach is not suitable for organic solar cells because the surface roughness would be larger than the actual film thickness of the organic semiconductor.[45] In this case, light management by colloidal particles is a suitable alternative.[41,122] In order to understand how such particles can contribute to the light management of organic solar cells, it is import to be familiar with the basic electronic processes and operation principles of the device at first.

2.2.1 The MIM Model

The basic device architecture of an organic solar cell is an organic semiconductor sandwiched between a transparent ITO anode and a metal cathode. This setup has a very high similarity to a dielectric material sandwiched between a parallel plate capacitor due to the very low charge density and the low charge carrier mobility of organic semiconductors. Hence, the metal-insulator-metal (MIM) model is instructive in order to understand the basic electronic processes of an organic solar cell.[47,54,123] Figure 2.3 shows the MIM model for four different scenarios.

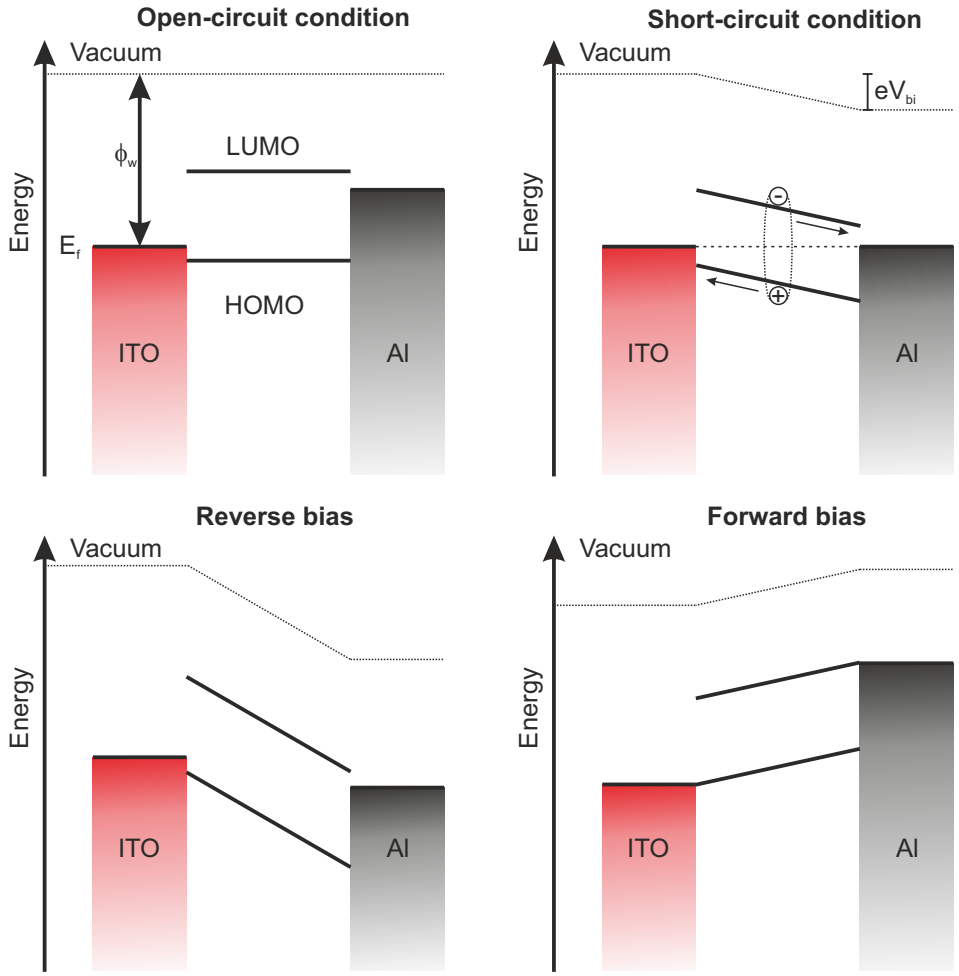

Figure 2.3. MIM model of organic diodes under different modes of operation. The electrodes are represented by their Fermi levels E_f, and the organic semiconductor is represented by its LUMO and HOMO levels. **Open-circuit condition**, V_{OC} is applied and the current is zero. **Short-circuit condition**, no voltage is applied. Photo-generated charge carriers drift in the build-in electric field to the electrodes, and the device operates as a solar cell. **Reverse bias**, a voltage is applied and photogenerated charge carries are extracted. The device operates as a photodetector. **Forward bias**, the applied voltage is reversed, and the device operates as an organic light emitting diode. The model is adapted from ref[47] and[54] .

The organic semiconductor is represented by its highest occupied molecular orbital (HOMO) and lowest unoccupied molecular orbital (LUMO) levels. The ITO and Al electrode, with different work functions (ϕ_w), are represented by their Fermi levels (E_f). Under **open-circuit conditions**, the solar cell device is not connected to an electric load and the energy levels of LUMO and HOMO align (flat band condition). The voltage associated with this condition is the open-circuit voltage (V_{OC}). There is no electron transfer between the organic semiconductor and the electrodes. Consequently, the current is zero because no driving force exists for the charge carriers.

Solar cells operate under **short-circuit conditions**. Connecting the ITO and Al electrodes by an external circuit results in an electron flow until the Fermi levels of both electrodes are equilibrated. The difference between ϕ_w of both electrodes causes a build-in potential (V_{bi}), which is indicated as displacement of the vacuum levels in Figure 2.3. V_{bi} causes a continuous tilt of the LUMO and HOMO levels of the organic semiconductor between the electrodes. Photogenerated charge carries follow the gradient in energy levels until they are extracted at the respective electrodes. As electrons look for the lowest possible energy levels, they will move downwards in the energy diagram and travel along the LUMO. Conversely, electron holes will move upwards in the energy diagram and travel along the HOMO.

Under **reverse bias conditions**, an external voltage is applied, which lowers E_f of Al compared to ITO. The tilt of LUMO and HOMO levels of the organic semiconductor increases, and the device no longer delivers electric power but it works as a photodetector.

Under **forward bias conditions**, the applied voltage is reversed and the energy tilt of the LUMO and HOMO levels reverses, too. The electrodes start injecting charges into the organic semiconductor, once the applied voltage is above V_{OC}. If the injected charges recombine radiatively, then the device operates as an organic light-emitting diode.

2.2.2 Fabrication and Operation of Organic Solar Cells

The sandwich-like layer stack is one of the standard geometries of organic thin film solar cell devices. The device geometry consists of an organic semiconductor sandwiched between two electrodes of different work functions, and the current flows perpendicular to the semiconductor layer. Commonly, ITO is used as the transparent bottom electrode of the device. The electrode is covered with a thin layer of poly(3,4-ethylenedioxythiophene)-poly(styrenesulfonate) (PEDOT:PSS), a water soluble, conductive polymer composite. PEDOT:PSS acts as electron blocking layer improving the collection of holes at the ITO electrode.[124,125] PEDOT:PSS and the organic semiconductor are usually deposited onto the substrate by sequential spin-coating. Next, the device is finished by evaporating a metal cathode with a very low workfunction such as Al or Ag, in order to facilitate electron collection.

The dissociation of photogenerated excitons is a bottleneck in organic semiconductors because the build-in electric field is not strong enough to directly separate the electron-hole pairs bound

by strong coulomb interactions. This fact is a fundamental difference compared to inorganic semiconductors such as silicon where charge dissociation happens instantly.[54,126–128] Due to the short exciton diffusion length in organic semiconducotrs, it is common to create heterojunctions – interfaces between two different semiconducting materials – by combining electron donor and electron acceptor materials with different HOMO and LUMO levels.[50,54,129] The heterojunction allows for an excited electron in the LUMO level of the donor material to be transferred to the LUMO level of the acceptor material. The gain in electron energy is used to separate the electron-hole pair.[54,130] Afterwards, electrons travel within the acceptor material whereas holes travel within the donor material towards the electrodes. Introducing heterojunctions significantly reduces charge recombination of organic solar cells.[54] Bulk heterojunctions use a similar concept. The heterojunction is prepared by intermixing donor and acceptor materials in order to maximize the interfacial area.[131,132] Since polymers have a low mixing entropy phase separation takes place, and a bicontinuous network of two phases is created on the lengthscale of the exciton diffusion length. This process requires a careful adjustment of the molar donor:acceptor ratio, temperature, and the choice of the solvent. Charge photogeneration in bulk heterojunction solar cells proceeds as follows:

1. Exciton generation by photon absorption.
2. Exciton diffusion to the heterojunction.
3. Exciton dissociation into spatially separated charge carriers at the donor/acceptor interface.
4. Charge transport to the electrodes.

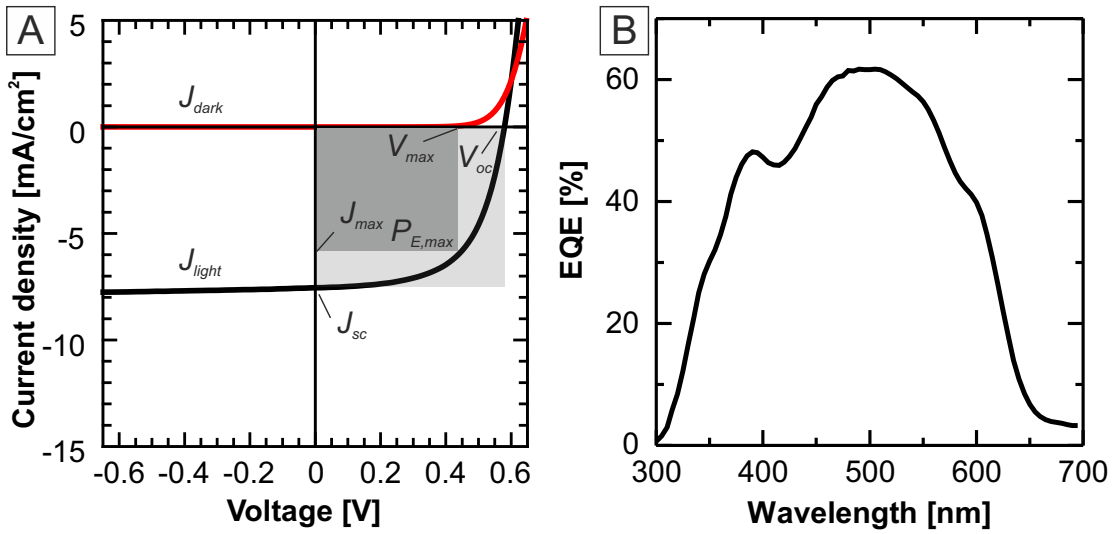

Figure 2.4. Evaluating the solar cell performance. A, IV-curve of a P3HT:PCBM bulk heterojunction solar cell. J_{dark} and J_{light} denote dark and light current densities of the device, J_{SC} is the short-circuit current. J_{max} and V_{max} correspond to current and voltage at the maximum power point $P_{E,max}$ of the device. V_{OC} is the open circuit voltage. B, EQE spectrum of the same device.

Commonly, the performance of organic solar cells is evaluated by recording current-voltage curves (IV-curves) and by measuring the external quantum efficiency (EQE) of the device. Figure 2.4 shows the IV-curve of a ITO/P3HT:PCBM/Ag solar cell in the dark (red) and under illumination

(black). The current density in the dark (J_{dark}) is close zero, until the electrodes start injecting charges under forward bias conditions above V_{OC}. Illuminating the device shifts the IV-curve curve into the fourth quadrant, and the device starts generating power. The short-circuit current density (J_{SC}) is the maximum attainable photocurrent density of the device. J_{SC} is measured at short-circuit conditions where the voltage is zero. Conversely, the photocurrent is zero under open-circuit conditions, and V_{OC} is the maximum attainable voltage of the device. Electric power is generated between J_{SC} and V_{OC}. The maximum generated electric power ($P_{E,max}$) is delivered at a certain point, where a rectangle, given by $J(V) \cdot V$, has the largest area.[47,54] The fill factor (FF) of a solar cell is given by Equation 2.7

$$FF = \frac{J_{max}\, V_{max}}{J_{SC}\, V_{OC}} \tag{2.7}$$

which is equal to the ratio between the two rectangles indicated in Figure 2.4 A. The FF of an ideal solar cell is one, and any values below one indicate the presence of loss channels such as leakage currents and charge-carrier recombination.[47,54,133] The power conversion efficiency of a solar cell (η_{OPV}) is given by Equation 2.8[54]

$$\eta_{OPV} = \frac{P_{E,max}}{P_I} = \frac{FF\, J_{sc}\, V_{OC}}{P_I} \tag{2.8}$$

where $P_{E,max}$ is the maximum electric power delivered by the device, and P_I is the incident light power.

In order to assess the electrical sensitivity of the device to light at a given wavelength, EQE measurements are carried out.[120,134–136] The EQE is defined as the ratio of collected charge carriers to the number of incident photons at a certain wavelength. The EQE is 100 % in an ideal solar cell, where all of the incident photons are absorbed, and all charge carriers are collected. Figure 2.4 B shows the EQE spectrum of a P3HT:PCBM device, and the EQE is high in a spectral range of 300 nm – 650 nm, where the active layer strongly absorbs incident photons. In practice, IV-curves and EQE spectra are measured under standard conditions. These conditions are: 25 °C, a total irradiance of 100 mW/cm^2, and the AM 1.5 solar spectrum. This solar spectrum is the absorption-corrected spectrum of the sun on the northern hemisphere.[47,137]

2.2.3 Strategies to Enhance the Photocurrent

The electrical current that a thin film organic solar cell produces corresponds to the number of photogenerated charges which are collected at the electrodes. The charge generation itself depends on the number of absorbed photons, the number of dissociated excitons, and the number

of charges reaching the electrodes. The overall photocurrent efficiency η_J is given by Equation 2.9[54]

$$\eta_J = \eta_{Abs}\,\eta_{Diss}\,\eta_{Out} \tag{2.9}$$

where η_{Abs}, η_{Diss}, and η_{Out} are the efficiencies of photon absorption, exciton dissociation, and charge collection, respectively. η_{Abs} depends on absorption spectrum, extinction coefficient, and thickness of the semiconducting layer. η_{Diss} depends on the probability of an exciton reaching the donor-acceptor heterojunction. η_{out} depends on the number of charges reaching the electrodes without recombination.[47,54,126] In order to improve the electrical current that a solar cell can provide, Equation 2.9 must be optimized. In practice this is a complex task, as there exists a mutual dependence between the different parameters, and improving one of them often results in a reduction of the other one. One approach is to tackle photon harvesting by the device.

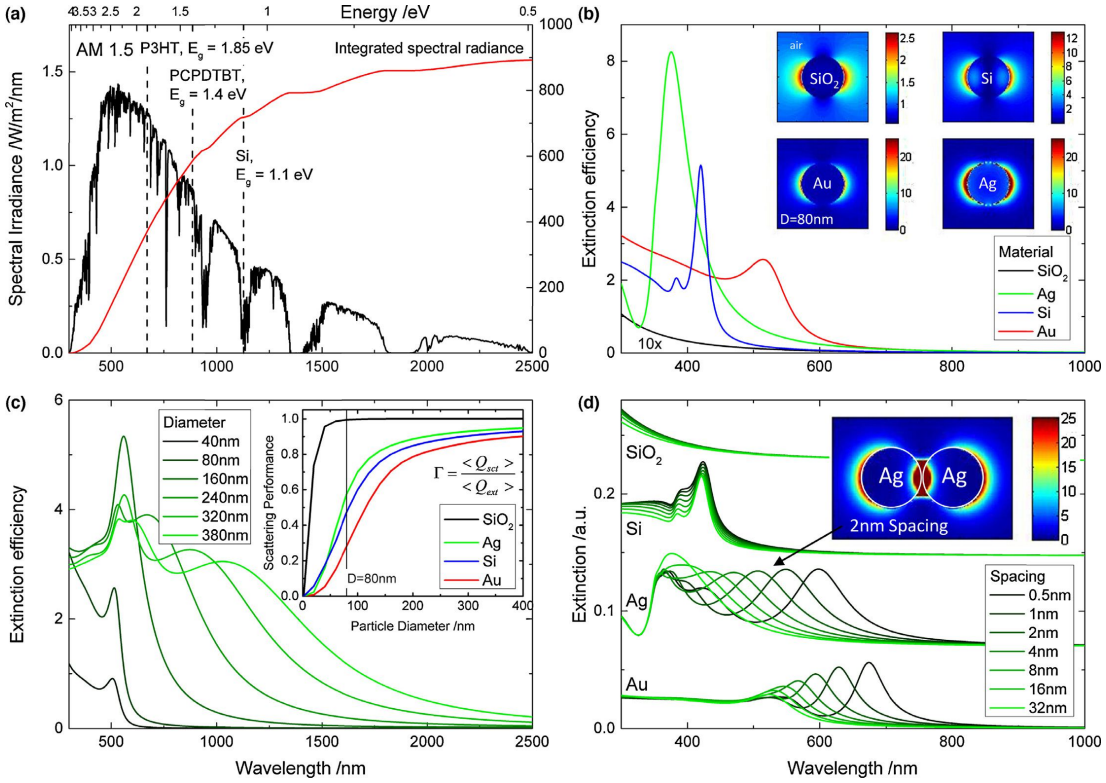

Figure 2.5. Solar spectrum and optical properties of colloidal particles. (a) Standard AM 1.5 solar spectrum and integrated spectral irradiance. Additionally, band gaps of common solar cell materials are included. (b) Extinction efficiency and enhancement factor of colloidal spheres made of different materials. Each sphere is 80 nm in diameter. (c) Extinction efficiency of spherical gold colloids of increasing size in air. The inset shows the scattering performance of different colloidal particles. (d) Extinction cross sections of two colloids at different interparticle spacings. Plots of the electric field intensity are included imaged at the resonance frequency (units $|E|^2/|E_0|^2$). Reprinted from "Colloidal self-assembly concepts for light management in photovoltaics", by Matthias Karg, Tobias A.F. König, Markus Retsch, Christian Stelling, Paul M. Reichstein, Tobias Honold, Mukundan Thelakkat, and Andreas Fery, *Materials Today*, *18*, 185-205. Copyright 2015 by Elsevier.

For instance, it is common to use back-reflecting metal electrodes as light-managing elements, which increase the path length of photons in the device.[47,138,139] Recently, light management by colloidal particles sparked great interest amongst researchers, because colloidal particles strongly interact with incident light by scattering and absorption.[41,45,58,140–145] Figure 2.5 summarizes the optical properties of different colloids. Additionally, the standard AM 1.5 solar spectrum is displayed in Figure 2.5 a) which defines the borders of the relevant spectral range. The band gaps of selected semiconducting materials such as P3HT,[146] PCPDTBT,[147] and n-type Si are also included. It is clear from Figure 2.5 a), that a significant part of the solar spectrum is excluded for semiconducting polymers due to their rather large band gaps.

In this case colloidal particles can serve as light managing structures by confining and/or redistributing additional light in the device. The extinction efficiency of colloids strongly depends on the material of the particles, as shown for four different colloidal spheres (SiO_2, Ag, Si, Au) of equal diameter in Figure 2.5 b). The dielectric silica sphere represents classical Rayleigh scattering by small particles (particle diameter $\ll \lambda/20$) with negligible absorption. The extinction efficiency of such particles increases towards smaller wavelengths. In contrast, the light interaction is more complex for Ag, Si, and Au colloids, because light absorption must be considered. In particular, the LSPR of Ag and Au causes a significant absorption of incident light. The extinction efficiency of different Au colloids is calculated in Figure 2.5 c) using Mie theory. Depending on the particle diameter (40 nm – 380 nm), single dipolar or dipolar as well as higher order plasmonic modes are excited. The scattering cross section of the colloids increases with increasing particle diameter as demonstrated in the inset of Figure 2.5 c). It is important to note, that the LSPR also causes strong electric fields close to the surface of the colloids, which can improve the dissociation of excitons.[34,41,148,149] The strength of the local electric field strongly depends on material, particle size, and interparticle distance as demonstrated in Figure 2.5 b) and d). The inset of Figure 2.5 d) shows that very high intensities of the electric filed occur, when the distance of two Ag colloids is reduced to a few nanometers.

In conclusion, colloidal particles have a great potential for improving the photon harvesting and light management of organic solar cells. The interaction with electromagnetic radiation is most pronounced for plasmonic nanoparticles due to their extraordinary high scattering cross sections. Additionally, the LSPR causes intense electric fields near the particles. Both effects contribute to the light harvesting of organic solar cells. It is important to know that plasmonic nanoparticles are commonly produced using wet-chemical synthesis. Functionalization of the particles with polymer shells strongly enhances their colloidal stability. Consequently, an appropriate deposition method is required in order to transfer the polymer-encapsulated particles from solution onto the device.

2.3 Self-Assembly of Soft Particles

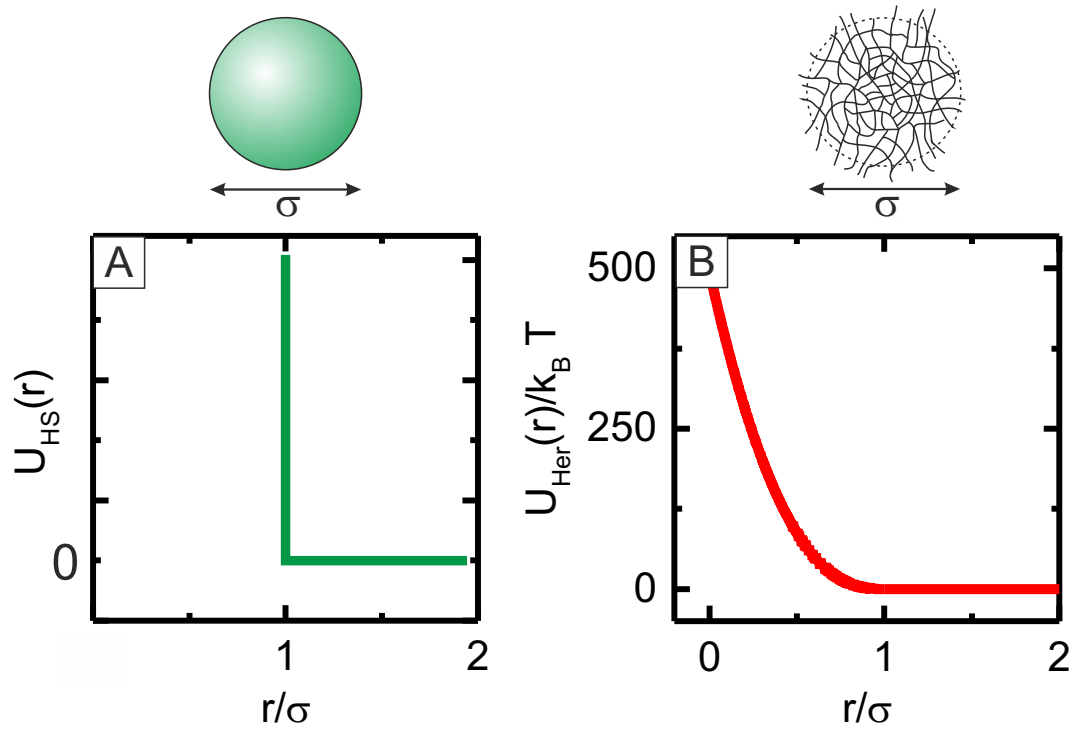

Figure 2.6. Interaction potentials of hard and soft colloidal spheres. A, illustration of the hard sphere interaction potential. B, calculation of a soft, Hertzian interaction potential of PNIPAM microgels using $\sigma = 0.714\,\mu$m and $\epsilon_H = 496\,k_B\,T$. The values are selected from ref.[150] and[151]. Additionally, schematic illustrations of the two different types of colloids are included.

Polymer-encapsulated nanoparticles are considered as "soft" particles because they have a softer pair-interaction potential as compared to classic "hard" sphere colloids. A typical colloidal particle with a hard sphere interaction potential is illustrated in Figure 2.6 A. The particle has a sphere diameter (σ), and the pair-interaction potential (U_{HS}) is zero for large distances but has a sharp discontinuity at σ. U_{HS} of hard sphere colloids is modelled using Equation 2.10

$$U_{HS}(r) = \begin{cases} \infty, & r < \sigma \\ 0, & r > \sigma \end{cases} \tag{2.10}$$

where r is the distance between the centers of the particles. It follows directly from Equation 2.10 that hard spheres are impenetrable, and that σ is the minimum interparticle distance of the system. U_{HS} also determines the phase behaviour of the colloids. Figure 2.7 schematically illustrates the phase diagram of a concentrated suspensions of hard spheres. Briefly, the colloids show a disordered fluid phase at volume fractions (ϕ) below approx. 0.49 without long-range correlation of the particle positions. Next, the coexistence of a fluid and an ordered crystalline phase is observed, after ϕ is increased to approx. 0.49 – 0.55. Beyond volume fractions of 0.55, homogeneous crystal, heterogeneous crystal, and glassy or jammed phases are discovered, until a dense, close-packed arrangement is reached at ϕ=0.74.[152–154]

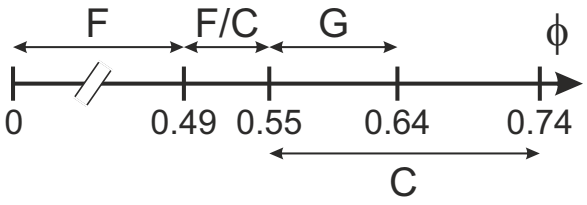

Figure 2.7. Schematic illustration of the phase diagram of a concentrated suspension of hard spheres. The following phases are observed with increasing ϕ: Fluid (F), fluid/crystal coexistence (F/C), glass (G), and crystal (C).

In contrast, the phase behaviour of soft colloidal particles is more complex because such particles can deform and interpenetrate. Thus, interparticle distances below σ are possible. PNIPAM microgels are one of the most studied examples of soft particles. Microgels are defined as colloidal gel particles with a diameter of 0.1 – 100 μm.[155] PNIPAM microgels have an internal cross-linked polymer network that can be swollen by a good solvent – water in the case of PNIPAM. The microgels are considered as "soft" because the water-swollen polymer network is elastic and deformable. Small angle neutron scattering experiments revealed two inherent lengthscales of PNIPAM microgels. The particles have a homogeneously cross-linked inner core region, surrounded by an outer shell region where the cross-linking density decreases exponentially.[156,157] It follows that the outer region of the microgel particle is more deformable as compared to the inner core.[158]

Paloli et al. investigated the interaction potential of soft PNIPAM microgels with relatively high cross-linker densities (5 mol%).[150,151] They modelled the particle-particle interaction using a soft Hertzian pair-interaction potential (U_{Her}) with a fixed repulsion strength. The energy penalty caused by the elastic deformation of PNIPAM microgels is given by Equation 2.11[150,151]

$$U_{Her}(r) = \begin{cases} \epsilon_H(1 - \frac{r}{\sigma})^{\frac{5}{2}}, & r \leq \sigma \\ 0, & r > \sigma \end{cases} \tag{2.11}$$

where ϵ_H denotes the repulsive strength of the potential. Figure 2.6 B shows U_{Her} of PNIPAM microgels, which was calculated using $\sigma = 0.714\,\mu$m and $\epsilon_H = 496\,k_B\,T$ according to ref.[150] and[151]. In contrast to U_{HS}, U_{Her} has no sharp discontinuity. Instead, U_{Her} increases continuously with decreasing r, until it reaches its maximum energy at zero separation of the colloids.[159]

Particles with a soft pair-interaction potential are intriguing materials for self-assembly experiments because they have a significantly different phase behaviour as compared to hard sphere colloids. The pair-interaction potential allows for the formation of dense particle assemblies with very high packing fractions, and the phase transition behaviour of microgel colloidal crystals is directly linked to the compressibility of the particles.[153,160] Thus, concentrations above the hard sphere packing limit (ϕ=0.74) are possible. Debord et al prepared PNIPAM microgel crystals with ϕ>0.74 exploiting the temperature modulated volume phase transition behaviour of PNIPAM.[161] They observed overpacking and particle deswelling below their equilibration volume in dilute solution. Further research by the same group revealed that PNIPAM microgels also have

a very high defect tolerance as demonstrated by the preparation of almost defect free colloidal crystals. This fact was explained by the ability of the microgels to dissipate defect energies through the lattice over long distances.[160,162]

Besides the intriguing properties of microgel colloidal crystals, microgels were also used as stimuli responsive coating materials in many studies.[163–171] In this case, the fundamental challenge is the transfer of the particles from the dispersed state onto an arbitrary substrate in order to fabricate a functional superstructure. Ideally, the transfer method is not only a random deposition of particles, but also provides control of structure, interparticle spacing, and particle density of the superstructure. When PNIPAM microgel particles were prepared for the first time by Pelton and Chibante in 1986,[172] they discovered that the particles self-assembled into two-dimensional hexagonally ordered superstructures. Today, a broad range of different methods is available for the controlled self-assembly of microgel particles into two-dimensional superstructures. The most popular methods are summarized in Figure 2.8. Each self-assembly method has its own advantages and challenges, as it provides different handles for controlling structure, interparticle spacing, and particle density of the superstructure.

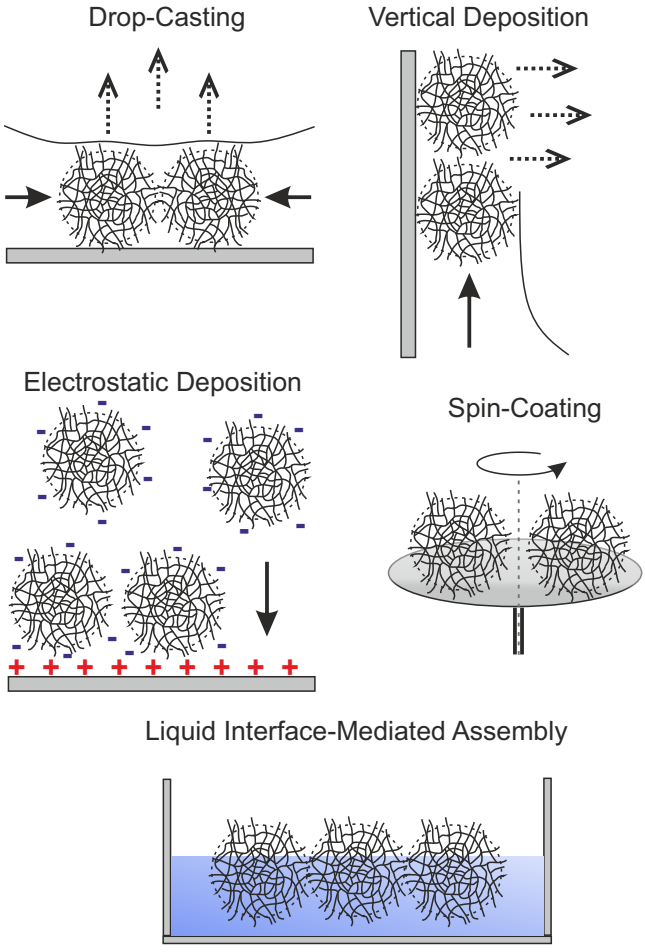

Figure 2.8. Overview of different self-assembly methods for the fabrication of two-dimensional microgel superstructures. Solid arrows indicate directional particle flux, and dashed arrows indicate solvent evaporation.

2.3.1 Deposition by Controlled Evaporation

The controlled evaporation of a microgel dispersion is one of the simplest methods for the self-assembly of a two-dimensional superstructure of soft particles. A droplet of the dispersion is carefully placed on a solid surface and subjected to evaporation. Next, a thin liquid film forms as the solvent evaporates, and once the height of the liquid film is below the microgel diameter, the particles are pushed together by immersion capillary forces.[173,174] Tsuji et al. prepared ordered monolayers of weakly charged PNIPAM microgels with uniform interparticle distances. They found that capillary interactions were mainly responsible for the monolayer formation, and that electrostatic interactions between the particles did not play a dominant role. This was evidenced by the formation of ordered monolayers from mixtures of oppositely charged particles, where hexagonally ordered superstructures with random particle distributions were found.[167,168] Drop-casting is a very simple self-assembly method, however it can be difficult to control the long-range order of the superstructure, and large area surface patterning is challenging. In addition, concentration and "coffee-stain" effects can lead to the formation of unwanted particle multilayers.[173]

A close follow-up on this approach is the vertical deposition method. In this process, a substrate is slowly retracted from a solution containing the dispersed colloids. A colloidal monolayer starts nucleating at the drying front of the substrate, and water evaporation causes a convective flux of the particles from the solution to the wetting film.[79,175] Vertical deposition was originally developed for hard spheres, but Zhang et al. demonstrated that the same method also works remarkably well for soft microgels. Using vertical deposition, they prepared non-close packed microgel monolayers. The interparticle distance of the microgels was tunable as a function of the withdrawal speed of the substrate.[169]

In conclusion, deposition by controlled evaporation is the first group of self-assembly methods providing access to two-dimensional superstructures of microgel particles. Ordered monolayers on small lengthscales are fabricated by drop-casting, whereas the regular patterning of larger areas is achieved by vertical deposition. A minor drawback of the vertical deposition method is the relatively high amount of material being consumed, which is especially difficult for samples that are only available in limited quantities.

2.3.2 Deposition by External Forces

Another approach to superstructures of soft particles is the application of external forces such as electrostatic forces or mechanical shear. The electrostatic deposition works best for strongly charged microgels such as poly(*N*-isopropylacrylamide-*co*-acrylic acid) (PNIPAM-*co*-AAc) microgels, which are synthesized by copolymerization of NIPAM and acrylic acid.[164–166,176] Schmidt et al. studied the impact of substrate, charge, pH, and preparation technique upon the electrostatic deposition of (PNIPAM-*co*-AAc) microgels. They found that the particle packing density of microgel monolayers was mainly influenced by the electrostatic interactions between the charged

microgels. Particle-substrate electrostatic interactions only played a minor role.[176] Although being weak, the particle-substrate interaction can still be exploited in order to control the order of the monolayer. This was demonstrated by Lu and Drechsler using charged PS-PNIPAM core-shell microgels. Superstructures with exceptional high hexagonal order and constant interparticle distance were obtained once the core-shell microgels and the surface carried opposite surface charges.[177]

Electrostatic deposition is a time consuming process. In contrast, a rapid fabrication of microgel monolayers is possible by spin-coating using mechanical shear forces.[78,166] This way, Schmidt et al. prepared close packed, hexagonally ordered monolayers of PNIPAM-*co*-AAc microgels. The formation of polycrystalline superstructures and a lack of long range order are common problems of the spin-coating process. However, Jaber et al. demonstrated that the order of microgel monolayers is improved by functionalizing the substrate with opposite surface charges.[78] The spin-coating method was further refined by Quint et al., who exploited the cononsolvency effect of PNIPAM microgels in water/ethanol mixtures. A substrate was covered with an aqueous droplet of a PNIPAM microgel suspension and the solubility of the microgels in the droplet was decreased by the addition of ethanol. The cononsolvency effect triggered the formation of polycrystalline patches of microgel monolayers at the air/liquid interface. Next, external shear was applied by an oscillatory gas flow directly followed by spin-coating. This three step process (ethanol addition, oscillatory gas flow, spin-coating) increased the crystalline domain size of the microgel monolayers considerably, and monolayers with extraordinary long-range order were obtained.[178]

In conclusion, self-assembly by external forces is the second group of self-assembly methods for soft particles. On the one hand highly ordered two-dimensional monolayers can be fabricated by external forces. On the other hand electrostatic self-assembly is a time consuming process, and spin-coating needs a meticulous adjustment of the high shear forces in order to prevent defects of the superstructure.

2.3.3 Deposition by Liquid Interface-Mediated Confinement

Self-assembly of soft particles at the air/liquid interface is the third group of fabrication methods for colloidal superstructures. In general, colloids are confined at liquid interfaces because they lower the interfacial energy of the interface.[173,179,180] Liquid interface-mediated confinement was already investigated for hard sphere colloids using different methods and equipments such as a Langmuir-Blodgett (L-B) trough,[181–185] floating,[186,187] or direct assembly at the air/water interface.[188,189] Briefly, hard spheres experience long-range attractive flotation forces at the liquid interface causing the colloids to crystallize into monolayers. A delicate balance of attractive short-range van der Waals forces, repulsive dipole, and repulsive electrostatic forces affects the particle arrangement of the monolayer. Highly ordered monolayers were fabricated by this method. The ordering of the colloids was preserved over large areas, and the monolayers were transferable onto different solid supports.[173,187]

In contrast, soft particles have a more complex behaviour at the air/water interface. PNIPAM microgels are surface active and lower the surface tension of water to approx 43 mJ/m^2.[190] Moreover, microgel monolayers are compressible at the liquid interface and they show an elastic deformation because the particles interpenetrate.[191,192] Additionally, microgels deform in an anisotropic manner at the interface. The particles stretch and transform into a "core-corona" shape. The deformation was verified by freeze-fracture shadow casting cryo scanning electron microscopy at oil/water interfaces.[193–195] Even though microgels behave more complex at liquid interfaces, the same methods as for fabrication of hard sphere monolayers can be applied. For instance, a L-B trough was used in order to crystallize microgels into highly ordered monolayers at the air/water or oil/water interface by compression. By this process, the interparticle distances was controllable over several hundreds of nanometers.[191,196–198] Liquid interface-mediated confinement also works for PNIPAM-encapsulated core-shell microgels with cores such as silica,[199–201] PS,[191] or Au.[79] This points towards the fact that the PNIPAM shell governs the self-assembly of these hybrid particles at the liquid interface. However, a L-B trough is not mandatory for the preparation of ordered superstructures by liquid interface-mediated confinement. Volk et al. fabricated highly ordered monolayers of PNIPAM-encapsulated silver nanoparticles at the water/air interface using a direct assembly method at the water surface.[202] Strikingly, the monolayers showed a time-dependent expansion behaviour at the water surface. The expansion was attributed to the anisotropic deformation of the hydrogel shell. Hence, interface-mediated confinement is a powerful method for the self-assembly of soft particles into ordered superstructures with exceptional long-range order. The superstructures are transferable onto flat as well as structured substrates without a loss of order.

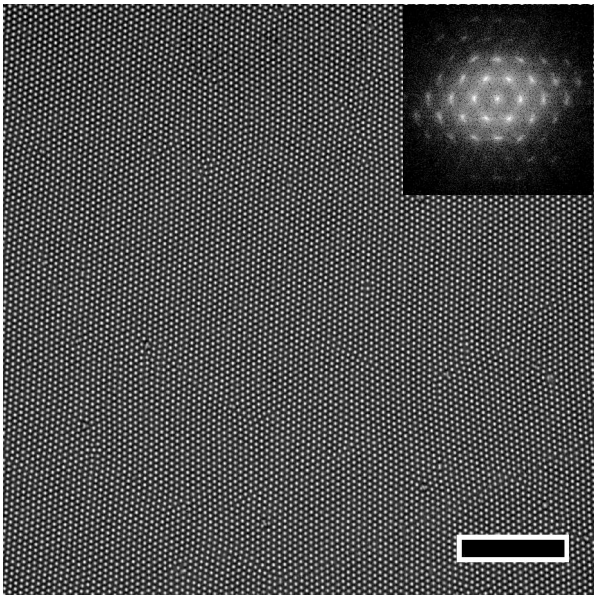

Figure 2.9. Low magnification TEM image of an Au-PNIPAM monolayer. The monolayer was prepared by direct assembly at the air/liquid interface and transferred onto a TEM grid. The inset shows the FFT of the image and the scale bar is 10 μm.

Figure 2.9 shows a low magnification TEM image of a monolayer of PNIPAM-encapsulated gold nanoparticles after transfer onto a TEM grid. Only a few local defects are observed and grain boundaries are hardly present. The long-range order is emphasized by the fast Fourier transformation (FFT) of the image, showing six fundamental Bragg peaks as well as higher order peaks in the power spectrum.

In conclusion, ordered superstructures of colloids with a soft pair-interaction potential can be produced using a broad range of different fabrication methods. Commonly the superstructures are investigated by techniques such as electron microscopy or atomic force microscopy. These techniques represent their data in the form of images. Hence, image analysis becomes an essential component in order to determine additional parameters such as interparticle distance, particle density, or symmetry of the nanostructure.

2.4 Image Analysis

2.4.1 Fourier Analysis

Superstructures made by colloidal self-assembly are classified as "ordered" by scientists to emphasise a certain correlation or symmetry in the arrangement of the constituent particles. Commonly, the structures are probed by imaging techniques such as AFM, TEM, or scanning electron microscopy (SEM). Using the obtained images, the particle arrangement and symmetry are evaluated by image processing techniques, for example Fourier analysis.

In Fourier analysis the Fourier transform of an image is computed by a fast Fourier transform algorithm, which is a standard feature in most of the image processing softwares. The FFT "expresses" the real space image in terms of its spatial frequencies with an amplitude and a phase associated with each spatial frequency. The representation of amplitude vs spatial frequency is denoted as power spectrum and conveys information about the distribution of spatial frequencies of the real space image. The representation in terms of frequencies is known as reciprocal space, and the FFT power spectrum can be directly linked to a diffraction pattern obtained from a scattering experiment on the sample. In this work, image processing of plasmonic superstructures is carried out using the freeware ImageJ and Gwyddion.

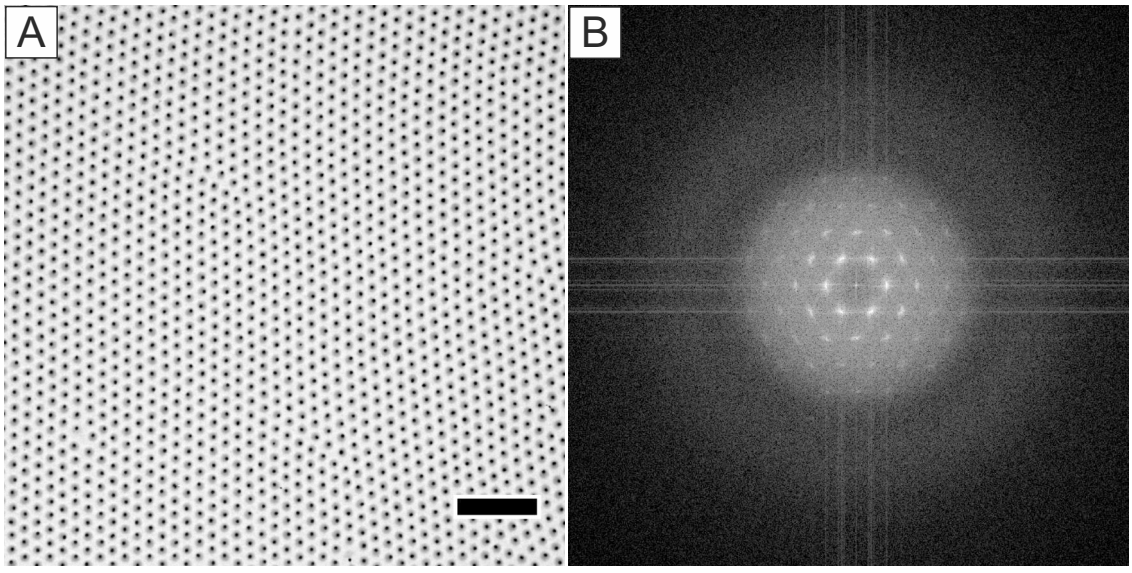

Figure 2.10. Fourier analysis of a periodic plasmonic superstructure. A, real space TEM image of a hexagonally ordered monolayer of PNIPAM-encapsulated gold nanoparticles. The scale bar is 3 μm. B, power spectrum computed by FFT of the real space image. The hexagonal order is evidenced by the six fold arrangement of the fundamental peaks.

Figure 2.10 shows a TEM brightfield image (real space image) of a periodic superstructure of PNIPAM-encapsulated gold nanoparticles and its power spectrum computed by the FFT algorithm. Every pixel of the power spectrum corresponds to a certain spatial frequency of the real space image with the relative occurrence of that frequency represented by the brightness of the pixel. The information is arranged by radius (frequency) and angle (θ) in a polar coordinate

system in the power spectrum. The reference point is the zero frequency spot in the center of the power spectrum encoding the average brightness of the real space image. Low spatial frequencies (large distances in real space) are displayed close to the image center. Moving radially away from the center of the power spectrum are increasing spatial frequencies, corresponding to shorter spatial periods, i.e., repetition lengths. When the image has a periodic pattern in multiple directions such as in Figure 2.10 A, the power spectrum will have a certain number of frequencies at different θ. In Figure 2.10 B six fundamental peaks of hexagonal symmetry are found in the power spectrum of the superstructure, and θ of those peaks represents the orientation angle of the pattern in the real space image. The average distance from the central spot to the fundamental peaks is the average nearest neighbor distance of the PNIPAM-encapsulated gold nanoparticles in Figure 2.10 A. Additionally, the presence of higher order peaks reveals long-range order of the particle array.

2.4.2 $g(r)$ Analysis

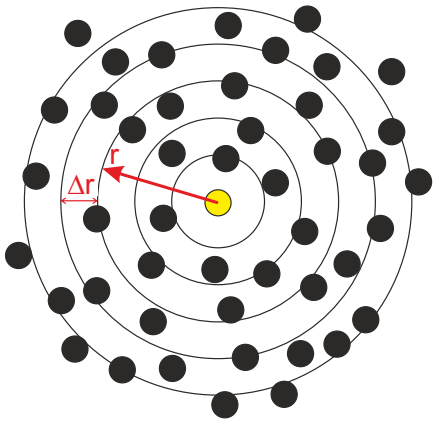

Figure 2.11. Schematic illustration of $g(r)$. The reference particle is colored in yellow.

In certain situations real space analysis using the particle positions can be more convenient compared to FFT analysis. For instance, the calculation of the radial distribution function ($g(r)$) allows for a quantitative analysis of the degree of order of a superstructure.[203,204] $g(r)$ is expressed by Equation 2.12[205]

$$g(r) = \frac{N(r)}{2\pi r\,\Delta r\,\rho} \tag{2.12}$$

where $N(r)$ represents the number of particles in a circular shell at a certain distance of r and $r + \Delta r$ from a reference particle. ρ is the particle density.[205] Briefly, $g(r)$ describes the probability of finding a particle in a shell Δr at a certain distance r from a reference particle, which is illustrated in Figure 2.11.

Figure 2.12 shows $g(r)$ of an ordered monolayer of PNIPAM-encapsulated gold nanoparticles. $g(r)$ was calculated from the positions of the particle centroids, which are determined by the "Ana-

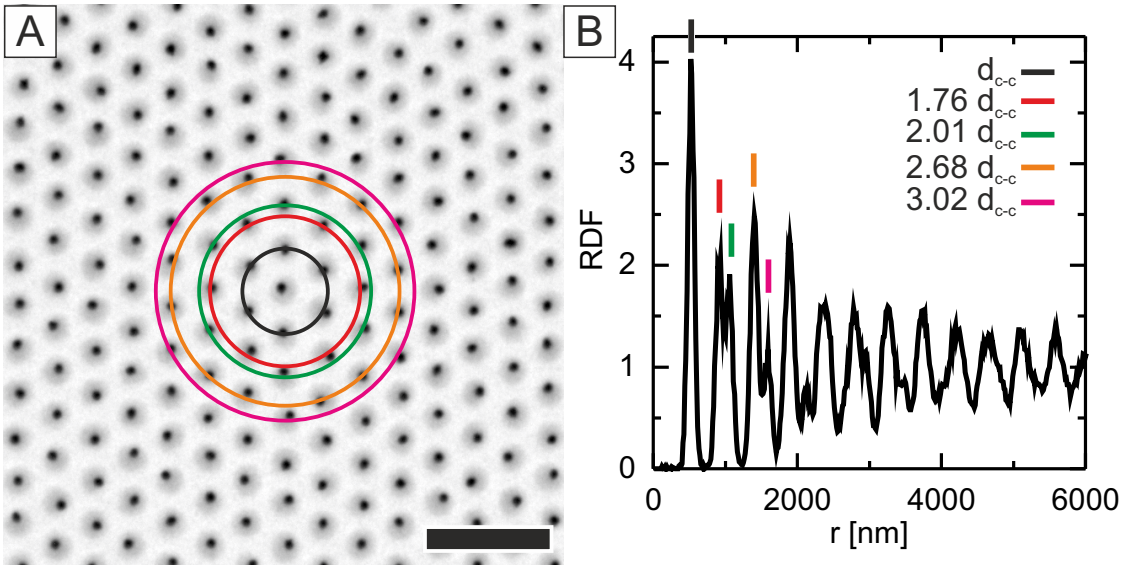

Figure 2.12. Analysis of a hexagonally ordered monolayer of PNIPAM-encapsulated gold nanoparticles by $g(r)$. A, TEM image of the monolayer. The five concentric rings illustrate $g(r)$ for five different d_{c-c}. The scale bar is 1.5 μm. B, calculated $g(r)$. The first five peaks are indexed corresponding the nearest neighbour distance (black) and the first four higher order neighbour sequences of the monolayer.

lyze Particles" algorithm of the ImageJ software. It requires a binary image, which can be created by using appropriate image brightness thresholds. $g(r)$ of the particle monolayer has a first peak at 524 nm as determined by a Lorentzian fit to the peak maximum. At this distance there is the highest probability of finding adjacent particles, and hence, it is the average center-to-center distance (d_{c-c}) between the nearest neighbor cores. This is illustrated by a black circle of radius 524 nm in Figure 2.12 A. Below 524 nm $g(r)$ rapidly drops to zero. It follows that there are no particles found below the diameter of the colloidal building blocks. In other words, the particles do not overlap. If the particles interact through hard pair-interaction potentials, it is impossible to squeeze another particle between two nearest neighbours. However, PNIPAM-encapsulated gold nanoparticles interact through soft pair-interactions potentials. Thus, in principle, interparticle distances below the diameter of the colloidal building blocks are possible because the particles can deform, and interpenetrate each other (cf. Section 1, Figure 1.2). Above 524 nm, $g(r)$ passes a (first) minimum at 715 nm, which means that the probability of finding particles at this distance is extremely low. A set of additional peaks is observable at higher r indicating long-range order of the monolayer. The peaks correspond to higher order neighbour sequences (second, third,... n th neighbours). The distances associated with the first four peaks of higher order are 920 nm (1.76 d_{c-c}), 1054 nm (2.01 d_{c-c}), 1403 nm (2.68 d_{c-c}) and 1585 nm (3.02 d_{c-c}), which is in close agreement to the first four higher order neighbor sequences of an ideal hexagonal array with 1.73 d_{c-c}, 2 d_{c-c}, 2.65 d_{c-c} and 3 d_{c-c}.[204] These four distances are illustrated in Figure 2.12 by concentric circles, clearly showing the connection between the peaks in $g(r)$ and the lattice order. At very high values of r, $g(r)$ drops and oscillates around 1 indicating random correlation of the particle positions.

2.4.3 Analysis by Autocorrelation Functions

Occasionally "noisy" images hamper the calculation of $g(r)$ because it is difficult to identify the exact particle coordinates. In this case, it is still possible to transform an image into a form that captures the regularity and geometry in the image by analysis of their autocorrelation functions (G). In general G describes the correlation of a signal with itself shifted by a displacement vector. In the case of an image the signal is the intensity distribution of the image, which is shifted in all possible directions with respect to itself. Importantly, G offers a simultaneous description of geometry at all lengthscales of the image. G of two-dimensional microscopy images is given by Equation 2.13[206]

$$G(j,l) = \frac{1}{(N-j)(M-l)} \sum_{i=1}^{N-j} \sum_{k=1}^{M-l} (a_{i,k} - \bar{a})(a_{i+j,k+l} - \bar{a}) \tag{2.13}$$

where j, l are the displacement shifts, M, N describe the number of data points in x and y direction, $a_{i,k}$, $a_{i+j,k+l}$ correspond to the fixed and the shifted signals, and $\bar{a}$ is the average of the whole signal.[206]

An instructive example of G are two identical, two-dimensional opaque films with circular apertures of the same diameter, illuminated by a light source. If both films are superimposed on each other in such a way that the apertures overlap exactly, the maximum possible transmission is achieved. Keeping one film fixed and shifting the other one in all possible x and y directions results in an overlap of opaque and transparent regions reducing the overall transmission. The change in transmission is an analogy to the value of G. Recording the transmission as one film is shifted in all possible x and y directions gives the brightness analog of G. A shift of zero will result in the highest possible transmission, hence a two-dimensional representation of G will have one peak of highest intensity, which is conventionally centered.[206,207]

Another access to G is given by the Wiener-Khinchin theorem stating that the autocorrelation function is the inverse Fourier transform of the power spectrum of the real space image.[208] Thus, the autocorrelation image provides the same information as the FFT power spectrum, but displayed in real space instead of reciprocal space. The calculation of G is readily implemented in software packages such as Gwyddion or ImageJ, for example.

Figure 2.13 displays G of the TEM image of the superstructure of PNIPAM-encapsulated gold nanoparticles already shown in Figure 2.10. In the central part of G, high intensity peaks are observable. The peak of highest intensity is located at the center of G (zero displacement). The shape of this peak represents the average shape of the particles, and the average diameter of the particles is given by the full width at half maximum (FWHM) of the peak. Next, a ring of six satellite peaks is visible, centered around the central peak of G. The positions of the satellite peaks indicate shifts of high correlation. Hence, the spacing between the central peak and the satellite peaks is equivalent to the average nearest neighbor distance of the particles.

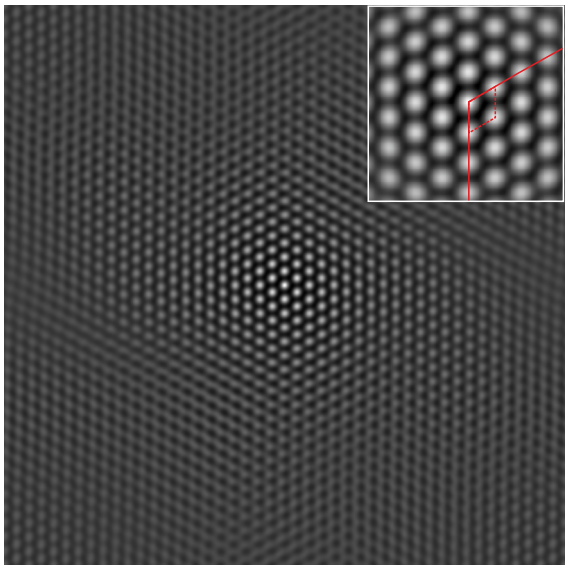

Figure 2.13. Two-dimensional autocorrelation function of the hexagonally ordered superstructure presented in Figure 2.10 A. The inset shows the central part of G and the unit cell of a hexagonal lattice is indicated in red.

In the case of an ordered array, peaks of G are found along and parallel to the principal axis of the lattice. The spacing of the peaks is equivalent to the lattice constant as indicated in the inset of Figure 2.13. It follows that G is well suited for the determination of the unit cell of an ordered superstructure. Lattice vectors a, b are found as 531 nm, and 533 nm, and $\theta = 120°$ which is characteristic for an ideal two-dimensional hexagonal lattice ($|a| = |b|$, $\theta = 120°$). The difference of lattice vectors and d_{c-c} between G and $g(r)$ analysis is 1 % and hence not significant. In the outer region of G, low intensity peaks are visible indicative of a reduced correlation between the image points with increasing displacement shifts, as expected for a non-ideal hexagonal lattice.

In conclusion FFT, $g(r)$, and G are powerful tools for image analysis and provide meaningful data. Each technique has its own strengths and weaknesses and offers different ways of data representation. The FFT excels at pattern analysis. For instance, it is easy to capture geometry and order of a particle arrangement, just by evaluating the fundamental peaks in the power spectrum. However, it is not straightforward to obtain information about the shape of the particles from the FFT. $g(r)$ provides immediate access to the particle distribution, spacing and the correlation of particle positions, but it is more difficult to extract information on the symmetry of the particle arrangement. Besides, $g(r)$ is a good way to display long-range order in the image. Finally, autocorrelation is useful because it is a more intuitive representation of an FFT image. In G "real" distances are measured, in contrast to the FFT analysis, where the information is plotted versus spatial frequency (1/distance). However, image analysis by autocorrelation is rarely encountered in the literature since it shows the same kind of information as the power spectrum of the FFT does.

Chapter 3

Experimental Section

3.1 Materials

L-ascorbic acid (>99 %, Aldrich), 2-(dodecylthiocarbonothioylthio)-2-methylpropanoic acid (DDMAT, 98 %, Aldrich), 3-butenylamine hydrochloride (97 %, Aldrich), 4, 4' - azobis(4-cyanovaleric acid) (ACVA, >98 %, Aldrich), acetone (>99.8 %), cetyltrimethylammonium bromide (CTAB, >98 %, Aldrich), cetyltrimethylammonium chloride (CTAC, 25 wt. % in water, Aldrich), chloroform (>99 %, Fisher Scientific), deuterium oxide (99.90 %, Deutero), dimethylformamide (DMF, >99.8 %, Aldrich), ethanol (abs., VWR), ethanolamine (>99.0 %, Aldrich), glycine (>99.7 %, Merck), gold chloride hydrate ($HAuCl_4$, 99.999 %, Aldrich), H_2O_2 (30 %, VWR), hexamethyldisilazane (HDMS, >99 %, Aldrich), hydrochloric acid (HCl, 0.1 M, Grüssing), 2-methoxyethanol (99.8 %, Aldrich), *N,N'*-methylenebisacrylamide (BIS, 99 %, Aldrich), NH_4OH_{aq} (25 %, Applichem), *N*-isopropylacrylamide (NIPAM, 97 %, Aldrich), phenyl-C_{61}-butyric acid methyl ester (PCBM, Solenne, M_w=910.9 g/mol), poly-3,4-ethylenedioxythiophene:polystyrene sulfonate (PEDOT:PSS, Baytron HTC solar), poly-3-hexylthiophene (P3HT, Rieke, $M_w = 60$-70 kg/mol, PDI = 2.0 - 2.3), potassium peroxodisulfate (KPS, 99 %, Merck), silver nitrate ($AgNO_3$, >99.5 %, Fluka), sodium citrate dihydrate (>99 %, Aldrich), sodium dodecylsulfate (SDS, 99 %, SERVA), and zinc acetate dehydrate (>99 %, Aldrich) were used as received. 2,2'-azoisobutyronitrile (AIBN, 98 %, Aldrich) was recrystallized twice from methanol. Ultrapure water (Milli-Q) with a resistivity of 18.2 M$\Omega \cdot$cm was used for all experiments unless indicated otherwise.

3.2 Synthesis

3.2.1 Gold Nanoparticles by Citrate Reduction

Each nanoparticle synthesis was carried out in glass beakers pre-cleaned with aqua regia. Gold nanoparticles of 15 nm in diameter (Au_{15}) were obtained following a slightly modified version of the Turkevich protocol.[209] 8.33 ml of a sodium citrate solution (100 mM) was prepared and incubated at 80 °C. 494.7 ml H_2O and 5.25 ml aqueous $HAuCl_4$ solution (47.6 mM) were combined and heated to heavy boiling under strong stirring. At this point, the prewarmed citrate solution was added in one shot to the mixture. Stirring and boiling were continued for 15 min. Gold nanoparticles of 19 nm in diameter (Au_{19}) were obtained following the same procedure. The small difference in size was attributed to slight differences of the $HAuCl_4$ reduction process during early stages of the nanoparticle growth.[210]

3.2.2 Gold Nanoparticles by Seed-Mediated Core Overgrowth

Gold nanoparticles of 22 nm – 53 nm in diameter were prepared by seed-mediated growth according to Bastús et al.[211] The synthesis was carried out with a metal heating mantle (EMA Electromantle, Electrothermal) under reflux conditions. Seed particles were synthesized by heating 150 ml sodium citrate solution (2.2 mM) to heavy boiling under strong stirring. At this point, 1 ml $HAuCl_4$ solution (25 mM) was added in one shot. After approx. 2 min, the reaction was cooled down and equilibrated at 90 °C. The seed particles were overgrown with gold by threefold addition of $HAuCl_4$ (25 mM) in 1 ml steps to the mixture (3 ml in total). The overgrowth was allowed to proceed for 30 min after each addition, before another 1 ml of $HAuCl_4$ was added. Next, 55 ml of the nanoparticle dispersion was collected as the first generation of particles (Au_{22}). Seed-mediated growth was continued as follows: 1) Addition of 55 ml citrate solution (2.26 mM) to the remaining dispersion, 2) equilibration at 90 °C, and 3) threefold addition of $HAuCl_4$ in 30 min steps. Afterwards, 55 ml of the nanoparticle dispersion were collected as the next generation of particles, and the core overgrowth was repeated. Seeded-mediated growth was continued until five generations of gold nanoparticles were obtained (Au_{22}, Au_{29}, Au_{36}, Au_{44}, and Au_{53}).

3.2.3 RAFT Synthesis of *l*-PNIPAM Ligands.

Non-cross-linked PNIPAM ligands with molecular weights of 9.5 kg/mol, 40 kg/mol, and 82 kg/mol were synthesized by reversible addition-fragmentation chain transfer polymerization (RAFT) following the protocol published by Ebeling et al.[23] The ligands are denoted as *l*-PNIPAM$_{M_n}$ according to their molecular weight. Briefly, NIPAM (monomer), DDMAT (RAFT agent) and AIBN (initiator) were dissolved in DMF in a glass vial and degassed for 20 min with nitrogen gas (grade 5.0). The polymerization was initiated by placing the glass vial in a prewarmed oil bath at 70 °C. During the polymerization, small aliquots of the reaction mixture were withdrawn with a syringe, quenched, and analyzed by ^{1}H-NMR spectroscopy. ^{1}H-NMR spectra of all ligands are

shown in the Appendix Figure 10.1 – 10.3. After a set polymerization time (t_p), the reaction was quenched by cooling in an ice bath and exposure of the reaction mixture to air. The polymer was purified by precipitation of the reaction mixture in diethyl ether, and the suspension was centrifuged for 30 min – 60 min at 10397 rcf (relative centrifugal force). The precipitate was re-dissolved in pure acetone, and the purification process was repeated twice. The solid polymer residue was dried under vacuum. Table 3.1 provides a detailed summary of the polymerization conditions and reagents employed for the synthesis of l-PNIPAM$_{9.5k}$, l-PNIPAM$_{40k}$, and l-PNIPAM$_{82k}$.

Table 3.1. Reagents and polymerization conditions for the synthesis of l-PNIPAM$_{M_n}$ ligands.

Sample	NIPAM	Initiator		DDMAT	DMF	T	t_p
	[mmol]	[mmol]		[mmol]	[ml]	[°C]	[h]
l-PNIPAM$_{9.5k}$	47.8	ACVA	0.017	0.239	11.4	70	1
l-PNIPAM$_{40k}$	47.8	AIBN	0.029	0.128	11.4	70	3
l-PNIPAM$_{82k}$	47.8	AIBN	0.029	0.066	11.4	70	3

Table 3.2. Volume of l-PNIPAM$_{M_n}$ for the functionalization of Au$_x$ nanoparticles.

Sample	$c_{part.}$ x 10^{11} [a]	V(l-PNIPAM$_{M_n}$) [μl][b]		
	[particles/ml]	9.5k	40k	82k
Au$_{15}$	3.3	37	155	318
Au$_{19}$	0.97	18	75	154
Au$_{22}$	5.8	139	587	1204
Au$_{29}$	3.5	145	612	1255
Au$_{36}$	2.6	165	695	1425
Au$_{44}$	1.4	134	563	1153
Au$_{53}$	0.93	130	547	1121

[a] $c_{part.}$, Gold nanoparticle concentration calculated from the nanoparticle absorbance at 400 nm.
[b] V_y, Volume of PNIPAM$_y$ solution (1 wt. %) for the functionalization of 1 ml Au$_x$ nanoparticles.

3.2.4 Ligand Exchange using *l*-PNIPAM

1 ml of citrate-stabilized gold nanoparticle dispersions (Au_{15} – Au_{53}) was diluted by the same volume of water. Next, a 1 wt. % *l*-PNIPAM$_{M_n}$ solution was added dropwise to the nanoparticle dispersion under heavy stirring. Stirring was continued for additional 30 min. The volume of ligand solution (V(*l*-PNIPAM$_{M_n}$)) was calculated considering an excess of polymer chains of 100 per nanoparticle and a surface grafting density of approx. 1 chain/nm^2.[212] The exact volumes of ligand solution for each gold nanoparticle dispersion are summarized in Table 3.2. Three centrifugation steps were carried out to remove excess polymer. Each time, the nanoparticle dispersion was centrifuged at 5400 rcf until the supernatant was completely colorless. The supernatant was discarded, and the precipitate was redispersed in water. The same method was also applied for the functionalization of gold nanorods. Rods with an aspect ratio of approx. 7 were synthesized according to Vigderman et al.[213] Ligand exchange of gold nanorods was carried out using *l*-PNIPAM$_{9.5k}$.

3.2.5 Colloidal Stability of Au_{22}-*l*-PNIPAM$_y$ Particles

Three dispersions of PNIPAM-encapsulated Au_{22} nanoparticles were prepared at pH 7. Previously, either *l*-PNIPAM$_{9.5k}$, *l*-PNIPAM$_{40k}$, or *l*-PNIPAM$_{82k}$ were selected as shelling materials for the nanoparticles. Next, ζ-potential and d_h were measured. Subsequently, HCl was used to decrease the pH of each dispersion stepwise in units of approx. 0.5. After each addition of HCl, ζ-potential and d_h were recorded.

3.2.6 Phase Transfer Experiments

Au_x-*l*-PNIPAM$_y$ dispersions were diluted by the same volume of a 1 wt. % *l*-PNIPAM$_{M_n}$ solution, and the mixture was left undisturbed for 30 min. Each dispersion was prepared in a pH range of 1 – 7 in pH steps of 1. A two-phase system was prepared for each sample containing 500 μl Au_x-*l*-PNIPAM$_y$ and 500 μl chloroform in a 2 ml snap cap vial. The vials were placed in a metal heating block (ThermoMix, MKR 13, HCL BioTech) and equilibrated at 60°C for 20 min. Afterwards, UV-Vis spectra of both phases were recorded. Next, the temperature was lowered to 4°C and the samples were equilibrated for 3 h. At this point UV-Vis spectroscopy of both phases was carried out anew.

3.2.7 Hydrogel Encapsulation by Precipitation Polymerization

Gold nanoparticles of 19 nm in diameter were prepared by citrate reduction following the same procedure as described in section 3.2.1. 500 ml Au_{19} were functionalized with butenylamine by dropwise addition of 1.63 ml of an aqueous butenylamine hydrochloride solution (1.44 mM) under stirring. After 30 min, the particles were centrifuged at 2599 rcf for 12 h and the precipitate was redispersed in approx. 5 ml of water (c[Au_{19}] = 13.46 mM). Three batches of cross-linked

PNIPAM-encapsulated gold nanoparticles (Au_{19}-x-$PNIPAM_{208}$, Au_{19}-x-$PNIPAM_{326}$, and Au_{19}-x-$PNIPAM_{508}$) were prepared by precipitation polymerization and variation of the monomer feed. For example, Au_{19}-x-$PNIPAM_{208}$ was synthesized by dissolving 226 mg NIPAM (0.02 M) and 46.2 mg BIS (15 mol % relative to NIPAM) in 100 ml water, and the solution was degassed for 20 min with nitrogen gas (grade 5.0). The solution was heated to 80 °C followed by addition of 541 μl of Au_{19} dispersion. Next, 2 mg KPS dissolved in 1 ml water was added, and the polymerization was carried out for 2 h. Afterwards, the particles were purified by threefold centrifugation at 10397 rpm until the supernatant was completely colourless (approx. 2 h). Finally, the particles were freeze-dried and stored in the dark upon further use. Au_{19}-x-$PNIPAM_{326}$ and Au_{19}-x-$PNIPAM_{508}$ were synthesized under similar conditions by increasing the monomer feed to 0.06 M and 0.1 M, respectively.

3.2.8 Post-Modification of the Plasmonic Core

Gold Overgrowth. Au_{19}-x-$PNIPAM_{326}$ particles were overgrown with gold following a modified protocol by Rodriguez-Fernández et al.[32] The core overgrowth was performed sequentially keeping a constant molar ratio of ascorbic acid/gold(III) chloride hydrate of 1.3 for each growing step. 1 wt. % of freeze-dried Au_{19}-x-$PNIPAM_{326}$ particles was dispersed in 50 mM CTAC solution and used as a precursor stock solution. A $HAuCl_4$ stock solution (feed solution) was prepared containing 0.5 mM $HAuCl_4$ and 4.75 mM CTAC. The solution was allowed to rest for 10 min to promote the formation of Au(III)-CTAC complexes. Next, 200 μl precursor stock solution, 8 ml CTAC (2.4 mM) and 80 μl of a freshly prepared ascorbic acid solution (10 mM) were mixed. Final core diameters of 30 nm were obtained by dropwise addition of 1.280 ml feed solution to the mixture under heavy stirring. The stirring was continued for additional 20 min. Purification was carried out by centrifugation of the particles at 3740 rcf, until the supernatant was completely colorless. The supernatant was discarded, and the precipitate redissolved in water. This purification procedure was performed three times in total. Larger core sizes of 41 nm, 60 nm, and 92 nm were obtained by increasing the amount of feed solution to 3.0 ml, 6.7 ml, and 29.3 ml, respectively. Each time, the amount of ascorbic acid was adjusted accordingly.

Silver Overgrowth. Au_{19}-x-$PNIPAM_{326}$ particles were overgrown with silver using a modified surfactant assisted protocol by Contreras-Cáceres et al.[30] A precursor stock solution was prepared containing 1 wt. % Au_{19}-x-$PNIPAM_{326}$, 50 mM CTAB and 400 mM glycine. 800 μl NaOH (0.1 M) and 450 μl freshly prepared ascorbic acid solution (100 mM) were mixed with 10 ml precursor stock solution. 1.31 ml $AgNO_3$ (15 mM) was added dropwise to the mixture under heavy stirring, and the reaction was finished after 20 min. The final diameter of the silver-overgrown gold cores was 28 nm. The particles were purified by three-fold centrifugation at 2400 rcf. Each time, the clear supernatant was discarded and the precipitate was redissolved in water. Larger silver cores of 46 nm, 73 nm, and 100 nm were achieved by reducing the amount of precursor stock solution to 800 μl, 146 μl, and 50 μl, respectively.

3.3 Self-Assembly of Au-PNIPAM Particles

3.3.1 Cleaning of Glass Substrates

Glass substrates of approx. 1 cm^2 in size were cut from microscopy slides (Thermo Scientific) and cleaned by sequential sonication in acetone, 2-propanol, and water for 20 min, each time. Next, cleaning of the substrates was carried out in a 5:1:1 mixture (by volume) of H_2O, NH_4OH_{aq} (25 %), and H_2O_2 (30 %) at 80 °C for 20 min. The slides were rinsed with water thoroughly and dried using pressured air.

3.3.2 Surface Functionalization of Glass Substrates

HDMS functionalization. Precleaned glass substrates were transferred into a desiccator, and a small crystallizing dish containing 200 μl of HDMS was placed below the glass substrates. The desiccator was sealed and evacuated until a final pressure of approx. 5×10^{-1} mbar was reached. The substrates were kept in the desiccator for 2 h. Afterwards, the glass substrates were cleaned carefully by pressured air.

Carbon Coating. A thin carbon film was deposited from a 0.4 g/m carbon thread on one side of precleaned glass substrates by a planar-magnetron sputtering device (Bal-Tec MED 010). The final film thickness of the carbon coating was approx. 40 nm.

3.3.3 Preparation of Monolayers by Spin-Coating

Aqueous dispersions of Au_{15}-*l*-$PNIPAM_y$ (1 wt. %) were prepared and homogenized thoroughly using a Vortex Mixer (VWR). Monolayers of Au_{15}-*l*-$PNIPAM_y$ on glass were fabricated by spin-coating at 4000 rpm for 30 s. The substrate was removed and cleaned carefully using pressured air.

3.3.4 Preparation of Monolayers by Interface-Mediated Self-Assembly

Au_{19}-*x*-$PNIPAM_y$ particles were self-assembled into monolayers at the air/water interface. The experiment was performed in a crystallizing dish filled with approx. 150 ml of water, which was illuminated sideways by a commercial halogen lamp (35 W). 10 μl of an ethanolic particle dispersion (approx. 1 wt.%) was spread slowly at the water surface using a 10 μl pipette (Eppendorf). After 10 min, a glass substrate was immersed carefully underneath the monolayer, and a part of the monolayer was collected by retracting the substrate out of the water – through the monolayer – at an angle of approx. 30 °. Immediately after leaving the water phase, the substrate was dried with a stream of hot air (heat gun, approx. 80 °C) pointing at the backside of the sample.

3.3.5 Preparation of Honeycomb Structures

Honeycomb structures of Au_x@Au- and Ag_x@Au-x-PNIPAM$_y$ particles were prepared by sequential deposition of two monolayers on the same substrate. Previously, the individual monolayers were prepared in separate crystallizing dishes as described in Section 3.3.4. Each monolayer was collected on glass substrates using a dip-coater (DC/D/LM, KSV Instruments) at a withdrawal rate of 5 mm/min. After collection of the first monolayer, the substrate was heated for 15 min at 200 °C on a hot plate to strengthen the adhesion between the monolayer and the glass substrate. Next, the deposition process was repeated and a second monolayer of Au_x@Au- or Ag_x@Au-x-PNIPAM$_y$ was collected on the same substrate. The dip-coater was stopped immediately once the substrate left the water phase, and it was waited until the substrate was completely dry (approx. 10 – 15 min), before it was fetched from the device. Honeycomb structures on carbon coated glass slides as well as on carbon coated TEM grids (200 mesh, Electron Microscopy Sciences) were prepared in a similar way.

3.3.6 Preparation of Superstructures Beyond Hexagonal Monolayers

Monolayers of square- or centered rectangular-like symmetry were fabricated using a dip-coater and HDMS functionalized glass substrates with a contact angle (θ_c) of approx. 60°. At first, a monolayer of Au_{95}@Au-x-PNIPAM$_{330}$ was prepared at the water surface according to Section 3.3.4. A glass substrate was mounted onto the dip-coater and a part of the monolayer was collected by immersing the substrate through the monolayer at an immersion speed of 15 mm/min. Any remains of the Au_{95}@Au-x-PNIPAM$_{330}$ monolayer which were not collected were removed by addition of 10 μl of l-PNIPAM$_{40k}$ to the water surface. Next, the substrate was collected from the water subphase and dried under ambient conditions.

3.4 Fabrication of Plasmonic Solar Cells

Transparent ITO patterned glass slides (Bte Bedampfungstechnik) with a thickness of the ITO layer of approx. 213 nm and a sheet resistivity of approx. 10 Ω/square were used as solar cell substrates. Each solar cell substrate consisted of four independent solar cell devices. The solar cell substrates were cleaned thoroughly by sequential sonication in acetone, isopropyl alcohol and water, for 15 min each time. Afterwards, the substrates were carefully dried with pressured air and stored in a dust-free storage chamber.

3.4.1 Solar Cells with Normal Cell Geometry

Organic thin film solar cells were fabricated by sequential spin-coating from PEDOT:PSS and P3HT:PCBM solutions on top of ITO patterned solar cell substrates. Solutions of PEDOT:PSS and P3HT:$PC_{61}BM$ were filtered using 0.45 μm filters prior to use. The active layer solution was prepared with a constant ratio of P3HT/$PC_{61}BM$ of 1/0.8. At first, a PEDOT:PSS layer of approx. 40 nm was deposited by spin-coating at 4000 rpm for 50 s, and the substrates were annealed for 15 min at 150 °C. Afterwards, the substrates were transferred into a glove box, and the active layer was applied by spin-coating from P3HT/PCBM solution. A spin-coating program was selected consisting of a first step of spinning at 550 rpm for 50 s, immediately followed by a second step of spinning at 2000 rpm for 2 s. The final film thickness was approx. 90 nm. The device was completed by vacuum deposition of an Al top electrode (215 nm in thickness) at 1.35×10^{-5} mbar. Post-annealing of the device was carried out at 170 °C for 5 min.

Plasmonic solar cell devices were fabricated by deposition of an Au_x@Au-x-$PNIPAM_y$ monolayer on top of ITO patterned glass slides, prior to the device assembly. Therefore, the ITO substrates were hydrophilized under oxygen plasma (100 W, 30 sec, MiniFlecto, Plasma Technology GmbH) to facilitate the deposition of the monolayer (θ_c (substrate) $\approx$ 0°). Next, a monolayer of Au_x@Au-x-$PNIPAM_y$ particles was prepared via interface-mediated self-assembly as described in Section 3.3.4. 10 μl of a 1 wt.% ethanolic Au_x@Au-x-$PNIPAM_y$ dispersion were used for the preparation of a freely floating monolayer having a surface area of approx. 28 cm^2. A part of the monolayer was collected by immersion of an ITO substrate (total surface area 6.45 cm^2) into the water subphase, immediately followed by retraction of the substrate – through the monolayer – at a shallow angle. Subsequently, the substrate was dried carefully using pressured air. Afterwards, assembly of solar cell devices was continued similar to the non-plasmonic solar cell devices.

3.4.2 Solar Cells with Inverted Cell Geometry

At first, a zinc acetate solution was prepared containing 109.75 mg zinc acetate dehydrate, 30.5 μl ethanol and 1 ml methoxyethanol. The solution was spin-coated at 4000 rpm for 50 s onto clean ITO patterned solar cell substrates. Zinc acetate was converted into zinc oxide by baking at 150 °C for 15 min in air. The final film thickness was approx. 40 nm. Next, a P3HT:PCBM layer was deposited in a glove box by spin-coating at 600 rpm or 850 rpm. This way, film thicknesses of 194 nm or 118 nm were obtained. Subsequently, the active layers were annealed for 15 min at 135 °C. The device was completed by vacuum deposition of MoO_3 (10 nm in thickness) and the Ag top electrode (150 nm in thickness) at approx. 1×10^{-6} mbar.

Plasmonic solar cell devices were fabricated by deposition of Au_{89}@Au-x-$PNIPAM_{330}$ monolayers at different interfaces of the solar cell substrates. Deposition of the monolayers onto the ITO or ZnO layer (**Type 1 – 3** devices) was carried out similar as in Section 3.4.1. In the case of **Type 3** devices, a second layer of ZnO was deposited on top of the particles. Monolayers on the active layer of inverted solar cell substrates (**Type 4** devices, $\theta_c \approx 60°$) were prepared by directly immersing the substrate through the monolayer at an angle of approx. 30 °. This way, a part of the particle monolayer stuck directly to the active layer and was pulled underwater. Any remaining parts of the floating monolayer on the water surface were removed by dropwise addition of 10 μl of a 1 wt.% aqueous l-$PNIPAM_{40k}$ solution onto the water surface. Afterwards, the solar cell substrate was retracted from the water subphase and dried with pressured air. A fresh monolayer was prepared for every device. Finally, the solar cell was finished by evaporation of the capping electrode as described above.

3.5 Experimental Methods

3.5.1 UV-Vis Spectroscopy

UV-Vis spectroscopy was carried out on two different devices – either on an Analytik Jena spectrophotometer (Specord 250) or on an Agilent 8453 UV-Vis spectrophotometer. Each time, UV-Vis absorbance spectra were recorded in a wavelength range of 190 nm – 1100 nm. Temperature controlled experiments were performed on the Agilent 8453 UV-Vis spectrophotometer equipped with a circulating water bath (Julabo F30-C). Dilute sample dispersions were measured in quartz cells with 1 cm light path. Quartz cells with 1 mm light path were used for the phase transfer experiments of Au_x-*l*-$PNIPAM_y$.

3.5.2 Theoretical Modelling of Extinction Spectra

Theoretical calculations were performed using the Mathematica 10 software. Mie theory and the multilayer recursive method were used for the calculation of plasmonic extinction spectra.[111] The dimension of the plasmonic core of Au_x- and Ag_x@Au-x-$PNIPAM_y$ particles was obtained from TEM measurements, and a hydrogel size of 326 nm was chosen from the results of DLS measurements of the particles. Refractive indices of silver and gold were selected from Johnson and Christiy[112] and modified to account for electron surface scattering at small sizes.[86] The refractive index of the water-swollen hydrogel shell was calculated from $n_{H_2O} + dn$. n_{H_2O} is the refractive index of water[214] and $dn = 0.05$ was obtained from the best fit value to the absorption spectra of Au_{19}-x-$PNIPAM_{326}$ particles. The host medium was water. Multiple expansions up to 5 – 8 terms were included to reduce the relative error of the calculated wavelengths to less than 0.1 %.

3.5.3 TEM

TEM samples were prepared on carbon coated copper grids (200 mesh, Electron Microscopy Sciences) either by drop casting from dilute dispersion or by floating at the air/water interface (see also Section 3.3.4). TEM investigation was conducted with a ZEISS CEM 902 TEM under bright field illumination at an acceleration voltage of 80 kV. Particle size distributions were obtained from grayscale TEM images using the software ImageJ.

3.5.4 AFM

Plasmonic superstructures on solid substrates were investigated by AFM in tapping mode. A Nanoscope Multimode AFM (Veeco) was used operating under ambient conditions in air. AFM probes (OTESPA-R3) were provided by Bruker having spring constants of approx. 26 N/m. Bow and tilt artifacts of the AFM images were corrected by 1^{rst} order flattening using the instrument's software (Bruker). Only the AFM height images were selected for further image analysis.

3.5.5 Light Scattering

DLS of Au_x-*l*-$PNIPAM_y$ particles

Dynamic light scattering experiments (DLS) of Au_x-*l*-$PNIPAM_y$ were carried out on a NanoZS Zetasizer (Malvern Instruments). The device was equipped with a HeNe laser ($\lambda = 632.8\,nm$) and the detector was located at a fixed detection angle of 173 °. Filtered, (5 μm PTFE membrane, Rotilabo©, Carl ROTH) strongly dilute aqueous dispersion of Au_x-*l*-$PNIPAM_y$ were measured in disposable PS plastic cuvettes (1.5 ml – 3.0 ml, VWR). Each sample was equilibrated for 2 min prior to the measurement. Three intensity-time autocorrelation functions ($g^{(2)}(q,\tau)$) were recorded for 60 s, each and analyzed by the instruments software. $g^{(2)}(q,\tau)$ is given by Equation 3.1

$$g^{(2)}(q,\tau) = \frac{\langle I(q,t)\, I(q,t+\tau)\rangle}{\langle I(q,t)\rangle^2} \tag{3.1}$$

where I is the scattering intensity, q the scattering vector, t the initial time, and τ the delay time. The average decay rate $\bar{\Gamma}$ of $g^{(2)}(q,\tau)$ is obtained by moment analysis of the linear form of $g^{(2)}(q,\tau)$ (method of cumulants)[215] given by Equation 3.2 and 3.3

$$g^{(2)}(q,\tau) = A[1 + B\ \exp(-2\Gamma\tau + \mu_2\tau^2)] \tag{3.2}$$

$$\begin{aligned}\frac{1}{2}\ln[g^{(2)}(q,\tau) - A] &= \frac{1}{2}\ln[A\,B\ \exp(-2\Gamma\tau + \mu_2\tau^2)] \\ &= \frac{1}{2}\ln[A\,B] - \bar{\Gamma}\tau + \frac{\mu_2}{2}\tau^2\end{aligned} \tag{3.3}$$

where A is the intercept and B the baseline of $g^{(2)}(q,\tau)$. The polydispersity index of the sample (PDI) is calculated by Equation 3.4

$$PDI = \frac{\mu_2}{\bar{\Gamma}^2} \tag{3.4}$$

where μ_2 represents the width of the decay rate distribution.

SLS and DLS of Au_{19}-*x*-$PNIPAM_y$ particles

Static light scattering (SLS) and DLS experiments of Au_{19}-*x*-$PNIPAM_y$ were carried out on a goniometer setup (ALV, Langen, Germany) using a HeNe laser ($P_{max} = 35\,mW$, $\lambda = 632.8\,nm$, JDSU, USA). Filtered (5 μm PTFE membrane, Rotilabo©, Carl ROTH), strongly dilute sample dispersions were prepared in cylindrical quartz cuvettes. The measurements were performed at a constant temperature of 25°C controlled by a toluene bath equipped with a PT100 thermocouple. Toluene also served as a refractive index matching fluid for the quartz cuvettes. Angular-dependent SLS measurements were performed in steps of 2° in a range of 30° – 150°.

Each measurement was carried out for 15 s. SLS profiles of Au_{19}-x-$PNIPAM_y$ were analyzed using the "SASfit" software (v. 0.94.7).[216]

Angular-dependent DLS measurements were carried out in steps of 5° in a range of 30° – 90°, and three intensity-time autocorrelation functions were recorded at each angle. Each measurement was performed for 60 s. Γ was obtained from intensity-time autocorrelation functions, which were analyzed by the CONTIN regularization method. Therefore, $g^{(2)}(q,\tau)$ is expressed in terms of the field-time correlation function $g^{(1)}(q,\tau)$ using the Siegert relation in Equation 3.5[217,218]

$$g^{(2)}(q,\tau) = 1 + A|g^{(1)}(q,\tau)|^2 \tag{3.5}$$

For polydisperse samples, $g^{(1)}(q,\tau)$ is given by Equation 3.6

$$g^{(1)}(q,\tau) = \int_0^\infty G(\Gamma)\exp(-\Gamma\tau)d\Gamma \tag{3.6}$$

where $G(\Gamma)$ is the distribution of decay rates, and $g^{(1)}(q,\tau)$ is the Laplace transformation of $G(\Gamma)$. A solution to Equation 3.6 is provided by the CONTIN algorithm. DLS measurements were evaluated by the CONTIN method using the software "AfterALV1.0d" by Dullware.

3.5.6 ζ-Potential

ζ-potential measurements were carried out on a NanoZS Zetasizer (Malvern Instruments). The electrophoretic mobility of dilute, aqueous particle dispersions was determined by electrophoresis, and the velocity of the particles was measured using Laser Doppler velocimetry. The Henry equation[219] and the Smoluchowski limit ($f(\kappa\,\alpha) = 1.5$) were chosen to calculate the ζ-potential of the particles from the electrophoretic mobility (μ_E) by Equation 3.7

$$\mu_E = \frac{2\,\epsilon_0\,\epsilon_r\,\zeta}{3\,\eta} f(\kappa\,\alpha) \tag{3.7}$$

where ϵ_0 and ϵ_r are the dielectric constants of free space and the dispersion medium, respectively.

3.5.7 SEM and EDX mapping

SEM measurements were carried out on a ZEISS Ultra plus field emission scanning electron microscope (FE-SEM). A thin carbon coating of approx. 30 nm was applied to all samples using a Balzers Union MED 010 sputtering device. Images of plasmonic nanostructures were recorded by an in-lens and a SE2 detector in a range of acceleration voltages between 2 kV and 10 kV.

Plasmonic honeycomb structures were investigated by SEM coupled with energy-dispersive X-ray spectroscopy (EDX). SEM images were acquired by an AsB (angle selective backscattered electron) detector. EDX spectra were recorded on a silicon drift detector (ThermoFisher). The

spectra were analysed using the NSS 3 X-Ray Microanalysis software (ThermoFisher). Elemental mapping of high resolution SEM images was carried out using only silver and gold X-ray emission lines.

3.5.8 SEC

Size exclusion chromatography (SEC) experiments were conducted on a liquid chromatograph (Waters Associates) with THF and 0.25 wt. % tetrabutylammonium bromide as eluent. Measurements were performed at 23 °C at a flow rate of 0.5 ml/min. The column setup comprised a guard column (PSS, 4 cm x 0.9 cm, SDV gel, particle size 5 μm, pore size 100 Å) and two separation columns (Varian, 30 cm x 0.8 cm, mixed C gel, particle size 5 μm). Two concentration sensitive detectors (UV and refractive index) recorded chromatograms of *l*-PNIPAM$_{M_n}$ polymers. The retention volume was converted into a molecular weight distribution using a PS calibration curve.

3.5.9 Solar Cell Performance

IV-curves of organic solar cells were measured under inert atmosphere employing a Keithley 2400 source measure unit with a power density of 100 mW/cm^2 from a class A solar simulator. The measurements were carried out under standard AM 1.5 illumination. Test cell masks with an aperture of 9 mm^2 were used to define the illuminated area. Reflectance and EQE spectra were recorded on a Bentham PVE 300 device. Reflectance spectra were measured by an integrating sphere under illumination from the glass side of the solar cell substrate. EQE measurements of **Type 4** inverted plasmonic solar cells were carried out at -4 V as well as under short circuit conditions.

Chapter 4

Colloidal Building Blocks

The colloidal stability of plasmonic nanoparticles is a crucial parameter for self-assembled superstructures.[220,221] A convenient way to enhance the colloidal stability of plasmonic nanoparticles is their encapsulation with polymer shells. In this work, PNIPAM is selected as a shelling material for gold nanoparticles. The particles are functionalized with either non-cross-linked PNIPAM or cross-linked PNIPAM shells. This way, the thickness of the PNIPAM shell is tunable form a few tens up to several hundreds of nanometers. Consequently a library of plasmonic building blocks is fabricated and subsequently used for the fabrication of superstructures via self-assembly.

4.1 Gold Nanoparticles with Non-Cross-Linked PNIPAM Shells

Citrate-stabilized gold nanoparticles aggregate easily because of their high Hamaker constant in water. In order to increase the colloidal stability of the particles, surface functionalization by ligand exchange is a convenient solution. The citrate ligand is replaced by a ligand which has a very high binding affinity towards the surface of the nanoparticles. Depending on the ligand architecture, the colloidal stability of the nanoparticles is enhanced by additional electrostatic and/or steric stabilization.[18,212,222] Even compatibility with different environments such as a polymer matrices[223] or solvents is possible.[6,221,224]

Non-cross-linked α-trithiocarbonate-ω-carboxyl terminated PNIPAM ligands are used for ligand exchange with citrate-stabilized gold nanoparticles of 15 nm – 53 nm in diameter. The trithiocarbonate function binds strongly to the gold surface,[225] and thus, the citrate molecules on the surface of the nanoparticles are replaced by the polymer. The ligand exchange reaction is followed by UV-Vis spectroscopy due to the LSPR of the gold nanoparticles. The reaction is carried out in a single phase (water) using mass exchange.[223] The polymer ligand is added in excess relative to the concentration of nanoparticles. Therefore, each nanoparticle dispersion was investigated by UV-Vis spectroscopy at first in order to calculate the concentration of gold nanoparticles.

4.1.1 Characterization of Gold Nanoparticles

Citrate-stabilized gold nanoparticles were synthesized following two different protocols. Gold nanoparticles of 15 nm and 19 nm in diameter (Au_{15} and Au_{19}) were prepared based on the well-known citrate reduction protocol by Turkevich.[209] Gold nanoparticles of 22 nm, 29 nm 36 nm, 44 nm, and 53 nm in diameter ($Au_{22} - Au_{53}$) were prepared following the seeded growth protocol by Bastús et al.[226] Further details are provided in Section 3.2.2. UV-Vis absorbance spectra of the particles are shown in Figure 4.1. The LSPR peak positions of all particles are summarized in Table 4.3.

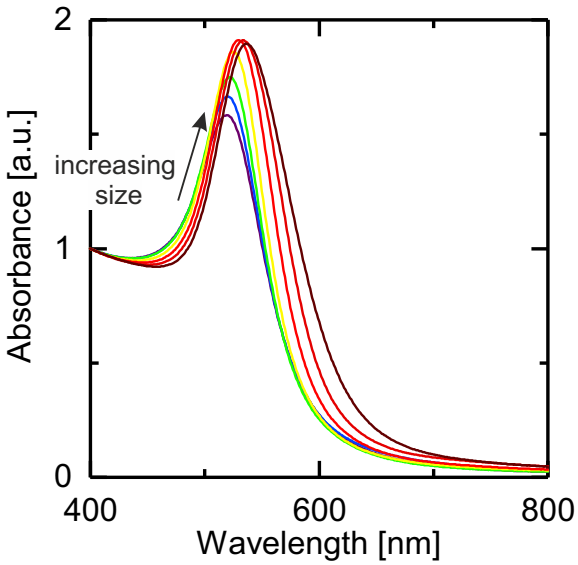

Figure 4.1. Investigation of $Au_{15} - Au_{53}$ by UV-Vis spectroscopy. The intensity of the LSPR increases for larger particles. All spectra are normalized at 400 nm.

The UV-Vis spectra show narrow LSPRs for all nanoparticles, without any signs of agglomeration at larger wavelengths. It is evident that the LSPR of larger gold nanoparticles is shifted towards longer wavelengths as a result of their weaker restoring force.[32,227] The concentration of gold (c_{Au_0}) of the gold nanoparticle dispersions was determined by UV-Vis spectroscopy using the Lambert-Beer law in Equation 4.1

$$c_{Au_0} = \frac{Abs_{400}}{\epsilon_{400}\, d_{cuv.}} \tag{4.1}$$

where ϵ_{400} is the extinction coefficient at a wavelength of 400 nm and $d_{cuv.}$ is the path length of the UV-Vis cuvette (1 cm). The size-dependent ϵ_{400} was selected for each batch of gold nanoparticles from reference [228]. Using c_{Au_0}, the concentration of gold nanoparticles is given by Equation

$$c_{part.} = \frac{6\, M_{Au}\, c_{Au_0}}{d_c^3\, \pi\, \rho_{Au_0}} \tag{4.2}$$

where ρ_{Au_0} is the bulk density (19.32 g/cm^3), and M_{Au_0} (196.96 g/mol) is the molecular weight of gold.

The diameter of the gold nanoparticles was determined by TEM. Figure 4.2 shows representative TEM images of all $Au_{15} - Au_{53}$ nanoparticles. The electron beam is strongly scattered by the gold nanoparticles, hence they appear as dark two-dimensional projections in the TEM images. Figure 4.2 reveals that all particles are of spherical shape. Size characterization of the particles was carried out using the ImageJ software. Particle size distributions are shown in Figure 4.2 for all gold nanoparticles. The average diameters were obtained from Gaussian fits to the particle size distributions, and all values of d_c are summarized in Table 4.1. Narrow size distributions were found for almost all seven batches of gold nanoparticles. A slight increase of the size distribution was only observed for Au_{53} nanoparticles.

Table 4.1. Characterization of citrate-stabilized gold nanoparticles.

Sample	d_c [nm]	Abs_{400}	ϵ_{400} x 10^3 [l mol^{-1} cm^{-1}]	$c_{part.}$ x 10^{11} [particles/ml]
Au_{15}	15±2	0.13	2.33	3.3
Au_{19}	19±2	0.08	2.36	0.9
Au_{22}	22±3	0.76	2.38	5.8
Au_{29}	29±3	1.06	2.43	3.5
Au_{36}	36±4	1.56	2.53	2.7
Au_{44}	44±5	1.60	2.63	1.4
Au_{53}	53±7	1.91	2.68	0.93

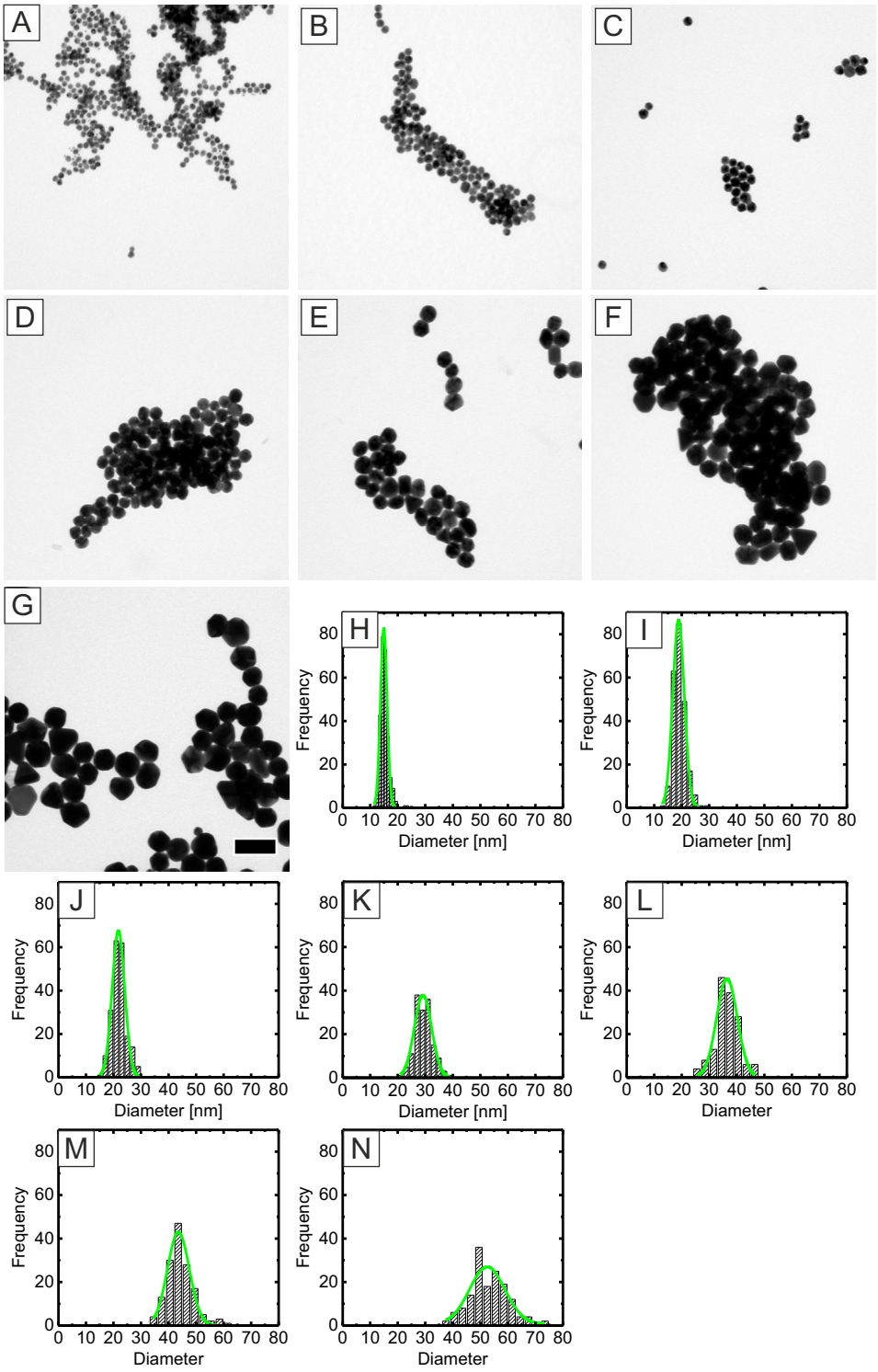

Figure 4.2. TEM investigation of citrate-stabilized gold nanoparticles. A – G, bright-field TEM images of Au_{15} – Au_{53}. The scale bar is 100 nm. H – N, show the respective particle size distribution histograms. A Gaussian size distribution was used to fit the data (green lines).

4.1.2 Ligand Exchange

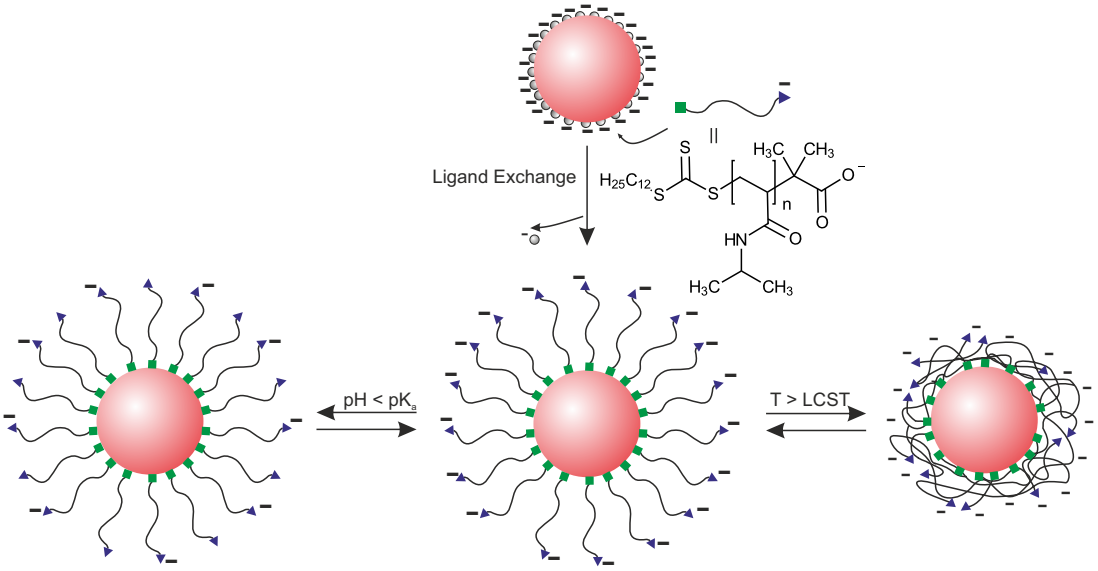

Figure 4.3. Schematic illustration of the ligand exchange of citrate-stabilized gold nanoparticles with l-PNIPAM$_{M_n}$. Upper part: citrate molecules on the surface of a gold nanoparticle are replaced by l-PNIPAM$_{M_n}$ due to the higher binding affinity of the trithiocarbonate group to the nanoparticle surface. Lower part: the PNIPAM shell is dual responsive and responds to temperature as well as pH. Lowering the pH below the pK$_a$ of the carboxyl function reduces the surface charge density of the PNIPAM shell. Increasing the temperature above the LCST of l-PNIPAM$_{M_n}$ collapses the PNIPAM shell.

Ligand exchange of citrate-stabilized $Au_{15} - Au_{53}$ nanoparticles with α-trithiocarbonate-ω-carboxyl terminated PNIPAM was carried out in water. Each time, the ligand was added in excess to the nanoparticles. The strong binding affinity of the trithiocarbonate function of l-PNIPAM$_{M_n}$ and the mass excess drive the ligand exchange reaction.[223] After ligand exchange, the gold nanoparticles are surrounded by a PNIPAM shell that responds to changes of ph *and* temperature. Thus, the particles are dual responsive as illustrated in Figure 4.3. A change of pH below the pK$_a$ of the carboxyl function of PNIPAM lowers the charge density of the PNIPAM-encapsulated gold nanoparticle. Conversely, the charge density of the core-shell particle increases, if the pH is increased above the pK$_a$ of the carboxyl function. In addition to pH responsiveness, the LCST behaviour of PNIPAM allows to change the thickness of the PNIPAM shell as a function of the temperature. The polymer shell is collapsed above the LCST of PNIPAM reducing the overall diameter of the particle. Conversely, the shell thickness is increased by lowering the temperature below the LCST of PNIPAM.

α-trithiocarbonate-ω-carboxyl terminated PNIPAM ligands were prepared by RAFT polymerization following the synthetic protocol of Ebeling et al.[23] Three ligands of 9.5 kg/mol, 40 kg/mol, and 82 kg/mol were synthesized to represent a broad range of molecular weights. M_n was calculated from the monomer conversion (X) according to Equation 4.3.[229]

$$M_n = \frac{M_{NIPAM}[NIPAM]_0}{[CTA]_0 + 2f[I]_0(1 - e^{-k_d t})} X + M_{CTA} \tag{4.3}$$

where M and M_{CTA} represent the molecular weights of NIPAM (monomer) and DDMAT (chain transfer agent). $[NIPAM]$ and $[CTA]_0$ are the initial concentrations of the reactants. $[I]_0$ and k_d denote concentration and decomposition rate of the initiator at the time t. f is the efficiency of the initiator. The right hand side of the denominator was neglected assuming that the amount of polymer chains derived only from the initiator is minimal.[229] The monomer conversion was obtained from ^{1}H-NMR spectra of the reaction mixtures which are provided in the Appendix Figures 10.1 – 10.3. X was calculated by comparing the signal intensity of the ethylene proton of residual NIPAM at 4.82 ppm and the mixed signal intensity of the isopropyl protons of NIPAM and PNIPAM at 3.25 ppm.

Additionally, SEC experiments were performed in order to determine the molecular weight distribution of the ligands. Narrow molecular weight distributions were found for each ligand which are presented in Figure 4.4. The SEC device was calibrated against polystyrene standards. Hence, only apparent molecular weights were calculated from SEC data. The results of the molecular weight characterization by ^{1}H-NMR and SEC are summarized in Table 4.2.

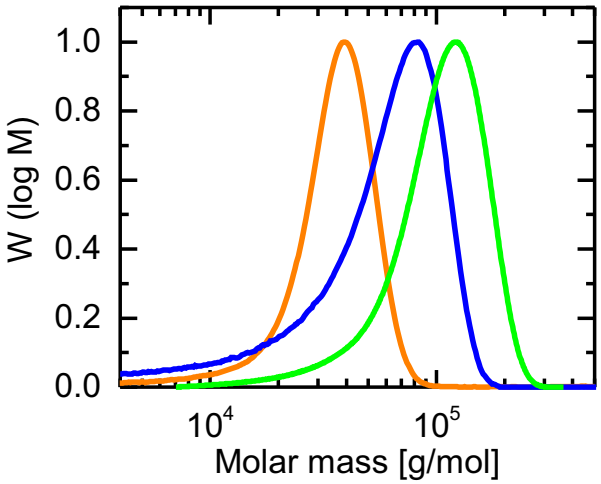

Figure 4.4. Molar mass distribution and apparent molecular weight of *l*-PNIPAM$_{9.5k}$ (orange), *l*-PNIPAM$_{40k}$ (blue) and *l*-PNIPAM$_{82k}$ (green) obtained by THF SEC measurements with PS calibration.

Table 4.2. Molecular weight characterization of *l*-PNIPAM$_{9.5k}$, *l*-PNIPAM$_{40k}$, and *l*-PNIPAM$_{82k}$ by ^{1}H-NMR and SEC.

Sample	X [%]	M_n (^{1}H-NMR) [kg/mol]	M_n (SEC) [kg/mol]	M_w (SEC) [kg/mol]	PDI
l-PNIPAM$_{9.5k}$	44	9.5	29.6	37.4	1.26
l-PNIPAM$_{40k}$	94	38.2	46.0	68.0	1.48
l-PNIPAM$_{82k}$	95	81.6	91.0	112.0	1.23

The ligand exchange reaction was carried out for all gold nanoparticles (Au_{15} – Au_{53}) resulting in 21 different samples of PNIPAM-encapsulated gold nanoparticles. TEM images of the core-shell nanoparticles are shown in Figure 4.5. Additionally, TEM images of citrate-stabilized gold nanoparticles are included for comparison. All samples were prepared by drop-casting from strongly dilute aqueous dispersions onto TEM grids. It is observed that the citrate-stabilized gold nanoparticles form dense agglomerates on the TEM grid which is attributed to a weak stabilization of the gold nanoparticles by the citrate ligands. The citrate ligand itself is invisible in the TEM images. In contrast, particle agglomeration is absent for gold nanoparticles stabilized by l-PNIPAM$_{M_n}$. This fact points towards a significantly higher colloidal stability of the PNIPAM-encapsulated nanoparticles. The PNIPAM shell is slightly visible as a low contrast shell surrounding every single nanoparticle in Figure 4.5.

Table 4.3. DLS and UV-Vis investigation of gold nanoparticles stabilized by citrate or l-PNIPAM$_{M_n}$.

Sample	Citrate		l-PNIPAM$_{9.5k}$		l-PNIPAM$_{40k}$		l-PNIPAM$_{82k}$	
	d_h[a] [nm]	λ_{LSPR} [nm]	d_h [nm]	λ_{LSPR} [nm]	d_h [nm]	λ_{LSPR} [nm]	d_h [nm]	λ_{LSPR} [nm]
Au_{15}	18.4	519	44.2	525	60	525	82.5	525
Au_{19}	23.6	521	48.1	526	72.6	526	96.1	526
Au_{22}	32.3	523	54.5	527	76.4	527	99.5	528
Au_{29}	34.4	526	58.7	531	75.3	531	91.5	531
Au_{36}	39.9	533	62.6	537	81.9	537	107.1	538
Au_{44}	41.8	534	68.6	539	89.2	539	122.9	539
Au_{53}	54.7	537	75.5	542	99.4	542	135.8	542

[a] d_h, measured by DLS at 25°C. The standard deviation of each measurement is below 5 %

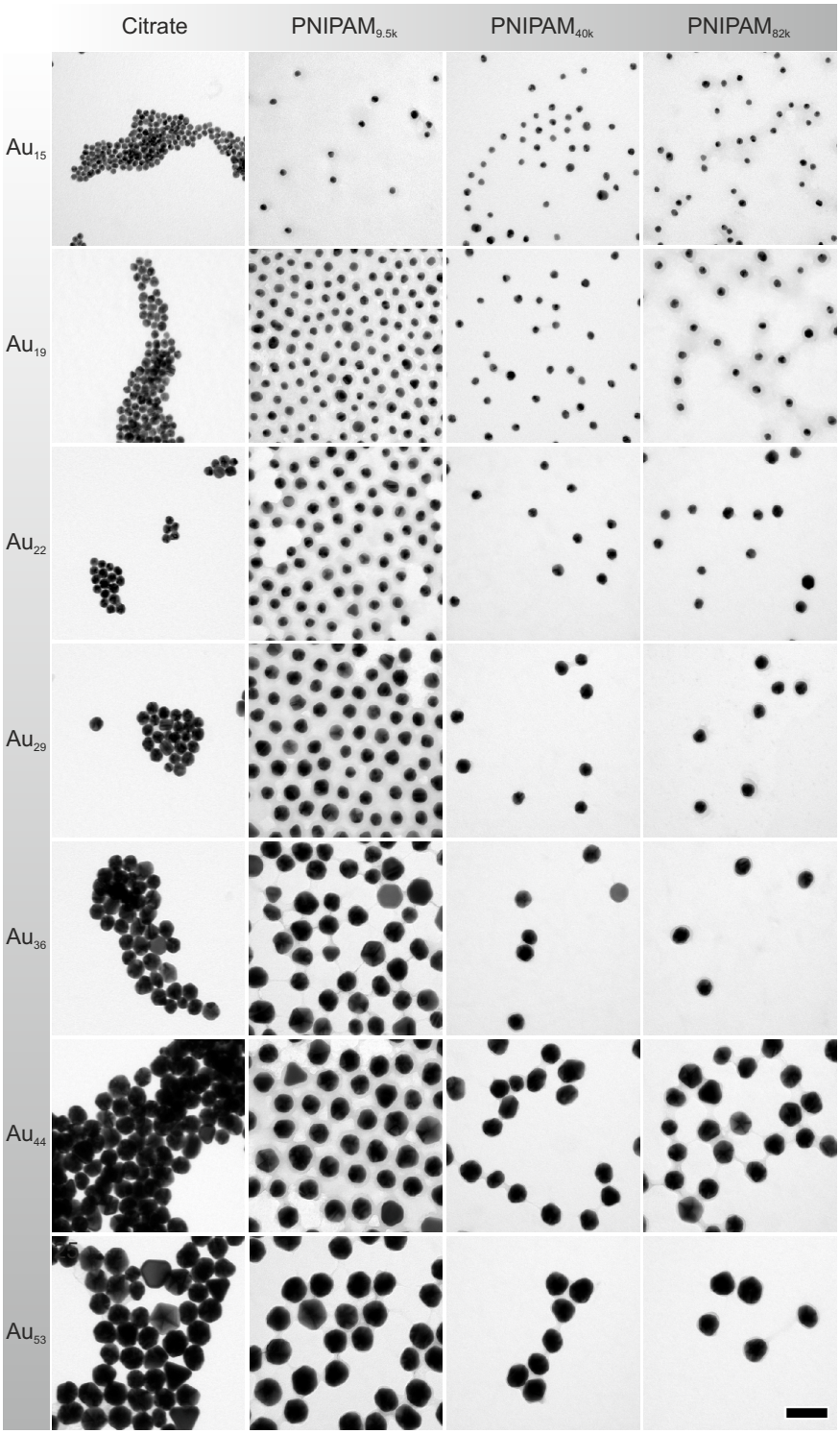

Figure 4.5. TEM investigation of citrate- or *l*-PNIPAM$_{M_n}$-stabilized gold nanoparticles. Each column represents a different ligand type. Each row represents a different size of Au$_x$ particles. The scale bar corresponds to 100 nm.

It is important to note that the TEM investigation was carried out under high vacuum. The vacuum causes a complete collapse of the PNIPAM shell. Hence, it is difficult to analyse shell morphology and shell thickness in full detail. Therefore, all dispersions were studied directly in solution by DLS. The hydrodynamic diameter (d_h) was obtained by cumulant analysis of intensity-time autocorrelation functions of all samples, and the results are presented in Table 4.3. Intensity-weighted size distributions of all citrate-stabilized and PNIPAM-encapsulated particles are provided in the Appendix Figure 10.4. For the sake of clarity PNIPAM-encapsulated gold nanoparticles are denoted as Au_x-*l*-$PNIPAM_y$, where x corresponds to d_c of the nanoparticles and y represents d_h the PNIPAM-encapsulated gold nanoparticles. DLS revealed monomodal size distributions for each system under investigation. d_h of citrate-stabilized gold nanoparticles was slightly larger compared to d_c (cf. Table 4.1) as a result of the solvation shell around each nanoparticle. All PNIPAM-encapsulated gold nanoparticles showed a significant increase of d_h after the ligand exchange. d_h of *l*-$PNIPAM_{9.5k}$-encapsulated Au_x particles was larger by approx. 20 nm compared to citrate-stabilized ones. Moreover, d_h increased with increasing size of the particles. These findings support the presence of a PNIPAM shell around the particles. d_h increased even further for gold nanoparticles encapsulated by *l*-$PNIPAM_{40k}$ or *l*-$PNIPAM_{82k}$. These ligands formed larger PNIPAM shells as compared to *l*-$PNIPAM_{9.5k}$ due to their higher molecular weight.

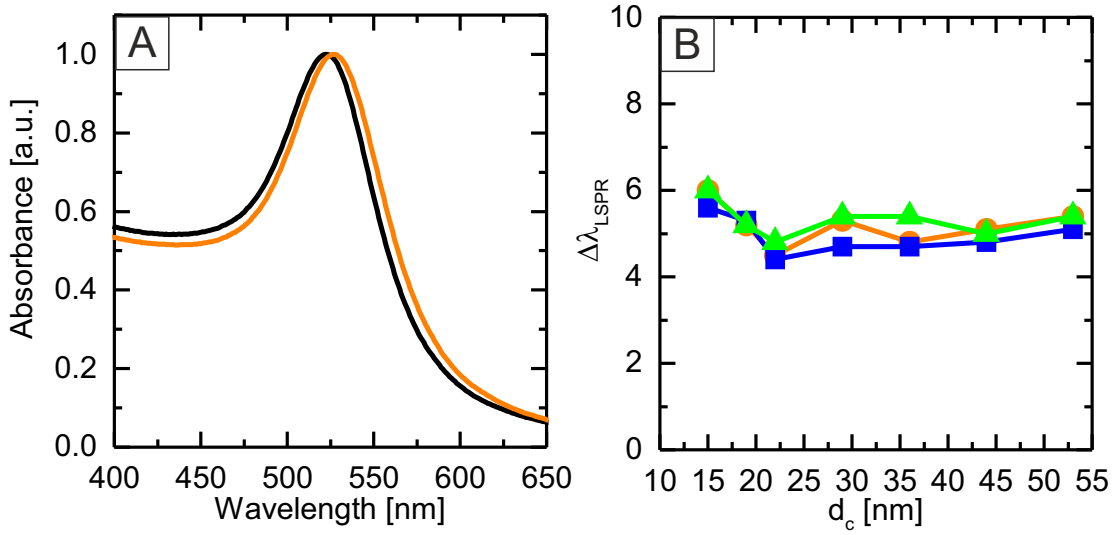

Figure 4.6. Investigation of gold nanoparticles before and after the ligand exchange reaction by UV-Vis spectroscopy. A, absorbance spectra of citrate-stabilized Au_{22} (reference, black) and Au_{22}-*l*-$PNIPAM_{54.5}$ particles (orange). B, shift of the LSPR position of Au_x particles after ligand exchange with *l*-$PNIPAM_{9.5k}$ (orange), *l*-$PNIPAM_{40k}$ (blue), and *l*-$PNIPAM_{82k}$ (green).

Next, the strong absorbance of gold nanoparticles in the visible range allows to evaluate the ligand exchange reaction by UV-Vis spectroscopy. Figure 4.6 A shows that the LSPR of Au_{22}-*l*-$PNIPAM_{54.5}$ particles is shifted by approx. 4 nm as compared to the citrate-stabilized Au_{22} particles. Since the refractive index of solvated PNIPAM ($n = 1.36$) is larger as compared to water ($n = 1.33$), the shift of the LSPR ($\Delta\lambda_{LSPR}$) indicates the presence of a PNIPAM shell around the nanoparticles. The impact of PNIPAM shell thickness upon $\Delta\lambda_{LSPR}$ is presented in Figure 4.6 B. It is found that $\Delta\lambda_{LSPR}$ is always around 4 nm – 5 nm and independent of the

shell thickness of the Au$_x$-*l*-PNIPAM$_y$ particles. In other words, the molecular weight of the *l*-PNIPAM$_{M_n}$ ligands does not affect $\Delta\lambda_{LSPR}$. It is important to note, that all Au$_x$-*l*-PNIPAM$_y$ particles have narrow dipolar plasmon resonances. Hence, no substantial particle agglomeration occurred during the ligand exchange reaction, which would result in a significant broadening of the plasmon resonance and the appearance of additional modes at longer wavelengths. All together, the results of TEM, DLS, and UV-Vis prove the presence of homogeneous PNIPAM shells around each Au$_x$ nanoparticle.

Furthermore, the versatility of the ligand exchange reaction was demonstrated by the encapsulation of CTAB-stabilized gold nanorods with *l*-PNIPAM$_{9.5k}$ which is demonstrated in Figure 4.7. Figure 4.7 A shows a shift of the longitudinal LSPR of 20 nm after the ligand exchange reaction. Additionally, comparing TEM images of gold nanorods stabilized by either CTAB (Figure 4.7 B) or *l*-PNIPAM$_{9.5k}$ (Figure 4.7 C), reveals that the PNIPAM shell clearly separates the nanorods. This example highlights the strong affinity of the trithiocarbonate group towards gold surfaces.

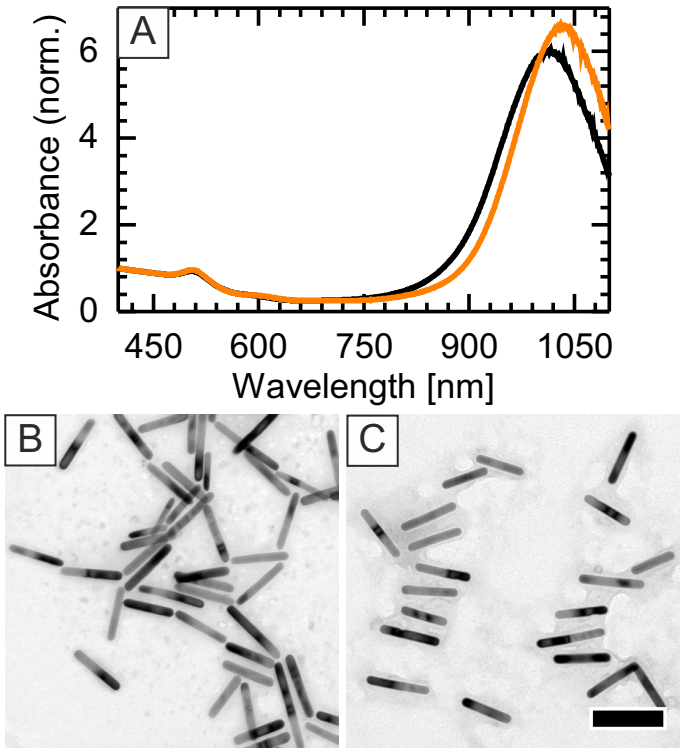

Figure 4.7. Ligand exchange of gold nanorods with *l*-PNIPAM$_{9.5k}$. A, UV-Vis spectra before (black) and after (orange) the ligand exchange reaction. B, TEM image of CTAB-stabilized gold nanorods with an aspect ratio of approx. 7. C, TEM image of *l*-PNIPAM$_{9.5k}$-encapsulated nanorods. The scale bar corresponds to 100 nm.

4.1.3 Colloidal Stability of Au$_x$-*l*-PNIPAM$_y$ particles

Au$_x$-*l*-PNIPAM$_y$ particles are stable at room temperature and neutral pH. The PNIPAM chains are in a random coil formation providing steric stabilization, and the carboxyl functions are deprotonated providing electrostatic stabilization. The colloidal stability was investigated as a function of pH by preparing aqueous dispersions of Au$_{22}$-*l*-PNIPAM$_{54.5}$, -PNIPAM$_{76.4}$, and -PNIPAM$_{99.5}$ particles at pH 7 and 25 °C. Next, the pH was lowered stepwise by addition of HCl, and the stability of the particles was monitored by recording ζ-potentials as well as d_h. Figure 4.8 ,A shows the evolution of the ζ-potential of the particles as a function of pH. The ζ-potential of Au$_{22}$-*l*-PNIPAM$_{54.5}$ is -31.2 mV under neutral conditions (pH 7). Decreasing the pH causes a neutralization of the PNIPAM shell, and hence, the ζ-potential drops continuously until a value close to 0 mV is reached at pH 2. It follows, that the electrostatic stabilization of the particles is getting weaker. At the same time, Figure 4.8 B shows that d_h of Au$_{22}$-*l*-PNIPAM$_{54.5}$ does not change significantly until pH 2.7 is reached. Therefore, the particles are still stable although their ζ-potential is very weak. Hence, the PNIPAM chains provide enough steric stabilization in order to suspend the gold particles in solution. A strong increase of d_h is observed below pH 2.7 indicating that the polymer chains can not prevent particle aggregation anymore at this pH. A similar trend is found for Au$_{22}$-*l*-PNIPAM$_{76.4}$ and -PNIPAM$_{99.5}$ – gold nanoparticles which are encapsulated by thicker PNIPAM shells. The colloidal stability of the particles was also investigated above the LCST of PNIPAM where water is a bad solvent for PNIPAM. The poor solvent conditions strongly reduce the steric stabilization of the PNIPAM chains. Thus, Au$_{22}$-*l*-PNIPAM$_y$ particles are only stable at pH 6 – 7, where the surface charge of the particles is high enough in order to prevent particle aggregation. Rapid aggregation and a strong increase of turbidity is observed for a range of pH were the particles were originally stable for temperatures below the LCST of PNIPAM. It follows that the particle-particle interactions can be switched between attractive and repulsive states by modulation of temperature and pH.

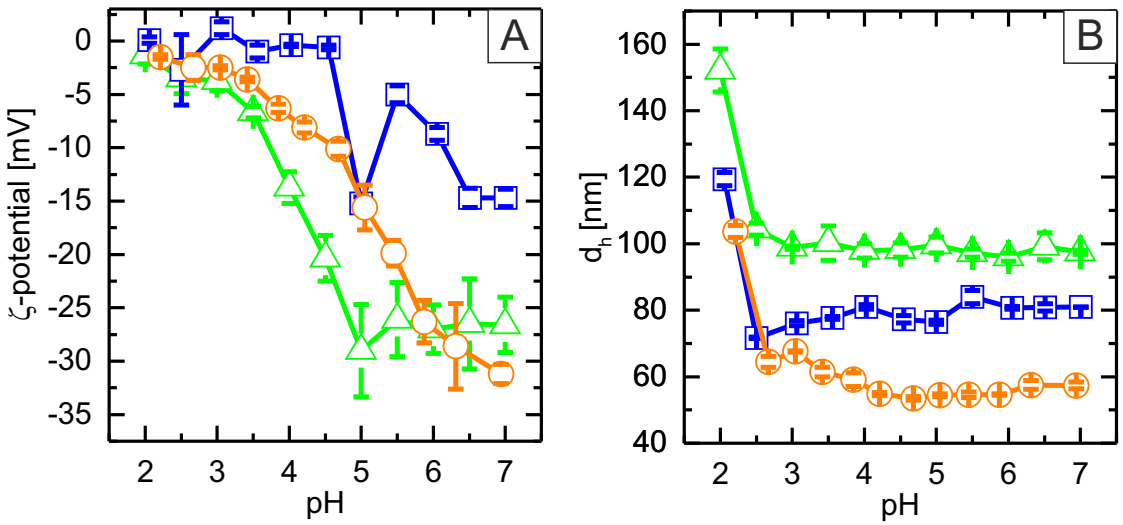

Figure 4.8. Investigation of the colloidal stability of Au$_{22}$-*l*-PNIPAM$_{54.5}$ (orange), Au$_{22}$-*l*-PNIPAM$_{76.4}$ (blue), and Au$_{22}$-*l*-PNIPAM$_{99.5}$ (green) as a function of pH. A, evolution of the ζ-potential. B, evolution of d_h.

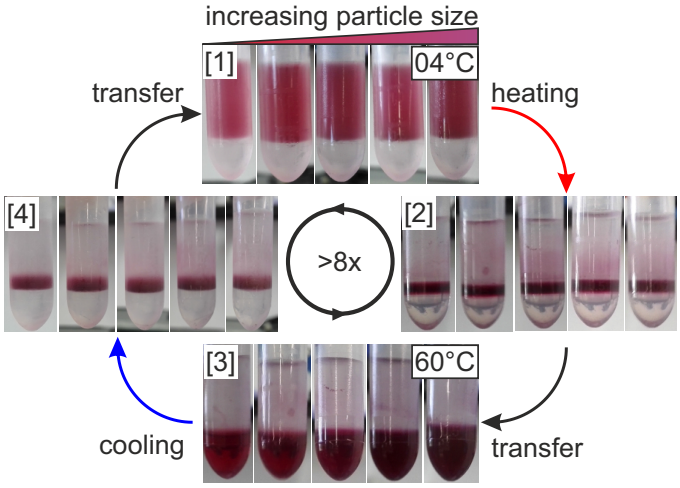

Figure 4.9. Fully reversible phase transfer of *l*-PNIPAM$_{40k}$-encapsulated Au$_x$ nanoparticles between water (upper phase) and chloroform (lower phase). Each subfigure shows a set of digital photographs of *l*-PNIPAM$_{40k}$-encapsulated Au$_{22}$, Au$_{29}$, Au$_{36}$, Au$_{44}$, and Au$_{53}$ particle dispersions. [1], at 4°C the particles are dispersed in the water phase. [2], upon heating to 60°C, the particles accumulate at the liquid/liquid interface. [3], quantitative phase transfer to the organic phase. [4], the phase transfer is completely reversible once the temperature is lowered to 4°C. The experiment can be repeated for eight times at least.

4.1.4 Reversible Phase Transfer of Au$_x$-*l*-PNIPAM$_y$ particles

A sudden change of colloidal stability can trigger phase transfer of colloids between two immiscible liquids. Phase transfer to organic solvents is useful because such solvents are frequently used as medium for the self-assembly of colloidal particles into superstructures.[221,230,231] In general, phase transfer between two immiscible liquids A and B is triggered once the affinity of a colloid to liquid B is greater as compared to liquid A.[232,233] In the case of Au$_{22}$-*l*-PNIPAM$_y$ particles, two different handles are available for controlling the colloidal stability and therefore the solvent affinity: pH and temperature. Phase transfer of Au$_x$-*l*-PNIPAM$_y$ was investigated between two immiscible liquids: water and chloroform. A screening of the optimal conditions for phase transfer was carried out using Au$_{22}$-*l*-PNIPAM$_{54.5}$ particles in a pH range of 2 – 7 and at 60° C (above the LCST of PNIPAM). It was observed that the particles only transferred to the chloroform phase at pH < 4. Surprisingly, the transfer was fully reversible at pH 2.7 once the temperature was lowered to 4 °C. Thus, three different scenarios were identified:

1. pH > pK$_a$, T > T$_{LCST}$: phase transfer was impossible. The particles aggregated in the water phase at pH 4 – 7. The turbidity of the water phase increased strongly and a gradual color change to purple was observed indicating aggregation of PNIPAM-encapsulated gold nanoparticles.

2. pH < pKa, T > T$_{LCST}$: phase transfer to chloroform occurred. This was attributed to a weak electrostatic repulsion of the particles under these conditions (see also Figure 4.8 A) and the strong affinity of PNIPAM to the organic phase at 60 °C. At ph 2.7 a quantitative *and* reversible transfer of the particles was observed.

3. pH < 2.7, T > T_{LCST}: the particles aggregated rapidly in the water phase and transferred to chloroform. However, a reversible transfer was no longer possible.

In order to investigate the phase transfer process in more detail, experiments were carried out for all 21 samples of PNIPAM-encapsulated gold nanoparticles at pH 2.7. Each time, the temperature was modulated between 4°C and 60°C. Surprisingly, the transfer was reversible in almost every case. Only Au_{15}-*l*-$PNIPAM_{44.2}$ and Au_{19}-*l*-$PNIPAM_{48.1}$ particles did not transfer back to water once they crossed the liquid/liquid interface. However, the transfer was still reversible once the same gold nanoparticles were encapsulated by one of the other two ligands – either *l*-$PNIPAM_{40k}$ or *l*-$PNIPAM_{82}$. Figure 4.9 shows a representative example for the phase transfer of *l*-$PNIPAM_{40k}$-encapsulated Au_{22}, Au_{29}, Au_{36}, Au_{44}, and Au_{53} particles:

1. At 4 °C all particles are stable in water as evidenced by the homogeneous colouration of the upper phase.

2. Heating the particle dispersions to 60°C results in an accumulation of the particles at the liquid/liquid interface. Under these conditions, the electrostatic and steric stabilization of the particles is very weak in water. Hence, van der Waals attractive forces cause a quick agglomeration of the particles. These agglomerates sediment rapidly to the liquid/liquid interface within 5 min – 10 min. It was observed that the particles remained trapped at the interface over the course of several hours. Thus, the interfaces is a bottleneck for the phase transfer process. This fact finds support considering three things: i) the particle concentration in the water phase is high enough for a rapid agglomeration of the particles ($0.46 - 1.65 \times 10^{11}$ particles/ml), ii) the surface area of the liquid/liquid interface is limited and below the collective surface area of all Au_x-*l*-$PNIPAM_y$ particles in solution, and iii), the thermal destabilization of the particles happens almost instantly. Hence, the particles are "jammed" at the interface. However, the particles still transferred to chloroform spontaneously after approx. 12 hours. Therefore, it is concluded that the particle jamming is a kinetic effect.

3. After crossing the interface, the particles are stable in chloroform as indicated by the homogeneous coloration of the lower phase of each sample in Figure 4.9. At this point it is possible to transfer the particles back to water by lowering the temperature to 4 °C.

4. Cooling the particle dispersion results in an accumulation of the particles at the interface again. In contrast to the transfer to chloroform (2), this accumulation took 2 h – 3 h which was significantly longer as compared to the transfer from water to chloroform. Aggregation of the particles in the chloroform phase was not observed. Therefore, another mechanism has to be responsible for this kind of accumulation. The longer time periods can be explained by statistical collision of the particles with the liquid/liquid interface due to Brownian motion. The affinity of the ligands towards the water phase is energetically favoured below the LCST of PNIPAM, because the Gibbs energy of the system is reduced by solvating the polymer chains with water. This process is slow and spontaneous transfer to water only occurred over the course of 2 weeks. However, the phase transfer can be

accelerated significantly by shaking the sample tubes which results in an instant transfer of all Au_x-*l*-$PNIPAM_y$ particles to the water phase.

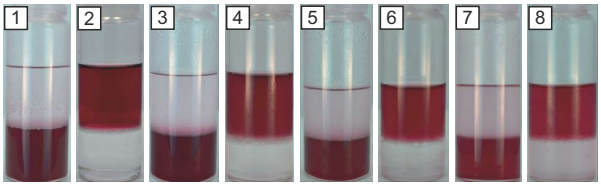

Figure 4.10. Successive phase transfer of Au_{15}-*l*-$PNIPAM_{82.5}$ particles between water and chloroform. The temperature is switched between 60 °C (1, 3, 5, 7) and 4 °C (2, 4, 6, 8). Quantitative phase transfer occurs up to eight times in a row.

It is important to note that the particles can cross the liquid/liquid interface for many times in a row which is demonstrated for Au_{15}-*l*-$PNIPAM_{82.5}$ particles in Figure 4.10. The particles are transferred between chloroform and water back and forth over eight times at least without any signs of aggregation. Consequently, UV-Vis spectroscopy was used in order to determine the efficiency of the phase transfer process of *l*-$PNIPAM_{40k}$-encapsulated Au_{22}, Au_{29}, Au_{36}, Au_{44}, and Au_{53} particles. Figure 4.11 A shows absorbance spectra of the chloroform (dotted lines) and water phases (solid lines) for all particles recorded at 60 °C. The particles absorb strongly in the chloroform phase whereas the absorbance of the water phase is very weak (inset of Figure 4.11 A). In contrast, the situation is completely reversed at 4 °C as demonstrated in Figure 4.11 B. Now, the absorbance of the water phase is strong, and conversely, the absorbance of the chloroform phase is almost negligible. Moreover the LSPRs of the strong absorbing phases are always narrow indicating that the all particles are stable.

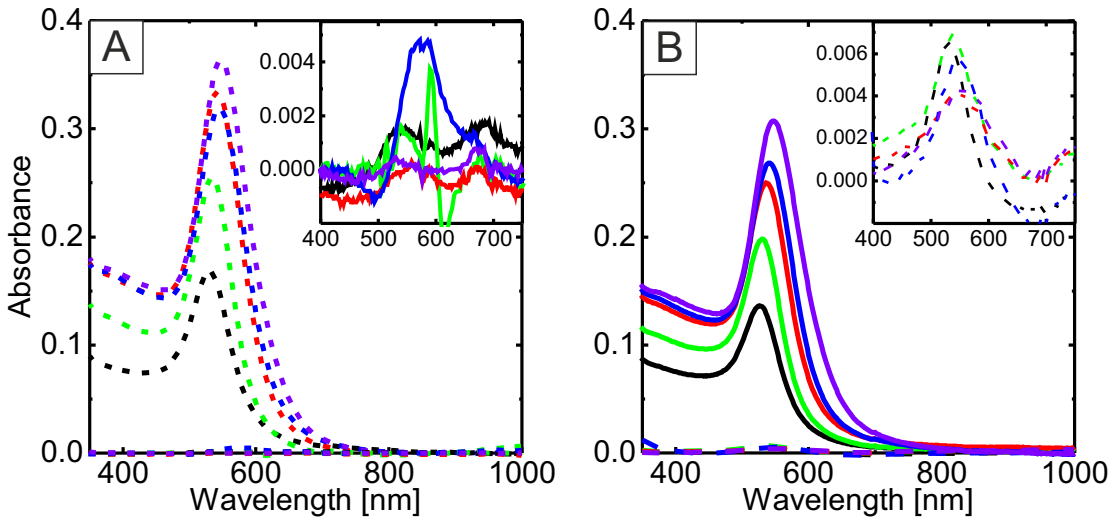

Figure 4.11. Spectroscopic investigation of the phase transfer of *l*-$PNIPAM_{40k}$-encapsulated Au_{22} (black), Au_{29} (green), Au_{36} (red), Au_{44} (blue), and Au_{53} (purple) particles. A, absorbance spectra of the chloroform (dashed lines) and water (solid lines) phase at 60 °C. B, absorbance spectra of both phases at 4 °C. The insets are magnifications of the weakly absorbing water (A) and chloroform phase (B).

The absorbance spectra also allow for the calculation of an efficiency parameter η_{trans} to evaluate the phase transfer of all PNIPAM-encapsulated gold nanoparticles. η_{trans} is given by Equation 4.4

$$\eta_{\text{trans}} = \frac{\Delta\text{Abs}_{400}}{\text{Abs}_{400}(\text{H}_2\text{O})} \tag{4.4}$$

where ΔAbs_{400} is the absorbance difference of the two phases at 400 nm, and $\text{Abs}_{400}(\text{H}_2\text{O})$ is the initial absorbance of the particles in the water phase before the phase transfer experiment was commenced. η_{trans} is summarized in Table 4.4 for all particles. At 60 °C, $\eta_{\text{trans, 60 °C}}$ is close to 100 % for the phase transfer to chloroform. Once the temperature is switched to 4 °C, $\eta_{\text{trans, 4 °C}}$ is close to 100 % again. Hence, the phase transfer is quantitative each time. The slight difference between $\eta_{\text{trans,60 °C}}$ and $\eta_{\text{trans,4 °C}}$ results from a small fraction of particles that are still dispersed in the respective other phase or trapped at the liquid/liquid interface.

Table 4.4. Efficiency of the phase transfer calculated from UV-Vis absorbance spectra of the chloroform and water phase at 60 °C and 4 °C.

Sample	$\Delta\text{Abs}_{400,\ 60\,°\text{C}}$ $(\text{CHCl}_3 - \text{H}_2\text{O})$[a]	$\eta_{\text{trans, 60 °C}}$ [%]	$\Delta\text{Abs}_{400,\ 4\,°\text{C}}$ $(\text{H}_2\text{O} - \text{CHCl}_3)$	$\eta_{\text{trans, 4 °C}}$ [%]
Au_{22}-*l*-$\text{PNIPAM}_{76.4}$	0.077	99	0.075	98
Au_{29}-*l*-$\text{PNIPAM}_{75.3}$	0.119	99	0.101	97
Au_{36}-*l*-$\text{PNIPAM}_{81.9}$	0.158	99	0.129	98
Au_{44}-*l*-$\text{PNIPAM}_{89.2}$	0.155	98	0.134	99
Au_{53}-*l*-$\text{PNIPAM}_{99.4}$	0.161	95	0.142	99

In conclusion, α-trithiocarbonate-ω-carboxyl terminated PNIPAM ligands render gold nanoparticles with bifunctional non-cross-linked polymer shells. The ligand exchange reactions works for nanoparticles of a broad range of sizes, and the colloidal stability of the particles is a function of pH *and* temperature. This is evidenced by the reversible phase transfer of the particles between water and chloroform, which is nearly quantitative each time.

4.2 Gold Nanoparticles with Cross-Linked PNIPAM Shells

Using non-cross-linked *l*-PNIPAM$_{M_n}$ ligands, Au$_x$-*l*-PNIPAM$_y$ particles were prepared with shell thicknesses as large as 37 nm ± 4 nm. Theoretically, even larger shell thicknesses could be obtained simply by constantly increasing the molecular weight of the *l*-PNIPAM$_{M_n}$ ligand. However, the synthesis of such ligands by RAFT polymerization gets more and more difficult due to the increasing risk of chain termination and side reactions.[24] Consequently, *cross-linking* is introduced and gold nanoparticles are encapsulated by cross-linked PNIPAM hydrogel shells in order to prepare larger polymer shells. Robust synthetic protocols are already available for the encapsulation of gold nanoparticles with PNIPAM hydrogel shells. These particles are prepared by free radical precipitation polymerization of NIPAM and BIS in the presence of gold nanoparticles.[28,29]

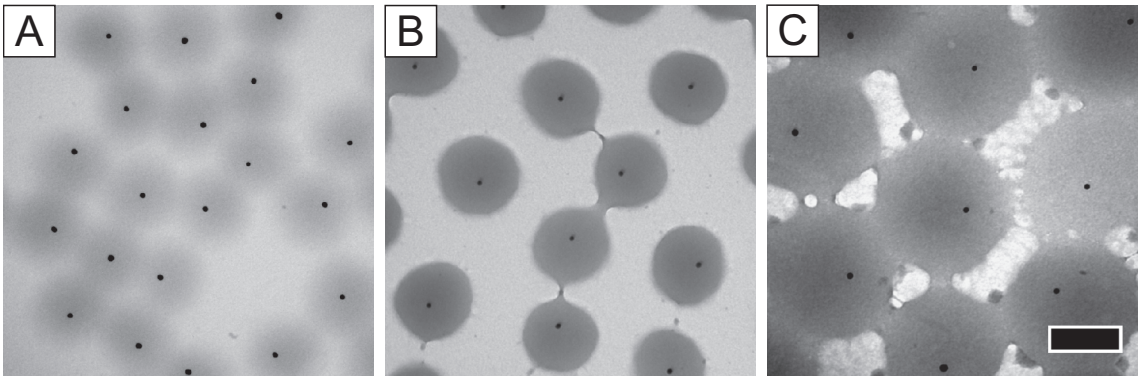

Figure 4.12. TEM investigation of Au-*x*-PNIPAM$_y$. A – C, TEM images of Au$_{19}$-*x*-PNIPAM$_{208}$, Au$_{19}$-*x*-PNIPAM$_{326}$, and Au$_{19}$-*x*-PNIPAM$_{508}$. The size of the cross-linked PNIPAM hydrogel shell increases from left to right. The scale bar corresponds to 200 nm.

Gold nanoparticles of 19 nm in diameter were synthesized by citrate reduction following the Turkevich protocol.[209] The nanoparticles were surface-functionalized with butenylamine to increase their hydrophobicity, which is mandatory for the hydrogel encapsulation.[29] Hydrogel encapsulation was carried out by precipitation polymerization according to Karg et al.[28] The size of the PNIPAM hydrogel shell was tuned by performing the reaction three times using nominal NIPAM concentrations of 0.02 M, 0.06 M, and 0.1 M. 15 mol % BIS cross-linker with respect to NIPAM were used for every synthesis, and the concentration of gold nanoparticles was kept constant every time. The cross-linked PNIPAM-encapsulated particles were investigated by TEM, UV-Vis spectroscopy, SLS and DLS. The particles are referred to as Au$_{19}$-*x*-PNIPAM$_y$ according to their overall hydrodynamic diameter.

Figure 4.12 shows representative TEM images of the three different particles. The cross-linked PNIPAM shell, surrounding every single gold nanoparticle, is clearly visible due to the strong difference in electron contrast between the polymer and the gold nanoparticle. It is important to note that gold nanoparticles without PNIPAM shell are not observed. Moreover, increasing the monomer feed for the reaction clearly increases the size of the polymer shell which is evident from Figure 4.12 A – C. UV-Vis absorbance spectra of Au$_{19}$-*x*-PNIPAM$_y$ are displayed in Figure 4.13.

The spectra are normalized to an equal concentration of particles. The absorbance of Au_{19}-x-$PNIPAM_{208}$, Au_{19}-x-$PNIPAM_{326}$, and Au_{19}-x-$PNIPAM_{508}$ increases towards shorter wavelengths and a small shoulder in the wavelength region of 500 nm – 540 nm is observable. The increasing absorbance at shorter wavelengths results from Rayleigh-Debye-Gans scattering by the cross-linked PNIPAM shell. The scattering is most pronounced for Au_{19}-x-$PNIPAM_{508}$ – the particles with the largest PNIPAM shell. The small shoulder visible in each spectrum matches well to the LSPR of 19 nm gold nanoparticles (without polymer shell), which is included in Figure 4.13 as a reference. Hence, the absorbance spectra of Au_{19}-x-$PNIPAM_y$ are the superposition of scattered light by the cross-linked PNIPAM hydrogel shell and scattered/absorbed light by the LSPR of the gold nanoparticles.

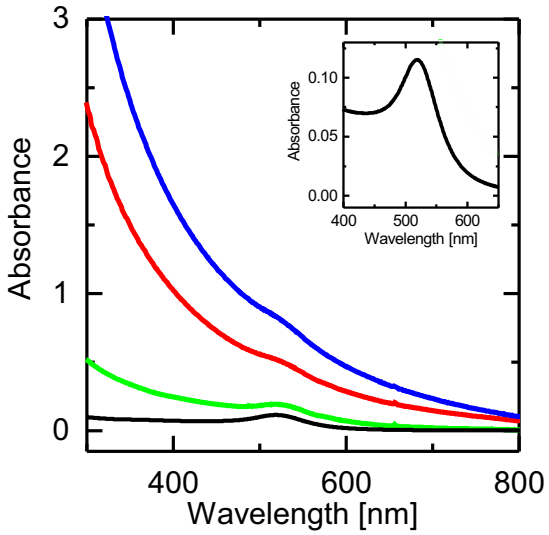

Figure 4.13. Absorbance spectra of Au_{19}-x-$PNIPAM_{208}$(green), Au_{19}-x-$PNIPAM_{326}$ (red) and Au_{19}-x-$PNIPAM_{508}$ (blue). A spectrum of Au_{19} particles without polymer shell is included as a reference (black). All spectra were recorded at 25°C and are normalized to the same particle concentration. The inset shows a magnification of the LSPR region of Au_{19} particles.

Light scattering was used in order to determine shape and diameter of the cross-linked PNIPAM-encapsulated gold nanoparticles in aqueous dispersion. SLS of Au_{19}-x-$PNIPAM_y$ particles was carried out in order to obtain form factor ($P(q)$) and radius of gyration (r_g). The hydrodynamic diameter was determined by DLS. Figure 4.14 A shows the small angle scattering profiles of the three different core-shell particles. The intensity of the scattered light (I_{sc}) depends on the scattering angle and decreases for increasing scattering vectors (q). The decrease of I_{sc} is most pronounced for Au_{19}-x-$PNIPAM_{508}$ particles, and the first minimum of $P(q)$ is clearly resolved. Thus, the sphere radius (r_s) is obtained by Equation 4.5

$$q_{min} = \frac{4.49}{r_s} \tag{4.5}$$

where q_{min} is the scattering vector of the first minimum of $P(q)$. r_s is 212 nm for Au_{19}-x-$PNIPAM_{508}$. The same approach does not work for Au_{19}-x-$PNIPAM_{208}$ and Au_{19}-x-$PNIPAM_{326}$ because their minima of $P(q)$ are located outside of the accessible q range of the light scattering

setup. Therefore, a fit to the experimental scattering profiles was performed using a polydisperse hard sphere form factor model. In this case, $P(q)$ is given by Equation 4.6 and 4.7[216]

$$I_{sphere}(q, r_s) = P^2(q, r_s, \Delta\eta_{SLS}) \tag{4.6}$$

$$P(q, r_s, \Delta\eta_{SLS}) = 4\pi r_s^3 \Delta\eta_{SLS} \frac{\sin(qr_s) - qR\cos(qr_s)}{(qr_s)^3} \tag{4.7}$$

where η_{SLS} is the scattering length density difference between the sphere and the solvent. Polydispersity was modelled using a Gaussian size distribution given by Equation 4.8[216]

$$\text{Gauss}(r_s, \sigma_S, r_0) = \frac{N}{c_{\text{Gauss}}} e^{-\frac{(r_s - r_0)^2}{2\sigma_S^2}} \tag{4.8}$$

$$c_{\text{Gauss}} = \sqrt{\frac{\pi}{2}}\sigma_S(1 + \text{erf}(\frac{r_0}{\sqrt{2}\sigma_S}))$$

$$\text{with} \int_0^\infty \text{Gauss}(r_s, \sigma_S, r_0) dr_s = N \tag{4.9}$$

where σ_S is the standard deviation. The corresponding fits are shown as solid lines in Figure 4.14 A, and a very good agreement is found for all three samples. Figure 4.14 B shows the Guinier representation of the light scattering profiles of the core-shell particles given by Equation 4.10[113]

$$\ln(I(q)) = \ln(I_0) - \frac{r_g^2 q^2}{3} \tag{4.10}$$

where r_g is the radius of gyration. Linear fits were used to describe the linear part of the SLS profiles, and r_g was calculated as 73 nm, 124 nm, and 187 nm for Au_{19}-x-$PNIPAM_{208}$, Au_{19}-x-$PNIPAM_{326}$ and Au_{19}-x-$PNIPAM_{508}$, respectively.

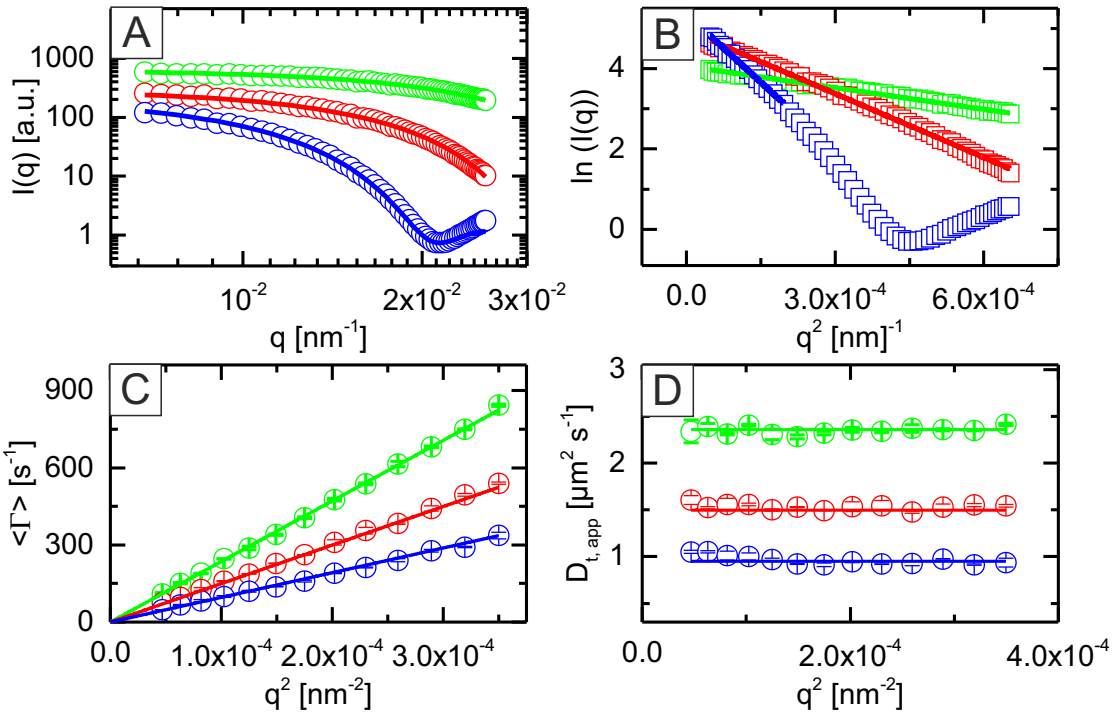

Figure 4.14. Investigation of Au_{19}-x-$PNIPAM_y$ by SLS and DLS. A, $P(q)$ analysis of SLS data of Au_{19}-x-$PNIPAM_{208}$ (green), Au_{19}-x-$PNIPAM_{326}$ (red), and Au_{19}-x-$PNIPAM_{508}$ (blue) using a hard sphere form factor model with Gaussian size distribution (solid lines). B, Guinier representation of A. The solid lines represent linear fits to the linear regime of the data. C, $\bar{\Gamma}$ as a function of q^2 obtained from CONTIN analysis of field-time autocorrelation functions. The solid lines are linear fits to the data with an intercept of zero. D, $D_{t,app}$ as a function of q^2. The solid lines are linear fits to the data with a slope of zero.

The hydrodynamic radius (r_h) of the particles was probed by angular dependent DLS measurements. $\bar{\Gamma}$ was obtained by CONTIN analysis of $g^{(1)}(\tau)$ and the results are presented in Figure 4.14 C. All three samples show a linear relationship of $\bar{\Gamma}$ as a function of q^2 with intercepts close to zero. It follows that purely translational diffusion of the particles is probed. In order to calculate r_h with high accuracy, the translational diffusion coefficient (D_t) was extracted from linear fits to the angular dependent DLS data in Figure 4.14 C. D_t is given by Equation 4.11

$$D_t = \frac{\bar{\Gamma}}{q^2} \tag{4.11}$$

where $q = \frac{4\pi n}{\lambda} \sin\frac{\theta}{2}$ is the scattering vector. r_h is given by the Stokes-Einstein Equation 4.12

$$r_h = \frac{k_B T}{6\pi\eta D_T} \tag{4.12}$$

where k_B is the Boltzmann constant and η is the dynamic viscosity of the solvent. r_h is 104 nm, 164 nm, and 254 nm for Au_{19}-x-$PNIPAM_{208}$, Au_{19}-x-$PNIPAM_{326}$, and Au_{19}-x-$PNIPAM_{508}$, respectively. Calculating the apparent diffusion coefficient ($D_{t,app}$) for each value of q^2 in Figure 4.14 D also reveals a linear relationship. A linear fit with a constant slope of zero matches

very well to the data points. Therefore, any particle concentration effects on the particle diffusion can be neglected. Using r_h, the relation r_g/r_h was calculated. r_g/r_h equals 0.775 in case of monodisperse hard spheres. Values in the range of 0.70 – 0.74 were found for the three different particles, which is slightly below the hard sphere limit. This observation is explained by an inhomogeneous cross-linking density of the PNIPAM shell. Varga et al. already demonstrated that the cross-linking density of colloidal PNIPAM hydrogels decreases with increasing distance from the particle center.[234] Hence, a similar effect is expected for the outer region of the PNIPAM shell of the Au_{19}-x-$PNIPAM_y$ particles. This affects the hydrodynamic diameter of the particles more strongly as compared to r_g.

All results of the SLS and DLS investigation are summarized in Table 4.5. r_s of Au_{19}-x-$PNIPAM_{508}$ determined by Equation 4.5 is almost identical to r_s from the polydisperse hard sphere model (Equation 4.7) indicating that the model is well-suited to describe the SLS profiles. r_h is larger as compared to r_g for all particles, as expected. Moreover, r_h increases with increasing size of the cross-linked polymer shell, which is in good agreement to the TEM images of the particles.

Table 4.5. Results of the light scattering experiments of Au_{19}-x-$PNIPAM_y$.

Sample	$r_s(q_{min})$[a] [nm]	r_s[b] [nm]	σ_S[b] [nm]	r_g[c] [nm]	r_h[d] [nm]	r_g/r_h
Au_{19}-x-$PNIPAM_{208}$	–	91	0.7	73	104	0.70
Au_{19}-x-$PNIPAM_{326}$	–	140	15	124	163	0.76
Au_{19}-x-$PNIPAM_{508}$	212	211	21	187	254	0.74

[a] r_s, calculated by Equation 4.5.
[b] r_s, σ_S, calculated by Equations 4.7 and 4.8.
[c] r_g, calculated by Equation 4.10
[d] r_h, calculated by Equation 4.12

In conclusion, the free radical seeded precipitation polymerization of NIPAM and BIS in the presence of gold nanoparticles produces core-shell particles with very large PNIPAM shells. Every single gold nanoparticle is encapsulated by a homogeneous cross-linked PNIPAM hydrogel shell, and the shell thickness is a function of the monomer feed of the reaction. Investigating Au_{19}-x-$PNIPAM_y$ particles by SLS and DLS allows for a thorough characterization of the core-shell particles in solution. Together with the non-cross-linked PNIPAM-encapsulated gold nanoparticles, a library of colloidal building blocks for plasmonic superstructures is now accessible, which is shown in Table 4.6. The shell thickness (d_s) of the non-cross-linked PNIPAM-encapsulated gold nanoparticles is tunable between approx. 28 nm – 74 nm for particles with the same gold core. Encapsulating gold nanoparticles with cross-linked PNIPAM hydrogel increases the shell thickness up to 189 nm – 489 nm.

Table 4.6. Library of PNIPAM-encapsulated gold nanoparticles – colloidal building blocks for plasmonic superstructures.

Building blocks	λ_{LSPR} [nm]	d_c [nm]	d_h [nm]	d_s [nm]
Au_{15}-*l*-$PNIPAM_{44.2}$	525	15 ± 2	44.2	14.6
Au_{15}-*l*-$PNIPAM_{60}$	525	15 ± 2	60	22.5
Au_{15}-*l*-$PNIPAM_{82.5}$	525	15 ± 2	82.5	33.8
Au_{19}-*l*-$PNIPAM_{48.1}$	526	19 ± 2	48.1	14.6
Au_{19}-*l*-$PNIPAM_{72.6}$	526	19 ± 2	72.6	26.8
Au_{19}-*l*-$PNIPAM_{96.1}$	526	19 ± 2	96.1	38.6
Au_{22}-*l*-$PNIPAM_{54.5}$	527	22 ± 3	54.5	16.3
Au_{22}-*l*-$PNIPAM_{76.4}$	527	22 ± 3	76.4	27.2
Au_{22}-*l*-$PNIPAM_{99.5}$	528	22 ± 3	99.5	38.8
Au_{29}-*l*-$PNIPAM_{58.7}$	531	29 ± 3	58.7	14.9
Au_{29}-*l*-$PNIPAM_{75.3}$	531	29 ± 3	75.3	23.2
Au_{29}-*l*-$PNIPAM_{91.5}$	531	29 ± 3	91.5	31.3
Au_{36}-*l*-$PNIPAM_{62.6}$	537	36 ± 4	62.6	13.3
Au_{36}-*l*-$PNIPAM_{81.9}$	537	36 ± 4	81.9	23.0
Au_{36}-*l*-$PNIPAM_{107.1}$	538	36 ± 4	107.1	35.6
Au_{44}-*l*-$PNIPAM_{68.6}$	539	44 ± 5	68.6	12.3
Au_{44}-*l*-$PNIPAM_{89.2}$	539	44 ± 5	89.2	22.6
Au_{44}-*l*-$PNIPAM_{122.9}$	539	44 ± 5	122.9	39.5
Au_{53}-*l*-$PNIPAM_{75.5}$	542	53 ± 7	75.5	11.3
Au_{53}-*l*-$PNIPAM_{99.4}$	542	53 ± 7	99.4	23.2
Au_{53}-*l*-$PNIPAM_{135.8}$	542	53 ± 7	135.8	41.4
Au_{19}-*x*-$PNIPAM_{208}$	524	19 ± 2	208	94.5
Au_{19}-*x*-$PNIPAM_{326}$	528	19 ± 2	326	153.5
Au_{19}-*x*-$PNIPAM_{508}$	-	19 ± 2	508	244.5

Chapter 5

Self-Assembly of Colloidal Building Blocks

The library of PNIPAM-encapsulated gold nanoparticles offers a large pool of colloidal building blocks for the fabrication of plasmonic superstructures via self-assembly. It is important to keep in mind that the superstructures will be integrated in organic thin film solar cells. In the laboratory, standard solar cell substrates have a surface area of 5.06 cm^2.[47] Therefore, any plasmonic superstructure must provide optical homogeneity on the same scale, which means that the interparticle distance between gold nanoparticles has to nearly identical everywhere on the substrate. Consequently, this chapter focuses on the preparation of optically homogeneous two-dimensional superstructures which will be referred to as plasmonic monolayers. In order to create plasmonic monolayers by self-assembly of Au_x-*l*-$PNIPAM_y$ and Au_x-*x*-$PNIPAM_y$ building blocks, two different fabrication methods are investigated: spin-coating and interface-mediated self-assembly.

5.1 Monolayers of Au-*l*-PNIPAM$_y$

Au_{15}-*l*-$PNIPAM_{60}$ and Au_{15}-*l*-$PNIPAM_{82.5}$ are selected from the particle library for the preparation of plasmonic monolayers. The size of the gold nanoparticles is identical in both samples, however the thickness of the *l*-$PNIPAM_y$ shell is different by a factor of 1.5. Plasmonic monolayers were fabricated by spin-coating from ethanolic particle dispersions on glass substrates, and the superstructures were investigated by AFM. Figure 5.1 A shows a regular, ordered monolayer of Au_{15}-*l*-$PNIPAM_{60}$ on the glass surface after spin-coating. The particles are homogeneously distributed on the substrate, and all particles are separated from each other. The particle spacing results from the *l*-$PNIPAM_{40k}$ ligand acting as a sterical spacer during the self-assembly process. The power spectrum of the AFM image in Figure 5.1 A has an anisotropic pattern with slight hexagonal features revealing that the particles are moderately ordered on the substrate. In contrast, the Au_{15}-*l*-$PNIPAM_{82.5}$ monolayer is more irregular which is shown in Figure 5.1 B. This is attributed to a sample concentration being slightly too low for and ideal surface coverage. The power spectrum has an ellipsoidal shape, which is an image artifact caused by damage to the AFM tip. Center-to-center distances and surface densities of particles (ρ_s) were determined by $g(r)$ analysis of the particle positions, and the results are presented in Table 5.1. d_{c-c} is 102 nm or 168 nm, and ρ_s is 84.8 particles/μm^2 or 25.6 particles/μm^2 for Au_{15}-$PNIPAM_{60}$ and

Au_{15}-$PNIPAM_{82.5}$, respectively. It follows that the thickness of the l-$PNIPAM_y$ shell influences $d_{c\text{-}c}$ and ρ_s of the monolayers. However, it was hard to control both parameters on larger scales (cm^2) by spin-coating. Consequently, it is challenging to use these particles for the fabrication of plasmonic monolayers for solar cells.

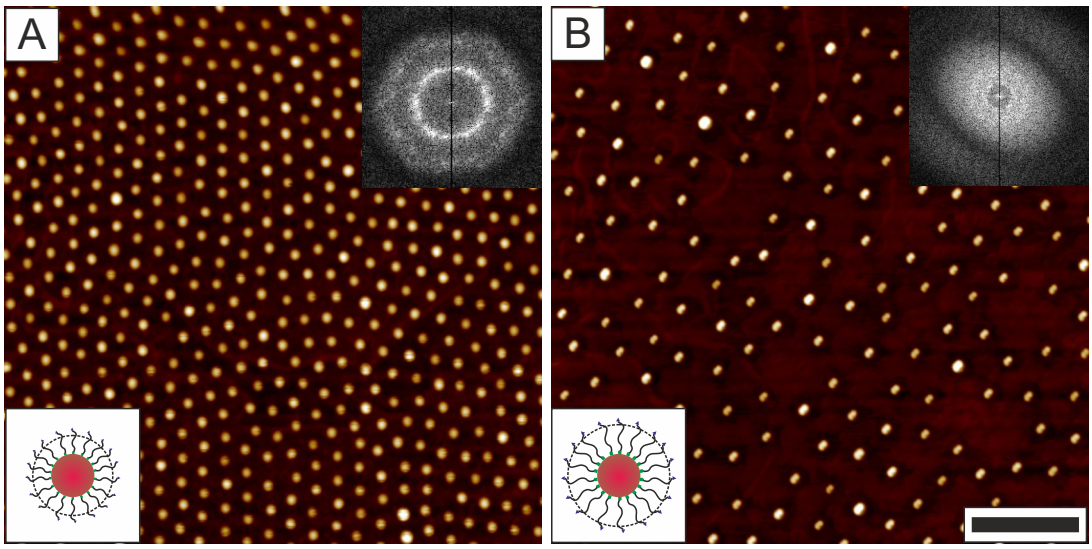

Figure 5.1. Monolayers of Au_x-l-$PNIPAM_y$ prepared by spin-coating. A, B, AFM height images of Au_{15}-l-$PNIPAM_{60}$ and Au_{15}-l-$PNIPAM_{82.5}$. The scale bar corresponds to 500 nm. The upper insets show the power spectra of the AFM images. The lower insets schematically indicates the different dimensions of the core-shell particles.

Table 5.1. Interparticle center-to-center distances and surface densities of Au_{15}-l-$PNIPAM_y$ and Au_{19}-x-$PNIPAM_y$ monolayers fabricated by spin-coating and interface-mediated self-assembly.

Sample	Self-Assembly method	$d_{c\text{-}c}$ [nm]	ρ_s particles/μm^2
Au_{15}-l-$PNIPAM_{60}$	spin-coating	102 ± 11	84.8
Au_{15}-l-$PNIPAM_{82.5}$	spin-coating	168 ± 26	25.6
Au_{19}-x-$PNIPAM_{208}$	spin-coating	250 ± 27	15.8
Au_{19}-x-$PNIPAM_{208}$	interface-mediated	251 ± 19	14.6
Au_{19}-x-$PNIPAM_{326}$	interface-mediated	386 ± 37	6.5
Au_{19}-x-$PNIPAM_{508}$	interface-mediated	617 ± 102	2.4

5.2 Monolayers of Au-*x*-PNIPAM$_y$

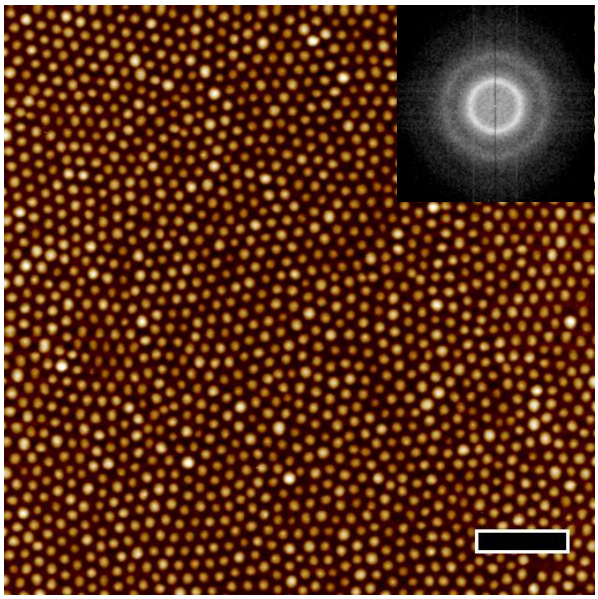

Figure 5.2. AFM height image of a Au_{19}-x-$PNIPAM_{208}$ monolayer fabricated by spin-coating. The scale bar corresponds to 1.5 μm. The inset shows the power spectrum of the monolayer.

In order to prepare plasmonic monolayers with large interparticle distances, self-assembly of cross-linked PNIPAM-encapsulated gold nanoparticles was investigated. Figure 5.2 shows a representative AFM image of an Au_{19}-x-$PNIPAM_{208}$ monolayer prepared by spin-coating. The monolayer is composed of regularly arranged Au_{19}-x-$PNIPAM_{208}$ particles, and the structure of the monolayer is comparable to the monolayer of Au_{15}-l-$PNIPAM_{60}$ particles in Figure 5.1 A. $g(r)$ analysis of the Au_{19}-x-$PNIPAM_{208}$ monolayer reveals an interparticle distance of 250 nm, which is higher by a factor of approx. 2.5 as compared to the interparticle distance of the Au_{15}-l-$PNIPAM_{60}$ monolayer. However, the long-range order of the monolayer is still low, and the rings in the FFT pattern indicate that the monolayer is polycrystalline. It follows that the particles are arranged in many small crystalline patches with different orientations relative to each other. This defect is attributed to the fast solvent evaporation rate and the presence of high shear forces during spin-coating. Consequently, even though larger interparticle spacings are accessible by using cross-linked PNIPAM-encapsulated gold nanoparticles, the preparation of highly ordered plasmonic monolayers is still challenging.

An alternative approach for the fabrication of Au_{19}-x-$PNIPAM_{208}$ monolayers is interface-mediated self-assembly. The cross-linked PNIPAM hydrogel shell is surface active and adsorbs at interfaces such as the oil/water or air/water interface.[193–195] This fabrication method was investigated for the preparation of Au_{19}-x-$PNIPAM_{208}$ monolayers. Therefore, a 1 wt.% ethanolic dispersion of Au_{19}-x-$PNIPAM_{208}$ particles was prepared and carefully deposited at the air/water interface of a water-filled crystallizing dish. The particle dispersion spread upon contact with the water surface, and a colloidal monolayer was formed covering the whole water surface. Afterwards, a part of the monolayer was transferred onto a glass substrate and investigated by AFM.

Interface-mediated self-assembly was repeated in the same manner for Au_{19}-x-$PNIPAM_{326}$ and Au_{19}-x-$PNIPAM_{508}$ particles.

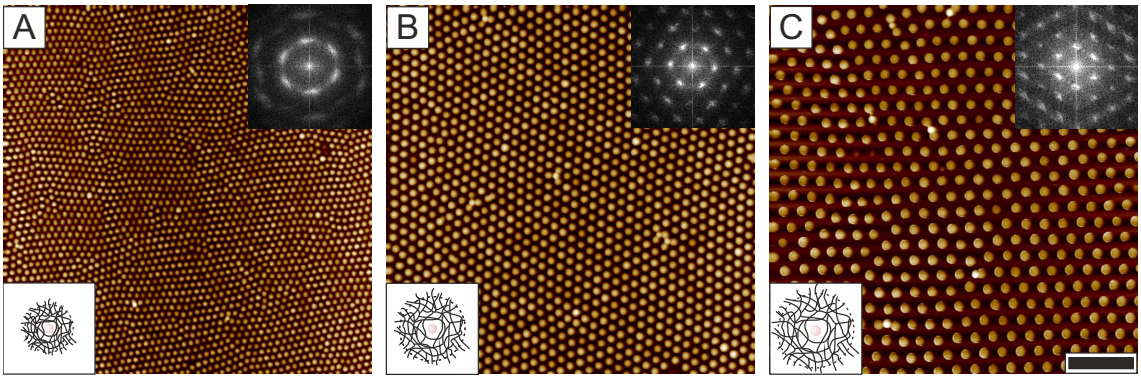

Figure 5.3. Self-assembly of Au_{19}-x-$PNIPAM_y$ particles. A – C, AFM height images of Au_{19}-x-$PNIPAM_{208}$, -$PNIPAM_{326}$, and -$PNIPAM_{508}$ monolayers. The inter-particle distances increase from 250 nm to 620 nm. The scale bar corresponds to 2.5 μm. The upper insets show the power spectra of the AFM images. The lower insets illustrate the different dimensions of the particles.

Figure 5.3 shows highly ordered monolayers of Au_{19}-x-$PNIPAM_y$ particles on the glass surface. All monolayers have a hexagonal symmetry as evidenced by the corresponding power spectra showing six characteristic Bragg peaks as well as higher order Bragg modes. $g(r)$ analysis of the Au_{19}-x-$PNIPAM_{208}$ monolayer reveals interparticle distances of 251 nm. This value is almost identical to $d_{c\text{-}c}$ of a monolayer of the same particles prepared by spin-coating (cf. Table 5.1). However, comparing Figure 5.2 and 5.3 reveals that interface-mediated self-assembly improves the long-range order of the monolayer tremendously. Using particles with larger PNIPAM shells, $d_{c\text{-}c}$ increases to 386 nm and 617 nm for Au_{19}-x-$PNIPAM_{326}$ and Au_{19}-x-$PNIPAM_{508}$ particles, respectively. Interestingly, $d_{c\text{-}c}$ of all three Au_{19}-x-$PNIPAM_y$ monolayers is larger by a factor of approx. 1.2 compared to d_h of the particles in solution (compare Table 4.5 and 5.1). The larger values of $d_{c\text{-}c}$ are explained by an anisotropic deformation of the hydrogel shell at the water surface. This result finds support from theoretical simulations based on a molecular dynamics approach as well as experimental studies carried out by other groups.[193,196,235]

Although the order of the plasmonic monolayers is improved significantly by interface-mediated self-assembly, the optical properties of all monolayers suffer from the small size of the gold cores of the PNIPAM-encapsulated particles. Figure 5.4 shows UV-Vis absorbance spectra of Au_{19}-x-$PNIPAM_y$ monolayers. Additionally, absorbance spectra of Au_{15}-l-$PNIPAM_{60}$ and Au_{15}-l-$PNIPAM_{82.5}$ monolayers are also included for comparison. The absorbance of all monolayers is very weak over the entire spectrum. A weak LSPR is only found for the Au_{15}-l-$PNIPAM_{60}$ monolayer because this monolayer has the highest surface density of plasmonic particles. The LSPR is at 535 nm and red-shifted by 10 nm as compared to the LSPR of the same particles in solution. The light absorbance of the Au_{15}-l-$PNIPAM_{82.5}$ monolayer is already outside the detection limit of the UV-Vis spectrometer. The overall absorbance of Au_{19}-x-$PNIPAM_y$ monolayers is slightly higher as compared to Au_{15}-l-$PNIPAM_y$ monolayers although the surface density of core-shell particles is considerably lower (cf. Table 5.1). However, no distinct plasmonic features are detected. It follows that the higher absorbance is caused by light scattering of the cross-linked

PNIPAM shell surrounding the particles.

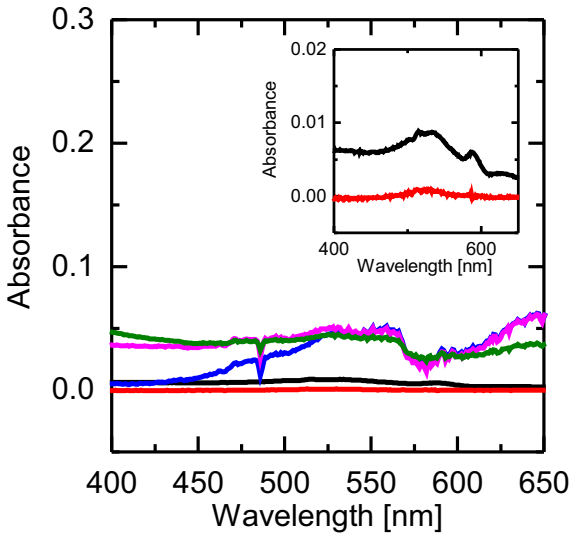

Figure 5.4. Absorbance spectra of Au_{15}-*l*-$PNIPAM_{60}$ (black), -*l*-$PNIPAM_{82.5}$ (red), Au_{19}-*x*-$PNIPAM_{208}$ (blue), -*x*-$PNIPAM_{326}$ (pink), and -*x*-$PNIPAM_{508}$ (green) monolayers on glass substrates. The inset shows a magnified region of the absorbance spectra.

In conclusion, the particle library provides colloidal building blocks for the fabrication of plasmonic superstructures with tunable interparticle distances from 102 nm up to 617 nm. The increasing interparticle distance is caused by the larger sterical demand of the PNIPAM shell of the gold nanoparticles. Monolayers with homogeneous interparticle distances and extraordinary long-range order are fabricated by interface-mediated self-assembly. However, light absorbance of the monolayers is an issue that must me solved in order to create plasmonic superstructures for thin film organic solar cells.

5.2.1 Post-Modification of Colloidal Building Blocks

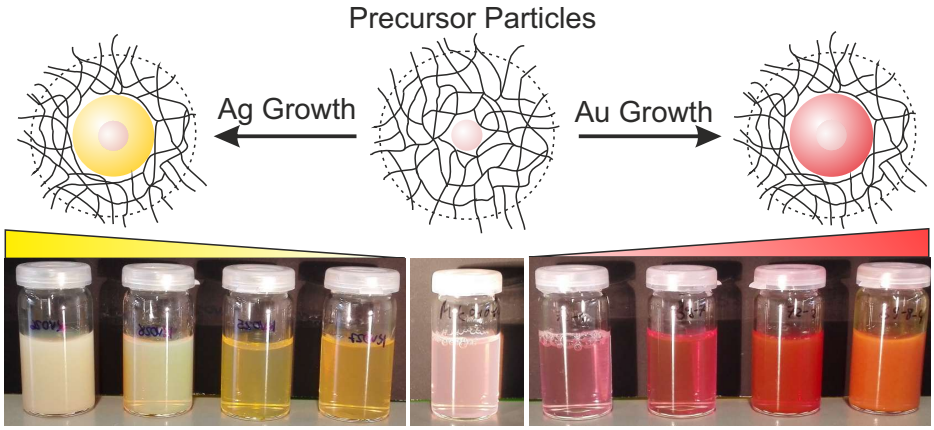

Figure 5.5. Overgrowing the gold core of Au_{19}-x-$PNIPAM_{326}$ particles with Ag (left) or Au (right). The top row shows a schematic illustration of the core overgrowth. The bottom row shows a set of digital photographs of Ag_x@Au-, and Au_x@Au-x-$PNIPAM_y$ particles in aqueous dispersion after the overgrowth process. The increasing dimensions of the plasmonic cores are represented by two color gradients. The light scattering by the particle dispersions increases strongly for samples with larger plasmonic cores due to their higher scattering cross-sections.

In order to overcome the limited light absorbance of Au_x-x-$PNIPAM_y$ monolayers, the optical properties of the colloidal building blocks are enhanced. Therefore, the gold core of PNIPAM-encapsulated nanoparticles is overgrown with gold because the scattering/absorbance cross-sections of light increase tremendously for larger gold nanoparticles.[93,236,237] Using silver as an overgrowth material is an alternative approach to enhance the optical properties of the particles because silver has a higher quality factor as compared to gold.[122,227,238]

Surfactant-assisted core overgrowth of Au_{19}-x-$PNIPAM_{326}$ particles was carried out using silver or gold as overgrowth materials. The core overgrowth was investigated by TEM and UV-Vis spectroscopy, and the stability of the particles was probed using ζ-potential as well as DLS measurements. The particles are denoted as Au_x@Au-, or Ag_x@Au-x-$PNIPAM_y$ which is a combination of the overgrowth material (Au or Ag), the final size of the metal core, and the seed particles used for the core overgrowth reaction (Au_{19}-x-$PNIPAM_{326}$). For, example Au_{30}@Au-x-$PNIPAM_{326}$ refers to particles overgrown with gold where the final size of the gold core is 30 nm, and the hydrodynamic diameter of the particles is 326 nm. In total eight different types of particles were prepared by core overgrowth. The thickness of the gold and silver shell was tuned between 5 nm and 40 nm by variation of the metal salt feed for each overgrowth reaction. Figure 5.5 shows digital photographs of the different Au_x@Au-, and Ag_x@Au-x-$PNIPAM_y$ particle dispersions after surfactant-assisted core overgrowth. It is already visible by the naked eye that the color of the initial Au_{19}-x-$PNIPAM_{326}$ dispersion (Figure 5.5, middle) intensifies and the light scattering increases strongly for samples with larger plasmonic cores. This trend is observable for both overgrowth materials.

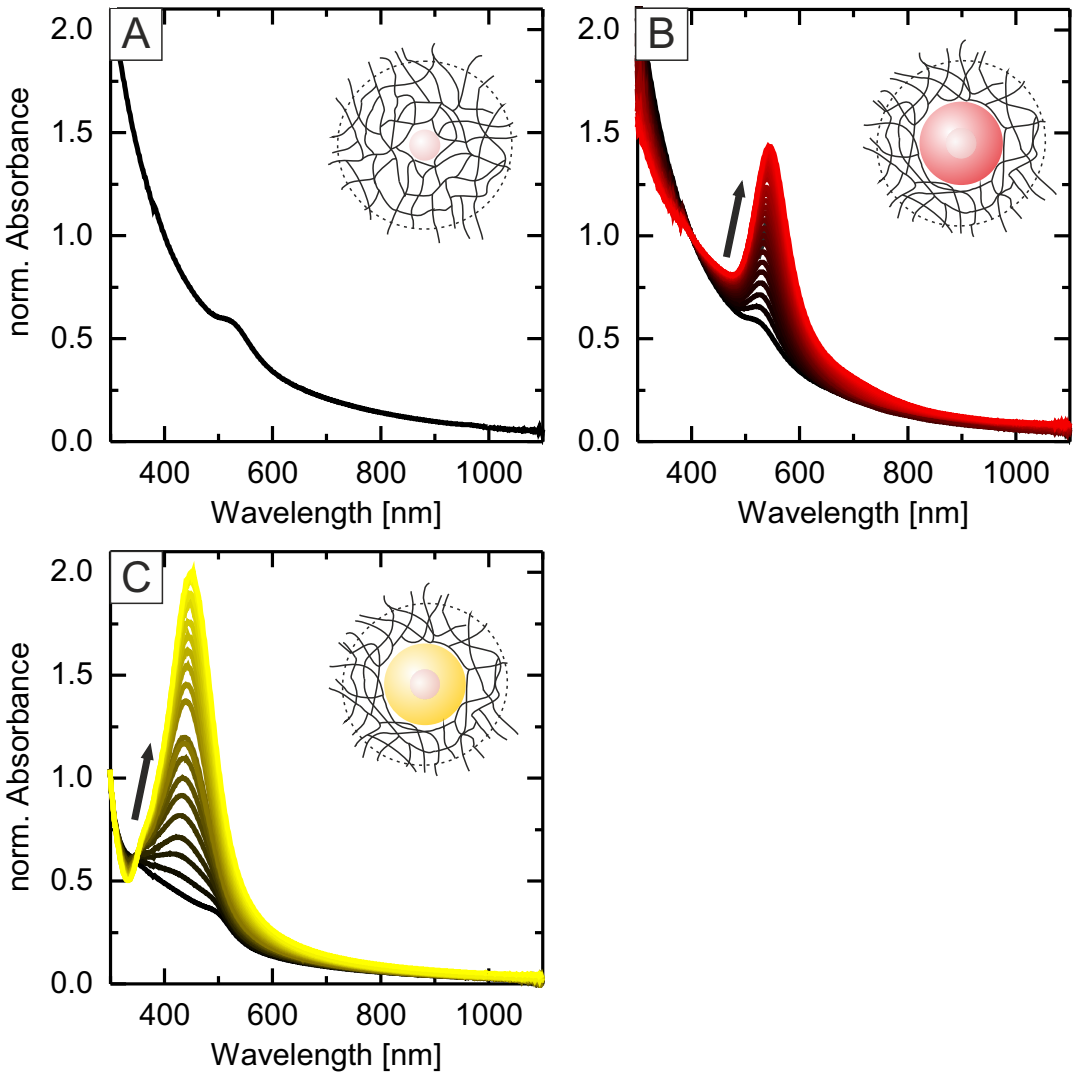

Figure 5.6. Core overgrowth in solution investigated by UV-Vis spectroscopy. A, absorbance spectrum of Au_{19}-x-$PNIPAM_{326}$ seed particles. B, C, overgrowth of Au_{19}-x-$PNIPAM_{326}$ particles with Au (B) or Ag (C). The spectra were taken at different times during the overgrowth reaction. The LSPR of the particles increases strongly as the reaction proceeds. Each spectrum was recorded at room temperature and is normalized to the absorbance at 400 nm.

The time-depended particle growth is followed by UV-Vis spectroscopy, as demonstrated in Figure 5.6. At first the absorbance spectrum of the Au_{19}-x-$PNIPAM_{326}$ seed particles is mostly dominated by Rayleigh-Debye-Gans scattering of the PNIPAM shell in Figure 5.6 A.[28] The intensity of the LSPR increases strongly once the gold core is overgrown with gold. This trend is clearly visible in Figure 5.6 B. Additionally, the LSPR of Au_x@Au-x-$PNIPAM_{326}$ particles shifts from 523 nm to 544 nm with increasing size of the gold core. The same trend is present in Figure 5.6 C once the overgrowth is carried out with silver. Here, a final shift of the LSPR to 420 nm is observed. The bimetallic Ag_x@Au-x-$PNIPAM_y$ particles behave almost like pure silver nanospheres due the low skin depth of the surface plasmon and the large size of the silver shell. The shift of the LSPR towards smaller wavelengths is explained by the higher restoring force of silver as compared to gold. After the overgrowth reaction, both types of particles have pronounced single plasmonic peaks that are attributed to the dipolar plasmonic mode of

spherical particles. It is important to note that the narrow shape of the LSPR is maintained for each overgrowth reaction. Moreover, the absence of additional plasmonic modes at higher wavelength positions points towards a spherical overgrowth of the particles.

In order to determine the exact size of the plasmonic core after the overgrowth reaction, and to exclude secondary nucleation, all particles were investigated by TEM. Figure 5.7 A shows the Au_{19}-x-$PNIPAM_{326}$ seed particles before the overgrowth reaction. The gold core of the core-shell particles is clearly visible, and each seed particle only contains one single gold core. The results of the core overgrowth with silver and gold are displayed in the TEM images B – E and J – M of Figure 5.7. It is evident that the diameter of the plasmonic cores increases from B – E (silver overgrowth) and J – M (gold overgrowth), respectively. Secondary nucleation or anisotropic particle shapes are not observed in all TEM images. Hence, the overgrowth was successful for all particles. The initial diameter of the gold core of Au_{19}-x-$PNIPAM_{326}$ particles was 19 nm. Overgrowing the particles with silver increases the final diameter of the plasmonic core up to 100 nm as demonstrated in Figure 5.7 E. Similar core dimensions are achievable when gold is used as an overgrowth material (Figure 5.7 M). The average core dimensions of all particles are summarized in Table 5.2.

Table 5.2. Summary of core-shell particles prepared by seed mediated core-overgrowth of Au_{19}-x-$PNIPAM_{336}$ seed particles.

Sample	d_c [nm]	λ_{LSPR} (Mie)[a] [nm]	λ_{LSPR} (Exp.)[b] [nm]	ζ-potential[d] [mV]	d_h[e] [nm]
Au_{19}-x-$PNIPAM_{326}$	19 ± 2	530	523	-17.3	326
Ag_{28}@Au-x-$PNIPAM_{336}$	28 ± 3	380	–	-11.5	336
Ag_{46}@Au-x-$PNIPAM_{318}$	46 ± 3	437	433	-6.8	318
Ag_{73}@Au-x-$PNIPAM_{330}$	73 ± 5	464	458	-9.3	330
Ag_{100}@Au-x-$PNIPAM_{336}$	100 ± 10	503	496	-9.6	336
Au_{30}@Au-x-$PNIPAM_{326}$	30 ± 4	532	532	-17.3	326
Au_{41}@Au-x-$PNIPAM_{316}$	41 ± 5	531	532	-2.9	316
Au_{60}@Au-x-$PNIPAM_{316}$	60 ± 7	541	540	-4.2	316
Au_{95}@Au-x-$PNIPAM_{316}$	95 ± 12	568	561	-1.1	316

[a] λ_{LSPR} (Mie), theoretical position of the LSPR calculated by Mie theory.
[b] λ_{LSPR} (Exp.), position of the LSPR measured by UV-Vis spectroscopy.
[d] ζ-potential, calculated from the electrophoretic mobility measured at 25 °C.
[e] d_h, determined by Cumulant analysis of $g^{(2)}(\tau)$ measured at 25 °C. The error of the DLS data is below 5 %.

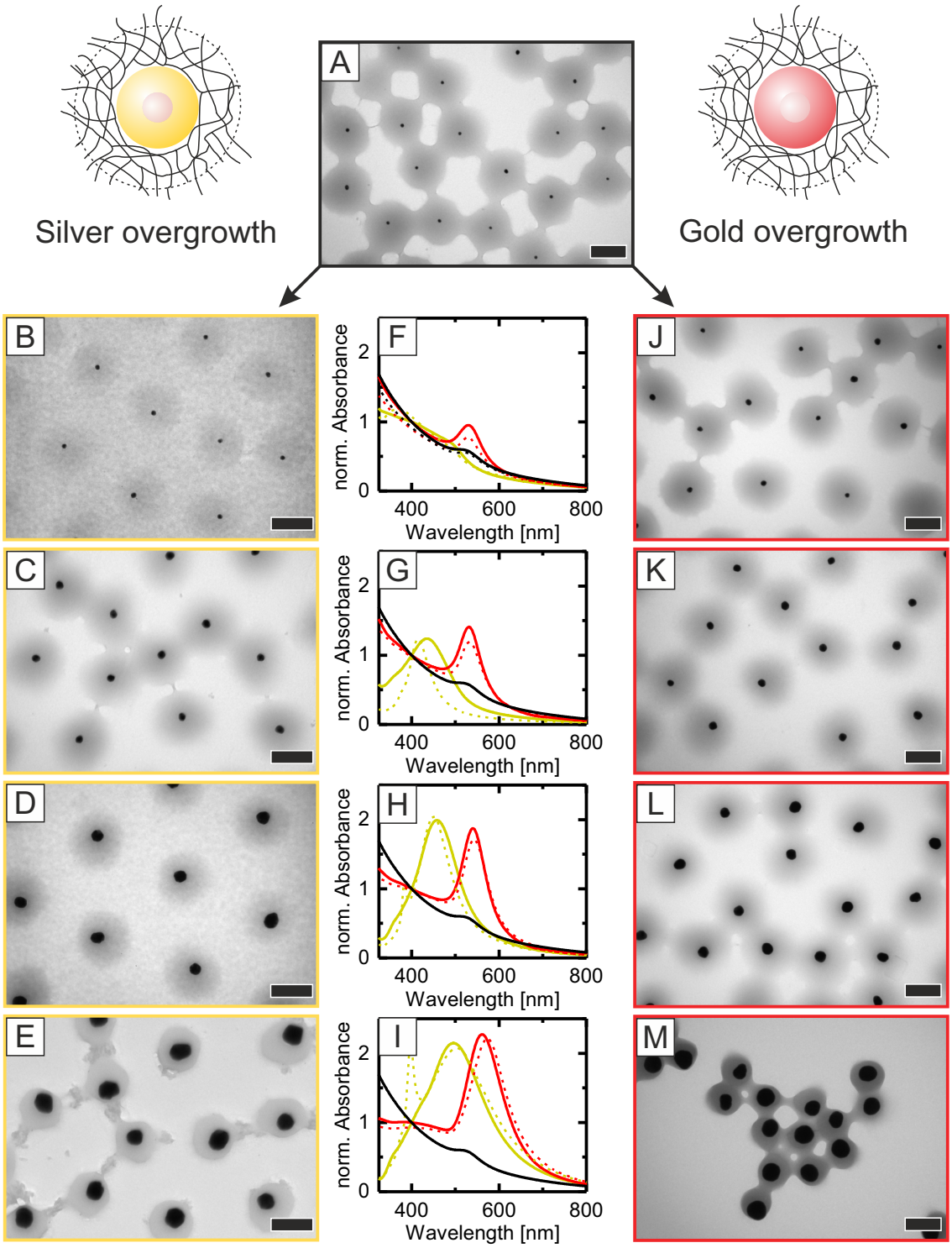

Figure 5.7. Post-modification of the gold core of Au_{19}-x-$PNIPAM_{326}$ particles. A, TEM image of Au_{19}-x-$PNIPAM_{326}$ seed particles before core overgrowth. B – E and J – M, TEM images after core overgrowth with silver (B – E) or gold (J – M). The average diameters of the silver cores are 28 nm (B), 46 nm (C), 73 nm (D), and 100 nm (E). The average diameters of the gold cores are 30 nm (J), 41 nm (K), 60 nm (L), and 95 nm (M). All scale bars are 100 nm. F – I, absorbance spectra of Ag_x@Au- (yellow) and Au_x@Au-x-$PNIPAM_y$ (red) particles of comparable sizes. Spectra of the precursor particles are also included (black). Simulated extinction spectra (dashed lines) are displayed in each graph for comparison.

Additionally, absorbance spectra of aqueous Au_x@Au-, and Ag_x@Au-x-PNIPAM$_y$ dispersions were recorded and compared to theoretical simulations which is demonstrated in Figure 5.7 F – I. Each time, spectra of Au_x@Au-x-PNIPAM$_y$ and Ag_x@Au-x-PNIPAM$_y$ particles with similar sizes of the plasmonic cores are combined in one graph. All spectra are normalized to the absorbance at 400 nm for better comparison. An absorbance spectrum of the precursor particles is included in each graph as a reference. Theoretical simulations of plasmonic extinction spectra were carried out using Mie theory and the multilayer recursive method.[111] The positions of experimental and theoretical plasmon resonances are provided in Table 5.2.

In general, a good agreement between the theoretical and the experimental data is found for the overgrowth with gold. Minor deviations between the LSPR positions are explained by particles having a non-ideal spherical symmetry, for example in Figure 5.7 M. A direct comparison between theoretical and experimental data of Ag_x@Au-x-PNIPAM$_y$ reveals more pronounced deviations. This divergence is attributed to synergistic effects of gold and silver and/or an anisotropic growth of the silver shell. The thickness of the silver shell of Ag_{28}@Au-x-PNIPAM$_{336}$ and Ag_{46}@Au-x-PNIPAM$_{318}$ particles is only 4.5 nm and 13.5 nm, respectively. Here, only a rough agreement between experimental and theoretical data is found. A distinct LSPR is missing for Ag_{28}@Au-x-PNIPAM$_{336}$ particles which is explained by significant damping of the LSPR due to a mismatch of the dielectric functions of the bimetallic cores.[239] The quadrupolar mode visible in the theoretical extinction spectra of Ag_{73}@Au-x-PNIPAM$_{330}$ and Ag_{100}@Au-x-PNIPAM$_{336}$ particles was not verified experimentally. This fact is attributed to surface roughness and an irregular morphology of the overgrown silver shells in both cases.

Investigation of the particle stability was carried out by ζ-potential and DLS experiments after the core overgrowth, and the results are provided in Table 5.2. The ζ-potential of Au_{19}-x-PNIPAM$_{326}$ particles is -17.3 mV and d_h is 326 nm indicating a good colloidal stability of the seed particles. A slight decrease of the ζ-potential is observable for Ag_x@Au- and Au_x@Au-x-PNIPAM$_y$ particles which is attributed to small amounts of residual cationic surfactant that were not removed during the purification process after the overgrowth reaction. However, even particles with very low ζ-potentials such as Au_{95}@Au-x-PNIPAM$_{316}$ are still stable in water as evidenced by d_h. It follows that the steric stabilization provided by the hydrogel shell is sufficient in order to suspend the particles in solution. Interestingly, d_h is almost unaffected after the core overgrowth even for Ag_{100}@Au-x-PNIPAM$_{336}$ and Au_{95}@Au-x-PNIPAM$_{316}$ particles – the particles with the largest plasmonic core. Although the volume of the plasmonic cores increased by a factor of 125 or 97 relative to the volume of the gold core of Au_{19}-x-PNIPAM$_{326}$ particles, the volume fraction of the plasmonic core is tiny (ϕ_{core}(Ag_{100}@Au-x-PNIPAM$_{336}$)=2.63 %) as compared to the volume fraction of the PNIPAM hydrogel shell of the core-shell particle (ϕ_{shell}(Ag_{100}@Au-x-PNIPAM$_{336}$)=97.36 %). Thus, overgrowing the gold nanoparticle core has only negligible influence on the overall dimensions of the core-shell particles.

Modification of the plasmonic core by core overgrowth completes the library of PNIPAM-encapsulated gold nanoparticles that are used as colloidal building blocks for plasmonic superstructures. A summary of all building blocks is provided in Table 5.3. Looking at Table 5.3 the most significant change is that the LSPR is now tunable in a spectral region as large as 128 nm for Au-x-PNIPAM$_{336}$ particles. Modification of shell thickness and core size allows for another classification of the particles using the shell-to-core ratio $\lambda_b = \frac{d_h}{d_c}$. Knowing λ_b is particularly important for self-assembly experiments because the formation of different phases such as hexagonal, stripe, sigma, honeycomb or quasicrystalline phases only occur at specific values of λ_b.[159,240,241]

Table 5.3. Full library of colloidal core-shell building blocks for plasmonic superstructures.

Building blocks	λ_{LSPR} [nm]	d_c [nm]	d_h [nm]	d_s [nm]	λ_b [nm]
Au_{15}-*l*-$PNIPAM_{44.2}$	525	15 ± 2	44.2	14.6	2.9
Au_{15}-*l*-$PNIPAM_{60}$	525	15 ± 2	60	22.5	4.0
Au_{15}-*l*-$PNIPAM_{82.5}$	525	15 ± 2	82.5	33.8	5.5
Au_{19}-*l*-$PNIPAM_{48.1}$	526	19 ± 2	48.1	14.6	2.5
Au_{19}-*l*-$PNIPAM_{72.6}$	526	19 ± 2	72.6	26.8	3.8
Au_{19}-*l*-$PNIPAM_{96.1}$	526	19 ± 2	96.1	38.6	5.1
Au_{22}-*l*-$PNIPAM_{54.5}$	527	22 ± 3	54.5	16.4	2.5
Au_{22}-*l*-$PNIPAM_{76.4}$	527	22 ± 3	76.4	27.2	3.5
Au_{22}-*l*-$PNIPAM_{99.5}$	528	22 ± 3	99.5	38.8	4.5
Au_{29}-*l*-$PNIPAM_{58.7}$	531	29 ± 3	58.7	14.9	2.0
Au_{29}-*l*-$PNIPAM_{75.3}$	531	29 ± 3	75.3	23.2	2.6
Au_{29}-*l*-$PNIPAM_{91.5}$	531	29 ± 3	91.5	31.3	3.2
Au_{36}-*l*-$PNIPAM_{62.6}$	537	36 ± 4	62.6	13.3	1.7
Au_{36}-*l*-$PNIPAM_{81.9}$	537	36 ± 4	81.9	23.0	2.3
Au_{36}-*l*-$PNIPAM_{107.1}$	538	36 ± 4	107.1	35.6	3.0
Au_{44}-*l*-$PNIPAM_{68.6}$	539	44 ± 5	68.6	12.3	1.6
Au_{44}-*l*-$PNIPAM_{89.2}$	539	44 ± 5	89.2	22.6	2.0
Au_{44}-*l*-$PNIPAM_{122.9}$	539	44 ± 5	122.9	39.5	2.8
Au_{53}-*l*-$PNIPAM_{75.5}$	542	53 ± 7	75.5	11.3	1.4
Au_{53}-*l*-$PNIPAM_{99.4}$	542	53 ± 7	99.4	23.2	1.9
Au_{53}-*l*-$PNIPAM_{135.8}$	542	53 ± 7	135.8	41.4	2.6
Au_{19}-*x*-$PNIPAM_{208}$	524	19 ± 2	208	94.5	10.9
Au_{19}-*x*-$PNIPAM_{326}$	528	19 ± 2	326	153.5	17.2
Au_{19}-*x*-$PNIPAM_{508}$	-	19 ± 2	508	244.5	26.7
Ag_{28}@Au-*x*-$PNIPAM_{336}$	-	28 ± 3	336	154.0	12.0
Ag_{46}@Au-*x*-$PNIPAM_{318}$	433	46 ± 3	318	136.0	6.9
Ag_{73}@Au-*x*-$PNIPAM_{330}$	458	73 ± 5	330	128.5	4.5
Ag_{100}@Au-*x*-$PNIPAM_{336}$	496	100 ± 10	336	118.0	3.4
Au_{21}@Au-*x*-$PNIPAM_{330}$	524	21 ± 2	330	154.5	15.7
Au_{30}@Au-*x*-$PNIPAM_{326}$	532	30 ± 4	326	148.0	10.9
Au_{41}@Au-*x*-$PNIPAM_{315}$	532	41 ± 5	315	137.0	7.7
Au_{58}@Au-*x*-$PNIPAM_{330}$	553	58 ± 4	330	136.0	5.7
Au_{60}@Au-*x*-$PNIPAM_{316}$	540	60 ± 7	316	128.0	5.3
Au_{68}@Au-*x*-$PNIPAM_{330}$	547	68 ± 6	330	131.0	4.9
Au_{75}@Au-*x*-$PNIPAM_{326}$	547	75 ± 2	340	132.5	4.5
Au_{89}@Au-*x*-$PNIPAM_{330}$	547	89 ± 5	330	120.5	3.7
Au_{95}@Au-*x*-$PNIPAM_{316}$	561	95 ± 4	316	112.0	3.4
Au_{100}@Au-*x*-$PNIPAM_{330}$	571	100 ± 3	330	115.0	3.3

5.2.2 Optically Homogeneous Plasmonic Superstructures

Core overgrowth of Au-x-PNIPAM$_{326}$ particles was the missing piece for the fabrication of optically homogeneous plasmonic superstructures. Knowing that interface-mediated self-assembly fabricates plasmonic monolayers of extraordinary long-range order, the same fabrication process was investigated for the preparation of Ag$_x$@Au- and Au$_x$@Au-x-PNIPAM$_y$ monolayers. In the following, plasmonic monolayers on solid substrates are denoted as M-Ag$_x$ or M-Au$_x$ depending on material and size of the plasmonic core of the PNIPAM-encapsulated core-shell particles.

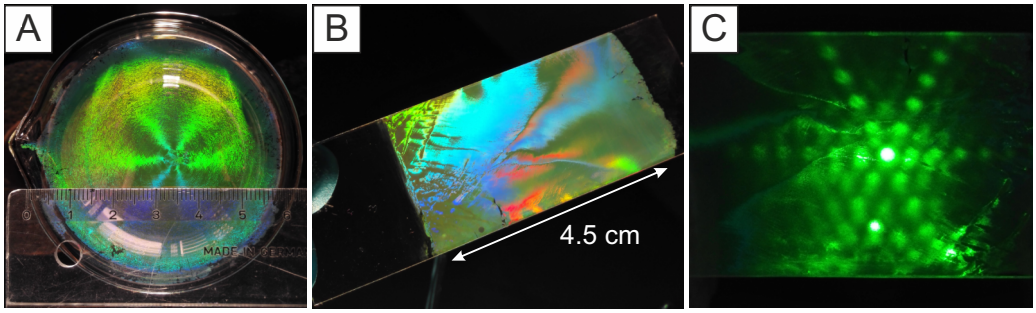

Figure 5.8. Well-defined plasmonic monolayer fabricated by interface-mediated self-assembly of Ag$_{100}$@Au-x-PNIPAM$_{336}$ particles. A, digital photograph of the monolayer floating at the air/water interface. B, photograph of the same monolayer after transfer onto a glass substrate. The total surface area of the monolayer is 11.4 cm^2. C, illumination of the substrate by a laser pointer ($\lambda = 530$ nm) showing six fundamental Bragg peaks as well as several higher order modes.

Figure 5.8 shows digital photographs of a M-Ag$_{100}$ monolayer highlighting the homogeneity of plasmonic superstructures fabricated by interface-mediated self-assembly. The diameter of the M-Ag$_{100}$ monolayer is approx. 6 cm, and the monolayer covers the entire size of the crystallizing dish as demonstrated in Figure 5.8 A. The Ag$_{100}$@Au-x-PNIPAM$_{336}$ particles form a strongly iridescent film on the water surface after they are deposited at the air/water interface. The iridescent color is caused by light diffraction at the Ag$_{100}$@Au-x-PNIPAM$_{336}$ monolayer on the water surface. The same phenomenon is observed once the monolayer is transferred onto a solid glass substrate as demonstrated in Figure 5.8 B. Is is important to note that the monolayer covers a total surface area of 11.4 cm^2 on the glass substrate. This surface area is sufficient for common organic thin film solar cell substrates as they are used in the laboratory.

Illuminating the monolayer by a laser pointer reveals a distinct diffraction pattern on the surface of the glass substrate as shown in Figure 5.8 C. Hence, the M-Ag$_{100}$ monolayer acts as a diffraction grating. Strikingly, the presence of individual diffraction spots proves the existence of large single-crystalline domains in the superstructure. The sixfold symmetry of the diffraction pattern indicates that the particles are arranged in a hexagonal lattice, and the presence of multiple diffractions spots results from diffraction at different lattice planes of the monolayer. Similar diffraction patterns were observed for every monolayer of Ag$_x$@Au- and Au$_x$@Au-x-PNIPAM$_{336}$ particles on glass. The reflexes were most pronounced for monolayers of Ag$_x$@Au-x-PNIPAM$_{336}$ particles with large silver cores due to the high scattering cross-section of silver. Microscopic investigation of Ag$_x$@Au- and Au$_x$@Au-x-PNIPAM$_y$ monolayers was carried out by SEM and AFM. The optical homogeneity was probed by UV-Vis spectroscopy.

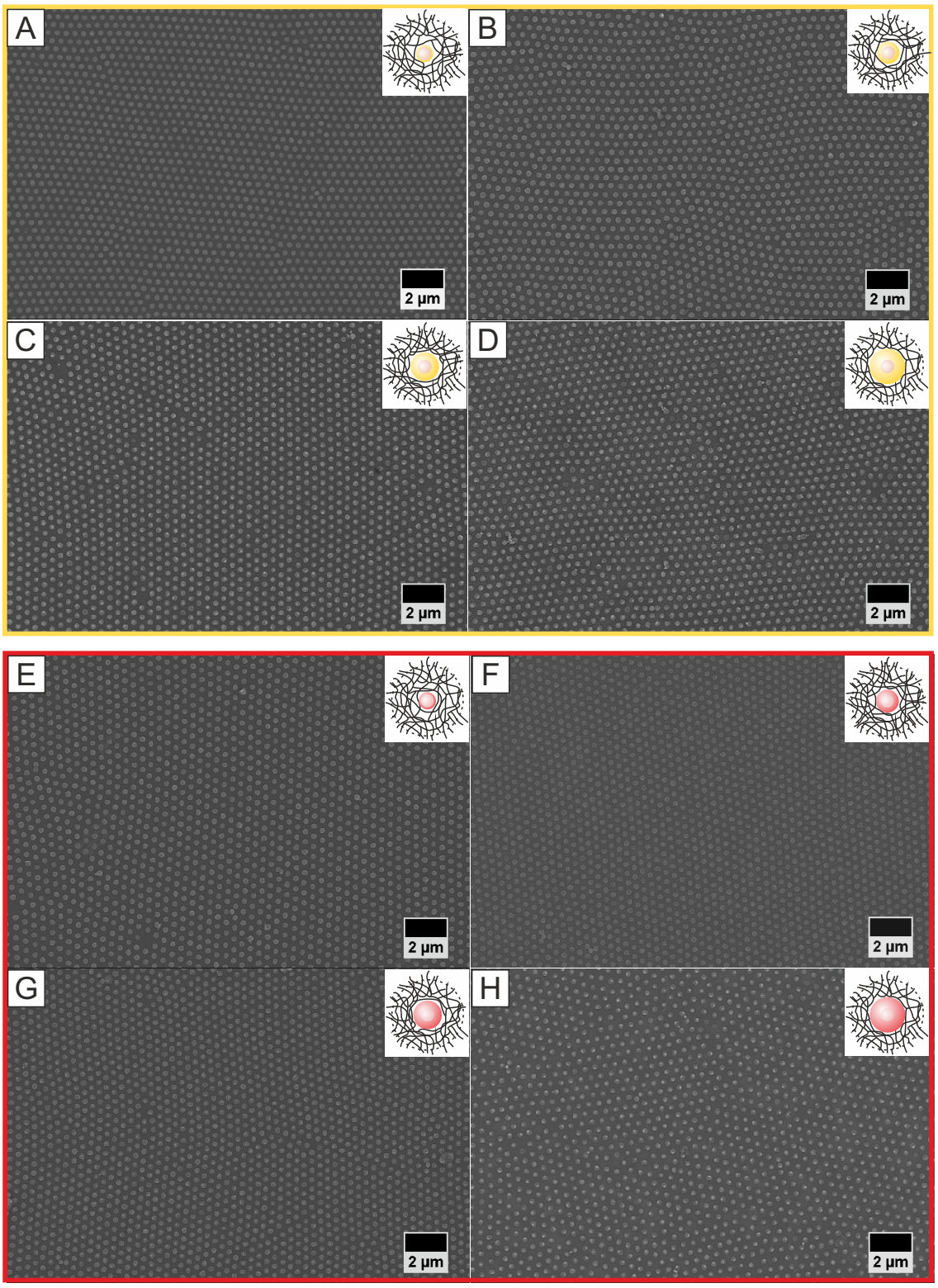

Figure 5.9. Investigation of plasmonic monolayers by SEM. A – D, M-Ag_x monolayers on glass substrates. E – H, M-Au_x monolayers on glass substrates. The insets illustrate the different sizes of the plasmonic cores of the cross-linked PNIPAM-encapsulated particles for each superstructure.

Figure 5.9 shows representative SEM images of each monolayer on glass. The SEM investigation was carried out at multiple positions of the substrate in order to probe its structural homogeneity. Each time, large single-crystalline domains are visible consisting of hexagonally ordered Ag$_x$@Au- or Au$_x$@Au-x-PNIPAM$_y$ particles. Only the PNIPAM hydrogel shell is visible in the SEM images because the images were taken at rather low magnifications in order to get a better overview of the samples. Importantly, only particle monolayers are found and unwanted particle multilayers are absent on all substrates. Moreover, all monolayers are almost identical and no significant differences regarding surface density of plasmonic particles or interparticle spacing are observed.

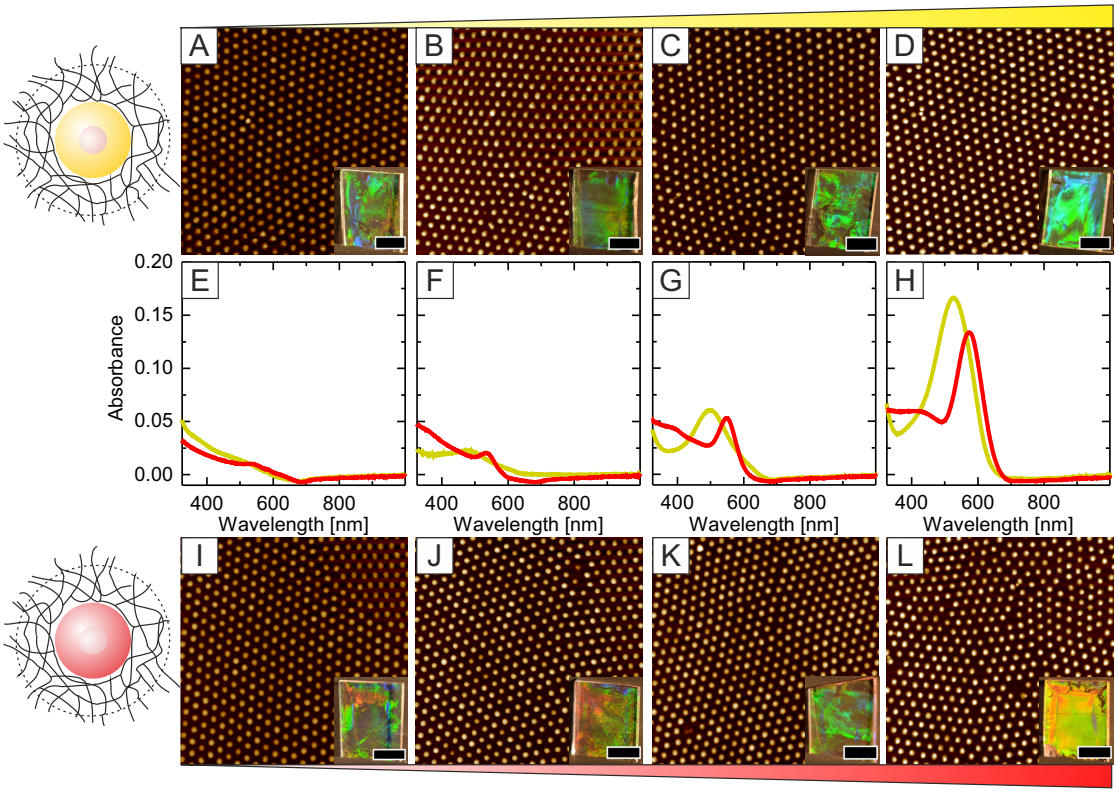

Figure 5.10. AFM investigation of M-Ag$_x$ (top row) and M-Au$_x$ monolayers (bottom row) on glass substrates. A – D and I – L, height images of the monolayers. The insets of the AFM images show digital photographs of the samples on 1 cm^2 glass slides. Color gradients indicate the increasing size of the plasmonic cores of the monolayer. The scan size of the AFM images is 10 x 10 μm^2. E – H, absorbance spectra of M-Ag$_x$ (yellow) and M-Au$_x$ (red) monolayers. Spectra of plasmonic monolayers with comparable core sizes (A & I, B & J, C & K, and D & L,) are included in one graph for comparison.

In order to investigate the particle spacing more closely, AFM investigation of the superstructures was performed. AFM images of M-Ag$_x$ and M-Au$_x$ monolayers on glass are presented in Figure 5.10. Large domains of single-crystalline hexagonally ordered superstructures are observed. The particles are non-close packed on the substrate. This observation is explained by shrinkage of the water-swollen PNIPAM shell once the samples are dried after the monolayer deposition process. d_{c-c} and ρ are determined by $g(r)$ analysis for each monolayer, and the results are summarized in Table 5.4.

Table 5.4. Surface coverages and optical properties of plasmonic monolayers.

Sample	d_{c-c} [nm]	ρ_s particles/μm^2	λ_{LSPR} (glass) [nm]	Abs. (λ_{LSPR})
M-Ag$_{28}$	461 ± 23	4.71	–	–
M-Ag$_{46}$	455 ± 22	4.77	484	0.022
M-Ag$_{73}$	453 ± 23	4.48	499	0.06
M-Ag$_{100}$	459 ± 20	4.67	527	0.166
M-Au$_{30}$	473 ± 15	4.49	–	–
M-Au$_{41}$	465 ± 14	4.76	536	0.02
M-Au$_{60}$	445 ± 15	4.94	547	0.053
M-Au$_{95}$	463 ± 19	4.45	573	0.133
M-Ag$_{100}$-Au$_{95}$[b]	455 ± 17	4.67	564	0.146

[b] M-Ag$_{100}$-Au$_{95}$, binary plasmonic monolayer

Looking at d_{c-c} and ρ, it is clear that the interparticle distances and surface densities of plasmonic particles are almost identical for all monolayers. This was further confirmed by performing AFM measurements at multiple, random locations of each sample. d_{c-c} and ρ vary slightly in a narrow range of 455 nm – 473 nm and 4.49 particles/μm^2 – 4.94 particles/μm^2 for all monolayers. Hence, it is deduced that the cross-linked PNIPAM hydrogel shell drives the particle self-assembly at the air/water interface, and that the plasmonic core does not influence the structure of the monolayer significantly at the water surface. d_{c-c} is approx. 44 % higher as compared to the hydrodynamic diameter of the overgrown particles in aqueous dispersion (cf. Table 5.2). An anisotropic deformation of the hydrogel shell at the air/water interface explains this effect, as already discussed in Section 5.2.

Digital photographs of the plasmonic monolayers on glass highlight the homogeneous surface coverage of the substrates in Figure 5.10. At a first glance, the optical homogeneity of the surfaces is already evidenced by the iridescent colors of the substrates due to light diffraction by the plasmonic monolayers. The optical properties of the monolayers were investigated in more detail by UV-Vis spectroscopy. Figure 5.10 E – H shows absorbance spectra of M-Ag$_x$ and M-Au$_x$ monolayers. Absorbance spectra of monolayers with similar dimensions of the plasmonic cores are plotted in one graph for better comparison. It is important to note that the sample area illuminated by the light beam is identical and that the displayed spectra are not normalized. It is evident that the light absorbance of the samples increases from E to H. Since UV-Vis spectroscopy always probes a constant circular area on each sample, and ρ_s is almost identical for each sample, it follows that approx. the same number of particles is probed in each measurement. Hence, the strong increase of absorbance is solely attributed to the increasing volume of the plasmonic core. The wavelength position and absorbance of the LSPR are extracted from the UV-Vis spectra and summarized in Table 5.4 for all monolayers. M-Ag$_{28}$ and M-Au$_{30}$ – the monolayers with the smallest plasmonic cores – show only a very weak absorbance due to the low absorption and scattering cross-sections of the plasmonic cores. However, the optical properties of the

monolayers are getting more pronounced with increasing size of the plasmonic cores.

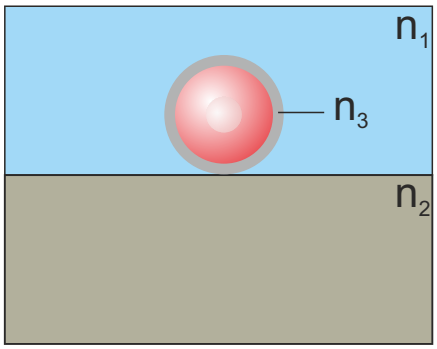

Figure 5.11. Schematic illustration of the refractive index environment of a plasmonic core shell particle at an interface. n_1, n_2 are the refractive indices of the two different materials, and n_3 is the refractive index of the collapsed dielectric shell.

Comparing Table 5.3 and 5.4 reveals that λ_{LSPR} of plasmonic monolayers on glass is constantly higher as compared to λ_{LSPR} of the respective building blocks in dilute dispersion. This is explained considering that the transfer of the particles from aqueous dispersion onto a solid surface changes their refractive index environment completely. Figure 5.11 shows a schematic illustration of a plasmonic core-shell particle located at an interface of two materials with different refractive indices. This is similar to PNIPAM-encapsulated gold nanoparticles on a glass substrate. The particles are in a complex inhomogeneous refractive index environment. Thus, the LSPR is influenced by the refractive indices of air ($n_1 = 1.00$), glass ($n_2 = 1.52$), and the collapsed PNIPAM shell ($n_3 = 1.45$). In air, the overall refractive index environment of the particles is rather low.[202] However, the local refractive index close to the plasmonic nanoparticles is high because the PNIPAM shell is strongly collapsed forming a dense polymer shell around the nanoparticles. Thus, the polymer density is higher as compared to dispersed PNIPAM-encapsulated nanoparticles in solution where the PNIPAM shell is highly swollen by water (below the VPTT of the particles). The increase of polymer density causes a higher refractive index environment close to the nanoparticle surface shifting λ_{LSPR} of the monolayers to higher wavelengths.

5.2.3 Binary Plasmonic Monolayers

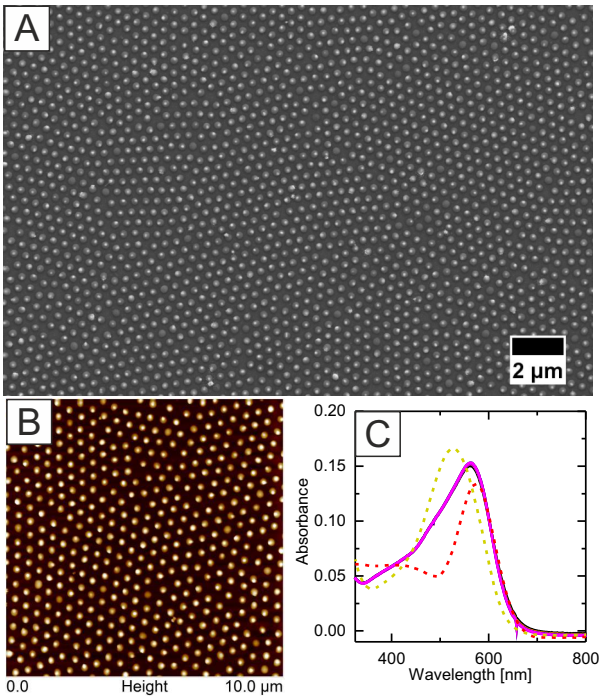

Figure 5.12. Investigation of a M-Ag_{100}-Au_{95} monolayer by SEM (A), AFM (B) and UV-Vis spectroscopy (C). Absorbance spectra (solid lines) were recorded at five random random positions of the monolayer. Absorbance spectra of M-Ag_{100} (yellow dashed lines) and M-Au_{95} (red dashed lines) monolayers are included as a reference.

Using Ag_x@Au- and Au_x@Au-x-PNIPAM$_y$ particles for plasmonic monolayers, light absorbance and position of the LSPR are already tunable in a range as large as 100 nm. The width of the LSPRs of M-Ag_x and M-Au_x monolayers is small due to the narrow size distribution and spherical shape of the silver and gold cores. For certain applications such as SERS substrates or plasmonic solar cells,[242,243] however, it is useful to increase the spectral window of light extinction by the plasmonic monolayer. One way to do so is to start from scratch and develop alternative core overgrowth protocols in order to modify shape and/or composition of the plasmonic particles. However, this requires elaborate synthetic effort. Given the Ag_x@Au- and Au_x@Au-x-PNIPAM$_y$ particles that are already at hand, mixing of the particle dispersions is a clever way in order to tune the optical properties of plasmonic monolayers. This way, *binary* plasmonic monolayers can be prepared.

A binary M-Ag_{100}-Au_{95} monolayer is presented in Figure 5.12. The superstructure was fabricated by mixing Ag_{100}@Au-x-PNIPAM$_{336}$ and Au_{95}@Au-x-PNIPAM$_{316}$ particles at a 1:1 ratio by volume. The binary monolayer was prepared by interface-mediated self-assembly as discussed in Section 5.2.2 and investigated by SEM, AFM, and UV-Vis. The SEM image in Figure 5.12 A reveals hexagonally ordered domains of core-shell particles, and the particles are homogeneously distributed on the glass surface. A center-to-center distance of 452 nm was determined from AFM measurements of the M-Ag_{100}-Au_{95} monolayer (Figure 5.12 B) by $g(r)$ analysis. d_{c-c} is almost identical to d_{c-c} of the non-binary M-Ag_{100} and M-Au_{95} monolayers in Table 5.4.

Absorbance spectra of the binary monolayer are displayed in Figure 5.12 C. Additionally, absorbance spectra of the non-binary Ag_{100}@Au-x-PNIPAM$_{336}$ and Au_{95}@Au-x-PNIPAM$_{316}$ monolayers are included for comparison. The peak position of the LSPR of the M-Ag_{100}-Au_{95} monolayer is located at 564 nm, and the binary monolayer absorbs incident light in a broad wavelength range of 345 nm – 662 nm. The width of the LSPR is significantly higher as compared to M-Ag_{100} or M-Au_{95} monolayers, as excepted. Absorbance spectra were measured at five random positions of the substrate and all spectra look almost identical. This fact demonstrates a homogeneous (random) distribution of Ag_{100}@Au-x-PNIPAM$_{336}$ and Au_{95}@Au-x-PNIPAM$_{316}$ particles within the monolayer. It follows that the fabrication of binary monolayers is a promising way in order to tune the light extinction of plasmonic superstructures.

In summary, interface-mediated self-assembly is a powerful method for the fabrication of optically homogeneous plasmonic superstructures with defined optical properties. The particle library allows for the fabrication of plasmonic superstructures with tailored absorbance and plasmon resonance position. The superstructures have almost identical interparticle distances and surface densities of plasmonic particles which is especially important for plasmonic solar cells. Using mixed dispersions of colloidal building blocks allows to manipulate absorbance, shape, and position of the LSPR of the superstructures even more which is interesting for broadband-absorbing plasmonic superstructures.

Chapter 6

Plasmonic Solar Cells

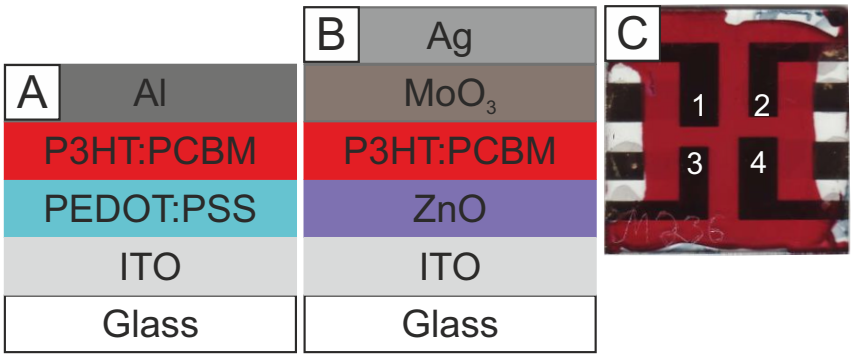

Figure 6.1. Illustration of two different thin film solar cell geometries used in this work. A, normal device geometry B, inverted device geometry. C, digital photograph of thin film solar cells on a standard solar cell substrate (2.54 x 2.54 cm^2). The substrate contains four individual solar cells, indicated by Arabic numbers.

Figure 6.1 shows two popular geometries of thin film organic solar cells that are frequently encountered in the literature.[57,59,244–247] The devices are classified based on the direction of charge flow. In the normal device geometry (Figure 6.1 A) holes are collected at the ITO electrode and electrons at the Al counter electrode. Hole collection is facilitated by the introduction of hole transport materials such as PEDOT:PSS or MoO_3. Conversely, this process is switched around in solar cells with an inverted device geometry (Figure 6.1 B). Electrons are now collected at the ITO site and ZnO is used as an electron transport material. In this work, organic thin film solar cells are prepared on structured ITO substrates with a surface area of 2.54 x 2.54 cm^2. Figure 6.1 C shows a digital photograph of a fully operational solar cell substrate. Each substrate consists of four independent solar cell devices indicated by Arabic numbers. It follows immediately that a light harvesting plasmonic superstructure must provide optical homogeneity on the same scale. Hence, the optically homogeneous plasmonic monolayers presented in Section 5.2.2 are perfectly suited for plasmonic solar cells.

Plasmonic monolayers of Au_x@Au-x-PNIPAM$_y$ particles were prepared by interface-mediated self-assembly and integrated in the layer stack of organic thin film solar cells with normal and inverted device geometry. Cross-linked PNIPAM-encapsulated particles based on Au_{19}-x-$PNIPAM_{326}$ were used for the monolayer fabrication. These particles form monolayers with

typical interparticle distances in the order of 445 nm – 461 nm (cf. Section 5.2.2). This rather large particle spacing was chosen in order to avoid plasmon-plasmon coupling between neighbouring particles. After deposition of the plasmonic monolayer, the solar cell device was finished by depositing the remaining solar cell layers onto the monolayer. P3HT:PCBM was selected as active layer material as it is the current benchmark of organic thin film solar cell devices.[50–52] Each time an organic thin film solar cell without plasmonic particles was prepared as a reference device.

6.1 Solar Cells with Normal Cell Geometry

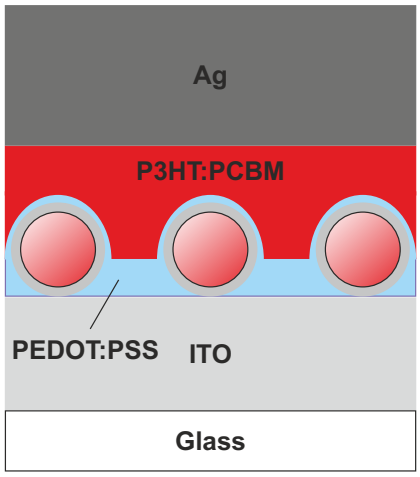

Figure 6.2. Schematic illustration of a plasmonic solar cell with normal cell geometry. PNIPAM-encapsulated gold nanoparticles are deposited on top of the ITO electrode and covered with a layer of PEDOT:PSS.

Plasmonic Monolayers on Top of ITO – Size Effect of Gold Nanoparticles. Au_x@Au-x-$PNIPAM_y$ particles with gold cores of 21 nm, 58 nm, 68 nm, and 100 nm in diameter were chosen from the particle library for the monolayer fabrication. The monolayers are denoted as M-Au_{21}, M-Au_{58}, M-Au_{68}, and M-Au_{100}, according to the average diameter of the gold cores. All monolayers were deposited on top of the ITO electrode of organic solar cells with normal cell geometry as illustrated in Figure 6.2. It is important to note that annealing steps, carried out during the device fabrication, cause a complete collapse of the cross-linked PNIPAM hydrogel shell. Thus, the PNIPAM shell is only a thin polymer layer surrounding the particles as illustrated in Figure 6.2.

Figure 6.3 A shows a representative AFM height image of a M-Au_{21} monolayer on the ITO electrode of a plasmonic solar cell. It is evident that the monolayer is highly ordered and that the particles are arranged in a hexagonal lattice. Similar particle arrangements are found for M-Au_{58}, M-Au_{68}, and M-Au_{100} monolayers. The respective AFM height images are provided in the Appendix, Figure 10.5. Interparticle center-to-center distances and the surface density of plasmonic particles were determined by $g(r)$ analysis of the monolayers. All results are summarized

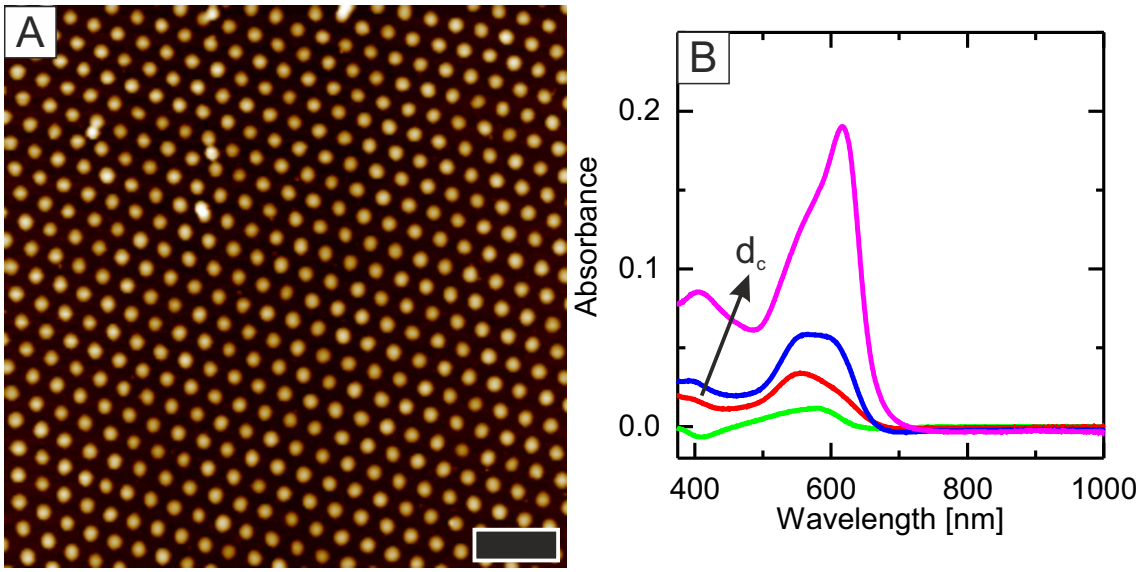

Figure 6.3. AFM and UV-Vis investigation of M-Au$_{21}$ on the ITO electrode of a plasmonic solar cell (normal cell geometry). A, representative AFM height image. The scale bar is 2 μm. B, UV-Vis absorbance spectra of M-Au$_{21}$ (green), M-Au$_{58}$ (red), M-Au$_{68}$ (blue), and M-Au$_{100}$ (pink) on ITO. Note that the absorbance increases strongly with increasing d_c.

in Table 6.1. d_{c-c} and ρ_s are almost identical for M-Au$_{21}$, M-Au$_{68}$, and M-Au$_{100}$ monolayers. Only d_{c-c} of the M-Au$_{58}$ monolayer is slightly higher by approx. 6 % as compared to the other three monolayers. An average surface density of 4.6 particles/μm^2 is found for each monolayer. ρ_s was used in order to calculate ϕ – the volume fraction of gold nanoparticles in a hypothetical layer of gold. ϕ is given by Equation 6.1.

$$\phi = \frac{\frac{4}{3}\,\pi\,(\frac{d_c}{2})^3\,\rho_s}{10^6\,h\,\mathrm{nm}^2} \tag{6.1}$$

where h defines the thickness of the hypothetical layer. h was selected based on AFM height images of the cross-linked PNIPAM-encapsulated gold nanoparticles. Comparing M-Au$_{21}$ and M-Au$_{100}$ monolayers reveals that ϕ increases by a factor of 21 due to the increasing size of the gold nanoparticles. However, ϕ is still rather low for all monolayers and it is assumed that the hole collection at the ITO electrode is not strongly affected by the presence of PNIPAM-encapsulated gold nanoparticles.

Figure 6.4 B shows absorbance spectra of all M-Au$_x$ monolayers on the ITO electrode. The absorbance increases strongly as a function of the gold core size of the plasmonic monolayers, as expected. Looking back at Equations 2.1 and 2.2, it is clear that light scattering is more pronounced for monolayers of larger plasmonic particles because the scattering cross-section increases much stronger than the absorbance cross-section as a function of the particle radius. Hence, monolayers of larger PNIPAM-encapsulated nanoparticles are supposed to act predominately as light scattering elements increasing the mean free path of photons in the device.[58,246] In contrast, near-field enhancement is assumed to play the dominant role for monolayers of smaller plasmonic particles because such particles mainly absorb incident light.

Table 6.1. Interparticle distance, surface density of plasmonic particles, and volume fraction of gold in organic thin film solar cells with normal cell geometry.

Sample	d_{c-c} [nm]	ρ_s [particles/μm^2]	ϕ [%]
M-Au$_{21}$	446 ± 50	4.9	0.11
M-Au$_{58}$	470 ± 43	4.2	0.74
M-Au$_{68}$	445 ± 52	4.6	1.11
M-Au$_{100}$	439 ± 44	4.6	2.41

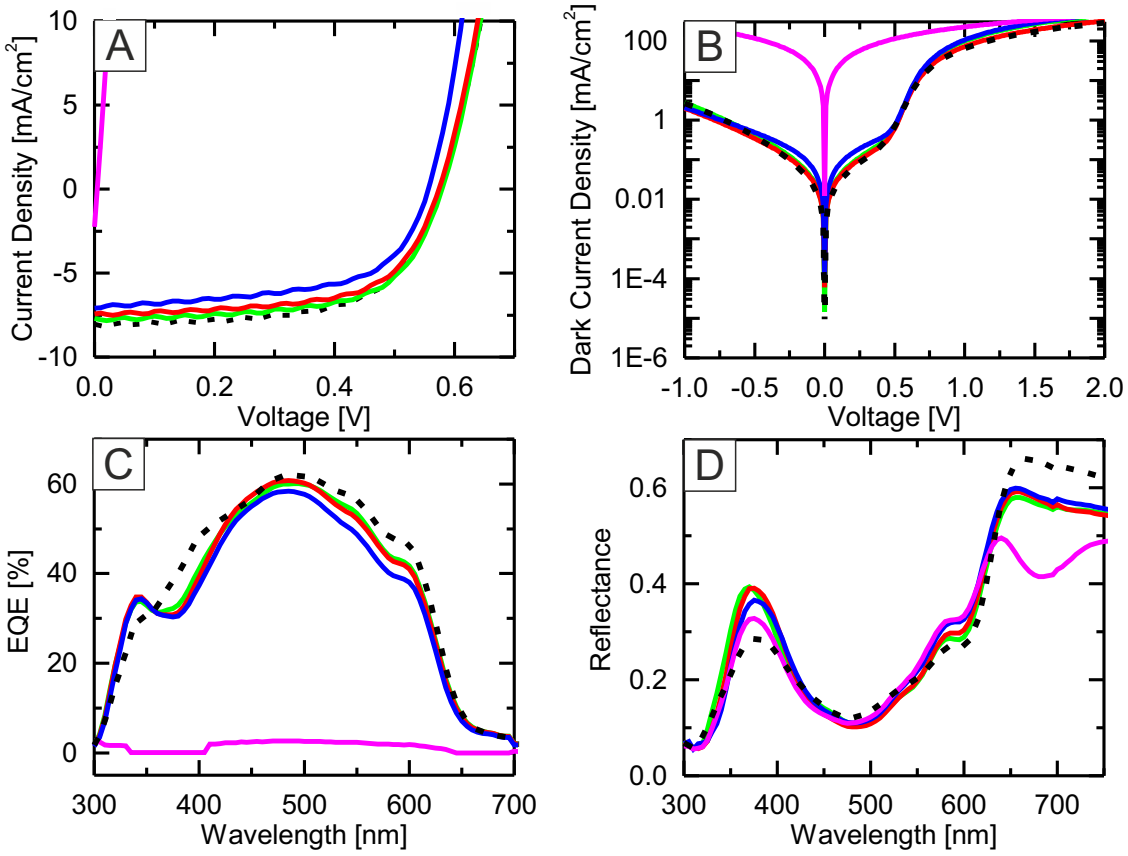

Figure 6.4. Characterization of plasmonic solar cells with normal cell geometry. A, IV-curve of solar cells with M-Au$_{21}$ (green), M-Au$_{58}$ (red), M-Au$_{68}$ (blue), or M-Au$_{100}$ (pink) monolayers. The dashed lines represent the reference device without plasmonic particles. B, IV-curves recorded in the dark. C, EQE spectra of the solar cell devices. D, total reflectance spectra recorded by an integrating sphere.

Evaluating the Solar Cell Performance. The performance of solar cell devices was evaluated by current-voltage, EQE, and reflectance measurements. Figure 6.4 A shows IV-curves of plasmonic solar cells measured under illumination using the standard AM 1.5 solar spectrum. The IV-curve is recorded by scanning an applied voltage across the solar cell device and measuring the corresponding current. This characterization method is carried out under illumination and in the dark in order to extract the following parameters of the device: short-circuit current (J_{SC}), open-circuit voltage (V_{OV}), fill factor (FF), power conversion efficiency (η_{OPV}), series resistance (R_S), and shunt resistance (R_{SH}). Table 6.2 summarizes all parameters of the solar cells.

Table 6.2. Performance of plasmonic solar cells with normal cell geometry.

Sample	J_{SC} [mA/cm^2]	V_{OC} [V]	FF [%]	η_{OPV} [%]	R_S [Ω cm^2]	R_{SH} [Ω cm^2]
reference	7.6	0.6	61.5	2.7	2.1	842
M-Au$_{21}$	7.5	0.6	62.41	2.7	1.9	767
M-Au$_{58}$	7.3	0.6	60.27	2.5	1.9	661
M-Au$_{68}$	6.4	0.6	58.71	2.1	1.8	680
M-Au$_{100}$	1.2	$4.6 \cdot 10^{-5}$	—	—	1.5	1.6

The IV-curves in Figure 6.4 A have the characteristic shape of a solar cell diode. The current increases exponentially in forward bias as a function of the applied voltage. Illuminating the solar cell shifts the IV-curve to the fourth quadrant of the coordinate system. It is clear from Figure 6.4 A that almost all plasmonic solar cells are fully operational. Only M-Au$_{100}$ solar cells do not show diode-like characteristics. Measuring IV-curves in the dark allows to assess the electrical parameters more clearly that limit the performance of solar cells such as the parasitic R_{SH}, for example.[248] Looking at Figure 6.4 B, it is clear that the dark current density of M-Au$_{100}$ devices is orders of magnitudes higher as compared to the other devices. Consequently, strong leakage currents are present causing a severe drop of R_{SH} and V_{OC}. The other plasmonic monolayers mainly affect J_{SC} and R_{SH} of the solar cells, whereas V_{OV} remains constant. Interestingly, the plasmonic monolayers could not improve η_{OPV} of the devices. Instead, J_{SC} decreases with increasing size of the gold nanoparticles and the following trend is observed: J_{SC} (M-Au$_{21}$) > J_{SC} (M-Au$_{58}$) > J_{SC} (M-Au$_{68}$). Moreover, all solar cell devices exhibit rather high leakage currents which is deduced from the decreasing values of R_{SH} in Table 6.2. It is supposed that R_{SH} is the most important source of parasitic losses, i.e. the plasmonic particles are short circuiting the device which causes J_{SC} to drop. Besides, R_S also decreases slightly for plasmonic solar cells. However this drop is far too weak in order to affect the performance of the devices significantly.

EQE measurements of the devices are presented in Figure 6.4 C. It is observed that the EQE spectra of the plasmonic devices closely match to the EQE spectrum of the reference device. It follows that the plasmonic monolayers do not contribute significantly to the photoelectron conversion process. More specifically, even a slight decrease of the EQE spectra can be seen for monolayers with larger gold nanoparticle cores. Reflectance measurements in Figure 6.4 D reveal that the reflectance of plasmonic solar cells decreases significantly in a wavelength region of

640 nm – 750 nm. This trend is most pronounced for solar cell devices with a M-Au_{100} monolayer. On the one hand, plasmonic monolayers increase the light absorbance of the solar cell devices. On the other hand, the photons do not contribute to the charge generation as their wavelengths are outside of the active region of the P3HT:PCBM layer (cf. Figure 6.4 C). Moreover, a slight increase of reflectance is observed in a wavelength range of 550 nm – 600 nm. This points towards parasitic backscattering of light by the plasmonic particles.

It follows that the location of plasmonic monolayers on top of the ITO electrode is not suitable in order to enhance the performance of organic thin film solar cell devices with normal cell geometry.

6.2 Solar Cells with Inverted Cell Geometry

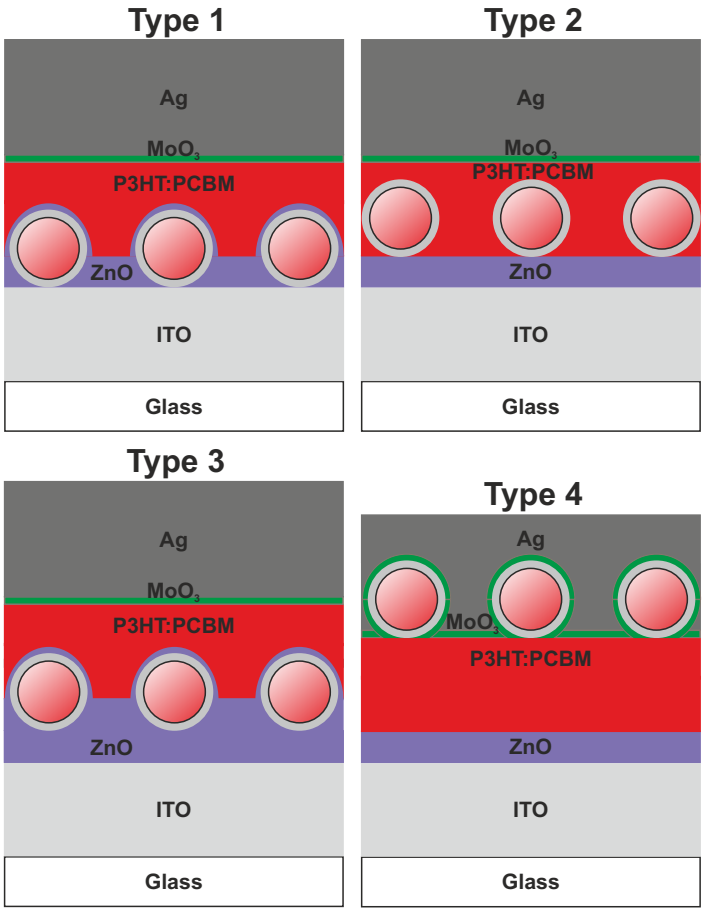

Figure 6.5. Schematic illustration of M-Au_{89} monolayers at different positions in the layer stack of plasmonic solar cell devices with inverted geometry. **Type 1** device: the monolayer is deposited onto the ITO electrode. **Type 2** device: the monolayer is deposited onto the ZnO layer. **Type 3** device: the monolayer is encapsulated within the ZnO layer. **Type 4** device: the monolayer is deposited onto the P3HT:PCBM layer.

Previously, leakage currents and backscattering of incident light was observed for plasmonic monolayers located at the ITO/PEDOT:PSS interface of solar cell devices. Consequently, a systematic investigation of the monolayers at different interfaces of the device is necessary in

order to assess the impact of the monolayer upon the charge photogeneration of the device more clearly. However, it was impossible to change the location of the monolayer in the layer stack of plasmonic solar cells with normal cell geometry because the monolayer deposition process was carried out in water and the PEDOT:PSS layer was water soluble. Therefore, the device geometry was changed to solar cell devices with inverted cell geometry. The most important change of the inverted device geometry is the replacement of PEDOT:PSS by ZnO. Hence, the inverted devices contain no water soluble materials anymore. Additionally, ZnO has a refractive index of 1.93 which is comparable to ITO ($n = 1.96$) and higher as compared to PEDOT:PSS ($n = 1.51$). Thus, backscattering of light by the gold nanoparticles is reduced.

Plasmonic monolayers were systematically introduced at different interfaces of inverted devices and four different types of solar cells were prepared as illustrated in Figure 6.5. The monolayers were deposited at the following locations: on top of the ITO electrode (**Type 1** device), on top of the ZnO layer (**Type 2** device), encapsulated within the ZnO layer (**Type 3** device), and deposited onto the active layer (**Type 4** device). All monolayers were fabricated by interface-mediated self-assembly of Au_{89}@Au-x-$PNIPAM_{330}$ particles and are referred to as M-Au_{89} monolayers. Each monolayer was investigated by UV-Vis spectroscopy and AFM. The performance of the plasmonic solar cell devices was evaluated by IV-curve, EQE, and reflectance measurements.

6.2.1 Plasmonic Monolayers at Different Positions in the Layer Stack

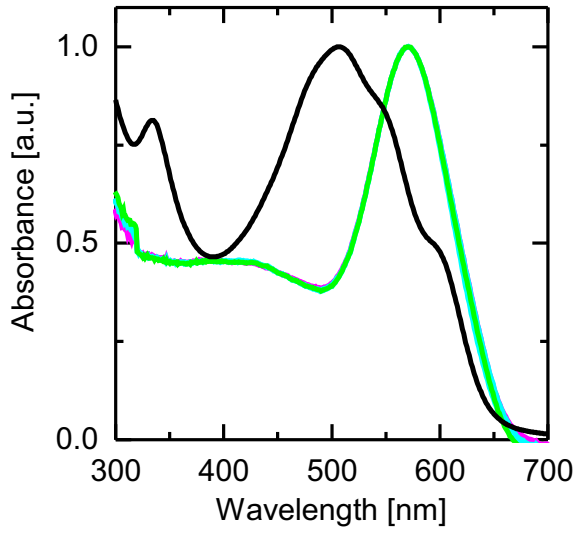

Figure 6.6. Absorbance spectra of a P3HT:PCBM film (black) and a M-Au_{89} monolayer (colored lines) on glass. Spectra of the M-Au_{89} monolayer were recorded at four random positions of the glass slide. All spectra are normalized to the peak maximum.

Before M-Au_{89} monolayers were integrated into organic solar cells, they were deposited onto plain glass substrates in order to probe the optical homogeneity of the monolayers. Figure 6.6 reveals a strong absorbance of the monolayers in the wavelength region of 500 nm – 650 nm and

the LSPR is at 571 nm. The plasmon resonance is within the active region of the P3HT:PCBM layer, and thus, the monolayer can contribute to the light management of the solar cell. Spectra of the M-Au_{89} monolayer were recorded at four random positions of the substrate. All spectra are fully overlapping highlighting the optical homogeneity of the monolayer.

After the **Type 1 − 4** devices were prepared, each device was investigated by AFM in order to determine interparticle spacing, surface density of plasmonic particles, and volume fraction of each device layout. The AFM measurements were always carried out on top of the Ag electrode of the finished solar cell devices. The AFM height images in Figure 6.7 reveal that all devices are covered by homogeneous particle monolayers. Hence, leakage currents from big particle agglomerates can be neglected. The AFM height images of **Type 1 − 3** devices are slightly textured which is attributed to the M-Au_{89} monolayer in the layer stack of the devices. The topographical contrast is rather low because the space between the core-shell particles is completely filled by the upper solar cell layers (ZnO, P3HT:PCBM, MoO_3, and Ag). A better topographical contrast is observed for **Type 4** devices. Individual Au_{89}@Au-x-$PNIPAM_{330}$ particles of the monolayer are resolved because the M-Au_{89} monolayer is only covered by the Ag counter-electrode.

Table 6.3. Interparticle distance, surface density of plasmonic particles, and volume fraction of gold in solar cell devices with inverted cell geometry.

Layout	d_{c-c} [nm]	ρ_s [particles/μm^2]	ϕ [%]
Type 1	486 ± 45	4.7	1.7
Type 2	461 ± 32	5.2	1.9
Type 3	464 ± 34	5.1	1.9
Type 4	488 ± 153	4.8	1.8

Next, d_{c-c} and ρ_s were determined by $g(r)$ analysis and ϕ was calculated for all devices. The results are provided in Table 6.3. d_{c-c} and ρ_s are similar for all devices and only minor deviations below 10 % are found. Consequently, the surface coverage of plasmonic particles is almost identical independent of their location in the layer stack of the devices. Thus, particle concentration effects can be excluded which would affect scattering and absorption of light by the monolayer. Calculating ϕ reveals low volume fractions of gold similar to plasmonic monolayers in solar cell devices with normal device geometry (cf. Section 6.1).

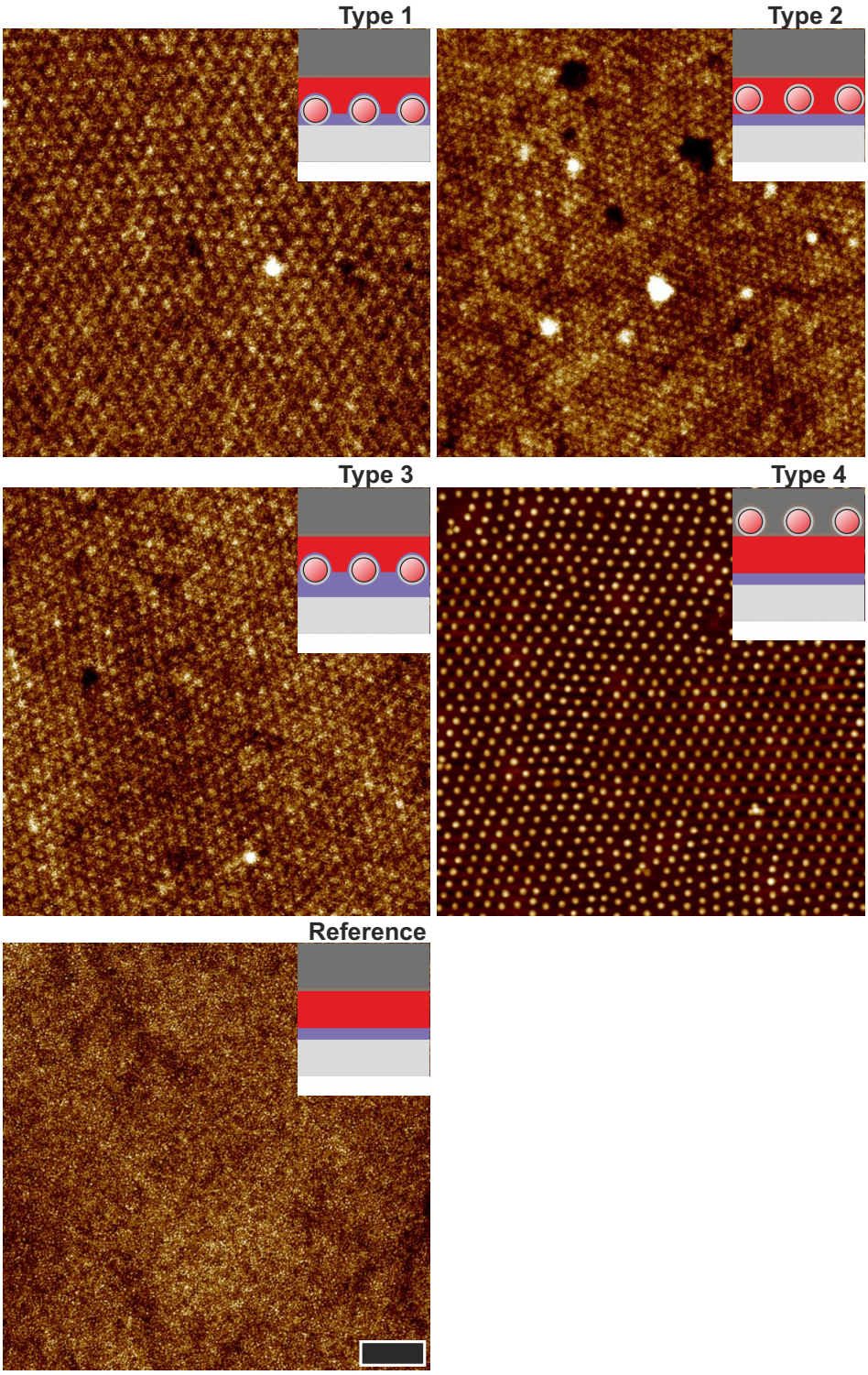

Figure 6.7. AFM investigation of **Type 1 – 4** inverted solar cell devices. The scale bar is 2 μm. The insets represent schematic illustrations of the different device layouts.

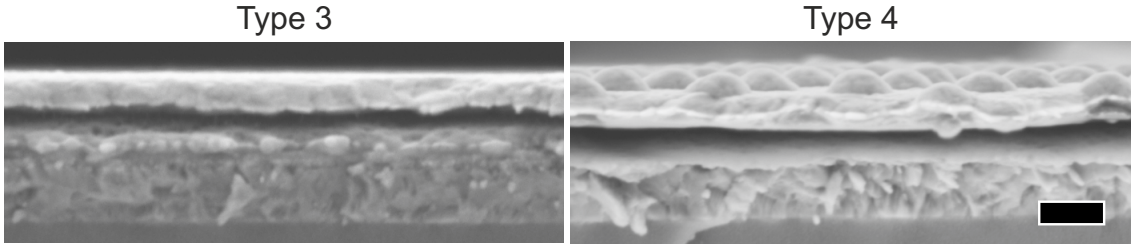

Figure 6.8. SEM investigation of **Type 3** and **Type 4** device of cross-sections. Both images are recorded using the same magnification. The scale bar is 250 nm.

In addition to AFM, cross-section analysis of the devices was carried out using SEM. Figure 6.8 shows cross-sections of **Type 3** and **Type 4** devices. The **Type 3** device was selected as a representative example for a M-Au_{89} monolayer embedded below the active layer of an inverted solar cell device. Starting from the top site, the layer stack of the **Type 3** device is identified as follows: Ag electrode, P3HT:PCBM, ZnO, ITO and glass. The monolayer is hardly visible because the Au_{89}@Au-x-$PNIPAM_{326}$ particles are completely embedded within the ZnO matrix. The **Type 4 device** uses the same layer stack. However, the M-Au_{89} monolayer is clearly visible and individual particles of the monolayer are observable as large hemispheres sitting on top of the device covered by the Ag counter-electrode.

6.2.2 Evaluating the Solar Cell Performance

The **Type 1 − 4** solar cell devices had an optimized film thickness of the P3HT:PCBM layer of 118 nm. This thickness was chosen to ensure a high internal quantum efficiency of the active layer.[249] Figure 6.9 shows the results of the solar cell characterization. It is evident from the shape of the IV-curves in Figure 6.9 A that all devices display the characteristic diode behaviour of a solar cell as discussed in Section 6.1. Additionally, it is important to note that the solar cell performance is reproducible which was confirmed by measuring the devices on different days. The average device parameters extracted from the IV-curves are presented in Table 6.4.

Looking at J_{SC} and FF, it is clear that each plasmonic device performs less efficiently as compared to the reference device. Unusual high leakage currents are observed for the **Type 2** device as evidenced by the high dark current density under reverse bias in Figure 6.9 B. The leakage currents decreasing J_{SC} and FF are attributed to a direct contact of the plasmonic particles with the P3HT:PCBM layer of the solar cell. This parasitic effect is prevented in **Type 3** devices where an additional layer of ZnO covers the M-Au_{89} monolayer. Interestingly, leakage currents are also absent in **Type 4** devices. Although the particles are sitting directly on top of the active layer, the spherical cap of the gold nanoparticles which is in direct contact with the P3HT:PCBM layer is significantly lower as compared to **Type 1** or **Type 2** devices. However, no enhancement of the photocurrent is found for either **Type 3** or **Type 4** devices.

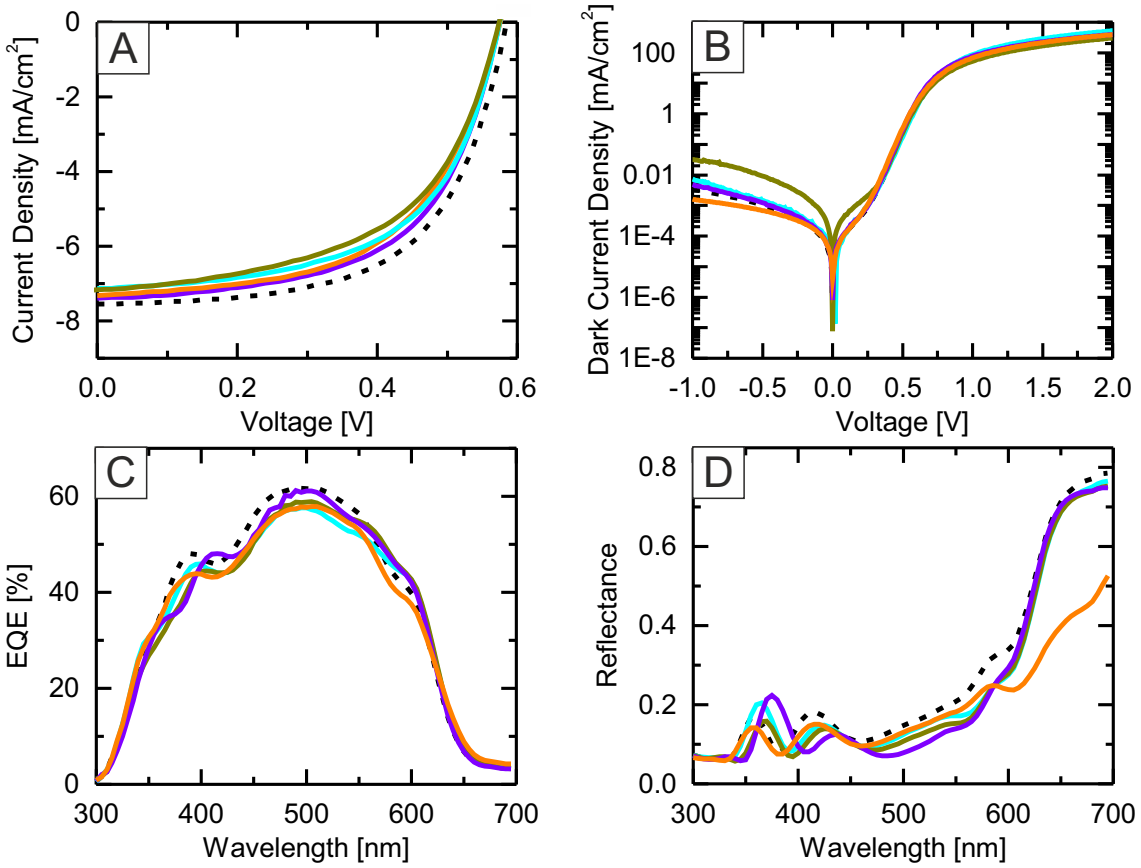

Figure 6.9. Characterization of plasmonic solar cells with inverted cell geometry and a layer thickness of 118 nm. A, *IV*-curves of **Type 1** (cyan), **Type 2** (green), **Type 3** (purple) and **Type 4** devices (orange). The performance of a reference device is shown as a black dashed line. B, *IV*-curves measured in the dark. C, *EQE* spectra of the different solar cell devices. D, total reflectance spectra recorded by an integrating sphere.

Table 6.4. Performance of plasmonic solar cells with inverted cell geometry.

Layout	J_{SC} [mA/cm^2]	V_{OC} [V]	FF [%]	η_{OPV} [%]
118 nm active layer				
reference	7.5	0.58	58	2.5
Type 1	6.7	0.58	57	2.2
Type 2	7.0	0.58	54	2.2
Type 3	7.3	0.58	54	2.4
Type 4	7.5	0.57	56	2.4
194 nm active layer				
reference	5.4	0.58	46	1.4
Type 3	4.9	0.58	46	1.3
Type 4	7	0.58	46	1.9

EQE spectra of **Type 1 – 4** devices were recorded with white bias light and a power density of 100 mW/cm^2. Figure 6.9 C shows that the shape of all spectra looks very similar. No significant effect of the plasmonic monolayer is visible. In contrast, total reflectance measurements in Figure 6.9 D reveal that the reflectance of all plasmonic solar cells is lower in a range of 400 nm – 630 nm as compared to the reference device. This spectral region agrees well with the LSPR region of the M-Au$_{89}$ monolayer (cf. Figure 6.6). The decrease of reflectance is most pronounced for **Type 4** devices in a wavelength range above 630 nm. It is follows that the plasmonic monolayers in **Type 1 – 4** devices act mostly as parasitic light absorption sites lowering the efficiencies of the solar cell devices.

6.2.3 Space Charge Limited Solar Cells

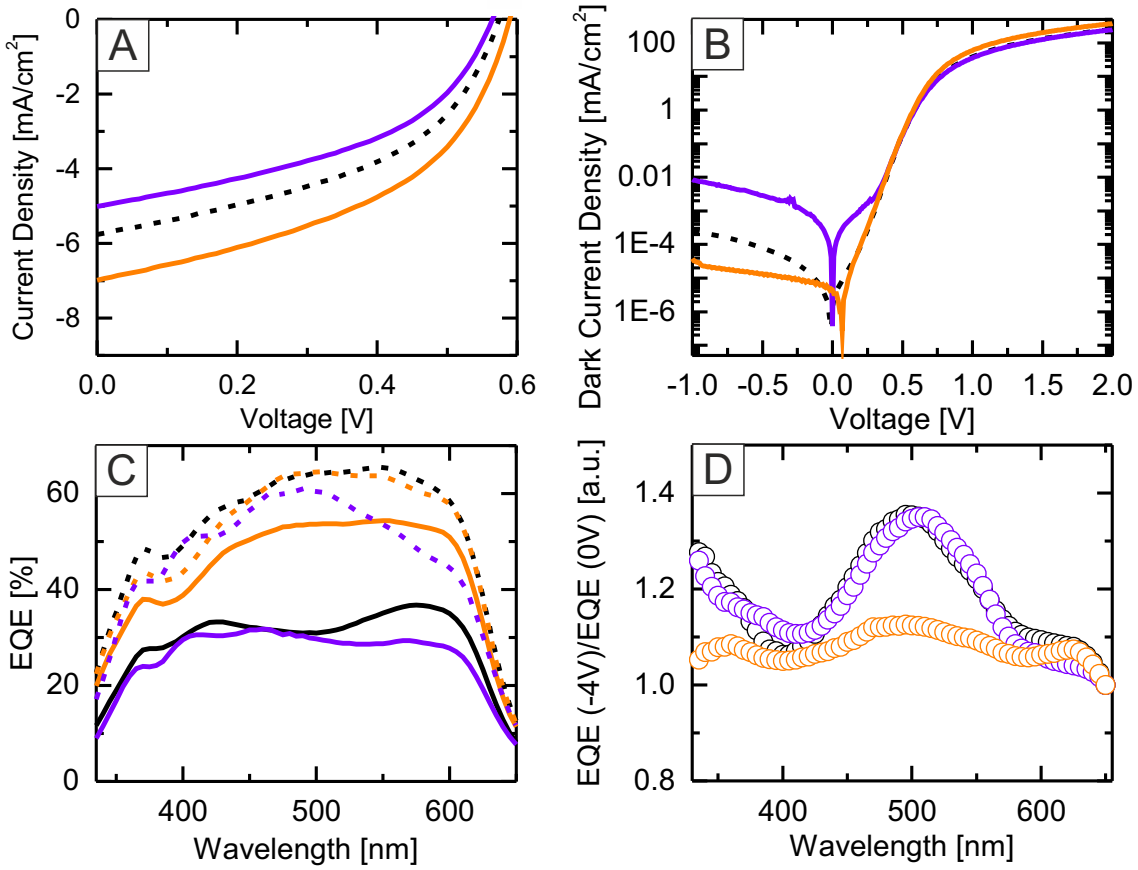

Figure 6.10. Characterization of SCL-devices with an active layer thickness of 194 nm. A, *IV*-curve of **Type 3** (purple) and **Type 4** devices (orange). The *IV*-curve of a reference device is shown as black dashed lines. B, dark *IV*-measurements. C, *EQE* spectra of **Type 3** and **Type 4** devices recorded at 0 V (solid lines) and -4 V(dashed lines) under white bias light with a power density of 80 mW/cm^2. D, normalized relation EQE(-4 V)/EQE(0 V).

In order to elucidate the light management of M-Au$_{89}$ monolayers more clearly, space charge limited solar cell devices (SCL-devices) were prepared. Briefly, space charge limit occurs in solar cell devices with a charge carrier mobility imbalance. Space charge limit is observed for solar cells with very thick active layers. Here, a space charge region is formed because the hole mobility of

the organic semiconductor is low and positive charges accumulate in the device. Consequently, space charge formation and bulk recombination of free charge carriers strongly decrease J_{SC} and FF.[250–254]

SCL-devices were prepared by increasing the layer thickness of the P3HT:PCBM layer to 194 nm. Either **Type 3** or **Type 4** devices were fabricated because these solar cells were least affected by leakage currents. IV-curves were recorded for both device layouts and are presented in Figure 6.10 A. J_{SC}, V_{OC}, FF, and η_{OPV} were determined and the results are included in Table 6.4. The SCL effect is clearly visible for the reference device reducing J_{SC} and η_{OPV} to 5.4 mA/cm^2 and 1.4 %, respectively. The same behaviour is observed for the **Type 3** device exhibiting a strong decrease of both parameters. Moreover, unusual high leakage currents are observed in the dark IV-measurements of the **Type 3** device in Figure 6.10 B. In contrast, the **Type 4** device performs significantly better as compared to the other two devices. J_{SC} is increased by 30 %, and η_{OPV} is increased by 36 % relative to J_{SC} and η_{OPV} of the reference cell.

EQE measurements were performed under short circuit conditions or at -4 V. Both measurements were carried out under white light bias with a power density of 80 mW/cm^2. A strong decrease of the carrier collection of the reference device is evident from the EQE spectrum in Figure 6.10 C. Moreover, the shape of the EQE spectrum reveals that the exciton dissociation is most efficient at 425 nm and 600 nm. The overall absorbance of the P3HT:PCBM film is low in this spectral region (cf. Figure 6.6), and hence, the SCL-effect is less pronounced. A similar effect is observed for **Type 3** devices. The EQE is even lower in a range of 500 nm – 620 nm as compared to the reference cell, which is attributed to parasitic plasmonic absorption by the M-Au$_{89}$ monolayer. In contrast, the EQE is significantly higher for **Type 4** devices. This points towards a more efficient extraction of holes at the Ag electrode. Measuring EQE under reverse bias conditions (-4 V) results in an increase of all EQE spectra as demonstrated in Figure 6.10 C. Under reverse bias conditions, photogenerated charges are extracted forcefully, and hence, optical losses are separated from electronic losses. Again, the **Type 3** device shows a clear drop of carrier generation in the spectral region of 500 nm – 620 nm further supporting the role of the M-Au$_{89}$ monolayer as a parasitic light absorption element in these devices. Surprisingly, no additional light absorption is detected for **Type 4** devices. Instead, the EQE spectrum is almost identical to the spectrum of the reference device.

Next, the ratio EQE(-4 V)/EQE(0 V) was also calculated. This allows a better representation of the charge carrier collection because parasitic absorption of any other layers than the P3HT:PCBM layer is eliminated.[255] Figure 6.10 D shows that the charge carrier collection of the reference and the **Type 3** devices is most efficient for photons with wavelengths of 400 nm – 580 nm which is in close agreement to the absorbance region of the P3HT:PCBM film (cf. Figure 6.6). Remarkably, the **Type 4** device does not follow this trend. Instead, an almost homogeneous exciton dissociation and charge collection, even for lower energy photons, is found. In conclusion, the horizontal trend of the EQE ratio reveals that the M-Au$_{89}$ monolayer acts as a light redistributing structure in **Type 4** devices, and thus, charge generation close to the Ag electrode enhances the performance of the device.

In summary, M-Au_{89} monolayers are successfully introduced into organic solar cell devices with inverted solar cell geometry. The plasmonic superstructures have similar surface coverages of plasmonic particles independent of the position in the layer stack of the devices. Plasmonic solar cells suffer from leakage currents and parasitic light absorption once the monolayer is integrated at any position below the P3HT:PCBM layer. Consequently, solar cells with an optimized active layer thickness are not enhanced by M-Au_{89} monolayers. However, plasmonic monolayers break the space charge limit of SCL-devices devices because they act as light-redistributing elements. This way, exciton dissociation close to the metal electrode results in a remarkable increase of the photocurrent by 30 %. In conclusion, plasmonic particles play an ambivalent role in organic thin film solar cells and they are not a panacea. In the future, mutually influencing factors such as dark leakage currents, parasitic absorption, near field enhancement, and light redistribution must be considered carefully for the design of thin film solar cell devices.

Chapter 7

Beyond Hexagonal Monolayers

Commonly, plasmonic superstructures beyond hexagonal monolayers such as honeycomb structures[256,257] or square lattices[258–260] are fabricated by top-down lithographic techniques. However, lithography is not suitable for large area surface patterning as it is often an expensive and time consuming process. Previously, self-assembled hexagonally ordered monolayers of PNIPAM-encapsulated gold nanoparticles were already prepared on the cm^2-scale. Here, it is shown that such monolayers can be used as a template for the fabrication of plasmonic superstructures beyond hexagonal monolayers. Therefore, two different strategies are investigated:

1. Sequential deposition of two monolayers on the same substrate.
2. Anisotropic deformation of a single hexagonal monolayer by transfer onto hydrophobic substrates.

7.1 Plasmonic Honeycomb Structures

The interparticle distance of Au-x-PNIPAM$_y$ monolayers on solid substrates is larger as compared to their hydrodynamic diameter (cf. Section 5.2.2). Motivated by this fact, such a monolayer was used as a template for the subsequent deposition of a second Au-x-PNIPAM$_y$ monolayer to create plasmonic honeycomb structures. In order to distinguish between particles of the first and the second monolayer in the final structure, it is clever to use different colloidal building blocks for each monolayer.

7.1.1 Building Blocks for Plasmonic Honeycomb Structures

Three different colloidal building blocks (Au_{75}@Au-PNIPAM$_{340}$, Au_{95}@Au-PNIPAM$_{316}$, and Ag_{100}@Au-PNIPAM$_{336}$) were chosen from the particle library for the fabrication of plasmonic honeycomb structures. The colloidal building blocks have almost identical hydrodynamic diameters, but they are different in terms of size and composition of their plasmonic cores.

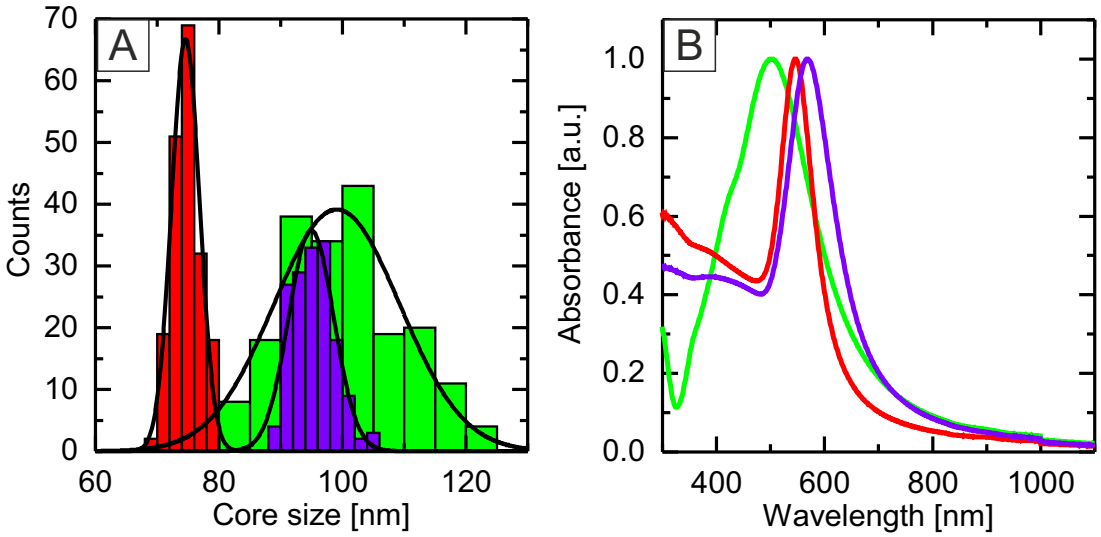

Figure 7.1. Characterization of colloidal building blocks for honeycomb structures. A, core size histograms of Au_{75}@Au- (red), Au_{95}@Au- (purple), and Ag_{100}@Au-x-PNIPAM$_y$ (green) obtained by TEM analysis. B, UV-Vis absorbance spectra of the particles in aqueous solution recorded at 25 °C. The spectra are normalized to the peak maximum for better comparison.

Figure 7.1 A shows size distribution histograms of the plasmonic cores of the core-shell particles obtained by TEM investigation. Average core diameters and standard deviations were obtained by fitting the data with Gaussian functions. d_c is 75 ± 2 nm, 95 ± 4 nm, and 100 ± 10 nm for Au_{75}@Au-, Au_{95}@Au-, and Ag_{100}@Au-x-PNIPAM$_y$, respectively. Narrow polydispersities of 3 % (Au_{75}@Au-x-PNIPAM$_{340}$) and 4 % (Au_{95}@Au-x-PNIPAM$_{330}$) were calculated for core-shell particles with overgrown gold cores using Equation 7.1. The PDI of Ag_{100}@Au-x-PNIPAM$_{336}$ is 10 % indicating a slight increase of heterogeneity of the particles.

$$PDI = \frac{\sigma_S}{d_c} \tag{7.1}$$

The optical properties of the particles were investigated by UV-Vis spectroscopy in dilute aqueous dispersion in Figure 7.1 B. Particles with overgrown gold cores show narrow dipolar plasmon resonances and λ_{LSPR} is at 547 nm and 568 nm, respectively. The LSPR peak maximum shifts towards longer wavelengths with increasing size of the gold cores, as expected. The LSPR of Ag_{100}@Au-x-PNIPAM$_{336}$ is at 497 nm and a small shoulder at approx. 420 nm reveals a weak quadrupolar contribution. The quadrupolar mode and the slightly increased PDI cause a higher full width half maximum ($FWHM$) of the LSPR as compared to the $FWHM$ of the Au_x@Au-x-PNIPAM$_y$ particles.

7.1.2 Fabrication of Plasmonic Honeycomb Structures

Plasmonic honeycomb structures were prepared by sequential deposition of two Ag_{100}@Au- or Au_{95}@Au-x-PNIPAM$_y$ monolayers on the same solid substrate (glass). Each monolayer was prepared by interface-mediated self-assembly as described in Section 5.2. For the sake of clarity, particle monolayers are denoted as M-Ag_{100} or M-Au_{95} and honeycomb structures are referred to as H-Ag_{100} or H-Au_{95}. After each deposition step, the plasmonic superstructures were investigated by AFM and UV-Vis spectroscopy.

Figure 7.2 A shows a representative AFM height image of a M-Ag_{100} template monolayer on glass. Large, single crystalline domains of hexagonally ordered particles are clearly visible. It is important to note that long-range order of the monolayer is a critical factor for the fabrication of honeycomb structures. The long-range order is improved if a dip-coater is used in order to collect the monolayer from the water surface. Details are provided in the Experimental Section 3.3.5. After collecting the first monolayer, the substrate is heated to 200 °C in order to strengthen the adhesion between the monolayer and the glass surface. By this process, particle detachment from the glass substrate is prevented if the substrate is immersed in water again. Next, a second freshly prepared monolayer is deposited onto the same substrate by dip-coating. After collecting the second monolayer, the substrate is carefully dried under ambient conditions. It is important to note that external heat treatment must not be applied after collecting the second monolayer as it would cause the formation of Moiré structures which will be discussed in Section 7.2.

Depositing a second monolayer on top of the M-Ag_{100} monolayer produces a plasmonic honeycomb structure which is demonstrated in Figure 7.2 B. Sequential deposition was also carried out using two M-Au_{95} monolayers. A similar honeycomb structure was obtained as evidenced in Figure 7.2 C. The formation of honeycomb structures is explained by assuming that the second particle monolayer is deposited into the "hollow" sites of the first monolayer on the substrate. The "hollow" sites are big enough in order to accommodate other core-shell particles because the PNIPAM shell of the particles of the first monolayer is fully collapsed after drying the substrate.

Next, binary plasmonic honeycomb structures (B-Ag_{100}-Au_{95}) were fabricated by depositing a M-Au_{95} monolayer on top of a M-Ag_{100} monolayer on the same solid substrate. Figure 7.2 D shows that the particle arrangement of the binary honeycomb structure is similar as compared to the non-binary counterparts. The formation of binary honeycomb structures points towards similar particle-particle interactions of Au_{95}@Au-PNIPAM$_{316}$ and Ag_{100}@Au-PNIPAM$_{336}$ particles. This is explained by the same shelling material (cross-linked PNIPAM) and the similar hydrodynamic diameters of the particles. Consequently, both core-shell particles form monolayers with almost identical interparticle distances on the water surface.

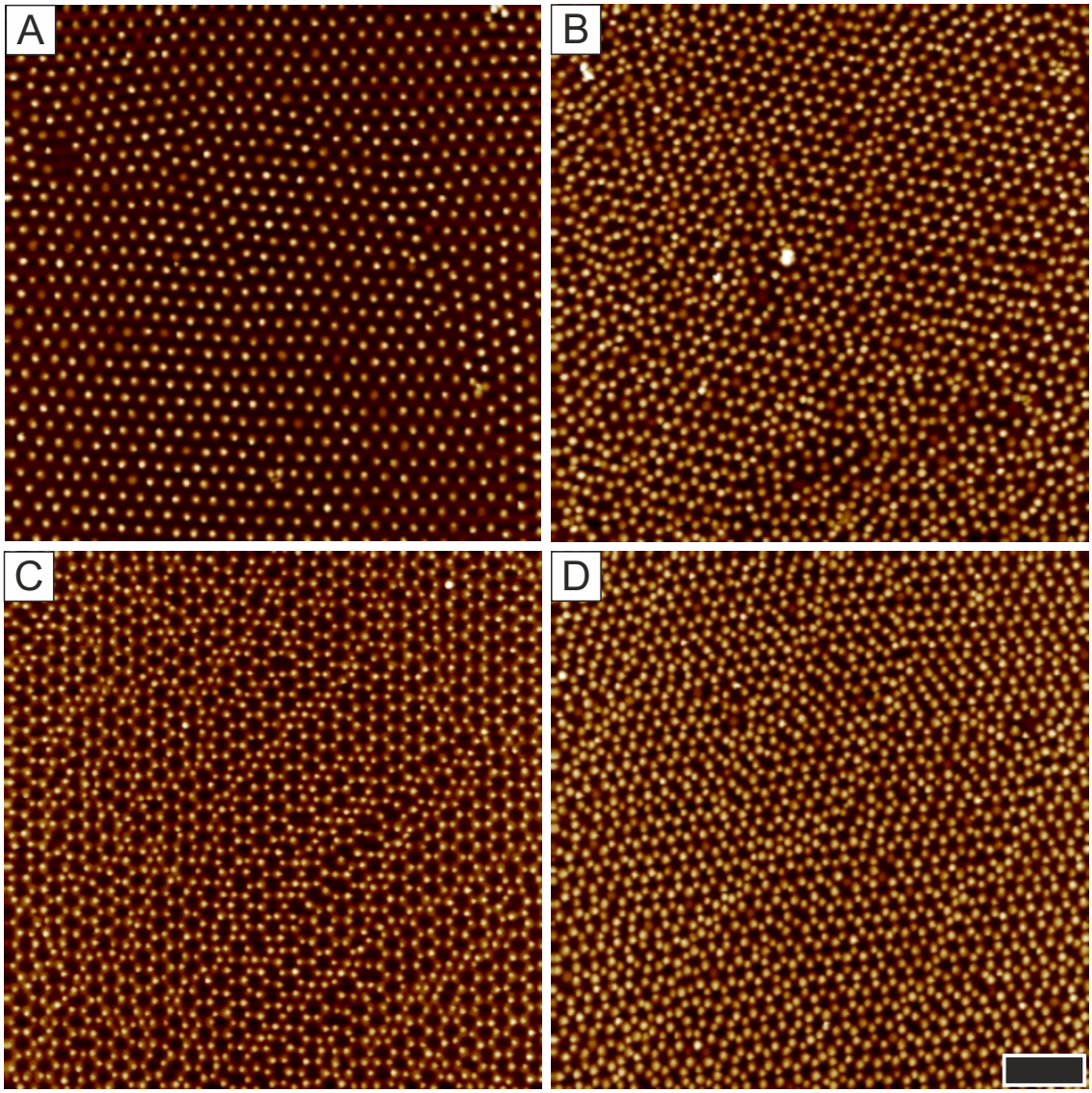

Figure 7.2. Fabrication of plasmonic honeycomb structures on glass. A, AFM height image of a M-Ag_{100} template monolayer. B, H-Ag_{100} honeycomb structure obtained by sequential deposition of two M-Ag_{100} monolayers on the same substrate. C, H-Au_{95} honeycomb structure fabricated in a similar way. D, binary honeycomb structure obtained by deposition of a M-Au_{95} monolayer on top of a M-Au_{100} monolayer. The scale bar is 2 μm.

Interparticle center-to-center distances were obtained by $g(r)$ analysis of the template monolayers and the finished honeycomb structures. The results are provided in Table 7.1. Almost identical interparticle distances and surface densities of plasmonic particles are found for M-Ag_{100}, M-Au_{95}, and the first monolayer of the binary structure (B-Ag_{100}). After deposition of the second particle monolayer, ρ almost doubles and smaller interparticle distances are determined for each honeycomb strucutre. A good match is found between the experimental (d_{c-c} (exp.)) and the theoretical interparticle distances of the honeycomb structures (d_{c-c} (calc.)). d_{c-c} (calc.) is obtained by multiplication of d_{c-c} of the template monolayers by a factor of $\frac{1}{\sqrt{3}}$.

Table 7.1. Interparticle distance, surface density of plasmonic particles, and position of the LSPR of monolayers and honeycomb structures.

Sample	d_{c-c} (exp.) [nm]	d_{c-c}(calc.) [nm]	ρ particles/μm^2	λ_{LSPR} [nm]
M-Ag_{100}	483 ± 58		4.9	520
H-Ag_{100}	294 ± 59	279	8.4	497
M-Au_{95}	482 ± 45		4.9	595
H-Au_{95}	305 ± 69	278	8.4	563
B-Ag_{100}[a]	488 ± 47		4.7	529
B-Ag_{100}-Au_{95}	282 ± 40	281	9.7	548

[a] First monolayer of the binary honeycomb structure.

The optical properties of the plasmonic honeycomb structures are investigated in Figure 7.3. M-Ag_{100} and M-Au_{95} monolayers show single plasmon resonance peaks at 520 nm and 595 nm, respectively. The resonance positions are red-shifted compared to λ_{LSPR} in solution due to the different refractive index environment around the particles. No signs of plasmon resonance coupling was observed between particles of the monolayers due to the rather large interparticle distances of approx. 483 nm. In contrast, the LSPRs of honeycomb structures are narrower and a strong shift of the LSPR towards smaller wavelengths is observable. It is assumed that both effects result from plasmon-plasmon coupling between neighbouring plasmonic cores due to the smaller interparticle distances of the honeycomb structures (approx. 300 nm) as compared to the monolayers (approx. 483 nm). This fact finds support from an earlier work by Volk et al. where plasmonic coupling was observed for a hexagonal lattice of Ag_{100}@Au-x-$PNIPAM_{336}$ particles with interparticle distances of approx. 360 nm.[202]

The absorbance spectrum of the binary honeycomb structure in Figure 7.3 C shows a broad plasmon resonance with a LSPR maximum at 548 nm and a small shoulder at approx. 472 nm. The absorbance of the honeycomb structure is stronger as compared to the individual M-Ag_{100} and M-Au_{95} monolayers which is in agreement with the results of the non-binary honeycomb structures in Figure 7.3 A and B. The shape of the LSPR is attributed to local plasmon resonance coupling between silver and gold cores influencing the LSPR intensity and position.[261]

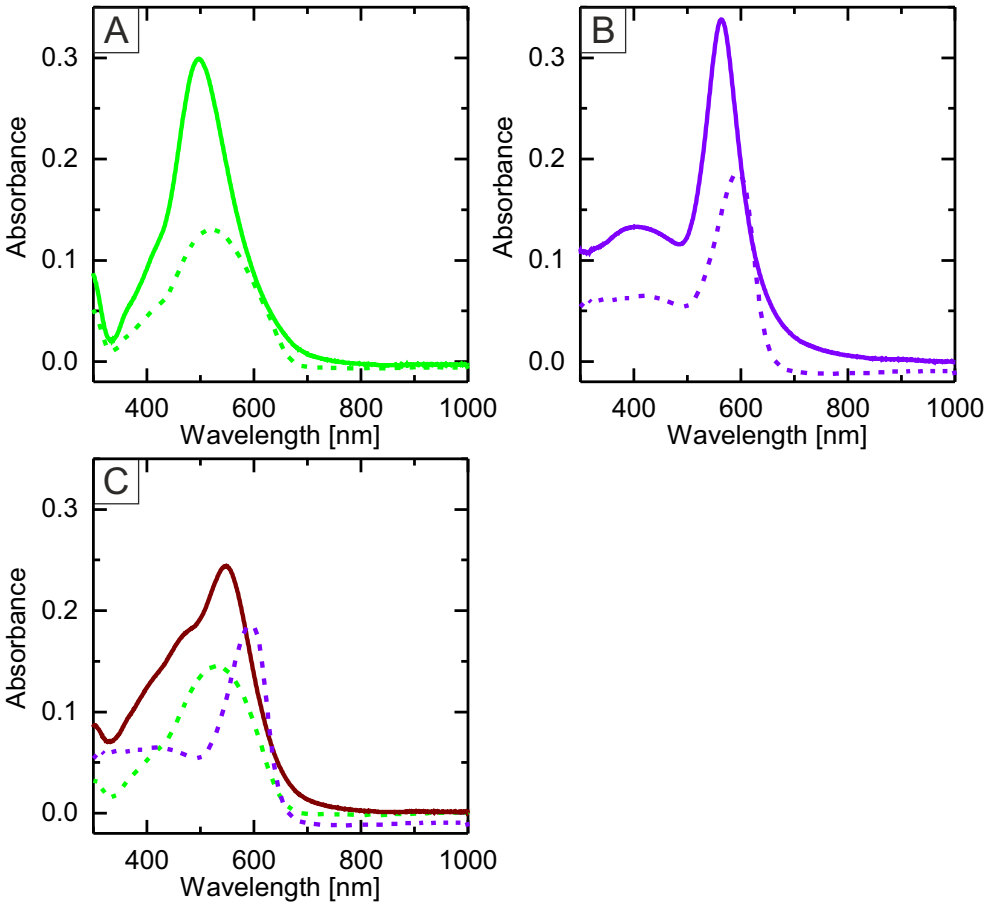

Figure 7.3. Investigation of plasmonic honeycomb structures by UV-Vis spectroscopy. A, B absorbance spectra of H-Ag_{100} (green solid line) and H-Au_{95} (purple solid line). Spectra of the template monolayers (M-Ag_{100} and M-Au_{95}) are included as dashed lines. C, absorbance spectrum of a binary honeycomb structure (brown solid line).

7.1.3 Structural Investigation of Binary Honeycomb Structures

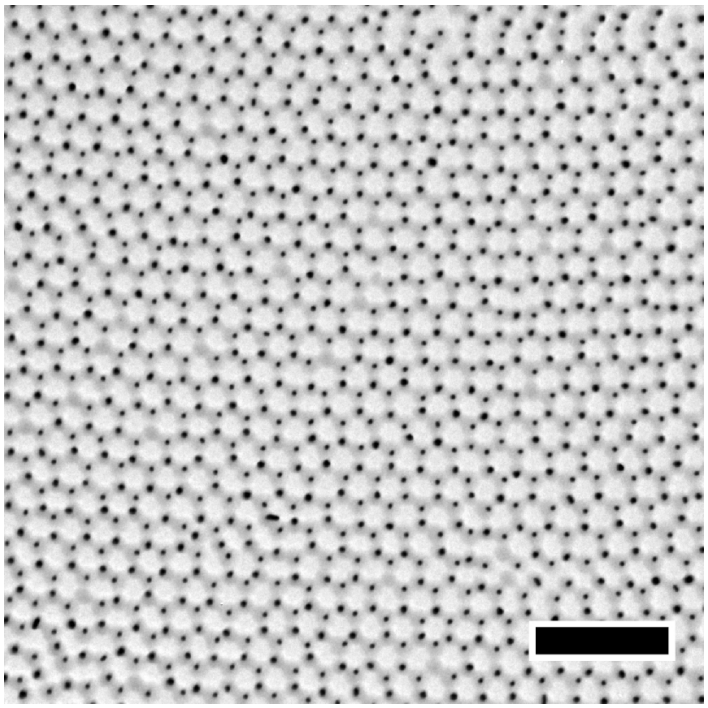

Figure 7.4. Binary honeycomb structure of Au_{75}@Au-x-PNIPAM$_{340}$ and Ag_{100}@Au-x-PNIPAM$_{336}$ particles on a TEM grid. The scale bar is 2 μm.

In order to elucidate the structural composition of binary honeycomb structures on the microscale, TEM, SEM, and high-resolution EDX mapping was carried out. This way, the exact location and composition of each metal core of the honeycomb structure can be identified. A binary honeycomb structure was fabricated by sequential deposition of a M-Au_{75} monolayer (d_c=75 nm) on top of a M-Ag_{100} monolayer (d_c=100 nm) on glass. Thus, particles of the honeycomb structure can be discriminated by their size *and* material. At first, EDX investigation of the binary structure failed due to the strong electron scattering by the glass substrate. Consequently, the binary honeycomb structure was prepared on a carbon coated TEM grid in order to reduce the electron excitation volume. Thus, the spacial resolution of the EDX mapping was increased.

Figure 7.4 shows a TEM image of the binary honeycomb strucutre. It is already possible to distinguish the particles by their size. The Ag_{100}@Au-x-PNIPAM$_{320}$ particles are the larger particles. Smaller particles correspond to the Au_{75}@Au-x-PNIPAM$_{340}$ particles. A closer look reveals that both particles are arranged in hexagonal sub-lattices, and it follows that every Au_{75}@Au-x-PNIPAM$_{340}$ particle is surrounded by three Ag_{100}@Au-x-PNIPAM$_{320}$ particles and vice-versa. Next, high-resolution SEM and EDX elemental mapping was carried out and the results are demonstrated in Figure 7.5. Figure 7.5 A shows a high-resolution SEM image of the binary honeycomb structure. The SEM image was acquired by an angle selective backscattered electron detector which allows for compositional imaging due to the energy difference of the backscattered electrons. Thus, the particles can be discriminated by their brightness. Brighter

particles are attributed to Au_{75}@Au-x-$PNIPAM_{340}$ particles and darker ones to Ag_{100}@Au-x-$PNIPAM_{336}$ particles due to the higher electron density of gold as compared to silver. The PNIPAM shell is invisible in the SEM images due to the weak electron contrast of the polymer. Elemental mapping by EDX confirms the binary composition of the honeycomb structure. Figure 7.5 B shows an overlay of the SEM image and the elemental map using only the Au Mα_1 emission lines (2.1 keV, red). It is clear that only one type of metal cores is highlighted by the EDX mapping. Conversely, if the mapping is performed using only the Ag Lα_1 emission lines (2.9 keV, green), the other group of metal cores is highlighted exclusively as demonstrated in Figure 7.5 C. Both metal cores form hexagonally ordered sub-lattices which is evidenced by the sixfold arrangement of the fundamental frequencies in the power spectra. It is important to note that the power spectra were obtained by FFT of the images using only the positions of the highlighted metal cores. Finally, EDX mapping using both emission lines recreates a honeycomb structure that is fully consistent with the original SEM image as demonstrated in Figure 7.5 D. Almost identical interparticle distances of 468 ± 63 nm and 467 ± 54 nm are obtained by $g(r)$ analysis of the particle positions of the hexagonal sub-lattices. These values match very close to the interparticle distances determined for honeycomb structures on glass (cf. Table 7.1).

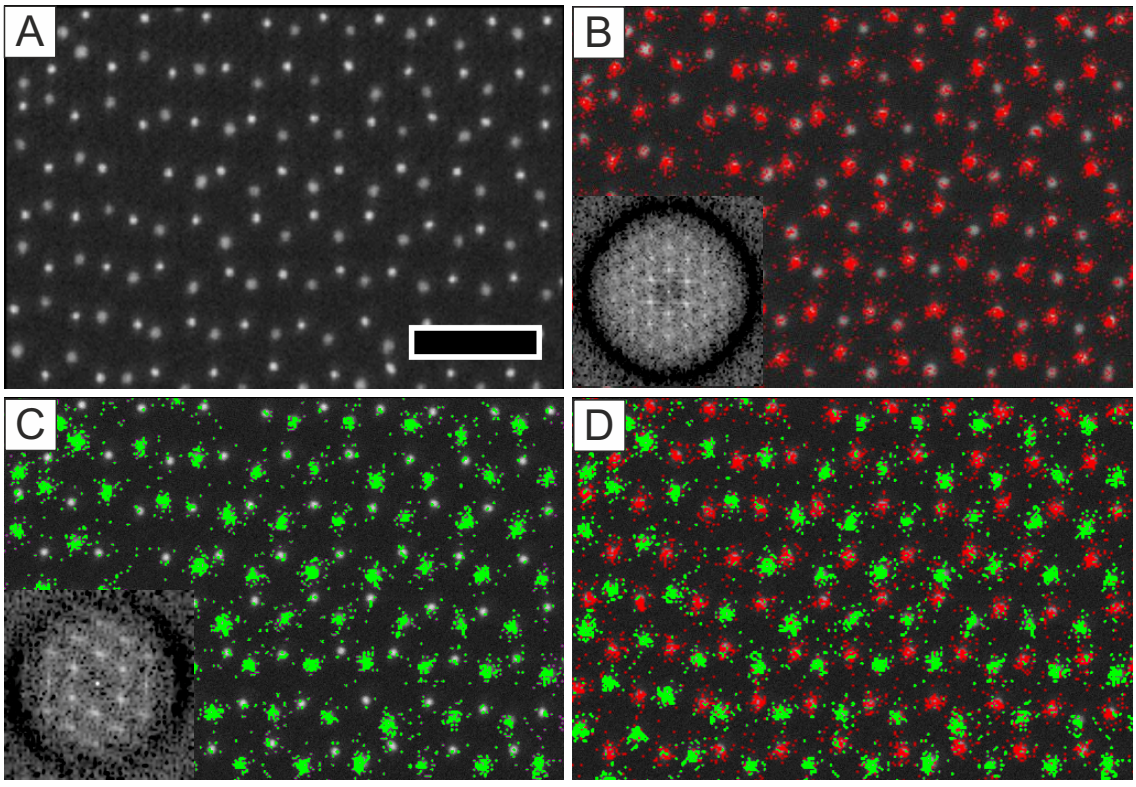

Figure 7.5. Investigation of a binary honeycomb structure on a TEM grid by high-resolution SEM and EDX mapping. A, SEM image of the superstructure composed of Au_{75}@Au-x-$PNIPAM_{340}$ and Ag_{100}@Au-x-$PNIPAM_{320}$ particles. The scale bar is 1 μm. B, C, EDX mapping using only the Au Mα_1 emission lines (B) or Ag Lα_1 emission lines (C). D, overlay of both elemental maps. The insets in B and C show power spectra of the images computed from the highlighted particle positions.

In conclusion, the sequential deposition of two Au-x-PNIPAM$_y$ monolayers on the same substrate produces plasmonic honeycomb superstructures. This deposition process also allows for the fabrication of binary honeycomb structures. Investigation of binary honeycomb structure by EDX mapping reveals hexagonally ordered sub-lattices of the two different PNIPAM-encapsulated plasmonic particles, and the exact location and composition of each metal core in the honeycomb structure is resolved.

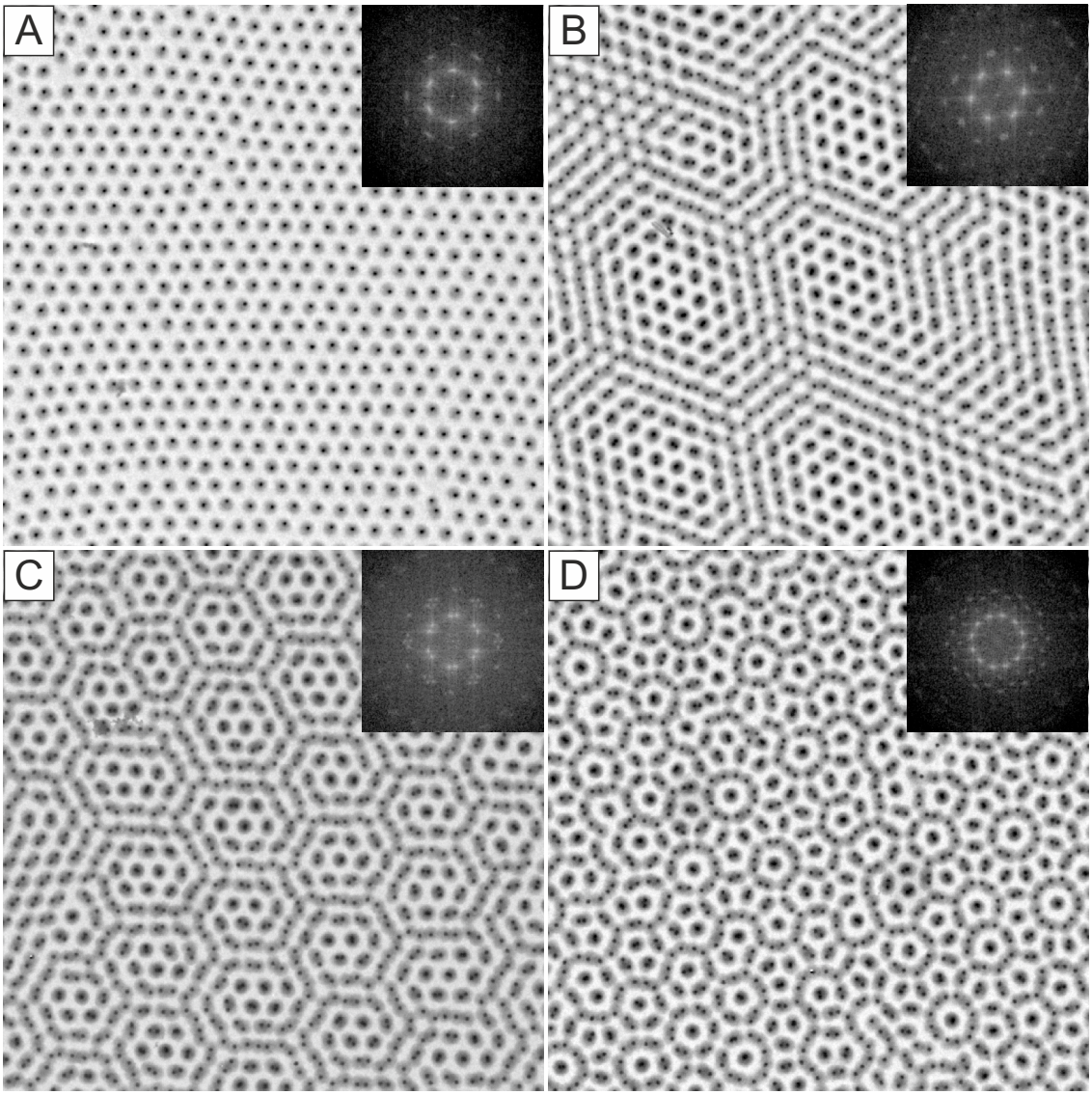

Figure 7.6. Different Moiré structures obtained by sequential deposition and rotation of two M-Au$_{75}$ monolayers against each other. A, TEM image of the template monolayer. B – D, Moiré structures formed by rotation angles of 8° (B), 14° (C), and 31°(D) of the second monolayer. The scale bar is 2 μm. The insets show power spectra calculated for each image.

7.2 Fabrication of Moiré Structures

Honeycomb structures are the result of a hexagonal monolayer of cross-linked PNIPAM-encapsulated particles settling into the hollow sites of another hexagonal monolayer of the same particles. However, if the second monolayer is rotated against the first one during the deposition process, Moiré structures are formed instead of honeycomb structures. Originally, rotation of monolayers was discovered as a side effect during the preparation of honeycomb structures. It frequently occurred once the substrate was dried quickly after sequential deposition of the second monolayer. For honeycomb structures, rotation was avoided by immersing the substrate normal to the water surface and letting the substrate dry under ambient conditions.

However, if the drying process is accelerated by using a stream of hot air, for example, Moiré structures are formed. Moiré structures were fabricated on carbon coated TEM grids (Figure 7.6, $\theta_c \approx 79°$) as well as on hydrophilic glass substrates (cf. Appendix, Figure 10.6, $\theta_{c,glass} \approx 0°$), although both substrates have completely different contact angles. It follows, that the surface chemistry of the substrate does not play a major role for the formation of the Moiré structures.

Changing the drying process does not affect the particle arrangement of the M-Au_{75} template monolayer significantly which is evidenced by the presence of single-crystalline hexagonally ordered domains of Au_{75}@Au-x-$PNIPAM_{340}$ particles in Figure 7.6 A. However, the second monolayer is no longer deposited exactly into the threefold hollow sites of the first monolayer if the substrate is dried quickly after the deposition process. Instead, different Moiré structures form as the two monolayers are rotated against each other by an arbitrary rotation angle (α) which is shown in Figure 7.6 B – D.

The Moiré structure in Figure 7.6 B is an instructive demonstration of the soft pair-interaction potential of the cross-linked PNIPAM-encapsulated nanoparticles. Particles are found that are either arranged in a shell-to-shell configuration separated by the hydrogel shell, or densely packed in a core-to-core configuration. The core-to-core configuration is possible because the PNIPAM hydrogel shells can deform and interpenetrate each other partially. Particles in a core-to-core configuration appear darker in the TEM image due to their higher mass contrast. FFTs of the Moiré structures in Figure 7.6 B – D reveal 12 fundamental peaks centered around the zero frequency spot of the power spectrum. It is important to note that the twelve peaks in Figure 7.6 B can only be distinguished upon close magnification of the FFT pattern. Similar structures were found by Luchnikov et al. for superimposed films of block-copolymers, and the FFT pattern was explained by the convolution of two Fourier transforms of single polymer films which are rotated against each other by a certain rotation angle.[262]

Hence, the angle between the fundamental peaks of the FFT pattern corresponds directly to the rotation angle α of the two M-Au_{75} monolayers forming each Moiré structure in Figure 7.6. α was measured from the angular splitting of the FFT peaks. α is 8°, 14°, and 31° for the Moiré structures in Figure 7.6 B – D. In the following, Moiré structures are denoted as P_8, P_{14}, or P_{31} according to their rotation angles. Since it is known that each Moiré structure was prepared from the overlay of two monolayers and that the particles of each monolayer are arranged in

hexagonal lattices, the theoretical periodicity (D_{theo}) of a Moiré structure is given by Equation 7.2[263]

$$D_{theo} = \frac{d_l}{2\ \sin(\frac{\alpha}{2})} \tag{7.2}$$

where d_l is the lattice constant of one hexagonally ordered monolayer forming the Moiré structure. Since both monolayers are fabricated by interface-mediated self-assembly using the same particles and the same preparation conditions, d_l is supposed to be identical for both monolayers. Unique Moiré structures are only observed for $0° < \alpha \leq 30°$. The structures repeat for higher rotation angles because of the hexagonal symmetry of the two monolayers. This leads to the following boundary conditions given by Equation 7.3 and 7.4

$$\alpha - 60° n \quad \text{if } 60° n < \alpha \leq 60° (n + 0.5) \tag{7.3}$$

$$60° (n + 1) - \alpha \quad \text{if } 60° (n + 0.5) \leq \alpha < 60° (n + 1) \tag{7.4}$$

for n=0, 1, 2...[264] For instance, rotation angles of 8°, 52°, 68°, and 112° will produce the same Moiré structure. In addition, rotation angles which are multiples of 60° will produce two identical overlapping lattices. The periodicity of the P_8 and P_{14} Moiré structures (D_P) is obtained by analysis of their autocorrelation functions as demonstrated in the Appendix in Figure 10.7. D_P is $3.595 \pm 0.350\,\mu$m and $2.024 \pm 0.226\,\mu$m for P_8 and P_{14}, respectively. D_{theo} is $3.622 \pm 80\,$nm and $1.972 \pm 53\,\mu$m for P_8 and P_{14}, respectively. Consequently, a close match is found between D_P and D_{theo} for both Moiré structures. It also follows from Equation 7.2 that the periodicity of the Moiré structures decreases for increasing rotation angles. This fact can be nicely seen in Figure 7.6 B and C, where the motif size of the Moiré structures decreases from P_8 ($\alpha = 8°$) to P_{14} ($\alpha = 14°$).

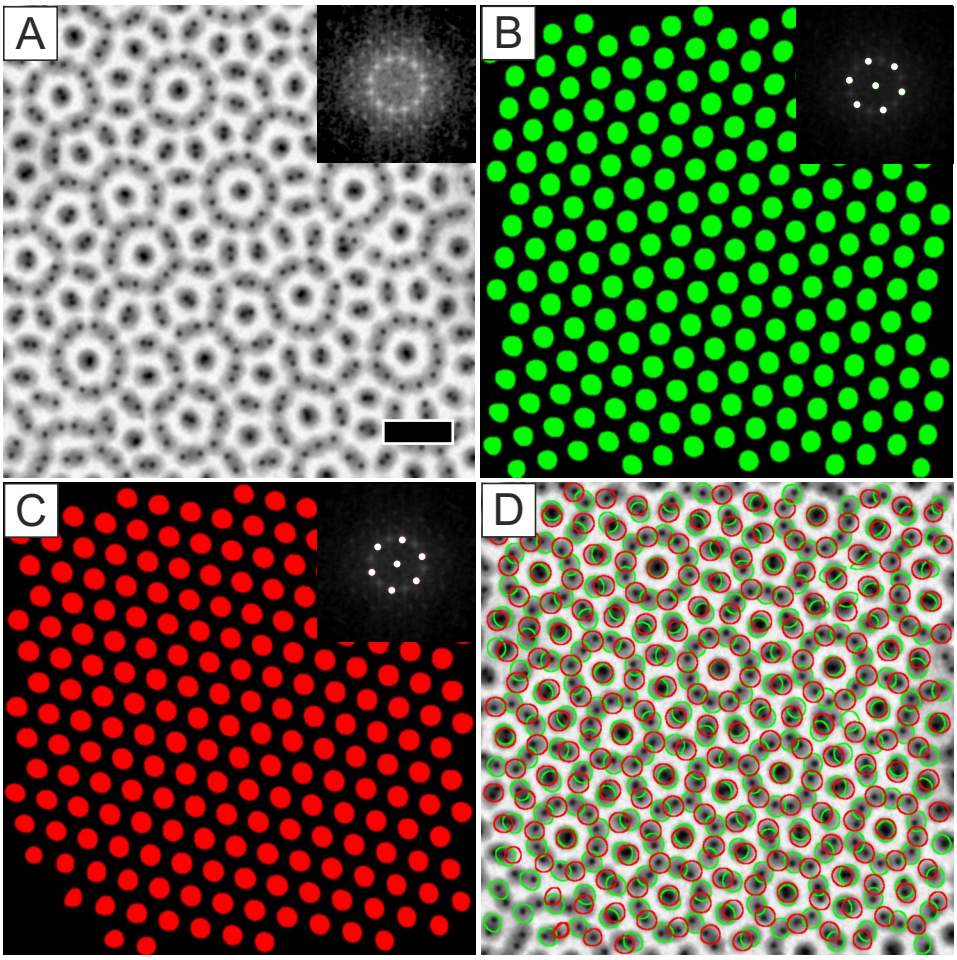

Figure 7.7. Analysis of the P_{31} Moiré structure by FFT-filtering. A, original TEM image. The inset shows the FFT of the image and the scale bar is 1 μm. B, C Reconstructed hexagonal sub-lattices obtained by FFT filtering of every other peak of the 12-fold FFT pattern in A. Both lattices are rotated against each other by 31°. D, overlay of the positions of the hexagonal lattices B and C with the original TEM image.

The interpretation of the P_{31} Moiré structure in Figure 7.6 D is more complex. The particles are ordered but a clear periodicity is hard to find. Fourier analysis reveals a 12-fold symmetry of the fundamental peaks in the power spectrum which is incommensurable with the classic crystallographic restriction theorem.[265] In order to identify the two monolayers that form the Moiré structure, Fourier filtering was carried out. Fourier filtering was performed for a magnified region of Figure 7.6 D using the freeware ImageJ, and the results are demonstrated in Figure 7.7. At first, the power spectrum of the TEM image is computed (inset of Figure 7.7 A). Next, every other peak of the fundamental frequencies is selected by white circles (pixel value = 255) followed by inverse FFT of the power spectrum. By this process, a hexagonal lattice is created as demonstrated in Figure 7.7 B. Another hexagonal lattice is created by selecting the other set of fundamental frequencies from the FFT pattern of Figure 7.7 A which is shown in Figure 7.7 C. Both lattices are rotated against each other by 31° which is equal to the angle between two peaks of the fundamental frequencies of the power spectrum in Figure 7.7 A. Figure 7.7 D shows an overlay of the two recreated hexagonal lattices and the original image. A perfect match is

found. It follows that each particle position can be assigned to a hexagonal lattice, and that the Moiré structure of Figure 7.7 is formed by two hexagonally ordered M-Au_{75} monolayers, rotated against each other by 31°. This Moiré structure is highly interesting, because the combination of two hexagonal periodic lattices can be used for the construction of a quasiperiodic dodecagonal tiling as demonstrated by Stampfli.[266] He used the grid-projection method in order to create a quasiperiodic tiling. Therefore, two hexagonal grids are drawn, rotated against each other by 90° (which is equal to a 30° rotation for hexagonal layers), and combined in one grid. The dual of this grid is a quasiperiodic tiling that contains three different tiles: equilateral triangles, squares and rhombs with an acute angle of 30°.

Figure 7.8 A and C demonstrate how such a quasiperiodic tiling is constructed by the overlay of two hexagonal grids rotated against each other by 30°. The overlay creates a pattern consisting of overlapping points as well as isolated single points. A quasiperiodic tiling of the pattern is possible using strongly overlapping points as the vertices for the three different tiles as illustrated in Figure 7.8 C. The pattern of Figure 7.8 A closely resembles the P_{31} Moiré structure in Figure 7.8 B. The Au_{75}@Au-x-$PNIPAM_{340}$ particles are arranged in core-to-core and shell-to-shell configurations. The core-to-core configuration creates strongly overlapping particle pairs. They are used as lattice points for the vertices of the Stampfli tiling. Consequently, tessellation of the Moiré structure of Figure 7.8 B is partially possible as demonstrated in Figure 7.8 D. The resemblance to a quasiperiodic tessellation is striking, although the pattern is not completely quasiperiodic yet. This stems from the fact that different motifs are found for the same tiles in Figure 7.8 D which is incommensurable with a quasicrystalline tiling.

In summary, Moiré structures are produced by the rotation of two hexagonally ordered monolayers against each other. The rotation angle determines the motif size of the Moiré structures, and the motif size decreases for increasing rotation angles. The Moiré structure formation is driven by the soft interaction potential of cross-linked PNIPAM-encapsulated gold nanoparticles allowing for particle-particle arrangements on different lengthscales.

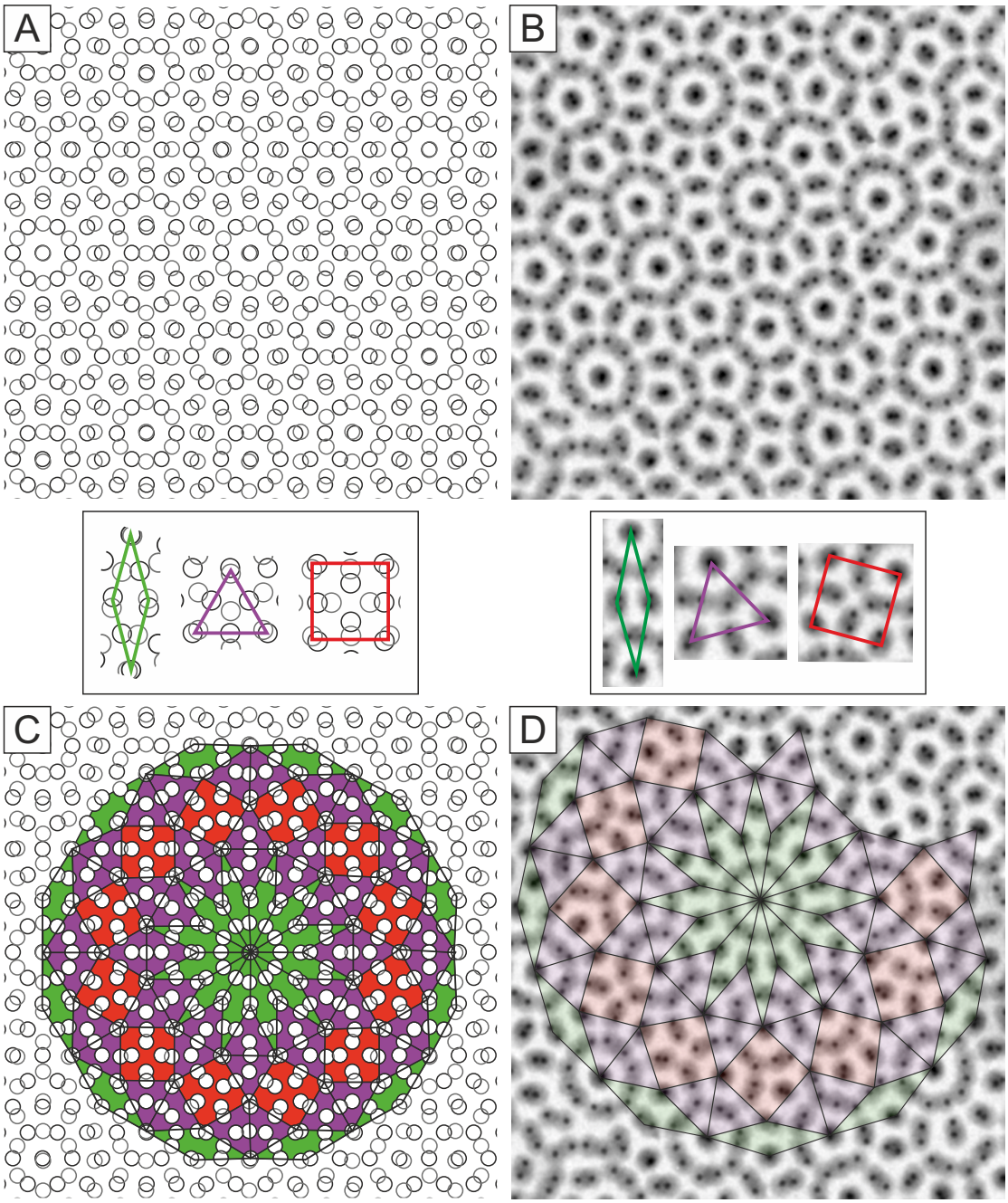

Figure 7.8. Tessellation of Moiré structures. A, C, formation (A) and quasiperiodic tiling (C) of a Moiré structure. The structure is formed by the overlay of two periodic hexagonal lattices rotated against each other by 30°. The insets show the three different tiles and motifs associated with each tile. B, D, P_{31} Moiré structure (B) and tiling of the pattern using triangles, squares and rhombs. The insets show the different tiles and the motifs associated with each of the tiles.

7.3 Anisotropic Deformation of Hexagonal Monolayers

Colloidal spheres crystallize into two-dimensional hexagonally ordered lattices at the air/water interface because it is the favoured minimum free energy position of the particles.[79,173] Yet, such a monolayer can be used for the preparation of other two-dimensional Bravais lattices by anisotropic deformation. The deformation requires two minor modifications to the monolayer deposition process:

1. A slightly hydrophobic substrate with a contact angle of approx. 60°.
2. An immersion angle normal to the water surface.

At first a M-Au_{95} monolayer was prepared using interface-mediated self-assembly. Next, the monolayer was transferred onto hydrophobic glass by immersing the substrate through the monolayer into the water subphase. Once the monolayer came in contact with the substrate it stuck to the glass surface and was pulled underwater. After the substrate was in the water subphase, any remains of the monolayer on the water surface were removed by a spreading agent such as *l*-$PNIPAM_{40k}$. Thus, a double deposition of M-Au_{95} monolayers was avoided once the glass substrate was retracted from the water subphase. Figure 7.9 shows AFM height images of M-Au_{95} monolayers after transfer onto hydrophobic HDMS-functionalized glass substrates ($\theta_{c,glass} \approx 60°$). The samples are denoted as $S_{90°-n}$ according to the immersion angle of the substrate. For reference, samples with an immersion angle of 0° were also prepared ($S_{0°}$).

If the immersion angle is 0° and contact angle, immersion direction, and immersion speed are kept constant, a hexagonally ordered M-Au_{95} monolayer is obtained as evidenced by the $S_{0°}$ monolayer in Figure 7.9 A. No deformation of the monolayer is observed, and the structure is identical to monolayers deposited onto hydrophilic substrates (cf. Section 5.2). However, once the substrate is immersed normal to the water surface centered rectangular-like ($S_{90°-1}$) as well as square-like particle arrangements ($S_{90°-2}$) are discovered as evidenced by AFM measurements in Figure 7.9 B and C. Analysis of the monolayers by their autocorrelation functions reveals that all structures are highly ordered which can be seen from the symmetric arrangement of the fundamental peaks in Figure 7.9 D – F. The central peak of G corresponds to the average particle diameter which is identical in all three images since the same particles (Au_{95}@Au-x-$PNIPAM_{316}$) were used for the fabrication of the monolayers.

In Figure 7.9 D, G of S_0 reveals a ring of six first order satellite peaks around the central peak, indicating that the monolayer has a hexagonal symmetry. Higher order satellite peaks are also observed reflecting the long-range order of the monolayer. The intensity of the higher order peaks decays with increasing distance from the central peak due to imperfections of the lattice structure such as local point defects, lattice distortions or directional anisotropies. The distance between the central peak and the first order satellite peaks is equal to the nearest neighbour distances, and hence, it can be used to determine the lattice parameters a, b, and θ of the monolayer. It is found that $|a| \approx |b|$ and $\theta \approx 60°$ which is characteristic for a two-dimensional hexagonal lattice. Table 7.2 summarizes the lattice parameters extracted from G for all monolayers.

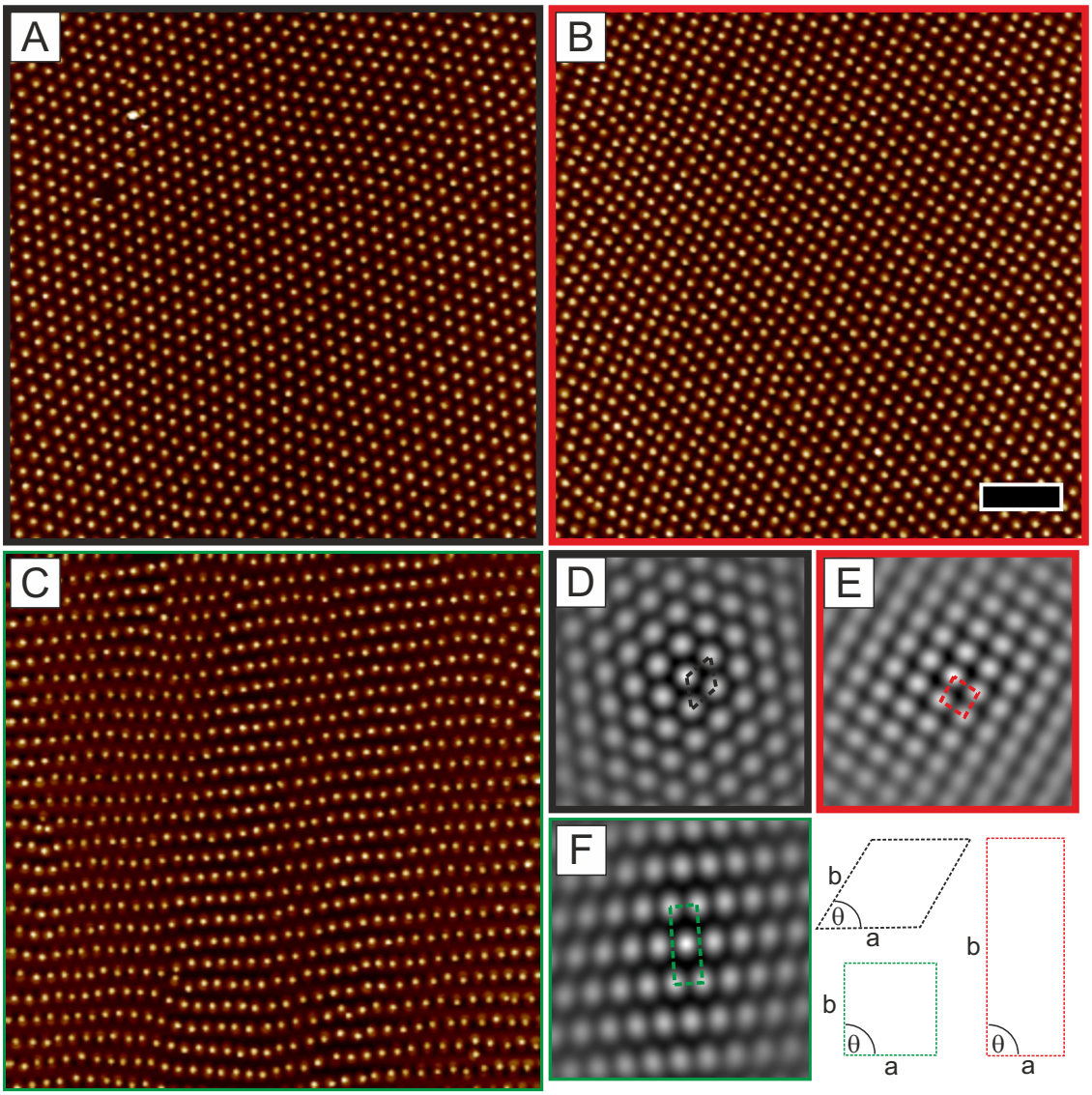

Figure 7.9. Influence of the deposition process on the structure of a M-Au_{95} monolayer. A, hexagonally ordered monolayer fabricated by an immersion angle of 0°. B, C, square-like (B), and rectangular-like (C) lattices obtained by an immersion angle of 90°. The scale bar is 2 μm. D – F, central region of G calculated from the AFM images A – C. The unit cells of each monolayer are indicated in each image.

Table 7.2. Lattice parameters derived from autocorrelation functions of $S_{0°}$ and $S_{90°}$.

Sample	a [nm]	b [nm]	θ [°]	proposed unit cell
S_0	451 ± 9	453 ± 10	58 ± 2	hexagonal
$S_{90°-1}$	408 ± 6	390 ± 8	90 ± 5	square
$S_{90°-2}$	393 ± 7	1101 ± 8	89 ± 3	centered rectangular

G of $S_{90°-1}$ reveals a square-like arrangement of the fundamental peaks in Figure 7.9 E. The fundamental peaks are well pronounced whereas higher order peaks, further away from the central peak, are increasingly smeared out. This points towards a high correlation of the local particle positions which decreases for larger distances. A square-like unit cell is found with $|a| = 1.05\,|b|$ and $\theta \approx 90°$ which is close to an ideal square lattice. Another non-hexagonal arrangement of the first order peaks is clearly visible for the S_{90-2} monolayer in Figure 7.9 F. A unit cell is found with $|a| < |b|$ and $\theta \approx 90°$ characteristic of a two-dimensional centered rectangular-like lattice. An anisotropic smearing of the higher order peaks of G indicates directional anisotropy of the lattice which is also observed in the corresponding AFM image. In this case, the degree of order in the vertical direction is slightly higher as compared to the degree of order in the horizontal direction of the lattice.

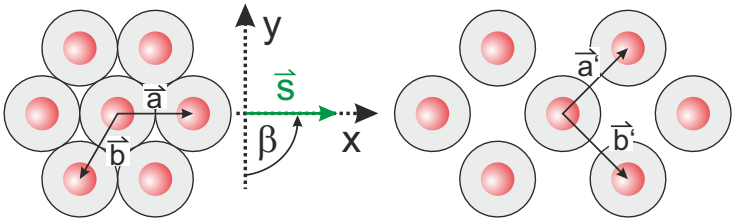

Figure 7.10. Deformation of a hexagonal monolayer of cross-linked PNIPAM-encapsulated particles by uniaxial stretching. The hexagonal unit cell of the monolayer is defined by the two vectors $\vec{a}$ and $\vec{b}$. β is the stretching angle and $\vec{s}$ the stretching vector of the unit cell. Stretching along $\vec{a}$ produces a square lattice.

The formation of a non-hexagonal particle monolayer by anisotropic deformation of a hexagonal monolayer is illustrated in Figure 7.10. The unit cell of the hexagonal monolayer is defined by the two vectors $\vec{a}$ and $\vec{b}$. In the sketch, the core-shell particles are closely packed which corresponds to a monolayer of PNIPAM-encapsulated particles floating at the water interface where the PNIPAM shell is highly swollen by water. Transfer onto a hydrophobic glass substrate induces an uniaxial stretching of the monolayer with a stretching vector ($\vec{s}$) and a stretching angle (β). By this process, a deformed non-close packed particle monolayer is produced. This hypothesis finds support from recent work by Mauer et al.[267] They reported an almost identical fabrication method for the preparation all two-dimensional Bravais lattices using poly(n-butyl acrylate-*co*-methyl methacrylate) colloids. It was proposed that the lattice type of the monolayer is fully defined by the transfer direction and the stretching factor $s = |\vec{s}|$ of the original hexagonal monolayer.

The monolayer transformation process is described mathematically by a sequence of rotation, stretching, and back rotation. Each transformation is defined by its own matrix. The rotation matrix (R_β) and the stretching matrix (T_s) are given by Equation 7.5 and 7.6[267]

$$R_\beta = \begin{bmatrix} \cos\beta & -\sin\beta \\ \sin\beta & \cos\beta \end{bmatrix} \tag{7.5}$$

$$T_s = \begin{bmatrix} 1 & 0 \\ 0 & S \end{bmatrix} \tag{7.6}$$

and the final transformation matrix $T = R_\beta \circ T_s \circ R_{-\beta}$ is given by Equation 7.7

$$T = \begin{bmatrix} \cos^2\beta + \sin^2\beta \cdot S & \sin\beta \cdot \cos\beta \cdot (1-S) \\ \sin\beta \cdot \cos\beta \cdot (1-S) & \cos^2\beta \cdot S + \sin^2\beta \end{bmatrix} \tag{7.7}$$

Thus, the vectors of deformed lattice $\vec{a'}$ and $\vec{b'}$ can be calculated using Equation 7.8 and 7.9

$$\vec{a'} = T \circ \vec{a} \tag{7.8}$$

$$\vec{b'} = T \circ \vec{b} \tag{7.9}$$

Consequently, the square-like lattice in Figure 7.9 B ($|a| \approx |b|$, $\theta \approx 90°$) is obtained by stretching the hexagonal M-Au_{95} monolayer along one of the vectors of the hexagonal unit cell ($\vec{a}$ or $\vec{b}$) with $s = |\vec{s}| = 1.73$ and $\beta = 30°$. Similar structures are observed for $|\beta \pm 60° \, n|$ because of the sixfold rotation symmetry of the hexagonal monolayer. n is an integer. The centered rectangular-like lattice ($|a| \neq |b|$, $\theta \approx 90°$) in Figure 7.9 C results from a stretching angle of 0° and an arbitrary stretching factor.

In summary, centered-rectangular and square-like monolayers complete the potpourri of plasmonic superstructures fabricated in this work by self-assembly of cross-linked PNIPAM-encapsulated nanoparticles. Representative examples of all superstructures are provided in Figure 7.11. The structure formation is driven by the soft pair-interaction potential of the core-shell particles allowing for particle arrangements on different lengthscales. Hexagonally ordered monolayers are fabricated by interface-mediated self-assembly. The monolayers are transferable onto many different substrates such as plain glass or carbon-coated TEM grids (Figure 7.11 A). However, slight modifications to the monolayer deposition process have tremendous influence on the particle arrangement. Sequential deposition of two hexagonally ordered monolayers on the same substrate leads to honeycomb structures (Figure 7.11 B). Moiré structures are obtained by the same process if both monolayers are rotated against each other. In this case, even quasiperiodic particle arrangements might be possible for rotation angles close to 30° (Figure 7.11 C). Finally, manipulating contact angle and immersions direction of the substrate induces an anisotropic

deformation of the hexagonal monolayer during the transfer process onto the substrate. Thus even square-like lattices can be fabricated as shown in Figure 7.11 D.

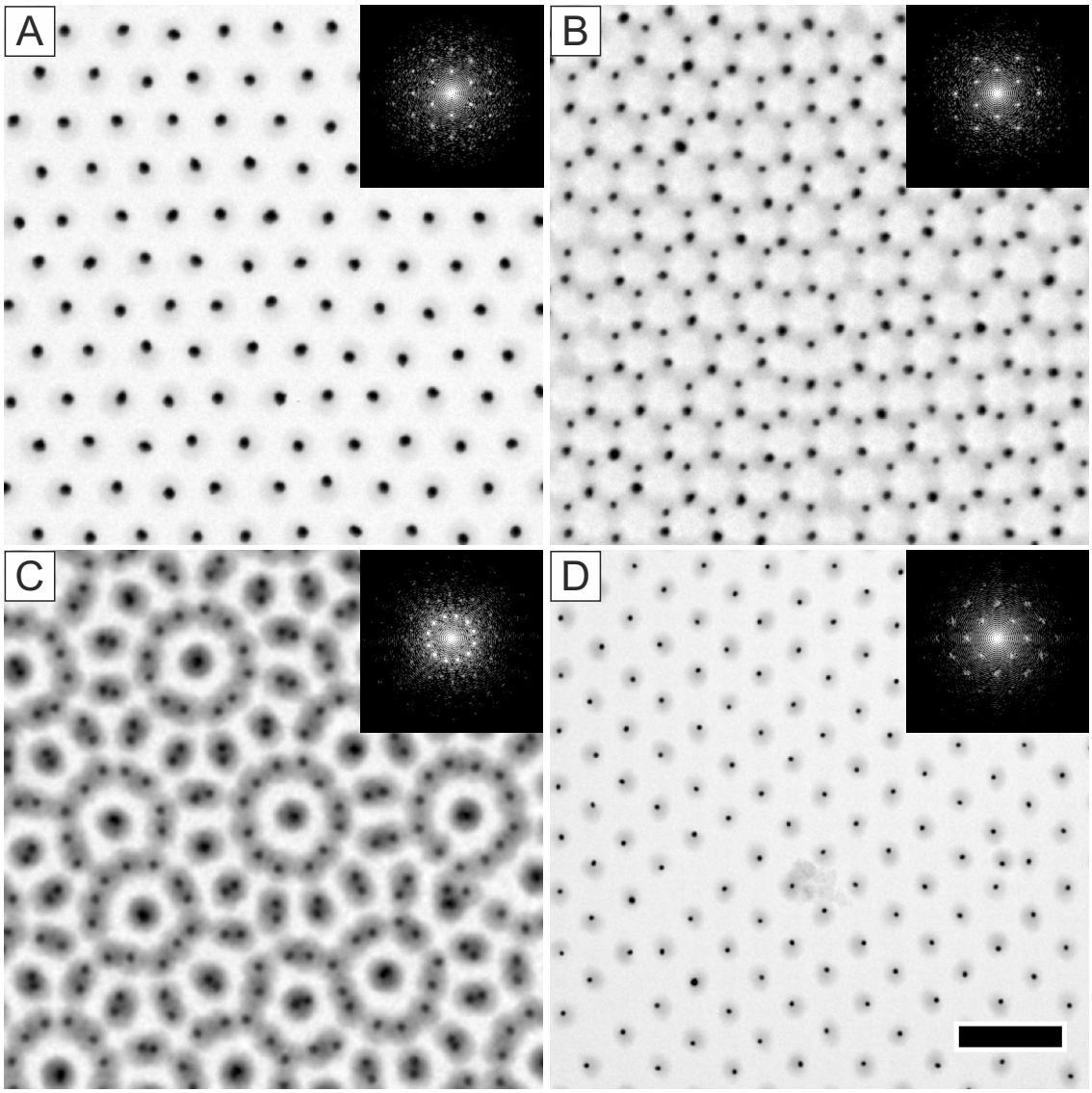

Figure 7.11. Potpourri of plasmonic superstructures prepared by interface-mediated self-assembly of cross-linked PNIPAM-encapsulated nanoparticles. A, hexagonally ordered monolayer obtained by single deposition onto a TEM grid. B, honeycomb structure fabricated by sequential deposition of two monolayers onto the same substrate. C, Moiré structure formed by a rotation angle of 30° between two hexagonal monolayers. D, square-like lattice fabricated by anisotropic stretching of a hexagonally ordered particle lattice. The insets show FFT of each image. The scale bar is 1 μm.

Chapter 8

Conclusion

This work describes the preparation of plasmonic superstructures via self-assembly of colloidal building blocks. The four key achievements are:

1. Synthesis of a library of colloidal building blocks with tunable plasmon resonance position.
2. Fabrication of hexagonally ordered monolayers with exceptional long-range order and controllable interparticle spacing on the cm^2-scale.
3. Integration of plasmonic superstructures into organic thin film solar cell devices. The photocurrent of space-charge limited devices increases by 30 %.
4. Fabrication of a potpourri of plasmonic superstructures: plasmonic honeycomb structures, Moiré patterns, square, and centered rectangular lattices.

1. A library of colloidal building blocks was prepared using plasmonic nanoparticles encapsulated by polymer shells. Size and composition of the plasmonic nanoparticles and the polymer shell were investigated as design parameters for colloidal building blocks. Gold nanoparticles encapsulated by non-cross-linked PNIPAM shells were produced by ligand exchange with α-trithiocarbonate-ω-carboxyl terminated PNIPAM chains. The PNIPAM ligands successfully stabilised a large variety of gold nanoparticles. Three different ligands of 9.5 kg/mol, 40 kg/mol, and 82 kg/mol were synthesized by RAFT polymerization and used for ligand exchange reactions with citrate-stabilized gold nanoparticles of 15 nm – 53 nm in diameter. After the ligand exchange reaction, homogeneous PNIPAM shells were observed around each gold nanoparticle by TEM. DLS measurements revealed a consistent increase of the PNIPAM shell with increasing molecular weight of the PNIPAM ligands. The ligand shell also enhanced the colloidal stability of the gold nanoparticles. Below the LCST of PNIPAM, the core-shell particles were stabilized through steric interactions provided by the PNIPAM chains. Additionally, negative surface charges originating from the ω-carboxyl function of the PNIPAM chains provided electrostatic repulsion at neutral pH. Decreasing the pH to 2.7 – 3.0 led to protonation of the carboxyl functions, and thus, surface charges close to zero were measured. At this point, temperature-mediated phase transfer of the particles was possible due to the LCST behaviour of PNIPAM. Increasing the temperature

to 60 °C led to a quantitative transfer of the particles from water to chloroform. Phase transfer to chloroform occurred because it was a much better solvent for the PNIPAM-encapsulated particles at this temperature. The particles did not aggregate after transfer to chloroform as evidenced by spectroscopic investigations. The phase transfer was fully reversible upon lowering the temperature to 4°C. Absorbance measurements revealed that the phase transfer was quantitative with efficiencies close to 100 % each time.

Ligand exchange with α-trithiocarbonate-ω-carboxyl terminated PNIPAM provided non-cross-linked polymer shells with thicknesses as large as 37 nm. In order to further increase the shell thickness, cross-linking was introduced to ensure a stable and homogeneous encapsulation of the gold nanoparticles. Cross-linked PNIPAM hydrogel-encapsulated gold nanoparticles were prepared by free radical seeded precipitation polymerization of NIPAM and BIS in the presence of gold nanoparticles. After the reaction, each nanoparticle was encapsulated by a homogeneous PNIPAM shell as evidenced by TEM. The thickness of the PNIPAM hydrogel shell was adjusted by the monomer feed of each reaction. Three types core-shell particles with increasing hydrogel shells were synthesized, and DLS revealed overall hydrodynamic dimensions of 208 nm, 326 nm, and 508 nm, respectively. Next, the gold core of the core-shell particles was overgrown with spherical silver or gold shells in order to tune scattering/absorbance cross-sections of the particles. A surfactant-assisted seeded growth protocol was developed. The protocol allowed for a spherical overgrowth of the gold nanoparticles without non-spherical side products or secondary nucleation. The core sizes could be adjusted in a range of 20 nm – 100 nm with a high precision of a few nanometers. Consequently, the LSPR of the colloidal building blocks was tunable in a range of 433 nm – 571 nm.

2. Hexagonally ordered monolayers were prepared by self-assembly of the colloidal building blocks using spin-coating or interface-mediated self-assembly. The interparticle center-to-center distance of non-cross-linked PNIPAM-encapsulated gold nanoparticles was a function of the PNIPAM shell thickness and tunable between 102 nm and 168 nm for gold nanoparticles of the same size. Larger interparticle distances of 250 nm were achieved by spin-coating of cross-linked PNIPAM-encapsulated gold nanoparticles. However, the fast solvent evaporation rate and the strong shear forces during the spin-coating process had adverse effects on the particle arrangement of the monolayer. The order of the monolayers was low and they were polycrystalline. In contrast, monolayers prepared by interface-mediated self-assembly were highly ordered. AFM measurements were carried out at multiple random positions of the samples and each time similar interparticle distances with narrow deviations were found. Using cross-linked PNIPAM-encapsulated gold nanoparticles for the monolayer fabrication, the interparticle distance was tunable in a range as large as 250 nm – 620 nm as a function of the PNIPAM shell thickness.

Monolayers of colloidal building blocks with overgrown gold cores had almost identical interparticle distances and surface densities of plasmonic particles – independent of size and composition of the plasmonic core. This showed that the self-assembly was mainly governed by the PNIPAM hydrogel shell. The LSPR of the monolayers was a function of size and composition of the plasmonic core of the PNIPAM-encapsulated particles. Thus, monolayers with LSPRs in a range as large as 484 nm – 573 nm were prepared. The LSPR was further tailored by the fabrication of binary plasmonic monolayers using a mixture of cross-linked PNIPAM-encapsulated core-shell particles with two different plasmonic cores.

3. Organic thin film solar cell devices. Plasmonic monolayer with tailored LSPR position were integrated in the layer stack of organic thin film solar cell devices. AFM experiments revealed almost identical interparticle distances and surface densities of plasmonic particles – independent of the location of the monolayer in the layer stack of the device. This was highly important for a systematic study of the optical effects of plasmonic superstructures in solar cell devices. The solar cell performance was investigated as a function of the diameter of the gold nanoparticles. Therefore, monolayers with gold core sizes of 21 nm, 58 nm, 68 nm, or 100 nm were prepared by interface-mediated self-assembly and deposited onto the ITO electrode of the devices. Almost all plasmonic devices showed the characteristic current-voltage curves of a solar cell diode indicating that the devices were fully functional. Current-voltage measurements revealed that the short-circuit current density and the open-circuit voltage of plasmonic solar cells decreased as compared to the reference devices. The reduced performance was attributed to parasitic absorption and backscattering of incident light by the plasmonic monolayers. This effect was most pronounced for larger gold nanoparticles.

Consequently, the location of the monolayers in the device stack was systematically changed. Parasitic light absorption was observed for plasmonic monolayers located at any interface below the photoactive layer of the solar cells. Additionally, strong leakage currents occurred for gold nanoparticles in direct contact with the photoactive layer of the solar cells even though all gold nanoparticles were encapsulated by a PNIPAM hydrogel shell. In contrast, a clear improvement of the solar cell efficiency was discovered in space-charge limited solar cells with a thick photoactive layer. Depositing a plasmonic monolayer on top of the photoactive layer led to a spatial redistribution of light. Thus, charge generation near the metal electrode increased the photocurrent of the plasmonic device by 30 % as compared to a reference device. These findings reveal that plasmonic particles are no panacea for organic solar cell devices and mutually influencing factors such as dark leakage currents, parasitic absorption, near field enhancement, and light redistribution must be considered carefully for the design of future plasmonic solar cells.

4. Potpourri of plasmonic superstructures. Plasmonic superstructures for organic thin film solar cells were prepared by interface-mediated self-assembly of PNIPAM-encapsulated gold nanoparticles. When such a monolayer was deposited onto a hydrophilic substrate, the particles were arranged in a non-close packed hexagonal lattice. However, what happens if another monolayer is deposited onto the same solid support? In this case, plasmonic honeycomb structures or Moiré patterns are obtained. The double deposition process even allows for the fabrication of binary plasmonic superstructures. Binary honeycomb structures were fabricated by sequential deposition of a monolayer of PNIPAM-encapsulated gold particles on top of a monolayer of PNIPAM-encapsulated silver particles. UV-Vis spectroscopy revealed a significant broadening of the LSPR, which was attributed to plasmon coupling between gold and silver cores. The structural composition of the binary honeycomb lattice was investigated by SEM and EDX elemental mapping. Using EDX, it was possible to distinguish between gold and silver cores in the binary structure exactly. Two underlying hexagonal sub-lattices – one for the gold core-shell particles and one for the silver core-shell particles – were identified. The interparticle distances between gold-gold and silver-silver cores of each sub-lattice was 470 nm in close agreement to monolayers of the same particles. Regarding the (complete) binary structure, smaller interparticle distances of 271 nm were measured, as expected for a honeycomb lattice.

Moiré patterns were formed once the second monolayer was rotated against the first one by a certain rotation angle. Three different patterns were discovered corresponding to rotation angles of 8°, 14°, and 31°. The periodicity of the Moiré pattern was a function of the rotation angle and decreased for higher rotation angles. Investigation of the Moiré patterns by TEM revealed that the PNIPAM-encapsulated nanoparticles were arranged on two different lengthscales: one due to a shell-to-shell arrangement and one due to a core-to-core arrangement of the particles. Shell-to-Shell arrangements were formed if the particles were completely separated by the PNIPAM shell. Core-to-core arrangement were formed from partially overlapping particles where the PNIPAM shells interpenetrated each other. An intriguing Moiré pattern was found for a rotation angle of 31°. Quasiperiodic tiling of the pattern was partially possible using the Stampfli tiling – combinations of equilateral triangles, squares, and rhombs with an acute angle of 30°. The lattice points of the tiling were created from particle pairs in a core-to-core arrangement.

A completely different approach towards plasmonic superstructures was the anisotropic deformation of a hexagonal lattice. This process required a monolayer of cross-linked PNIPAM-encapsulated nanoparticles floating at the air/water interface, a substrate with a water contact angle of 60°, and an immersion angle of the substrate of 90°. Transfer of the monolayer onto the substrate induced an anisotropic stretching of the monolayer. The structure of the stretched monolayer was given by the stretching angle and the stretching factor. A stretching factor of 1.73 and a stretching angle of 30° produced a square lattice of plasmonic particles. If the stretching factor changed for the same stretching angle, then a centered-rectangular lattice was obtained.

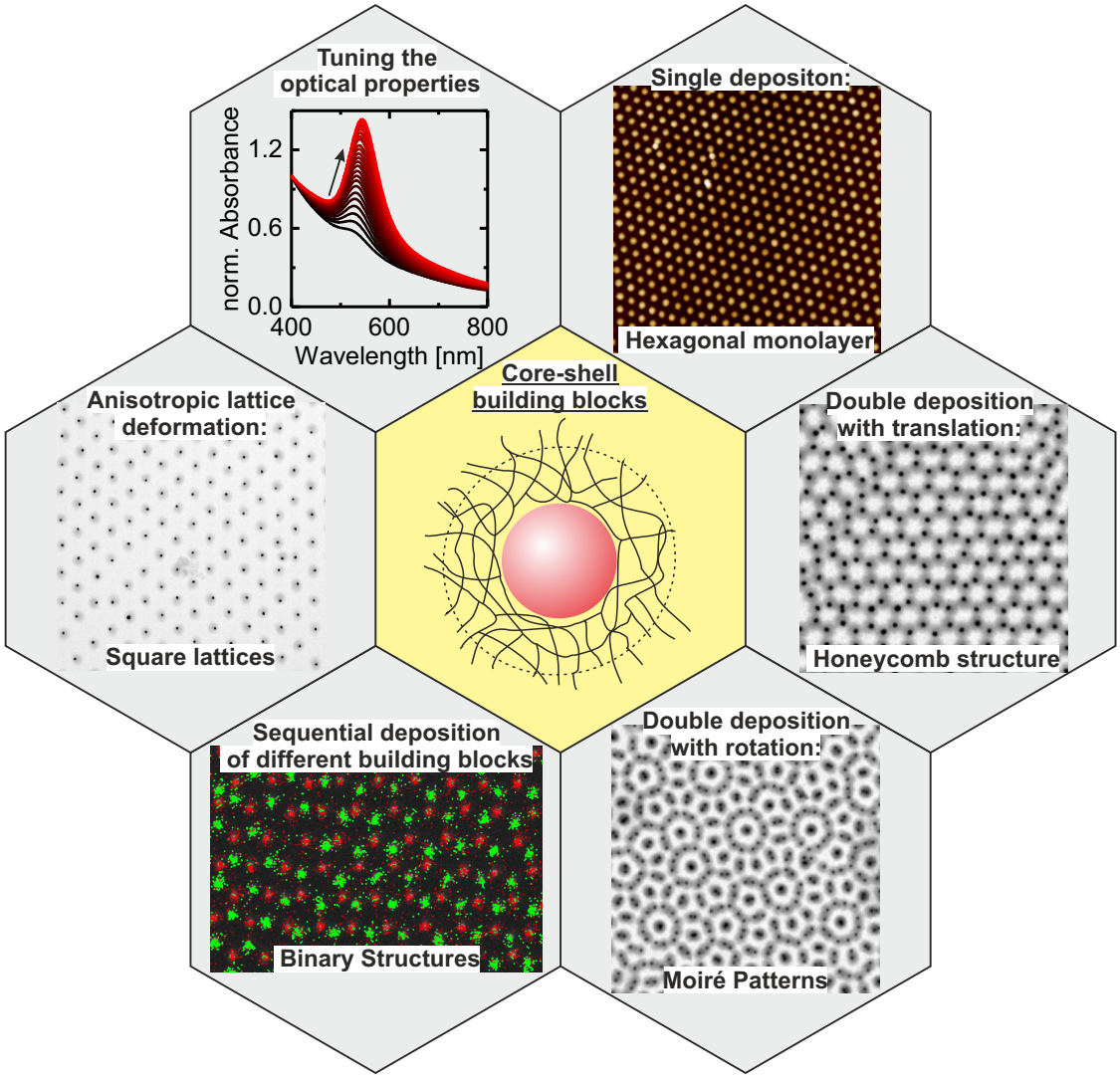

Figure 8.1. Potpourri of plasmonic superstructures fabricated via self-assembly of colloidal building blocks. The optical properties of the building blocks are precisely tunable by sequential core-overgrowth. The particles are self-assembled into superstructures by interface-mediated self-assembly at the air/water interface. Single deposition of the superstructures onto solid substrates reveals hexagonally ordered monolayers. Honeycomb structures are fabricated by double deposition with translation of two monolayers onto the same substrate. Moiré patterns are fabricated by double deposition with rotation of two monolayers against each other. Binary structures are obtained by sequential deposition of two monolayers with different metal cores. Anisotropic deformation of a hexagonally ordered monolayer can lead to plasmonic square lattices.

In conclusion, Figure 8.1 provides a brief overview of all plasmonic superstructures fabricated in this work. The superstructures are prepared via self-assembly of colloidal building blocks – gold nanoparticles encapsulated by soft, deformable PNIPAM shells. Shape and position of the plasmon resonance of the building blocks are tunable by post-modification of their plasmonic cores. This way, the optical properties of plasmonic superstructures are tailored precisely. Interface-mediated self-assembly of PNIPAM-encapsulated gold nanoparticles produces hexagonally ordered monolayers with exceptional long-range order. Beyond hexagonal monolayers, access to honeycomb structures or Moiré patterns is provided by sequential deposition of two monolayers on top of each other. This way, even binary lattices are created by choosing appropriate core-shell particles from the preformed particle library. Finally, anisotropic deformation of a single hexagonal monolayer leads to centered or square-like plasmonic superstructures. These monolayers conclude the structural diversity of plasmonic superstructures described in this work.

Chapter 9

Future Perspectives

As demonstrated in this work, overgrowing the gold core of PNIPAM-encapsulated gold nanoparticles with spherical silver or gold shells enhances the plasmonic properties of the particles significantly. However, this post-modification procedure represents only a fraction of the current possibilities available for the overgrowth of gold nanoparticles.[99,268–270] An alternative approach is the anisotropic overgrowth of the particles. Particularly interesting are gold nanorods due to their ability to support two plasmon resonance modes[213,271] or gold nanostars which have a strong absorbance in the entire visible range.[81,272]

Self-assembly of PNIPAM-encapsulated gold nanoparticles revealed that the PNIPAM shell acts as a sterical spacer and determines the interparticle distance of plasmonic superstructures. However, this is not the only parameter affecting the particle separation. Recently, Volk et. al discovered that the interparticle distance of similar plasmonic monolayers is not constant but changes as a function of the dwell time on the water surface.[202] Hence, two handles are available for controlling the interparticle distance of plasmonic monolayers: the thickness of the PNIPAM shell and the dwell time of the monolayer on the air/water interface. This way, precise investigations of distance depended plasmonic effects such as plasmon-plasmon or plasmon-lattice coupling can be conducted.

Particle design by post-modification and interface-mediated self-assembly are two sequential steps on the road to well-defined plasmonic superstructures for photovoltaic devices. Even though plasmonic monolayers were integrated successfully in solar cell devices, parasitic light absorption was an issue. A potential work-around strategy are colloidal non-absorbing superstructures that act purely as light scattering elements. They can be fabricated by using PNIPAM-encapsulated particles without plasmonic cores. Promising core-shell particles are PNIPAM-encapsulated silica or PS colloids. Synthetic protocols for such particles are already available.[25,177,273–275]

Interface-mediated self-assembly even allows for the fabrication of plasmonic superstructures beyond hexagonal monolayers. Sequential deposition is a versatile strategy in order to fabricate plasmonic honeycomb structures and Moiré patterns. Fully understanding plasmonic coupling in such structures is the next challenge. Plasmonic coupling is enhanced by creating a homogeneous refractive index environment between the particles of the superstructure. Recently, the impact of refractive index variation upon plasmonic coupling in hexagonally ordered superstructures was

investigated thoroughly in our group.[276] Consequently, the same concept can be adapted in order to elucidate the optical properties of plasmonic honeycomb structures and Moiré patterns.

Moiré patterns are intriguing superstructures, especially once the rotation angle of the two monolayers approaches 30°. In this case a quasiperiodic tiling of the structure was partially possible. Although this finding was striking, further investigations were difficult due to the small domain sizes and the large variety of different Moiré patterns on the same substrate. One way to increase the domain size of Moiré patterns is to fabricate colloidal monolayers with single crystalline domains as large as possible. Shinotsuka et al. demonstrated that the crystalline domains of colloidal silica monolayers increased at the air/water interface by a factor of 20 – 60 through ultrasonic annealing or a barrier-sway treatment of the monolayer.[277] The same approach is also promising for hexagonally ordered monolayers of PNIPAM-encapsulated gold nanoparticles floating at the air/water interface.

A hexagonally ordered monolayer represents only one of five possible two-dimensional Bravais lattices in the Euclidean plane. It was demonstrated that square as well as centered rectangular lattices are obtained by anisotropic stretching of a hexagonal monolayer. This was done by transfer of the monolayer from the air/water interface onto a hydrophobic substrate. The future challenge is the arrangement of plasmonic particles in all possible two-dimensional Bravais lattices. Therefore, variation of the contact angle of the substrate is a promising approach in order to control the stretching factor and hence the structure of the monolayer.

In summary, this work describes strategies in order to create a large variety of plasmonic superstructures using well-defined core-shell blocks and simple, yet efficient, self-assembly methods. In the future, plasmonic superstructures might stimulate the development of emerging optoelectronic applications such as sensors, waveguide materials, or nanolasers.

Chapter 10

Appendix

10.1 ^{1}H-NMR spectra of *l*-PNIPAM reaction mixtures

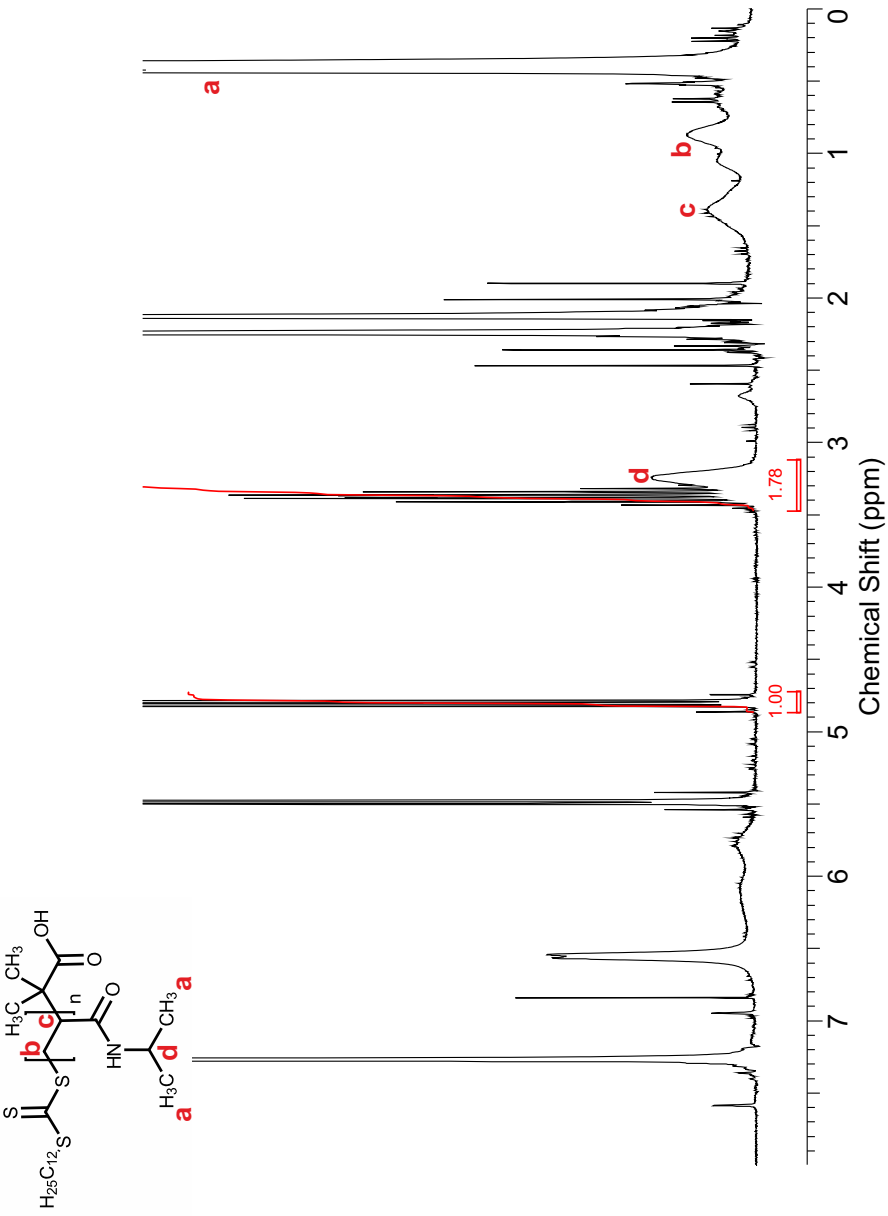

Figure 10.1. Reaction mixture of *l*-PNIPAM$_{9.5k}$ investigated by ^{1}H-NMR spectroscopy after 1 h polymerization time. Signals of the polymer protons are indicated in the spectrum. The monomer conversion is calculated by integrating the signal intensity of the ethylene proton of the residual monomer at 4.82 ppm and the signal intensity of the isopropyl moiety of monomer and polymer at 3.25 ppm.

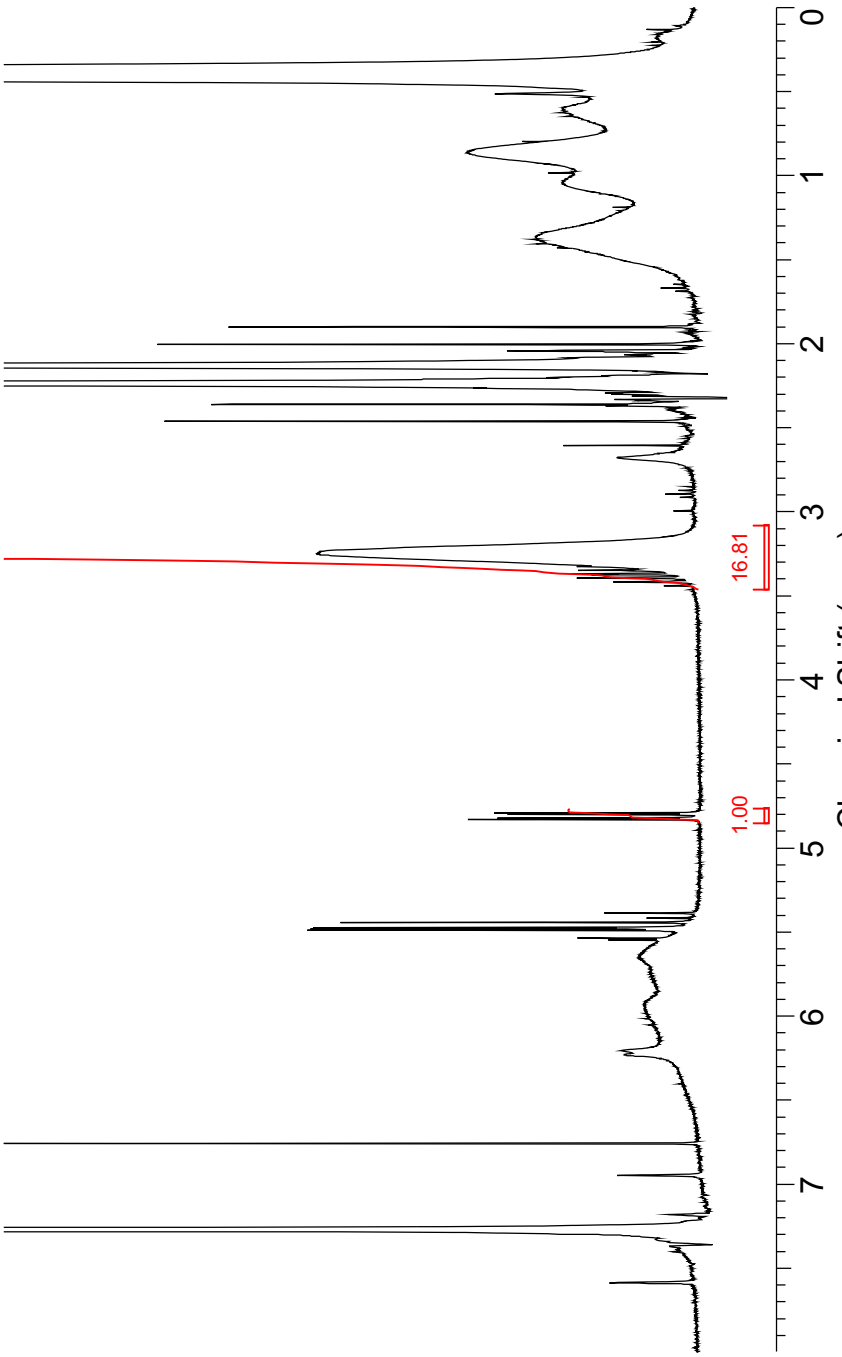

Figure 10.2. Reaction mixture of *l*-PNIPAM$_{40k}$ investigated by ^{1}H-NMR spectroscopy after 3 h polymerization time. The monomer conversion is determined similar to Figure 10.1.

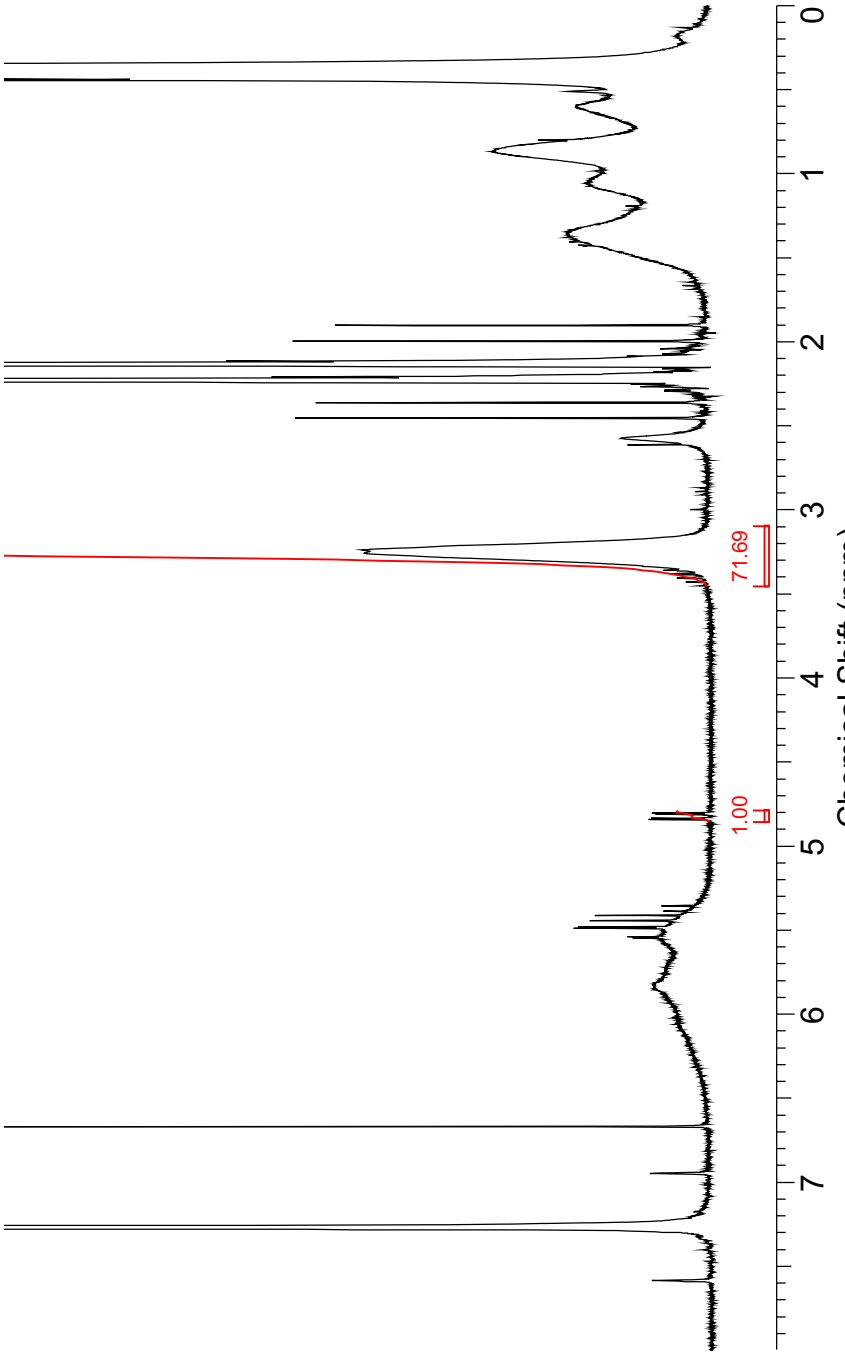

Figure 10.3. Reaction mixture of *l*-PNIPAM$_{82k}$ investigated by ^{1}H-NMR spectroscopy after 3 h polymerization time. The monomer conversion is determined similar to Figure 10.1.

10.2 Investigation of Au$_x$-*l*-PNIPAM$_y$ by DLS

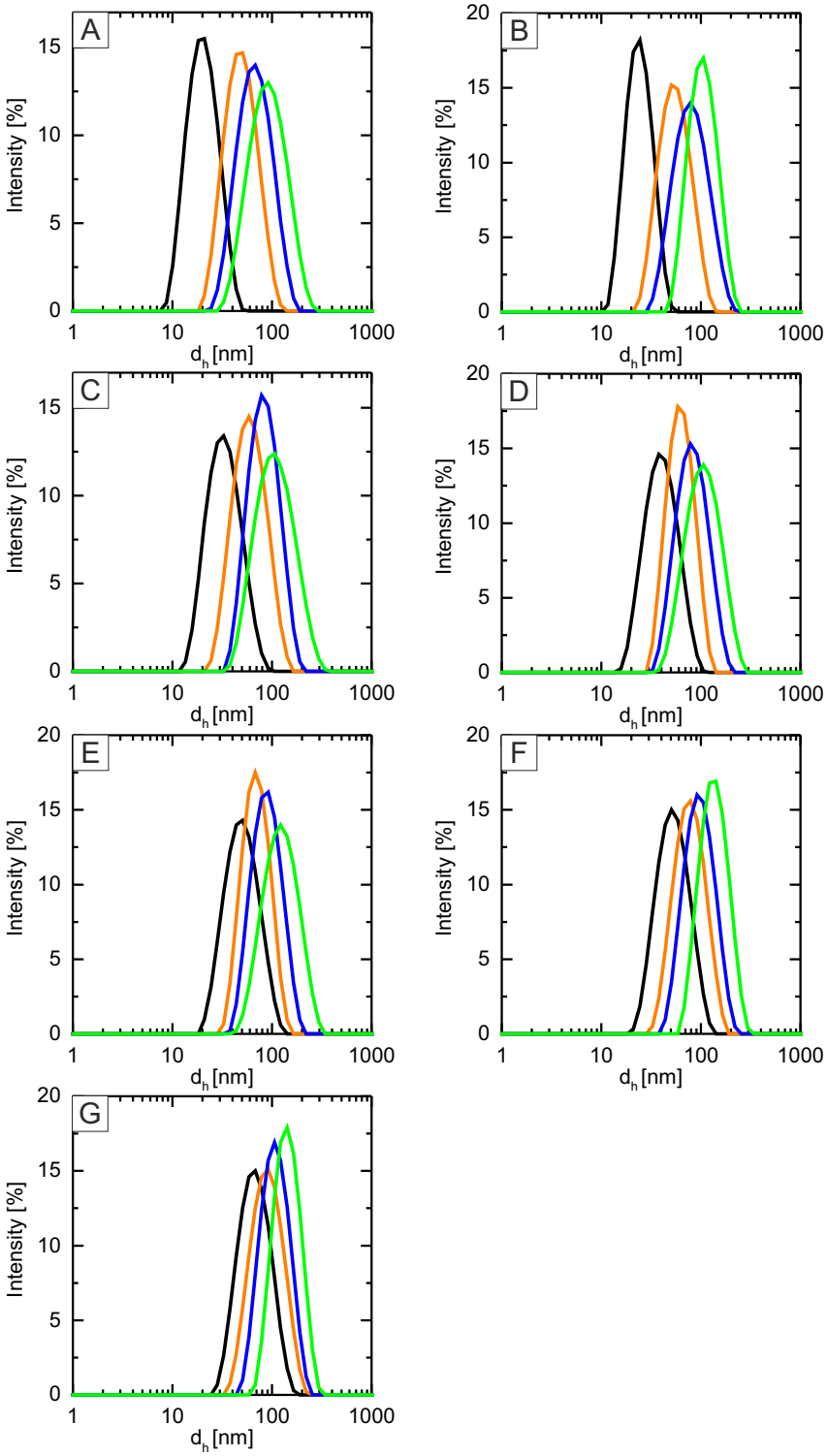

Figure 10.4. Intensity-weighted size distributions of Au$_x$-*l*-PNIPAM$_y$ obtained by cumulant analysis of $g^{(2)}(\tau)$. A – G: Au$_{15}$ – Au$_{53}$ nanoparticles stabilized by citrate (black) or encapsulated by *l*-PNIPAM$_{9.5k}$ (orange), *l*-PNIPAM$_{40k}$ (blue), or *l*-PNIPAM$_{82k}$ (green).

10.3 AFM Height Images of Solar Cells with Normal Cell Geometry

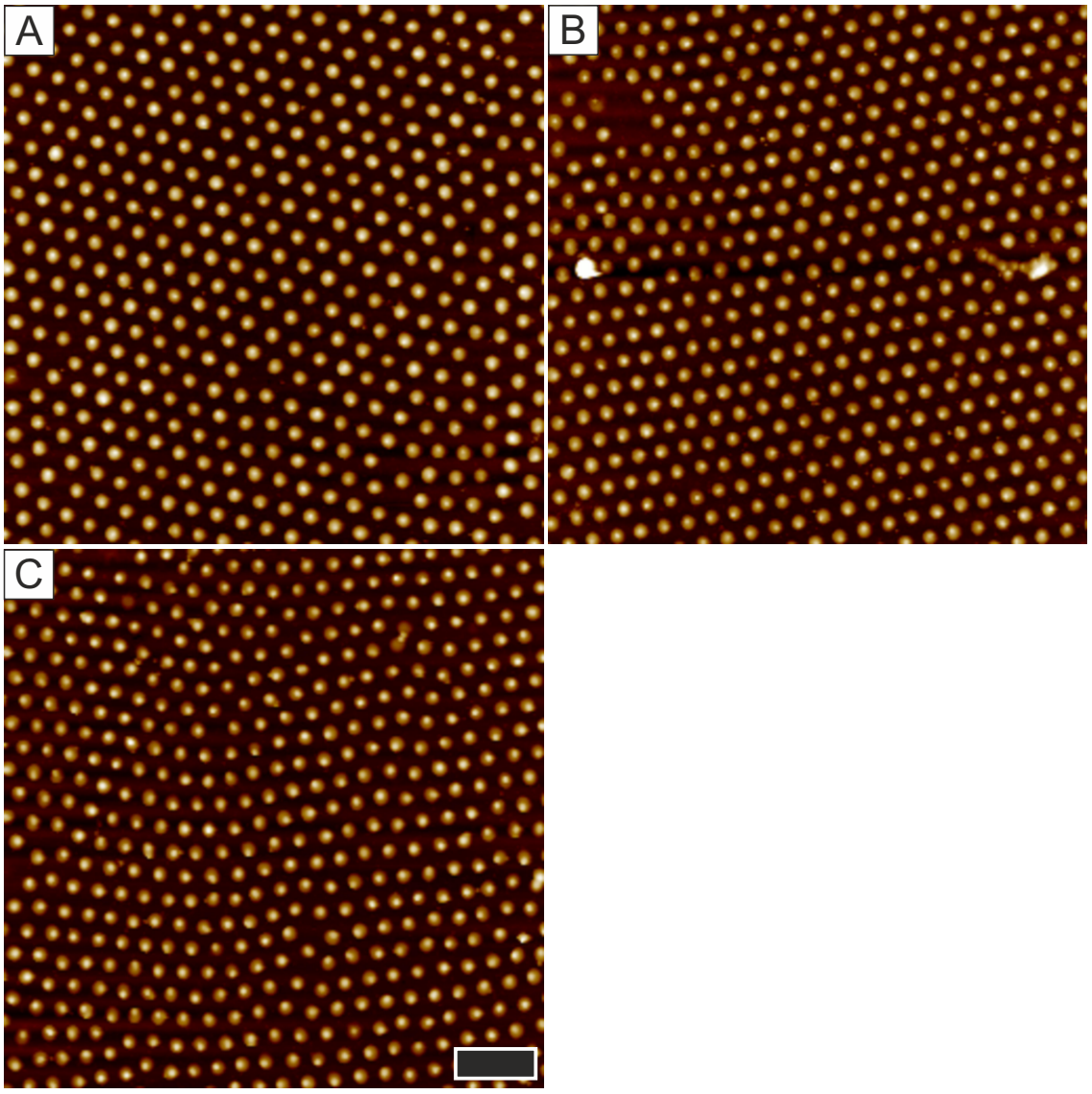

Figure 10.5. AFM investigation of M-Au_{58}, M-Au_{68}, and M-Au_{100} monolayers on the ITO electrode of plasmonic solar cells with normal cell geometry. The scale bar is 2 μm.

10.4 AFM Height Images of Moiré Structures

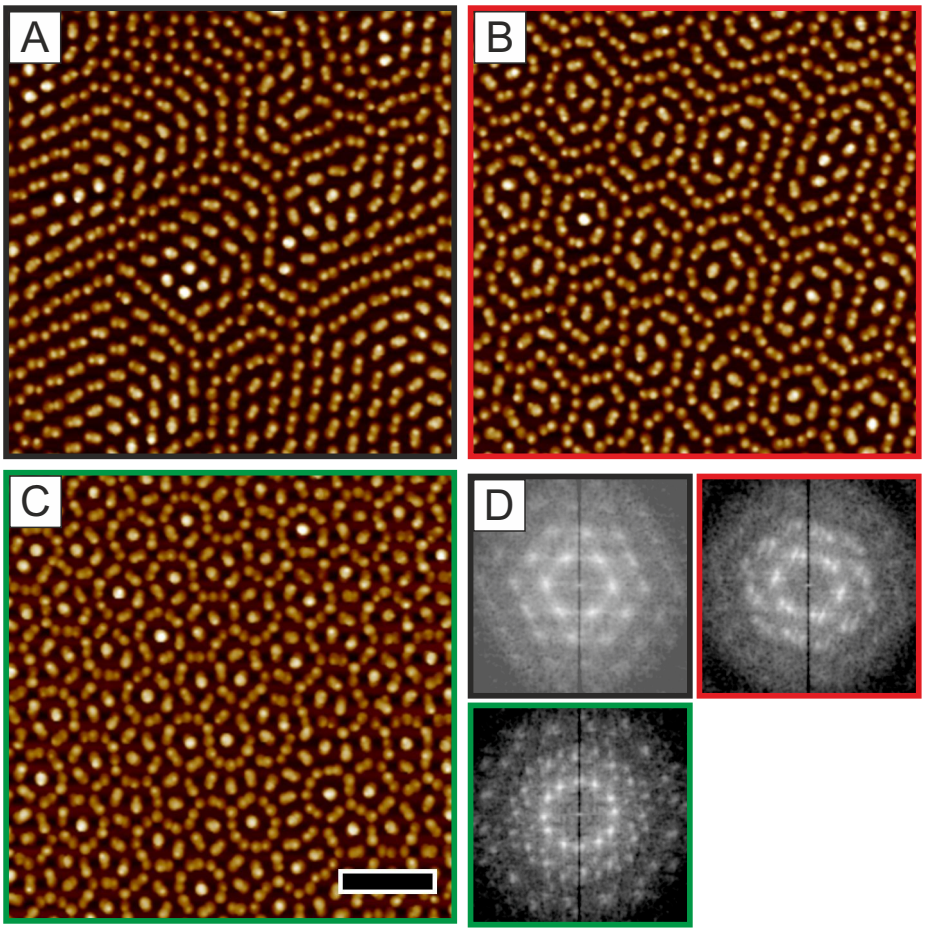

Figure 10.6. Different Moiré patterns of Au_{75}@Au-x-$PNIPAM_{340}$ particles on a glass substrate. The rotation angles are 15° and 35° for images B and C, respectively. The rotation angle of A could not be determined due to the close overlap of the peaks in the power spectrum. The scale bar is 2 μm. D, power spectra obtained by computing FFT of the AFM images A – C.

10.5 Analysis of Moiré Structures by Their Autocorrelation Functions

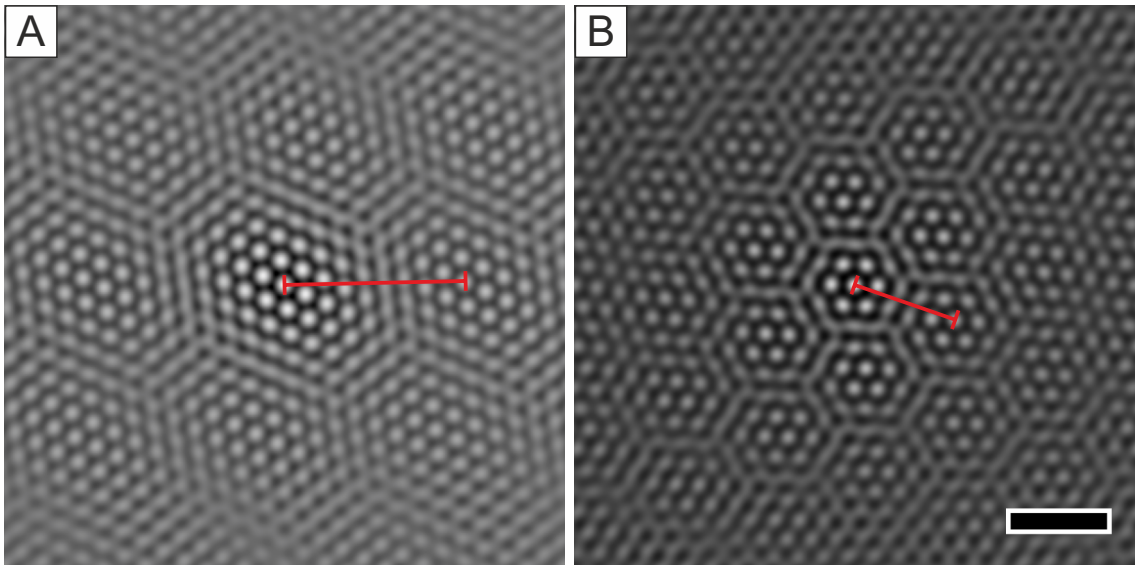

Figure 10.7. Autocorrelation functions of Moiré patterns with rotation angles of 8° (A) and 14° (B). The periodicity of the Moiré patterns is indicated by a red line in each image. The scale bar is 2 μm.

References

[1] Hamaker, H. C. The London-van der Waals Attraction between Spherical Particles. *Physica* **1937**, *4*, 1058–1072.

[2] Visser, J. On Hamaker Constants : A Comparison between Hamaker Constants and Lifshitz-van der Waals Constants. *Advan. Colloid Interface Sci.* **1972**, *3*, 331–363.

[3] Giersig, M.; Mulvaney, P. Preparation of Ordered Colloid Monolayers by Electrophoretic Deposition. *Langmuir* **1993**, *9*, 3408–3413.

[4] Fink, J.; Kiely, C. J.; Bethell, D.; Schiffrin, D. J. Self-Organization of Nanosized Gold Particles. *Chem. Mater.* **1998**, *10*, 922–926.

[5] Bigioni, T. P.; Lin, X.-M.; Nguyen, T. T.; Corwin, E. I.; Witten, T. A.; Jaeger, H. M. Kinetically Driven Self Assembly of Highly Ordered Nanoparticle Monolayers. *Nat. Mater.* **2006**, *5*, 265–270.

[6] Karg, M.; Schelero, N.; Oppel, C.; Gradzielski, M.; Hellweg, T.; von Klitzing, R. Versatile Phase Transfer of Gold Nanoparticles from Aqueous Media to Different Organic Media. *Chem. Eur. J.* **2011**, *17*, 4648–4654.

[7] Mayya, K. S.; Caruso, F. Phase Transfer of Surface-Modified Gold Nanoparticles by Hydrophobization with Alkylamines. *Langmuir* **2003**, *19*, 6987–6993.

[8] Liz-Marzán, L. M.; Giersig, M.; Mulvaney, P. Synthesis of Nanosized Gold-silica Core-Shell Particles. *Langmuir* **1996**, *12*, 4329–4335.

[9] Pastoriza-Santos, I.; Pérez-Juste, J.; Liz-Marzán, L. M. Silica-Coating and Hydrophobation of CTAB-Stabilized Gold Nanorods. *Chem. Mater.* **2006**, *18*, 2465–2467.

[10] Bahadur, N. M.; Furusawa, T.; Sato, M.; Kurayama, F.; Siddiquey, I. A.; Suzuki, N. Fast and Facile Synthesis of Silica Coated Silver Nanoparticles by Microwave Irradiation. *J. Colloid Interface Sci.* **2011**, *355*, 312–320.

[11] Barrow, S. J.; Wei, X.; Baldauf, J. S.; Funston, A. M.; Mulvaney, P. The Surface Plasmon Modes of Self-Assembled Gold Nanocrystals. *Nat. Commun.* **2012**, *3*, 1275.

[12] Lalander, C. H.; Zheng, Y.; Dhuey, S.; Cabrini, S.; Bach, U. DNA-Directed Self-Assembly of Gold Nanoparticles onto Nanopatterned Surfaces: Controlled Placement of Individual Nanoparticles into Regular Arrays. *ACS Nano* **2010**, *4*, 6153–6161.

[13] Barrow, S. J.; Funston, A. M.; Wei, X. Z.; Mulvaney, P. DNA-Directed Self-Assembly and Optical Properties of Discrete 1D, 2D and 3D Plasmonic Structures. *Nano Today* **2013**, *8*, 138–167.

[14] Tan, S. J.; Campolongo, M. J.; Luo, D.; Cheng, W. Building Plasmonic Nanostructures with DNA. *Nat. Nanotechnol.* **2011**, *6*, 268–76.

[15] Mirkin, C. A.; Letsinger, R. L.; Mucic, R. C.; Storhoff, J. J. A DNA-based Method for Rationally Assembling Nanoparticles into Macroscopic Materials. *Nature* **1996**, *382*, 607–609.

[16] Del Pino, P.; Yang, F.; Pelaz, B.; Zhang, Q.; Kantner, K.; Hartmann, R.; Martinez de Baroja, N.; Gallego, M.; Moller, M.; Manshian, B. B.; Soenen, S. J.; Riedel, R.; Hampp, N.; Parak, W. J. Basic Physicochemical Properties of Polyethylene Glycol Coated Gold Nanoparticles that Determine Their Interaction with Cells. *Angew. Chem. Int. Ed. Engl.* **2016**, *55*, 5483–7.

[17] Hühn, J. et al. Selected Standard Protocols for the Synthesis, Phase Transfer, and Characterization of Inorganic Colloidal Nanoparticles. *Chem. Mater.* **2017**, *29*, 399–461.

[18] Sperling, R. A.; Parak, W. J. Surface Modification, Functionalization and Bioconjugation of Colloidal Inorganic Nanoparticles. *Phil. Trans. R. Soc. A* **2010**, *368*, 1333–1383.

[19] Alkilany, A. M.; Yaseen, A. I. B.; Park, J.; Eller, J. R.; Murphy, C. J. Facile Phase Transfer of Gold Nanoparticles from Aqueous Solution to Organic Solvents with Thiolated Poly(ethylene Glycol). *RSC Advances* **2014**, *4*, 52676–52679.

[20] Mulvaney, P. Surface Plasmon Spectroscopy of Nanosized Metal Particles. *Langmuir* **1996**, *12*, 788–800.

[21] Liz-Marzán, L. M. Tailoring Surface Plasmons through the Morphology and Assembly of Metal Nanoparticles. *Langmuir* **2006**, *22*, 32–41.

[22] Novo, C.; Funston, A. M.; Pastoriza-Santos, I.; Liz-Marzán, L. M.; Mulvaney, P. Influence of the Medium Refractive Index on the Optical Properties of Single Gold Triangular Prisms on a Substrate. *J. Phys. Chem. C* **2008**, *112*, 3–7.

[23] Ebeling, B.; Vana, P. RAFT-Polymers with Single and Multiple Trithiocarbonate Groups as Uniform Gold-Nanoparticle Coatings. *Macromolecules* **2013**, *46*, 4862–4871.

[24] Hill, M. R.; Carmean, R. N.; Sumerlin, B. S. Expanding the Scope of RAFT Polymerization: Recent Advances and New Horizons. *Macromolecules* **2015**, *48*, 5459–5469.

[25] Karg, M.; Pastoriza-Santos, I.; Liz-Marzán, L. M.; Hellweg, T. A Versatile Approach for the Preparation of Thermosensitive PNIPAM Core-Shell Microgels with Nanoparticle Cores. *Chem. Phys. Chem.* **2006**, *7*, 2298–2301.

[26] Contreras-Cáceres, R.; Sánchez-Iglesias, A.; Karg, M.; Pastoriza-Santos, I.; Pérez-Juste, J.; Pacifico, J.; Hellweg, T.; Fernández-Barbero, A.; Liz-Marzán, L. M. Encapsulation and Growth of Gold Nanoparticles in Thermoresponsive Microgels. *Adv. Mater.* **2008**, *20*, 1666–1670.

[27] Contreras-Cáceres, R.; Pacifico, J.; Pastoriza-Santos, I.; Pérez-Juste, J.; Fernández-Barbero, A.; Liz-Marzán, L. M. Au@PNIPAM Thermosensitive Nanostructures: Control over Shell Cross-linking, Overall Dimensions, and Core Growth. *Adv. Funct. Mater.* **2009**, *19*, 3070–3076.

[28] Karg, M.; Jaber, S.; Hellweg, T.; Mulvaney, P. Surface Plasmon Spectroscopy of Gold-Poly-N-isopropylacrylamide Core-Shell Particles. *Langmuir* **2011**, *27*, 820–827.

[29] Rauh, A.; Honold, T.; Karg, M. Seeded Precipitation Polymerization for the Synthesis of Gold-Hydrogel Core-Shell Particles: The Role of Surface Functionalization and Seed Concentration. *Colloid. Polym. Sci.* **2016**, *294*, 37–47.

[30] Contreras-Cáceres, R.; Pastoriza-Santos, I.; Álvarez Puebla, R. A.; Pérez-Juste, J.; Fernández-Barbero, A.; Liz-Marzán, L. M. Growing Au/Ag Nanoparticles within Microgel Colloids for Improved Surface-Enhanced Raman Scattering Detection. *Chem. Eur. J.* **2010**, *16*, 9462–7.

[31] Sánchez-Iglesias, A.; Grzelczak, M.; Rodríguez-González, B.; Guardia-Girós, P.; Pastoriza-Santos, I.; Pérez-Juste, J.; Prato, M.; Liz-Marzán, L. M. Synthesis of Multifunctional Composite Microgels via In Situ Ni Growth on pNIPAM-Coated Au Nanoparticles. *ACS Nano* **2009**, *3*, 3184–3190.

[32] Rodriguez-Fernández, J.; Pérez-Juste, J.; de Abajo, F. J. G.; Liz-Marzán, L. M. Seeded Growth of Submicron Au Colloids with Quadrupole Plasmon Resonance Modes. *Langmuir* **2006**, *22*, 7007–7010.

[33] Hamon, C.; Novikov, S.; Scarabelli, L.; Basabe-Desmonts, L.; Liz-Marzán, L. M. Hierarchical Self-Assembly of Gold Nanoparticles into Patterned Plasmonic Nanostructures. *ACS Nano* **2014**, *8*, 10694–703.

[34] Willets, K. A.; Van Duyne, R. P. Localized Surface Plasmon Resonance Spectroscopy and Sensing. *Annu. Rev. Phys. Chem.* **2007**, *58*, 267–97.

[35] Haes, A. J.; Haynes, C. L.; McFarland, A. D.; Schatz, G. C.; Van Duyne, R. R.; Zou, S. L. Plasmonic Materials for Surface-Enhanced Sensing and Spectroscopy. *MRS Bull.* **2005**, *30*, 368–375.

[36] Stewart, M. E.; Anderton, C. R.; Thompson, L. B.; Maria, J.; Gray, S. K.; Rogers, J. A.; Nuzzo, R. G. Nanostructured Plasmonic Sensors. *Chem. Rev.* **2008**, *108*, 494–521.

[37] Thai, T.; Zheng, Y.; Ng, S. H.; Mudie, S.; Altissimo, M.; Bach, U. Self-Assembly of Vertically Aligned Gold Nanorod Arrays on Patterned Substrates. *Angew. Chem. Int. Ed.* **2012**, *51*, 8732–8735.

[38] Müller, M.; Karg, M.; Fortini, A.; Hellweg, T.; Fery, A. Wrinkle-Assisted Linear Assembly of Hard-core/soft-shell Particles: Impact of the Soft Shell on the Local Structure. *Nanoscale* **2012**, *4*, 2491–2499.

[39] Vogel, N.; Jung, M.; Bocchio, N. L.; Retsch, M.; Kreiter, M.; Köper, I. Reusable Localized Surface Plasmon Sensors Based on Ultrastable Nanostructures. *Small* **2010**, *6*, 104–109.

[40] Zhou, W.; Dridi, M.; Suh, J. Y.; Kim, C. H.; Co, D. T.; Wasielewski, M. R.; Schatz, G. C.; Odom, T. W. Lasing Action in Strongly Coupled Plasmonic Nanocavity Arrays. *Nat. Nanotechnol.* **2013**, *8*, 506–11.

[41] Karg, M.; König, T. A. F.; Retsch, M.; Stelling, C.; Reichstein, P. M.; Honold, T.; Thelakkat, M.; Fery, A. Colloidal Self-Assembly Concepts for Light Management in Photovoltaics. *Mater. Today* **2015**, *18*, 185–205.

[42] Choi, H.; Lee, J. P.; Ko, S. J.; Jung, J. W.; Park, H.; Yoo, S.; Park, O.; Jeong, J. R.; Park, S.; Kim, J. Y. Multipositional Silica-Coated Silver Nanoparticles for High-Performance Polymer Solar Cells. *Nano Lett.* **2013**, *13*, 2204–8.

[43] Gao, H. L.; Zhang, X. W.; Yin, Z. G.; Tan, H. R.; Zhang, S. G.; Meng, J. H.; Liu, X. Plasmon Enhanced Polymer Solar Cells by Spin-Coating Au Nanoparticles on Indium-Tin-Oxide Substrate. *Appl. Phys. Lett.* **2012**, *101*.

[44] Morfa, A. J.; Rowlen, K. L.; Reilly III, T. H.; Romero, M. J.; Lagemaat, J. v. d. Plasmon-Enhanced Solar Energy Conversion in Organic Bulk Heterojunction Photovoltaics. *Appl. Phys. Lett.* **2008**, *92*, 013504.

[45] Atwater, H. A.; Polman, A. Plasmonics for Improved Photovoltaic Devices. *Nat. Mater.* **2010**, *9*, 205–213.

[46] Reineck, P.; Lee, G. P.; Brick, D.; Karg, M.; Mulvaney, P.; Bach, U. A Solid-State Plasmonic Solar Cell via Metal Nanoparticle Self-Assembly. *Adv. Mater.* **2012**, *24*, 4750–4755.

[47] Köhler, A.; Bässler, H. *Electronic Processes in Organic Semiconductors*; Wiley-VCH: Weinheim, 2015.

[48] Dang, M. T.; Hirsch, L.; Wantz, G. P3HT:PCBM, Best Seller in Polymer Photovoltaic Research. *Adv. Mater.* **2011**, *23*, 3597–3602.

[49] Holliday, S. et al. High-Efficiency and Air-Stable P3HT-Based Polymer Solar Cells with a New Non-Fullerene Acceptor. *Nat. Commun.* **2016**, *7*, 11585.

[50] Dang, M. T.; Hirsch, L.; Wantz, G.; Wuest, J. D. Controlling the Morphology and Performance of Bulk Heterojunctions in Solar Cells. Lessons Learned from the Benchmark Poly(3-hexylthiophene):[6,6]-Phenyl-C_{61}-Butyric Acid Methyl Ester System. *Chem. Rev.* **2013**, *113*, 3734–3765.

[51] Schilinsky, P.; Waldauf, C.; Brabec, C. J. Recombination and Loss Analysis in Polythiophene Based Bulk Heterojunction Photodetectors. *Appl. Phys. Lett.* **2002**, *81*, 3885–3887.

[52] Padinger, F.; Rittberger, R. S.; Sariciftci, N. S. Effects of Postproduction Treatment on Plastic Solar Cells. *Adv. Funct. Mater.* **2003**, *13*, 85–88.

[53] Ko, D.-H.; Tumbleston, J. R.; Gadisa, A.; Aryal, M.; Liu, Y.; Lopez, R.; Samulski, E. T. Light-Trapping Nano-Structures in Organic Photovoltaic Cells. *J. Mater. Chem.* **2011**, *21*, 16293–16303.

[54] Hoppe, H.; Sariciftci, N. S. Organic Solar Cells: An Overview. *J. Mater. Res.* **2004**, *19*, 1924–1945.

[55] Brabec, C. J.; Gowrisanker, S.; Halls, J. J. M.; Laird, D.; Jia, S.; Williams, S. P. Polymer-Fullerene Bulk-Heterojunction Solar Cells. *Adv. Mater.* **2010**, *22*, 3839–3856.

[56] Shrotriya, V.; Wu, E. H.-E.; Li, G.; Yao, Y.; Yang, Y. Efficient Light Harvesting in Multiple-Device Stacked Structure for Polymer Solar Cells. *Appl. Phys. Lett.* **2006**, *88*, 064104.

[57] Jang, Y. H.; Jang, Y. J.; Kim, S.; Quan, L. N.; Chung, K.; Kim, D. H. Plasmonic Solar Cells: From Rational Design to Mechanism Overview. *Chem. Rev.* **2016**,

[58] Catchpole, K. R.; Polman, A. Plasmonic Solar Cells. *Opt. Express* **2008**, *16*, 21793–21800.

[59] Chou, C.-H.; Chen, F.-C. Plasmonic Nanostructures for Light Trapping in Organic Photovoltaic Devices. *Nanoscale* **2014**, *6*, 8444–8458.

[60] Baek, S.-W.; Noh, J.; Lee, C.-H.; Kim, B.; Seo, M.-K.; Lee, J.-Y. Plasmonic Forward Scattering Effect in Organic Solar Cells: A Powerful Optical Engineering Method. *Sci. Rep.* **2013**, *3*, 1726.

[61] Wang, J.; Lee, Y. J.; Chadha, A. S.; Yi, J.; Jespersen, M. L.; Kelley, J. J.; Nguyen, H. M.; Nimmo, M.; Malko, A. V.; Vaia, R. A.; Zhou, W. D.; Hsu, J. W. P. Effect of Plasmonic Au Nanoparticles on Inverted Organic Solar Cell Performance. *J. Phys. Chem. C* **2013**, *117*, 85–91.

[62] Chen, F.-C.; Wu, J.-L.; Lee, C.-L.; Hong, Y.; Kuo, C.-H.; Huang, M. H. Plasmonic-Enhanced Polymer Photovoltaic Devices Incorporating Solution-Processable Metal Nanoparticles. *Appl. Phys. Lett.* **2009**, *95*, 013305.

[63] Chen, X.; Zuo, L.; Fu, W.; Yan, Q.; Fan, C.; Chen, H. Insight into the Efficiency Enhancement of Polymer Solar Cells by Incorporating Gold Nanoparticles. *Sol. Energy Mater. Sol. Cells* **2013**, *111*, 1–8.

[64] Yoon, W.-J.; Jung, K.-Y.; Liu, J.; Duraisamy, T.; Revur, R.; Teixeira, F. L.; Sengupta, S.; Berger, P. R. Plasmon-Enhanced Optical Absorption and Photocurrent in Organic Bulk Heterojunction Photovoltaic Devices Using Self-Assembled Layer of Silver Nanoparticles. *Sol. Energy Mater. Sol. Cells* **2010**, *94*, 128–132.

[65] Kulkarni, A. P.; Noone, K. M.; Munechika, K.; Guyer, S. R.; Ginger, D. S. Plasmon-Enhanced Charge Carrier Generation in Organic Photovoltaic Films Using Silver Nanoprisms. *Nano Lett.* **2010**, *10*, 1501–1505.

[66] Spyropoulos, G. D.; Stylianakis, M.; Stratakis, E.; Kymakis, E. Plasmonic Organic Photovoltaics Doped with Metal Nanoparticles. *Phot. Nano. Fund. Appl.* **2011**, *9*, 184–189.

[67] Liu, H.; Goh, W.-P.; Leung, M.-Y.; Li, Y.; Norsten, T. B. Effect of Nanoparticle Stabilizing Ligands and Ligand-Capped Gold Nanoparticles in Polymer Solar Cells. *Sol. Energy Mater. Sol. Cells* **2012**, *96*, 302–306.

[68] Kalfagiannis, N.; Karagiannidis, P. G.; Pitsalidis, C.; Panagiotopoulos, N. T.; Gravalidis, C.; Kassavetis, S.; Patsalas, P.; Logothetidis, S. Plasmonic Silver Nanoparticles for Improved Organic Solar Cells. *Sol. Energy Mater. Sol. Cells* **2012**, *104*, 165–174.

[69] Kim, S.-S.; Na, S.-I.; Jo, J.; Kim, D.-Y.; Nah, Y.-C. Plasmon Enhanced Performance of Organic Solar Cells Using Electrodeposited Ag Nanoparticles. *Appl. Phys. Lett.* **2008**, *93*, 073307.

[70] Kao, C.-S.; Chen, F.-C.; Liao, C.-W.; Huang, M. H.; Hsu, C.-S. Plasmonic-Enhanced Performance for Polymer Solar Cells Prepared with Inverted Structures. *Appl. Phys. Lett.* **2012**, *101*, 193902.

[71] Cheng, P.-P.; Ma, G.-F.; Li, J.; Xiao, Y.; Xu, Z.-Q.; Fan, G.-Q.; Li, Y.-Q.; Lee, S.-T.; Tang, J.-X. Plasmonic Backscattering Enhancement for Inverted Polymer Solar Cells. *J. Mater. Chem.* **2012**, *22*, 22781–22787.

[72] Chaturvedi, N.; Swami, S. K.; Dutta, V. Plasmonic Effect of Spray-Deposited Au Nanoparticles on the Performance of Inverted Organic Solar Cells. *Nanoscale* **2014**, *6*, 10772–10778.

[73] Brambley, D.; Martin, B.; Prewett, P. D. Microlithography: An Overview. *Adv. Mater. Opt. Electron.* **1994**, *4*, 55–74.

[74] Menon, R.; Patel, A.; Gil, D.; Smith, H. I. Maskless Lithography. *Mater. Today* **2005**, *8*, 26–33.

[75] Matsui, S.; Kojima, Y.; Ochiai, Y.; Honda, T. High Resolution Focused Ion Beam Lithography. *J. Vac. Sci. Technol. B* **1991**, *9*, 2622–2632.

[76] Lohmüller, T.; Aydin, D.; Schwieder, M.; Morhard, C.; Louban, I.; Pacholski, C.; Spatz, J. P. Nanopatterning by Block Copolymer Micelle Nanolithography and Bioinspired Applications. *Biointerphases* **2011**, *6*, MR1–MR12.

[77] Clara-Rahola, J.; Contreras-Cáceres, R.; Sierra-Martin, B.; Maldonado-Valdivia, A.; Hund, M.; Fery, A.; Hellweg, T.; Fernández-Barbero, A. Structure and Plasmon Coupling of Gold-Poly(N-isopropylacrylamide) Core-Shell Microgel Arrays with Thermally Controlled Interparticle Gap. *Colloids Surf., A* **2014**, *463*, 18–27.

[78] Jaber, S.; Karg, M.; Morfa, A.; Mulvaney, P. 2D Assembly of Gold-PNIPAM Core-Shell Nanocrystals. *Phys. Chem. Chem. Phys.* **2011**, *13*, 5576–8.

[79] Vogel, N.; Fernández-Lopez, C.; Pérez-Juste, J.; Liz-Marzán, L. M.; Landfester, K.; Weiss, C. K. Ordered Arrays of Gold Nanostructures from Interfacially Assembled Au@PNIPAM Hybrid Nanoparticles. *Langmuir* **2012**, *28*, 8985–8993.

[80] Kraus, T.; Brodoceanu, D.; Pazos-Perez, N.; Fery, A. Colloidal Surface Assemblies: Nanotechnology Meets Bioinspiration. *Adv. Funct. Mater.* **2013**, *23*, 4529–4541.

[81] Müller, M.; Tebbe, M.; Andreeva, D. V.; Karg, M.; Alvarez Puebla, R. A.; Pazos Perez, N.; Fery, A. Large-Area Organization of PNIPAM-Coated Nanostars as SERS Platforms for Polycyclic Aromatic Hydrocarbons Sensing in Gas Phase. *Langmuir* **2012**, *28*, 9168–73.

[82] Velev, O. D.; Gupta, S. Materials Fabricated by Micro- and Nanoparticle Assembly - The Challenging Path from Science to Engineering. *Adv. Mater.* **2009**, *21*, 1897–1905.

[83] Ghosh, S. K.; Pal, T. Interparticle Coupling Effect on the Surface Plasmon Resonance of Gold Nanoparticles: From Theory to Applications. *Chem. Rev.* **2007**, *107*, 4797–4862.

[84] Kelly, K. L.; Coronado, E.; Zhao, L. L.; Schatz, G. C. The Optical Properties of Metal Nanoparticles: The Influence of Size, Shape, and Dielectric Environment. *J. Phys. Chem. B* **2003**, *107*, 668–677.

[85] Jones, M. R.; Osberg, K. D.; Macfarlane, R. J.; Langille, M. R.; Mirkin, C. A. Templated Techniques for the Synthesis and Assembly of Plasmonic Nanostructures. *Chem. Rev.* **2011**, *111*, 3736–3827.

[86] Bohren, C. F.; Huffman, D. R. *Absorption and Scattering of Light by Small Particles*; Wiley Interscience New York, 1983.

[87] Eustis, S.; El-Sayed, M. A. Why Gold Nanoparticles Are More Precious Than Pretty Gold: Noble Metal Surface Plasmon Resonance and Its Enhancement of the Radiative and Nonradiative Properties of Nanocrystals of Different Shapes. *Chem. Soc. Rev.* **2006**, *35*, 209–217.

[88] Klinkova, A.; Choueiri, R. M.; Kumacheva, E. Self-Assembled Plasmonic Nanostructures. *Chem. Soc. Rev.* **2014**, *43*, 3976–3991.

[89] Daniel, M. C.; Astruc, D. Gold Nanoparticles: Assembly, Supramolecular Chemistry, Quantum-Size-Related Properties, and Applications Toward Biology, Catalysis, and Nanotechnology. *Chem. Rev.* **2004**, *104*, 293–346.

[90] Corma, A.; Garcia, H. Supported Gold Nanoparticles as Catalysts for Organic Reactions. *Chem. Soc. Rev.* **2008**, *37*, 2096–126.

[91] Chanana, M.; Liz-Marzán, L. M. Coating Matters: The Influence of Coating Materials on the Optical Properties of Gold Nanoparticles. *Nanophotonics* **2012**, *1*, 199–220.

[92] Sun, Y.; Xia, Y. Shape-Controlled Synthesis of Gold and Silver Nanoparticles. *Science* **2002**, *298*, 2176–2179.

[93] Lee, K. S.; El-Sayed, M. A. Gold and Silver Nanoparticles in Sensing and Imaging: Sensitivity of Plasmon Response to Size, Shape, and Metal Composition. *J. Phys. Chem. B* **2006**, *110*, 19220–5.

[94] Ghosh, S. K.; Nath, S.; Kundu, S.; Esumi, K.; Pal, T. Solvent and Ligand Effects on the Localized Surface Plasmon Resonance (LSPR) of Gold Colloids. *J. Phys. Chem. B* **2004**, *108*, 13963–13971.

[95] Underwood, S.; Mulvaney, P. Effect of the Solution Refractive Index on the Color of Gold Colloids. *Langmuir* **1994**, *10*, 3427–3430.

[96] Miller, M. M.; Lazarides, A. A. Sensitivity of Metal Nanoparticle Surface Plasmon Resonance to the Dielectric Environment. *J. Phys. Chem. B* **2005**, *109*, 21556–21565.

[97] Mock, J. J.; Barbic, M.; Smith, D. R.; Schultz, D. A.; Schultz, S. Shape Effects in Plasmon Resonance of Individual Colloidal Silver Nanoparticles. *J. Chem. Phys.* **2002**, *116*, 6755–6759.

[98] Halas, N. Playing with Plasmons: Tuning the Optical Resonant Properties of Metallic Nanoshells. *MRS Bull.* **2005**, *30*, 362–367.

[99] Pérez-Juste, J.; Pastoriza-Santos, I.; Liz-Marzán, L. M.; Mulvaney, P. Gold Nanorods: Synthesis, Characterization and Applications. *Coord. Chem. Rev.* **2005**, *249*, 1870–1901.

[100] Link, S.; Mohamed, M. B.; El-Sayed, M. A. Simulation of the Optical Absorption Spectra of Gold Nanorods as a Function of Their Aspect Ratio and the Effect of the Medium Dielectric Constant. *J. Phys. Chem. B* **1999**, *103*, 3073–3077.

[101] Link, S.; El-Sayed, M. A. Spectral Properties and Relaxation Dynamics of Surface Plasmon Electronic Oscillations in Gold and Silver Nanodots and Nanorods. *J. Phys. Chem. B* **1999**, *103*, 8410–8426.

[102] Su, K. H.; Wei, Q. H.; Zhang, X.; Mock, J. J.; Smith, D. R.; Schultz, S. Interparticle Coupling Effects on Plasmon Resonances of Nanogold Particles. *Nano Lett.* **2003**, *3*, 1087–1090.

[103] Hao, E.; Schatz, G. C. Electromagnetic Fields around Silver Nanoparticles and Dimers. *J. Chem. Phys.* **2004**, *120*, 357–366.

[104] Maier, S. A. *Plasmonics: Fundamentals and Applications*; Springer US, 2007.

[105] Aizpurua, J.; Hillenbrand, R. *Localized Surface Plasmons: Basics and Applications in Field-Enhanced Spectroscopy*; Springer Berlin, 2012.

[106] Davis, T. J.; Vernon, K. C.; Gómez, D. E. Effect of Retardation on Localized Surface Plasmon Resonances in a Metallic Nanorod. *Opt. Express* **2009**, *17*, 23655–23663.

[107] Mie, G. Beiträge zur Optik Trüber Medien, Speziell Kolloidaler Metallösungen. *Ann. Phys.* **1908**, *330*, 377–445.

[108] Meier, M.; Wokaun, A. Enhanced Fields on Large Metal Particles: Dynamic Depolarization. *Opt. Lett.* **1983**, *8*, 581–583.

[109] Kuwata, H.; Tamaru, H.; Esumi, K.; Miyano, K. Resonant Light Scattering from Metal Nanoparticles: Practical Analysis Beyond Rayleigh Approximation. *Appl. Phys. Lett.* **2003**, *83*, 4625–4627.

[110] Myroshnychenko, V.; Rodríguez-Fernández, J.; Pastoriza-Santos, I.; Funston, A. M.; Novo, C.; Mulvaney, P.; Liz-Marzán, L. M.; García de Abajo, F. J. Modelling the Optical Response of Gold Nanoparticles. *Chem. Soc. Rev.* **2008**, *37*, 1792–1805.

[111] Moroz, A. A Recursive Transfer-Matrix Solution for a Dipole Radiating inside and Outside a Stratified Sphere. *Ann. Phys.* **2005**, *315*, 352–418.

[112] Johnson, P. B.; Christy, R. W. Optical Constants of the Noble Metals. *Phys. Rev. B* **1972**, *6*, 4370–4379.

[113] Dulle, M.; Jaber, S.; Rosenfeldt, S.; Radulescu, A.; Förster, S.; Mulvaney, P.; Karg, M. Plasmonic Gold-Poly(N-isopropylacrylamide) Core-Shell Colloids with Homogeneous Density Profiles: A Small Angle Scattering Study. *Phys. Chem. Chem. Phys.* **2015**, *17*, 1354–1367.

[114] Roncali, J. Molecular Engineering of the Band Gap of π-Conjugated Systems: Facing Technological Applications. *Macromol. Rapid Commun.* **2007**, *28*, 1761–1775.

[115] Liu, C.; Wang, K.; Gong, X.; Heeger, A. J. Low Bandgap Semiconducting Polymers for Polymeric Photovoltaics. *Chem. Soc. Rev.* **2016**, *45*, 4825–4846.

[116] Blom, P. W. M.; Mihailetchi, V. D.; Koster, L. J. A.; Markov, D. E. Device Physics of Polymer:Fullerene Bulk Heterojunction Solar Cells. *Adv. Mater.* **2007**, *19*, 1551–1566.

[117] Riedel, I.; Dyakonov, V. Influence of Electronic Transport Properties of Polymer-Fullerene Blends on the Performance of Bulk Heterojunction Photovoltaic Devices. *Phys. Stat. Sol. (a)* **2004**, *201*, 1332–1341.

[118] Sievers, D. W.; Shrotriya, V.; Yang, Y. Modeling Optical Effects and Thickness Dependent Current in Polymer Bulk-Heterojunction Solar Cells. *J. Appl. Phys.* **2006**, *100*, 114509.

[119] Liang, Y.; Wu, Y.; Feng, D.; Tsai, S.-T.; Son, H.-J.; Li, G.; Yu, L. Development of New Semiconducting Polymers for High Performance Solar Cells. *J. Am. Chem. Soc.* **2009**, *131*, 56–57.

[120] Liang, Y.; Xu, Z.; Xia, J.; Tsai, S.-T.; Wu, Y.; Li, G.; Ray, C.; Yu, L. For the Bright Future – Bulk Heterojunction Polymer Solar Cells with Power Conversion Efficiency of 7.4 %. *Adv. Mater.* **2010**, *22*, E135–E138.

[121] Jung, J. W.; Jo, J. W.; Jung, E. H.; Jo, W. H. Recent Progress in High Efficiency Polymer Solar Cells by Rational Design and Energy Level Tuning of Low Bandgap Copolymers with Various Electron-withdrawing Units. *Org. Electron.* **2016**, *31*, 149–170.

[122] Rycenga, M.; Cobley, C. M.; Zeng, J.; Li, W.; Moran, C. H.; Zhang, Q.; Qin, D.; Xia, Y. Controlling the Synthesis and Assembly of Silver Nanostructures for Plasmonic Applications. *Chem. Rev.* **2011**, *111*, 3669–712.

[123] Sze, S. *Physics of Semiconductor Devices*; John Wiley & Sons: New York, 1981.

[124] Crispin, X.; Marciniak, S.; Osikowicz, W.; Zotti, G.; van der Gon, A. W. D.; Louwet, F.; Fahlman, M.; Groenendaal, L.; De Schryver, F.; Salaneck, W. R. Conductivity, Morphology, Interfacial Chemistry, and Stability of Poly(3,4-ethylene Dioxythiophene)-Poly(styrene Sulfonate): A Photoelectron Spectroscopy Study. *J. Polym. Sci. B Polym. Phys.* **2003**, *41*, 2561–2583.

[125] Elschner, A.; Bruder, F.; Heuer, H. W.; Jonas, F.; Karbach, A.; Kirchmeyer, S.; Thurm, S.; Wehrmann, R. PEDT/PSS for Efficient Hole-Injection in Hybrid Organic Light-Emitting Diodes. *Synth. Met.* **2000**, *111-112*, 139–143.

[126] Gregg, B. A. Excitonic Solar Cells. *J. Phys. Chem. B* **2003**, *107*, 4688–4698.

[127] Gregg, B. A.; Hanna, M. C. Comparing Organic to Inorganic Photovoltaic Cells: Theory, Experiment, and Simulation. *J. Appl. Phys.* **2003**, *93*, 3605–3614.

[128] Pope, M.; Swenberg, C. *Electronic Processes in Organic Crystals and Polymers*, 2nd ed.; Oxford University Press: New York, 1999.

[129] Clarke, T. M.; Durrant, J. R. Charge Photogeneration in Organic Solar Cells. *Chem. Rev.* **2010**, *110*, 6736–6767.

[130] Sariciftci, N. S.; Smilowitz, L.; Heeger, A. J.; Wudl, F. Photoinduced Electron Transfer from a Conducting Polymer to Buckminsterfullerene. *Science* **1992**, *258*, 1474–1476.

[131] Halls, J. J. M.; Walsh, C. A.; Greenham, N. C.; Marseglia, E. A.; Friend, R. H.; Moratti, S. C.; Holmes, A. B. Efficient Photodiodes from Interpenetrating Polymer Networks. *Nature* **1995**, *376*, 498–500.

[132] Yu, G.; Gao, J.; Hummelen, J. C.; Wudl, F.; Heeger, A. J. Polymer Photovoltaic Cells: Enhanced Efficiencies via a Network of Internal Donor-Acceptor Heterojunctions. *Science* **1995**, *270*, 1789–1791.

[133] Green, M. A. Solar Cell Fill Factors: General Graph and Empirical Expressions. *Solid-State Electron.* **1981**, *24*, 788–789.

[134] Chen, H.-Y.; Hou, J.; Zhang, S.; Liang, Y.; Yang, G.; Yang, Y.; Yu, L.; Wu, Y.; Li, G. Polymer Solar Cells with Enhanced Open-Circuit Voltage and Efficiency. *Nat. Photon.* **2009**, *3*, 649–653.

[135] Huynh, W. U.; Dittmer, J. J.; Alivisatos, A. P. Hybrid Nanorod-Polymer Solar Cells. *Science* **2002**, *295*, 2425–2427.

[136] Scharber, M. C.; Mühlbacher, D.; Koppe, M.; Denk, P.; Waldauf, C.; Heeger, A. J.; Brabec, C. J. Design Rules for Donors in Bulk-Heterojunction Solar Cell - Towards 10 % Energy-Conversion Efficiency. *Adv. Mater.* **2006**, *18*, 789–794.

[137] Riordan, C.; Hulstron, R. What is an Air Mass 1.5 Spectrum? Proceedings 21st IEEE PV Specialists Conference, Institute of Electrical and Electronic Engineers. 1999; pp 1085–1088.

[138] Pandey, A. K.; Shaw, P. E.; Samuel, I. D. W.; Nunzi, J.-M. Effect of Metal Cathode Reflectance on the Exciton-Dissociation Efficiency in Heterojunction Organic Solar Cells. *Appl. Phys. Lett.* **2009**, *94*, 103303.

[139] Peumans, P.; Yakimov, A.; Forrest, S. R. Small Molecular Weight Organic Thin-Film Photodetectors and Solar Cells. *J. Appl. Phys.* **2003**, *93*, 3693–3723.

[140] Uddin, A.; Yang, X. Surface Plasmonic Effects on Organic Solar Cells. *J. Nanosci. Nanotechnol.* **2014**, *14*, 1099–1119.

[141] Cole, J. R.; Halas, N. J. Optimized Plasmonic Nanoparticle Distributions for Solar Spectrum Harvesting. *Appl. Phys. Lett.* **2006**, *89*, 153120.

[142] Mendes, M. J.; Morawiec, S.; Simone, F.; Priolo, F.; Crupi, I. Colloidal Plasmonic Back Reflectors for Light Trapping in Solar Cells. *Nanoscale* **2014**, *6*, 4796–4805.

[143] Wang, D. H.; Kim, D. Y.; Choi, K. W.; Seo, J. H.; Im, S. H.; Park, J. H.; Park, O. O.; Heeger, A. J. Enhancement of Donor-Acceptor Polymer Bulk Heterojunction Solar Cell Power Conversion Efficiencies by Addition of Au Nanoparticles. *Angew. Chem. Int. Ed.* **2011**, *50*, 5519–5523.

[144] Yang, J.; You, J.; Chen, C.-C.; Hsu, W.-C.; Tan, H.-r.; Zhang, X. W.; Hong, Z.; Yang, Y. Plasmonic Polymer Tandem Solar Cell. *ACS Nano* **2011**, *5*, 6210–6217.

[145] Brongersma, M. L.; Cui, Y.; Fan, S. Light Management for Photovoltaics Using High-Index Nanostructures. *Nat. Mater.* **2014**, *13*, 451–460.

[146] Cai, W.; Gong, X.; Cao, Y. Polymer Solar Cells: Recent Development and Possible Routes for Improvement in the Performance. *Sol. Energy Mater. Sol. Cells* **2010**, *94*, 114–127.

[147] Mühlbacher, D.; Scharber, M.; Morana, M.; Zhu, Z.; Waller, D.; Gaudiana, R.; Brabec, C. High Photovoltaic Performance of a Low-Bandgap Polymer. *Adv. Mater.* **2006**, *18*, 2884–2889.

[148] Spinelli, P.; Polman, A. Prospects of Near-Field Plasmonic Absorption Enhancement in Semiconductor Materials Using Embedded Ag Nanoparticles. *Opt. Express* **2012**, *20*, A641–A654.

[149] Hägglund, C.; Apell, S. P. Plasmonic Near-Field Absorbers for Ultrathin Solar Cells. *J. Phys. Chem. Lett.* **2012**, *3*, 1275–1285.

[150] Mohanty, P. S.; Paloli, D.; Crassous, J. J.; Zaccarelli, E.; Schurtenberger, P. Effective Interactions between Soft-Repulsive Colloids: Experiments, Theory, and Simulations. *J. Chem. Phys.* **2014**, *140*, 094901.

[151] Paloli, D.; Mohanty, P. S.; Crassous, J. J.; Zaccarelli, E.; Schurtenberger, P. Fluid-Solid Transitions in Soft-Repulsive Colloids. *Soft Matter* **2013**, *9*, 3000–3004.

[152] Pusey, P. N.; van Megen, W. Phase Behaviour of Concentrated Suspensions of Nearly Hard Colloidal Spheres. *Nature* **1986**, *320*, 340–342.

[153] Lyon, L. A.; Debord, J. D.; Debord, S. B.; Jones, C. D.; McGrath, J. G.; Serpe, M. J. Microgel Colloidal Crystals. *J. Phys. Chem. B* **2004**, *108*, 19099–19108.

[154] Hoover, W. G.; Ree, F. H. Melting Transition and Communal Entropy for Hard Spheres. *J. Chem. Phys.* **1968**, *49*, 3609–3617.

[155] Alemán, J. V.; Chadwick, A. V.; He, J.; Hess, M.; Horie, K.; Jones, R. G.; Kratochvíl, P.; Meisel, I.; Mita, I.; Moad, G.; Penczek, S.; Stepto, R. F. T. Definitions of Terms Relating to the Structure and Processing of Sols, Gels, Networks, and Inorganic-Organic Hybrid Materials (IUPAC Recommendations 2007). *Pure Appl. Chem.* **2007**, *79*, 1801–1829.

[156] Stieger, M.; Richtering, W.; Pedersen, J. S.; Lindner, P. Small-Angle Neutron Scattering Study of Structural Changes in Temperature Sensitive Microgel Colloids. *J. Chem. Phys.* **2004**, *120*, 6197–6206.

[157] Fernández-Barbero, A.; Fernández-Nieves, A.; Grillo, I.; López-Cabarcos, E. Structural Modifications in the Swelling of Inhomogeneous Microgels by Light and Neutron Scattering. *Phys. Rev. E* **2002**, *66*, 051803.

[158] Heyes, D. M.; Brańka, A. C. Interactions between Microgel Particles. *Soft Matter* **2009**, *5*, 2681–2685.

[159] Pàmies, J. C.; Cacciuto, A.; Frenkel, D. Phase Diagram of Hertzian Spheres. *J. Chem. Phys.* **2009**, *131*, 044514.

[160] St. John, A. N.; Breedveld, V.; Lyon, L. A. Phase Behavior in Highly Concentrated Assemblies of Microgels with Soft Repulsive Interaction Potentials. *J. Phys. Chem. B* **2007**, *111*, 7796–7801.

[161] Debord, S. B.; Lyon, L. A. Influence of Particle Volume Fraction on Packing in Responsive Hydrogel Colloidal Crystals. *J. Phys. Chem. B* **2003**, *107*, 2927–2932.

[162] Iyer, A. S. J.; Lyon, L. A. Self-Healing Colloidal Crystals. *Angew. Chem. Int. Ed.* **2009**, *48*, 4562–4566.

[163] Lyon, L. A.; Meng, Z.; Singh, N.; Sorrell, C. D.; St. John, A. Thermoresponsive Microgel-Based Materials. *Chem. Soc. Rev.* **2009**, *38*, 865–874.

[164] Nerapusri, V.; Keddie, J. L.; Vincent, B.; Bushnak, I. A. Swelling and Deswelling of Adsorbed Microgel Monolayers Triggered by Changes in Temperature, pH, and Electrolyte Concentration. *Langmuir* **2006**, *22*, 5036–5041.

[165] Serpe, M. J.; Kim, J.; Lyon, L. A. Colloidal Hydrogel Microlenses. *Adv. Mater.* **2004**, *16*, 184–187.

[166] Schmidt, S.; Motschmann, H.; Hellweg, T.; von Klitzing, R. Thermoresponsive Surfaces by Spin-Coating of PNIPAM-co-PAA Microgels: A Combined AFM and Ellipsometry Study. *Polymer* **2008**, *49*, 749–756.

[167] Tsuji, S.; Kawaguchi, H. Colored Thin Films Prepared from Hydrogel Microspheres. *Langmuir* **2005**, *21*, 8439–8442.

[168] Tsuji, S.; Kawaguchi, H. Self-Assembly of Poly(N-isopropylacrylamide)-Carrying Microspheres into Two-Dimensional Colloidal Arrays. *Langmuir* **2005**, *21*, 2434–2437.

[169] Zhang, G.; Wang, D.; Gu, Z.-Z.; Hartmann, J.; Möhwald, H. Two-Dimensional Non-Close-Packing Arrays Derived from Self-Assembly of Biomineralized Hydrogel Spheres and Their Patterning Applications. *Chem. Mater.* **2005**, *17*, 5268–5274.

[170] Serpe, M. J.; Jones, C. D.; Lyon, L. A. Layer-by-Layer Deposition of Thermoresponsive Microgel Thin Films. *Langmuir* **2003**, *19*, 8759–8764.

[171] Sorrell, C. D.; Lyon, L. A. Bimodal Swelling Responses in Microgel Thin Films. *J. Phys. Chem. B* **2007**, *111*, 4060–4066.

[172] Pelton, R. H.; Chibante, P. Preparation of Aqueous Latices with N-Isopropylacrylamide. *Colloids Surf.* **1986**, *20*, 247–256.

[173] Vogel, N.; Retsch, M.; Fustin, C.-A.; del Campo, A.; Jonas, U. Advances in Colloidal Assembly: The Design of Structure and Hierarchy in Two and Three Dimensions. *Chem. Rev.* **2015**, *115*, 6265–6311.

[174] Kralchevsky, P. A.; Nagayama, K. Capillary Interactions between Particles Bound to Interfaces, Liquid Films and Biomembranes. *Adv. Colloid Interface Sci.* **2000**, *85*, 145–192.

[175] Dimitrov, A. S.; Nagayama, K. Continuous Convective Assembling of Fine Particles into Two-Dimensional Arrays on Solid Surfaces. *Langmuir* **1996**, *12*, 1303–1311.

[176] Schmidt, S.; Hellweg, T.; von Klitzing, R. Packing Density Control in P(NIPAM-co-AAc) Microgel Monolayers: Effect of Surface Charge, pH, and Preparation Technique. *Langmuir* **2008**, *24*, 12595–12602.

[177] Lu, Y.; Drechsler, M. Charge-Induced Self-Assembly of 2-Dimensional Thermosensitive Microgel Particle Patterns. *Langmuir* **2009**, *25*, 13100–13105.

[178] Quint, S. B.; Pacholski, C. Extraordinary Long Range Order in Self-Healing Non-Close Packed 2D Arrays. *Soft Matter* **2011**, *7*, 3735–3738.

[179] Vogel, N.; Weiss, C. K.; Landfester, K. From Soft to Hard: The Generation of Functional and Complex Colloidal Monolayers for Nanolithography. *Soft Matter* **2012**, *8*, 4044–4061.

[180] Pieranski, P. Two-Dimensional Interfacial Colloidal Crystals. *Phys. Rev. Lett.* **1980**, *45*, 569–572.

[181] Weekes, S. M.; Ogrin, F. Y.; Murray, W. A.; Keatley, P. S. Macroscopic Arrays of Magnetic Nanostructures from Self-Assembled Nanosphere Templates. *Langmuir* **2007**, *23*, 1057–1060.

[182] Lenzmann, F.; Li, K.; Kitai, A. H.; Stover, H. D. H. Thin-Film Micropatterning Using Polymer Microspheres. *Chem. Mater.* **1994**, *6*, 156–159.

[183] van Duffel, B.; Ras, R. H. A.; De Schryver, F. C.; Schoonheydt, R. A. Langmuir-Blodgett Deposition and Optical Diffraction of Two-Dimensional Opal. *J. Mater. Chem.* **2001**, *11*, 3333–3336.

[184] Reculusa, S.; Ravaine, S. Synthesis of Colloidal Crystals of Controllable Thickness through the Langmuir-Blodgett Technique. *Chem. Mater.* **2003**, *15*, 598–605.

[185] Sirotkin, E.; Apweiler, J. D.; Ogrin, F. Y. Macroscopic Ordering of Polystyrene Carboxylate-Modified Nanospheres Self-Assembled at the Water-Air Interface. *Langmuir* **2010**, *26*, 10677–10683.

[186] Burmeister, F.; Schäfle, C.; Matthes, T.; Böhmisch, M.; Boneberg, J.; Leiderer, P. Colloid Monolayers as Versatile Lithographic Masks. *Langmuir* **1997**, *13*, 2983–2987.

[187] Retsch, M.; Zhou, Z. C.; Rivera, S.; Kappl, M.; Zhao, X. S.; Jonas, U.; Li, Q. Fabrication of Large-Area, Transferable Colloidal Monolayers Utilizing Self-Assembly at the Air/Water Interface. *Macromol. Chem. Phys.* **2009**, *210*, 230–241.

[188] Meng, X.; Qiu, D. Gas-Flow-Induced Reorientation to Centimeter-Sized Two-Dimensional Colloidal Single Crystal of Polystyrene Particle. *Langmuir* **2014**, *30*, 3019–3023.

[189] Vogel, N.; Goerres, S.; Landfester, K.; Weiss, C. K. A Convenient Method to Produce Close- and Non-Close-Packed Monolayers using Direct Assembly at the Air-Water Interface and Subsequent Plasma-Induced Size Reduction. *Macromol. Chem. Phys.* **2011**, *212*, 1719–1734.

[190] Zhang, J.; Pelton, R. Poly(N-isopropylacrylamide) Microgels at the Air-Water Interface. *Langmuir* **1999**, *15*, 8032–8036.

[191] Nakahama, K.; Fujimoto, K. Thermosensitive Two-Dimensional Arrays of Hydrogel Particles. *Langmuir* **2002**, *18*, 10095–10099.

[192] Brugger, B.; Vermant, J.; Richtering, W. Interfacial Layers of Stimuli-Responsive Poly-(N-isopropylacrylamide-co-methacrylicacid) (PNIPAM-co-MAA) Microgels Characterized by Interfacial Rheology and Compression Isotherms. *Phys. Chem. Chem. Phys.* **2010**, *12*, 14573–14578.

[193] Geisel, K.; Isa, L.; Richtering, W. Unraveling the 3D Localization and Deformation of Responsive Microgels at Oil/Water Interfaces: A Step Forward in Understanding Soft Emulsion Stabilizers. *Langmuir* **2012**, *28*, 15770–15776.

[194] Destribats, M.; Lapeyre, V.; Wolfs, M.; Sellier, E.; Leal-Calderon, F.; Ravaine, V.; Schmitt, V. Soft Microgels as Pickering Emulsion Stabilisers: Role of Particle Deformability. *Soft Matter* **2011**, *7*, 7689–7698.

[195] Style, R. W.; Isa, L.; Dufresne, E. R. Adsorption of Soft Particles at Fluid Interfaces. *Soft Matter* **2015**, *11*, 7412–7419.

[196] Geisel, K.; Richtering, W.; Isa, L. Highly Ordered 2D Microgel Arrays: Compression Versus Self-Assembly. *Soft Matter* **2014**, *10*, 7968–76.

[197] Pinaud, F.; Geisel, K.; Massé, P.; Catargi, B.; Isa, L.; Richtering, W.; Ravaine, V.; Schmitt, V. Adsorption of Microgels at an Oil-Water Interface: Correlation between Packing and 2D Elasticity. *Soft Matter* **2014**, *10*, 6963–6974.

[198] Rey, M.; Fernández-Rodríguez, M. A.; Steinacher, M.; Scheidegger, L.; Geisel, K.; Richtering, W.; Squires, T. M.; Isa, L. Isostructural Solid-Solid Phase Transition in Monolayers of Soft Core-Shell Particles at Fluid Interfaces: Structure and Mechanics. *Soft Matter* **2016**, *12*, 3545–3557.

[199] Özlem Nazli, K.; Pester, C. W.; Konradi, A.; Böker, A.; van Rijin, P. Cross-Linking Density and Temperature Effects on the Self-Assembly of SiO_2-PNIPAAM Core-Shell Particles at Interfaces. *Chem. Eur. J.* **2013**, *19*, 5586–5594.

[200] Geisel, K.; Rudov, A. A.; Potemkin, I. I.; Richtering, W. Hollow and Core-Shell Microgels at Oil-Water Interfaces: Spreading of Soft Particles Reduces the Compressibility of the Monolayer. *Langmuir* **2015**, *31*, 13145–13154.

[201] Rauh, A.; Rey, M.; Barbera, L.; Zanini, M.; Karg, M.; Isa, L. Compression of Hard Core-Soft Shell Nanoparticles at Liquid-Liquid Interfaces: Influence of the Shell Thickness. *Soft Matter* **2017**, *13*, 158–169.

[202] Volk, K.; Fitzgerald, J. P. S.; Retsch, M.; Karg, M. Time-Controlled Colloidal Superstructures: Long-Range Plasmon Resonance Coupling in Particle Monolayers. *Adv. Mater.* **2015**, *27*, 7332–7337.

[203] Kaatz, F. H.; Bultheel, A.; Egami, T. Real and Reciprocal Space Order Parameters for Porous Arrays from Image Analysis. *J. Mater. Sci.* **2009**, *44*, 40–46.

[204] Kaatz, F. H. Measuring the Order in Ordered Porous Arrays: Can Bees Outperform Humans? *Naturwissenschaften* **2006**, *93*, 374–378.

[205] Scheeler, S. P.; Mühlig, S.; Rockstuhl, C.; Hasan, S. B.; Ullrich, S.; Neubrech, F.; Kudera, S.; Pacholski, C. Plasmon Coupling in Self-Assembled Gold Nanoparticle-Based Honeycomb Islands. *J. Phys. Chem. C* **2013**, *117*, 18634–18641.

[206] Pichler, S.; Bodnarchuk, M. I.; Kovalenko, M. V.; Yarema, M.; Springholz, G.; Talapin, D. V.; Heiss, W. Evaluation of Ordering in Single-Component and Binary Nanocrystal Superlattices by Analysis of Their Autocorrelation Functions. *ACS Nano* **2011**, *5*, 1703–1712.

[207] Heilbronner, R. P. The Autocorrelation Function: An Image Processing Tool for Fabric Analysis. *Tectonophysics* **1992**, *212*, 351–370.

[208] Weisstein, E. W. "Wiener-Khinchin Theorem." from *MathWorld* – a Wolfram Web Resource. http://mathworld.wolfram.com/Wiener-KhinchinTheorem.html.

[209] Turkevich, J.; Stevenson, P. C.; Hillier, J. A Study of the Nucleation and Growth Processes in the Synthesis of Colloidal Gold. *Discuss. Faraday Soc.* **1951**, *11*, 55–75.

[210] Wuithschick, M.; Birnbaum, A.; Witte, S.; Sztucki, M.; Vainio, U.; Pinna, N.; Rademann, K.; Emmerling, F.; Kraehnert, R.; Polte, J. Turkevich in New Robes: Key Questions Answered for the Most Common Gold Nanoparticle Synthesis. *ACS Nano* **2015**, *9*, 7052–7071.

[211] Bastús, N. G.; Merkoçi, F.; Piella, J.; Puntes, V. Synthesis of Highly Monodisperse Citrate-Stabilized Silver Nanoparticles of up to 200 nm: Kinetic Control and Catalytic Properties. *Chem. Mater.* **2014**, *26*, 2836–2846.

[212] Shan, J.; Tenhu, H. Recent Advances in Polymer Protected Gold Nanoparticles: Synthesis, Properties and Applications. *Chem Commun* **2007**, 4580–98.

[213] Vigderman, L.; Zubarev, E. R. High-Yield Synthesis of Gold Nanorods with Longitudinal SPR Peak Greater Than 1200 nm Using Hydroquinone as a Reducing Agent. *Chem. Mater.* **2013**, *25*, 1450–1457.

[214] Hale, G. M.; Querry, M. R. Optical Constants of Water in the 200-nm to 200-micron Wavelength Region. *Appl. Opt.* **1973**, *12*, 555–63.

[215] Koppel, D. E. Analysis of Macromolecular Polydispersity in Intensity Correlation Spectroscopy: The Method of Cumulants. *J. Chem. Phys.* **1972**, *57*, 4814–4820.

[216] Kohlbrecher, J. *SASfit: A Program for Fitting Simple Structural Models to Small Angle Scattering Data*. Paul Scherrer Institute, Laboratory for Neutron Scattering: Villigen Switzerland, 2014.

[217] Borsali, R.; Pecora, R. *Soft Matter Characterization*; Springer Science + Business Media, 2008.

[218] Scotti, A.; Liu, W.; Hyatt, J. S.; Herman, E. S.; Choi, H. S.; Kim, J. W.; Lyon, L. A.; Gasser, U.; Fernandez-Nieves, A. The Contin Algorithm and Its Application to Determine the Size Distribution of Microgel Suspensions. *J. Chem. Phys.* **2015**, *142*, 234905.

[219] Hiemenz, P. C. *Principles of Colloid and Surface Chemistry*, 2nd ed.; M. Dekker: New York, 1986.

[220] Karg, M. Functional Materials Design through Hydrogel Encapsulation of Inorganic Nanoparticles: Recent Developments and Challenges. *Macromol. Chem. Phys.* **2016**, *217*, 242–255.

[221] Serrano-Montes, A. B.; Jimenez de Aberasturi, D.; Langer, J.; Giner-Casares, J. J.; Scarabelli, L.; Herrero, A.; Liz-Marzán, L. M. A General Method for Solvent Exchange of Plasmonic Nanoparticles and Self-Assembly into SERS-Active Monolayers. *Langmuir* **2015**, *31*, 9205–13.

[222] Zhang, Z. Y.; Maji, S.; Antunes, A. B. D.; De Rycke, R.; Zhang, Q. L.; Hoogenboom, R.; De Geest, B. G. Salt Plays a Pivotal Role in the Temperature-Responsive Aggregation and Layer-by-Layer Assembly of Polymer-Decorated Gold Nanoparticles. *Chem. Mater.* **2013**, *25*, 4297–4303.

[223] Ehlert, S.; Taheri, S. M.; Pirner, D.; Drechsler, M.; Schmidt, H.-W.; Förster, S. Polymer Ligand Exchange to Control Stabilization and Compatibilization of Nanocrystals. *ACS Nano* **2014**, *8*, 6114–6122.

[224] Lista, M.; Liu, D. Z.; Mulvaney, P. Phase Transfer of Noble Metal Nanoparticles to Organic Solvents. *Langmuir* **2014**, *30*, 1932–1938.

[225] Duwez, A. S.; Guillet, P.; Colard, C.; Gohy, J. F.; Fustin, C. A. Dithioesters and Trithiocarbonates as Anchoring Groups for the "Grafting-To" Approach. *Macromolecules* **2006**, *39*, 2729–2731.

[226] Bastús, N. G.; Comenge, J.; Puntes, V. Kinetically Controlled Seeded Growth Synthesis of Citrate-Stabilized Gold Nanoparticles of up to 200 nm: Size Focusing Versus Ostwald Ripening. *Langmuir* **2011**, *27*, 11098–105.

[227] Fan, X. F.; Zheng, W. T.; Singh, D. J. Light Scattering and Surface Plasmons on Small Spherical Particles. *Light Sci. Appl.* **2014**, *3*, e179.

[228] Hendel, T.; Wuithschick, M.; Kettemann, F.; Birnbaum, A.; Rademann, K.; Polte, J. In Situ Determination of Colloidal Gold Concentrations with UV-Vis Spectroscopy: Limitations and Perspectives. *Anal. Chem.* **2014**, *86*, 11115–24.

[229] Thomas, D. B.; Convertine, A. J.; Myrick, L. J.; Scales, C. W.; Smith, A. E.; Lowe, A. B.; Vasilieva, Y. A.; Ayres, N.; McCormick, C. L. Kinetics and Molecular Weight Control of the Polymerization of Acrylamide via RAFT. *Macromolecules* **2004**, *37*, 8941–8950.

[230] Zhou, J.; Liu, H.; Wang, T.; Li, Y.; Zhang, J.; Lu, Z.; Fu, Y.; Li, F. Adjusting the Inter-Particle Spacing of a Nanoparticle Array at the Sub-Nanometre Scale by Thermal Annealing. *Chem. Commun.* **2014**, *50*, 14547–14549.

[231] Yoshida, A.; Imazu, K.; Li, X.; Okamoto, K.; Tamada, K. Spectroscopic Properties of Multilayered Gold Nanoparticle 2D Sheets. *Langmuir* **2012**, *28*, 17153–17158.

[232] Li, D. J.; Zhao, B. Temperature-Induced Transport of Thermosensitive Hairy Hybrid Nanoparticles between Aqueous and Organic Phases. *Langmuir* **2007**, *23*, 2208–2217.

[233] Bao, C. H.; Horton, J. M.; Bai, Z. F.; Li, D. J.; Lodge, T. P.; Zhao, B. Stimuli-Triggered Phase Transfer of Polymer-Inorganic Hybrid Hairy Particles between Two Immiscible Liquid Phases. *J. Polym. Sci. Part B: Polym. Phys.* **2014**, *52*, 1600–1619.

[234] Varga, I.; Gilányi, T.; Mészáros, R.; Filipcsei, G.; Zrínyi, M. Effect of Cross-Link Density on the Internal Structure of Poly(N-isopropylacrylamide) Microgels. *J. Phys. Chem. B* **2001**, *105*, 9071–9076.

[235] Mehrabian, H.; Harting, J.; Snoeijer, J. H. Soft Particles at a Fluid Interface. *Soft Matter* **2016**,

[236] Jain, P. K.; Huang, X.; El-Sayed, I. H.; El-Sayed, M. A. Noble Metals on the Nanoscale: Optical and Photothermal Properties and Some Applications in Imaging, Sensing, Biology, and Medicine. *Acc. Chem. Res.* **2008**, *41*, 1578–86.

[237] Link, S.; El-Sayed, M. A. Size and Temperature Dependence of the Plasmon Absorption of Colloidal Gold Nanoparticles. *J. Phys. Chem. B* **1999**, *103*, 4212–4217.

[238] Stockman, M. I. Nanoplasmonics: Past, Present, and Glimpse into Future. *Opt. Express* **2011**, *19*, 22029–22106.

[239] Tebbe, M.; Kuttner, C.; Mayer, M.; Männel, M.; Pazos-Perez, N.; König, T. A. F.; Fery, A. Silver-Overgrowth-Induced Changes in Intrinsic Optical Properties of Gold Nanorods: From Noninvasive Monitoring of Growth Kinetics to Tailoring Internal Mirror Charges. *J. Phys. Chem. C* **2015**, *119*, 9513–9523.

[240] Pattabhiraman, H.; Dijkstra, M. On the Formation of Stripe, Sigma, and Honeycomb Phases in a Core-Corona System. *Soft Matter* **2017**,

[241] Dotera, T.; Oshiro, T.; Ziherl, P. Mosaic Two-Lengthscale Quasicrystals. *Nature* **2014**, *506*, 208–211.

[242] Choi, M.; Kang, G.; Shin, D.; Barange, N.; Lee, C. W.; Ko, D. H.; Kim, K. Lithography-Free Broadband Ultrathin-Film Absorbers with Gap-Plasmon Resonance for Organic Photovoltaics. *ACS Appl. Mater. Interfaces* **2016**, *8*, 12997–3008.

[243] Manuel, J. M.; Seweryn, M.; Tiago, M.; Andriy, L.; Hugo, A.; Isabel, F.; Elvira, F.; Rodrigo, M.; Francesco, P.; Isodiana, C. Broadband Light Trapping in Thin Film Solar Cells with Self-Organized Plasmonic Nano-Colloids. *Nanotechnology* **2015**, *26*, 135202.

[244] Lim, E. L.; Yap, C. C.; Teridi, M. A. M.; Teh, C. H.; Yusoff, A. R. b. M.; Jumali, M. H. H. A Review of Recent Plasmonic Nanoparticles Incorporated P3HT:PCBM Organic Thin Film Solar Cells. *Org. Electron.* **2016**, *36*, 12–28.

[245] Lu, L.; Zheng, T.; Wu, Q.; Schneider, A. M.; Zhao, D.; Yu, L. Recent Advances in Bulk Heterojunction Polymer Solar Cells. *Chem. Rev.* **2015**, *115*, 12666–12731.

[246] Sungmo, A.; Devin, R.; Wounjhang, P. Plasmonic Nanostructures for Organic Photovoltaic Devices. *J. Opt.* **2016**, *18*, 033001.

[247] Stratakis, E.; Kymakis, E. Nanoparticle-Based Plasmonic Organic Photovoltaic Devices. *Mater. Today* **2013**, *16*, 133–146.

[248] King, D. L.; Hansen, B. R.; Kratochvil, J. A.; Quintana, M. A. Dark Current-Voltage Measurements on Photovoltaic Modules as a Diagnostic or Manufacturing Tool. Conference Record of the Twenty Sixth IEEE Photovoltaic Specialists Conference - 1997. 1997; pp 1125–1128.

[249] Liu, B.; Png, R.-Q.; Zhao, L.-H.; Chua, L.-L.; Friend, R. H.; Ho, P. K. H. High Internal Quantum Efficiency in Fullerene Solar Cells Based on Crosslinked Polymer Donor Networks. *Nat. Commun.* **2012**, *3*, 1321.

[250] Sha, W. E.; Li, X.; Choy, W. C. Breaking the Space Charge Limit in Organic Solar Cells by a Novel Plasmonic-Electrical Concept. *Sci. Rep.* **2014**, *4*, 6236.

[251] Wagenpfahl, A.; Rauh, D.; Binder, M.; Deibel, C.; Dyakonov, V. S-Shaped Current-Voltage Characteristics of Organic Solar Devices. *Phys. Rev. B* **2010**, *82*, 115306.

[252] Mihailetchi, V. D.; Wildeman, J.; Blom, P. W. M. Space-Charge Limited Photocurrent. *Phys. Rev. Lett.* **2005**, *94*, 126602.

[253] Kirchartz, T.; Agostinelli, T.; Campoy-Quiles, M.; Gong, W.; Nelson, J. Understanding the Thickness-Dependent Performance of Organic Bulk Heterojunction Solar Cells: The Influence of Mobility, Lifetime, and Space Charge. *J. Phys. Chem. Lett.* **2012**, *3*, 3470–3475.

[254] Di Nuzzo, D.; van Reenen, S.; Janssen, R. A. J.; Kemerink, M.; Meskers, S. C. J. Evidence for Space-Charge-Limited Conduction in Organic Photovoltaic Cells at Open-Circuit Conditions. *Phys. Rev. B* **2013**, *87*, 085207.

[255] Ray, B.; Baradwaj, A. G.; Khan, M. R.; Boudouris, B. W.; Alam, M. A. Collection-Limited Theory Interprets the Extraordinary Response of Single Semiconductor Organic Solar Cells. *Proc. Natl. Acad. Sci.* **2015**, *112*, 11193–11198.

[256] Chen, Y.; Dai, J.; Yan, M.; Qiu, M. Honeycomb-Lattice Plasmonic Absorbers at NIR: Anomalous High-Order Resonance. *Opt. Express* **2013**, *21*, 20873–9.

[257] Humphrey, A. D.; Barnes, W. L. Plasmonic Surface Lattice Resonances on Arrays of Different Lattice Symmetry. *Phys. Rev. B* **2014**, *90*, 075404.

[258] Väkeväinen, A. I.; Moerland, R. J.; Rekola, H. T.; Eskelinen, A. P.; Martikainen, J. P.; Kim, D. H.; Törmä, P. Plasmonic Surface Lattice Resonances at the Strong Coupling Regime. *Nano Lett.* **2014**, *14*, 1721–1727.

[259] Mahi, N.; Lévêque, G.; Saison, O.; Marae-Djouda, J.; Caputo, R.; Gontier, A.; Maurer, T.; Adam, P.-M.; Bouhafs, B.; Akjouj, A. In Depth Investigation of Lattice Plasmon Modes in Substrate-Supported Gratings of Metal Monomers and Dimers. *J. Phys. Chem. C* **2017**, *121*, 2388–2401.

[260] Humphrey, A. D.; Meinzer, N.; Starkey, T. A.; Barnes, W. L. Surface Lattice Resonances in Plasmonic Arrays of Asymmetric Disc Dimers. *ACS Photonics* **2016**, *3*, 634–639.

[261] Schatz, G. C. Electrodynamics of Nonspherical Noble Metal Nanoparticles and Nanoparticle Aggregates. *J. Mol. Struct. THEOCHEM* **2001**, *573*, 73–80.

[262] Luchnikov, V.; Kondyurin, A.; Formanek, P.; Lichte, H.; Stamm, M. Moirépatterns in Superimposed Nanoporous Thin Films Derived from Block-Copolymer Assemblies. *Nano Lett.* **2007**, *7*, 3628–3632.

[263] Oster, G.; Wasserman, M.; Zwerling, C. Theoretical Interpretation of Moiré Patterns. *J. Opt. Soc. Am.* **1964**, *54*, 169–175.

[264] Choi, J.; Wehrspohn, R. B.; Gösele, U. Moiré Pattern Formation on Porous Alumina Arrays Using Nanoimprint Lithography. *Adv. Mater.* **2003**, *15*, 1531–1534.

[265] Bamberg, J.; Cairns, G.; Kilminster, D. The Crystallographic Restriction, Permutations, and Goldbach's Conjecture. *Am. Math. Monthly* **2003**, *110*, 202–209.

[266] Stampfli, P. A Dodecagonal Quasiperiodic Lattice in Two Dimensions. *Helv. Phys. Acta* **1986**, *59*, 1260–1263.

[267] Mauer, M. E.; Stelling, C.; Kopera, B. A.; Nutz, F. A.; Karg, M.; Retsch, M.; Förster, S. Solution-Based Fabrication of Ordered Particle Arrays for All Two-Dimensional Bravais Lattices. *submitted to Nat. Nanotechnol.* **2017**,

[268] Lohse, S. E.; Burrows, N. D.; Scarabelli, L.; Liz-Marzán, L. M.; Murphy, C. J. Anisotropic Noble Metal Nanocrystal Growth: The Role of Halides. *Chem. Mater.* **2014**, *26*, 34–43.

[269] Grzelczak, M.; Perez-Juste, J.; Mulvaney, P.; Liz-Marzán, L. M. Shape Control in Gold Nanoparticle Synthesis. *Chem. Soc. Rev.* **2008**, *37*, 1783–1791.

[270] Scarabelli, L.; Sánchez-Iglesias, A.; Pérez-Juste, J.; Liz-Marzán, L. M. A "Tips and Tricks" Practical Guide to the Synthesis of Gold Nanorods. *J. Phys. Chem. Lett.* **2015**, *6*, 4270–4279.

[271] Mayer, M.; Scarabelli, L.; March, K.; Altantzis, T.; Tebbe, M.; Kociak, M.; Bals, S.; García de Abajo, F. J.; Fery, A.; Liz-Marzán, L. M. Controlled Living Nanowire Growth: Precise Control Over the Morphology and Optical Properties of AgAuAg Bimetallic Nanowires. *Nano Lett.* **2015**, *15*, 5427–5437.

[272] Pandian Senthil, K.; Isabel, P.-S.; Benito, R.-G.; de Abajo, F. J. G.; Liz-Marzán, L. M. High-Yield Synthesis and Optical Response of Gold Nanostars. *Nanotechnology* **2008**, *19*, 015606.

[273] Ballauff, M.; Lu, Y. "Smart" Nanoparticles: Preparation, Characterization and Applications. *Polymer* **2007**, *48*, 1815–1823.

[274] Karg, M.; Hellweg, T. Smart Inorganic/Organic Hybrid Microgels: Synthesis and Characterisation. *J. Mater. Chem.* **2009**, *19*, 8714–8727.

[275] Karg, M.; Wellert, S.; Prevost, S.; Schweins, R.; Dewhurst, C.; Liz-Marzán, L. M.; Hellweg, T. Well Defined Hybrid PNIPAM Core-Shell Microgels: Size Variation of the Silica Nanoparticle Core. *Colloid. Polym. Sci.* **2011**, *289*, 699–709.

[276] Volk, K.; Fitzgerald, J. P. S.; Ruckdeschel, P.; Retsch, M.; König, T. A. F.; Karg, M. Reversible Tuning of Visible Wavelength Surface Lattice Resonances in Self-Assembled Hybrid Monolayers. *Adv. Opt. Mater.* **2017**, 1600971.

[277] Shinotsuka, K.; Kajita, Y.; Hongo, K.; Hatta, Y. Crystal Perfection of Particle Monolayer at the Air-Water Interface. *Langmuir* **2015**, *31*, 11452–7.

Eidesstattliche Versicherungen und Erklärungen

(§5 Nr. 4 PromO)

Hiermit erkläre ich, dass keine Tatsachen vorliegen, die mich nach den gesetzlichen Bestimmungen über die Führung akademischer Grade zur Führung eines Doktorgrades unwürdig erscheinen lassen.

(§8 S.2 Nr. 5 PromO)

Hiermit erkläre ich mich damit einverstanden, dass die elektronische Fassung meiner Dissertation unter Wahrung meiner Urheberrechte und des Datenschutzes einer gesonderten Überprüfung hinsichtlich der eigenständigen Anfertigung der Dissertation unterzogen werden kann.

(§8 S.2 Nr. 7 PromO)

Hiermit erkläre ich eidesstattlich, dass ich die Dissertation selbstständig verfasst und keine anderen als die von mir angegebenen Quellen und Hilfsmittel benutzt habe.

(§8 S.2 Nr. 8 PromO)

Ich habe die Dissertation nicht bereits zur Erlangung eines akademischen Grades anderweitig eingereicht und habe auch nicht bereits diese oder eine gleichartige Doktorprüfung endgültig nicht bestanden.

(§8 S.2 Nr. 9 PromO)

Hiermit erkläre ich, dass ich keine Hilfe von gewerblichen Promotionsberatern bzw. -vermittlern in Anspruch genommen habe und auch künftig nicht nehmen werde.

.....

Ort, Datum, Unterschrift